**Unraveling Santa Barbara Basin Lithogenic Sediment Composition and Application to Southern California Quaternary Hydroclimate**

by

Tiffany J. Napier

A dissertation submitted in partial fulfillment
of the requirements for the degree of
Doctor of Philosophy
(Earth and Environmental Sciences)
in the University of Michigan
2017

Doctoral Committee:

Professor Ingrid L. Hendy, Chair
Associate Professor Marin Kristen Clark
Associate Professor Aline J. Cotel
Associate Research Scientist James D. Gleason
Professor Christopher James Poulsen

Tiffany J. Napier
tinapier@umich.edu
ORCID iD: 0000-0001-5982-8468

## DEDICATION

This dissertation is dedicated to my husband, my parents, brothers, and especially to my son, Alexander.

## ACKNOWLEDGEMENTS

First and foremost, I must thank my advisor, Ingrid Hendy, for taking me on as a student, believing in me, for her patience in teaching me, and for knowing how to get the most out of me (deadlines!). Thank you for letting me run with some of your ideas, and for helping me to develop my own and bring them into fruition. I would like to thank my committee for their guidance and for sitting through several, very long meetings. I especially need to thank Jamie Gleason, who has been instrumental in teaching me geochemistry and helping me to interpret the results of my provenance work.

Second, it takes a village to put together a research project, and so I thank the many people who helped me in sample prep and analysis. David, Ryan, Naomi, and Zach, who crushed, picked, weighed, split, and/or sieved, your help was critical, and I appreciate all the hours you spent in lab for me. Thank you Meghan W., for learning to wash, pick, and weigh foraminifera alongside me, so that I could get my oxygen isotope results as quickly as possible. Anja, Austin, Erin, and Jerry, without you I would have no idea how to prep samples for the XRD, run them, or interpret them. Flor, I am utterly indebted to you for the countless days you spent preparing my samples for REE and radiogenic isotope analysis. Wally, thank you for scanning several sections of core. Ethan, thank you for running my forams. Tim and Allie, thank you so much for all of your patience and answering all of my novice questions!

My collaborators have been essential to getting the most out of my data and helping me to understand my results. Arndt Schimmelmann, thank you for thoughtful discussions of SBB. Despite all of my pestering about offsets, Erik Brown has been essential for understanding the scanning XRF results. Linda Hinnov has been a joy to work with. Thank you for your constant enthusiasm, patience and teaching in all things time series analysis and statistics, help in interpretation, and your hospitality. Julie Bryce I must thank for your expertise in geochemistry and taking on a project with a student who knows (knew?) very little about it! I appreciate your patience, guidance, and editing of some dismal chapter drafts.

To my labmates, you have all been so wonderful and supportive. To Meghan, Allie, and Tim, thank you for reading some rough manuscripts and helping me to improve them, for interesting discussions of science and other things at happy hours. To Allie especially, thank you for your constant advice and encouragement. Katy, Xiaojing, and Yi, thank you for reading nearly half of this dissertation in the span of two months. I've sent you some pretty abysmal drafts and you've gamely read through them, and given insightful advice that has helped me to improve them.

Thank you to my wonderful family and amazing friends, both here in Michigan and afar. Your constant support has been essential to getting me to this point. My fellow grad students, you are all so supportive and helpful to one another. Thank you for all the camaraderie, encouragement, discussions, parties, and fun. You are lifelong friends. Mom and Dad, I know you probably weren't too sure about this choice that I made to attend grad school, but thank you for being supportive anyway. Thank you for fostering my curiosity, and instilling the values of hard work and tenacity–I wouldn't have gotten where I am without you.

Finally, I need to thank my new little family. Jimmy, you have been critical to me getting to the finish line. Thank you for being so supportive, and for pulling me out of the lows and helping celebrating the victories. Thank you for picking up the slack while I wrote this dissertation and prepared to defend. Thank you for being a loving husband and father. I love you. To my little Alex, thank you for being the happy, wonderful boy that you are. Thank you for your sometimes short, sometimes long, naps that allowed me to get some writing done. Thank you especially for being a new joy in my life. You are my baby; you'll always be mine.

Acknowledgement is made to the National Science Foundation, the Geological Society of America, the University of Michigan Rackham Graduate School, and the University of Michigan Earth and Environmental Sciences Department for funding that made this work possible.

## TABLE OF CONTENTS

## LIST OF TABLES

## LIST OF FIGURES

## LIST OF APPENDICES

## ABSTRACT

The demand for fresh water outpaces the supply in southern California. Fresh water resources will become increasingly limited as anthropogenic-forced air temperatures rise, and populations grow. Water management is challenging, as the hydroclimate of southern California is highly erratic, with intervals of drought punctuated by intense rainfall. This rainfall variability is influenced by the strength and position of the North Pacific high pressure system, atmospheric rivers, and the El Niño-Southern Oscillation (ENSO). Understanding the natural hydroclimate variability beyond the instrumental record is critical to meeting water resource management requirements.

On the coast of southern California Santa Barbara Basin (SBB) sediments preserve a record of flood deposits and annual rainfall, enabling hydroclimate reconstruction over millennia. In this dissertation, I analyze the natural and anthropogenic influences on SBB detrital sediment. In Chapter 2, I identify the provenance of Holocene flood deposits and Last Glacial Maximum (LGM) sediment in SBB through mineralogical and geochemical comparison to stream-bed sediments collected from adjacent river catchments. The southern slopes of the Santa Ynez and Topatopa Mountains are the primary source of Holocene flood deposits. Detrital sediment deposited during the LGM indicates increased sediment flux from the eastern Santa Ynez Mountain (Southern Slopes) and the Channel Islands, compensating the loss of Santa Clara River input at this time. In Chapter 3, I discern the impact of hydroclimate events and dam construction on SBB sediment composition since ~ A.D. 1760. Modeling results predict kaolinite and Ti content using precipitation, and indicate that Ti can be used as a paleoprecipitation proxy beyond the instrumental record. However, damming impounds sediment and impacts clay mineralogy disproportionately, indicating an anthropogenic impact on SBB sediments. In Chapter 4, I investigate southern California's natural hydroclimate variability during glacial Termination V ($T_V$, ~430-420 ka) using the siliciclastic elemental paleoprecipitation proxy developed for the annually laminated SBB sediments. Flooding, prolonged droughts, and ENSO variability are captured in the $T_V$ paleoprecipitation record, similar to the present. Prolonged

droughts are attributed to poleward expansion of the subtropical dry zone during deglaciation. Thus the precipitation patterns characterizing southern California hydroclimate are remarkably persistent through time.

# CHAPTER 1

## Introduction

California, particularly the southern portion, has limited fresh water resources. As anthropogenic climate change forces air temperatures to rise and as populations increase, water resources are expected to become increasingly stressed. Water availability and management has a significant societal impact in southern California, where the demand for fresh water outpaces the supply. Water management is further stressed by the geography of the state as nearly 75% of the population lives in the southern two-thirds of the state, but the majority of precipitation occurs in northern California (Dettinger et al., 2011). Furthermore, precipitation in southern California is highly erratic, with intervals of drought punctuated by intense precipitation events. This limited fresh water supply and increasing demand has resulted in diversion and transport of water southwards from other areas of the state that typically receive more precipitation (northern California, Sierra Nevada Mountains, Colorado River) (Los Angeles County Waterworks Districts, 2017).

Water availability is directly tied to the influence of climate on rainfall events, or hydroclimate. Southern California has a Mediterranean climate, with warm, dry summers and cool winters (Peel et al., 2007). This hydroclimate consists of two extremes: intense rainfall events in winter leading to flooding, and drought conditions when winter rains do not arrive. These extremes make water management in the region particularly challenging, as both flood control and water storage are necessary, and often in conflict with one another. While needed rainfall fills water-depleted reservoirs after intervals of drought, flood mitigation and reservoir fill capacity often require water to be released from storage.

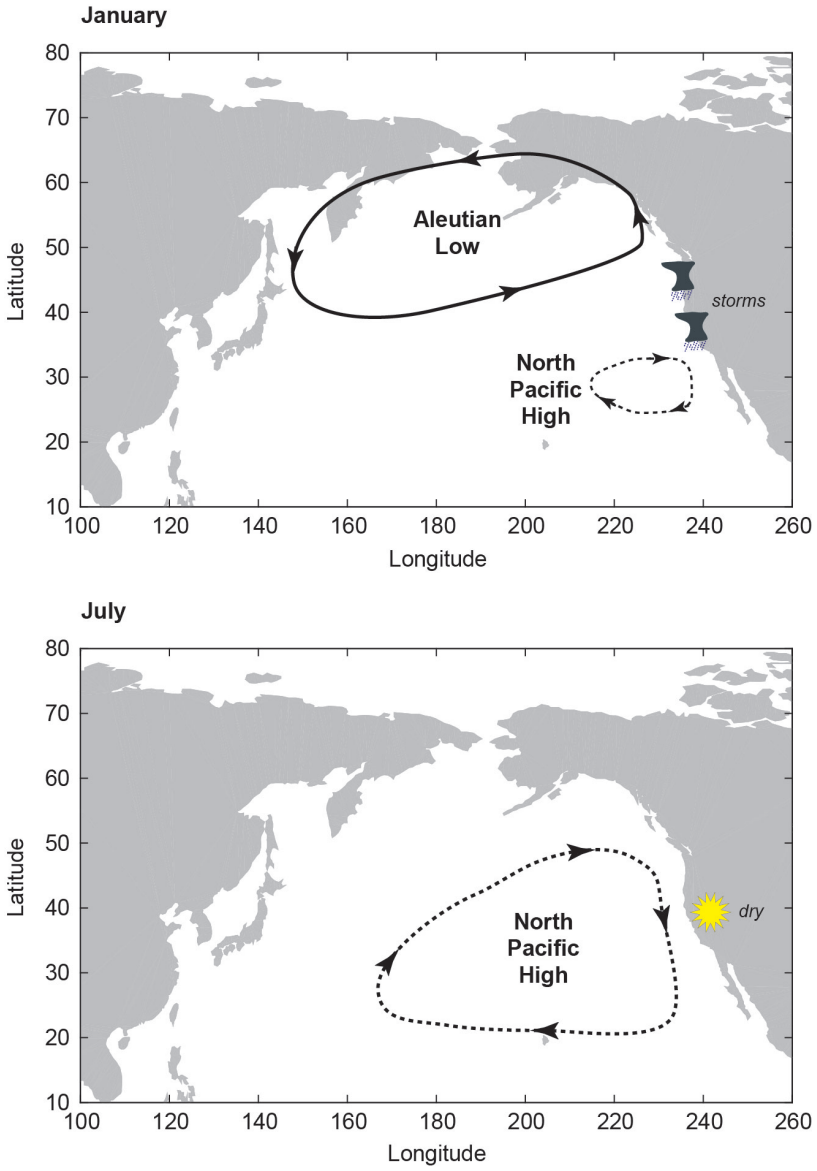


**Figure 1.1.** Average positioning of the semi-permanent North Pacific atmospheric pressure systems in January (top panel) and July (bottom panel).

The hydroclimate of southern California is determined by the strength and position of the North Pacific high pressure system (NPH) (Lu et al., 2003). In summer the NPH is located off the coast of southern California, and blocks moisture transport into the region (Figure 1.1). The NPH moves southwest in winter, allowing storm tracks to impact southern California. Droughts occur when the NPH is persistently positioned throughout the year off California. The recent 2012-2016 extreme drought was the result of this resilient NPH position (Swain et al., 2016). This drought was broken in the 2016-2017 winter by a series of intense precipitation events associated with atmospheric rivers—long, narrow bands (<1,000 km in width, >2,000 km in

length) of moisture in the atmosphere (Dettinger et al., 2011) (Figure 1.2). Over the span of three months, many California reservoirs rose from ~ 40% to 90% of capacity (California Department of Water Resources, 2017). However, flash flooding and landslides due to these precipitation events also impacted the region and led to infrastructural damage estimated to cost more than $539 million US dollars (Brown, 2017).

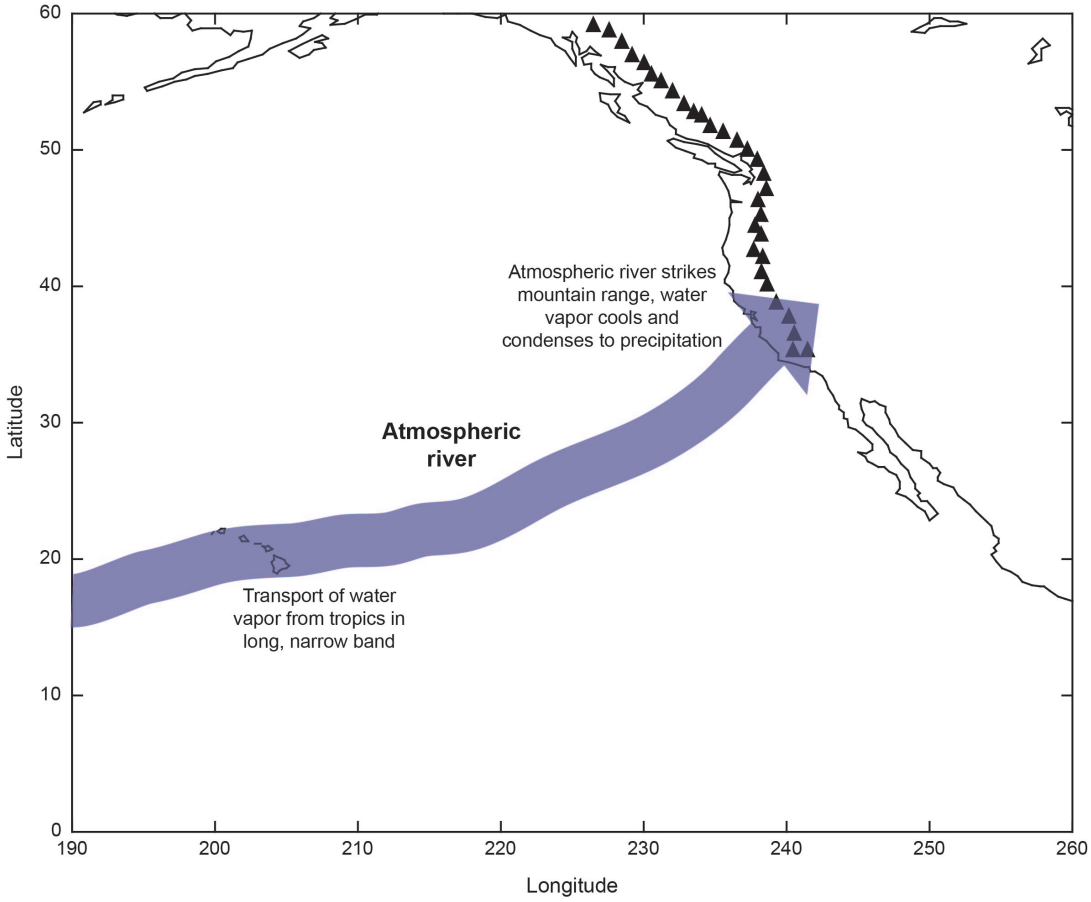


**Figure 1.2.** Simplified cartoon of an atmospheric river.

Precipitation in southern California is also influenced by the El Niño-Southern Oscillation (ENSO) (Andrews et al., 2004; Cayan et al., 1999; Dettinger et al., 1998; Hoell et al., 2016; Mo and Higgins, 1998; Schonher and Nicholson, 1989; Sun et al., 2015). This interannual climate phenomenon is related to the distribution of equatorial Pacific sea surface temperatures (SST) and atmospheric pressure systems. ENSO varies between La Niña, neutral, and El Niño phases. The neutral state of the equatorial Pacific consists of warm SSTs in the western Pacific and cool SSTs in the eastern Pacific (Figure 1.3). During a La Niña event, these conditions are

exaggerated. During an El Niño event, diminished trade winds lead a reduced east-west SST gradient such that warmer than average SSTs are observed off of coastal South America, and cooler than average SSTs occur in the western Pacific (Figure 1.3). In southern California, extreme precipitation events that result in flooding are more frequent during the El Niño phase. From 1950 to 1999, ~ 90% percent of flood events in the Santa Clara River catchment in southern California occurred during El Niño years (Warrick and Farnsworth, 2009).

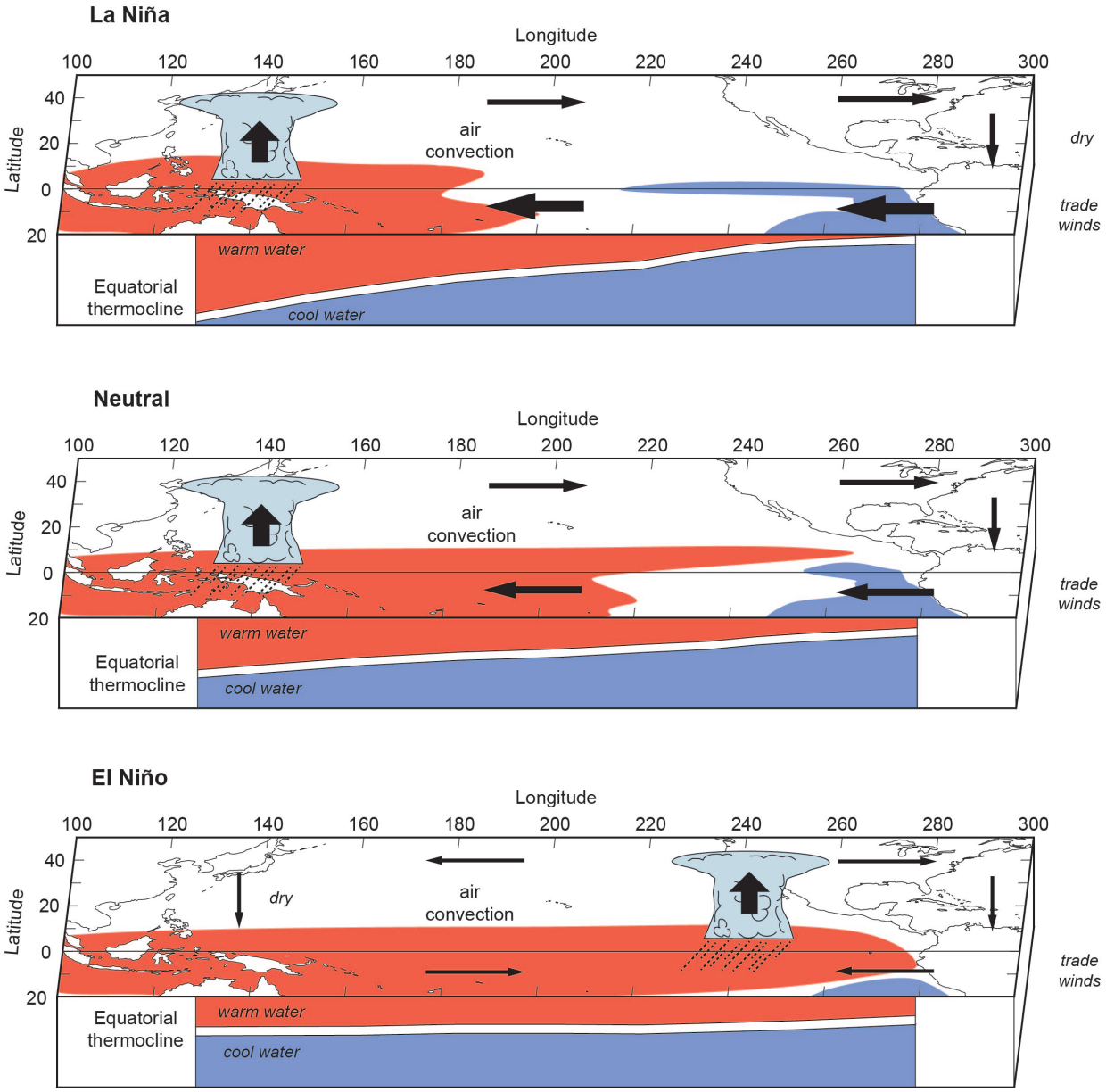


**Figure 1.3.** Simplified diagrams of atmospheric and oceanic conditions during La Niña, neutral, and El Niño phases.

Many studies have focused on the impact of anthropogenic climate change on precipitation in California through the 21st century using model ensembles. Projected changes in precipitation and drought are mostly extreme: extreme precipitation events and drought are predicted to become more frequent in California (Berg and Hall, 2015; Dettinger, 2011). In particular, the frequency of multiple atmospheric river event years is expected to increase (Dettinger, 2011), and atmospheric rivers are anticipated to make landfall further south, increasing the impact on southern California (Shields and Kiehl, 2016). Extreme dryness during the typical wet season is projected to become 1.5-2 times more common in the latter half of the 21st century (Berg and Hall, 2015). The increase in extreme events and greater precipitation variability will have a marked impact on the success of fresh water management in southern California, which will have to contend with both too much water during some years, and insufficient water during others. Additionally, since southern California receives most of its fresh water from other regions, water resource managers must also consider the climate change impact on water resources in those regions. In particular, decreased annual runoff, less snowfall, and earlier snowmelt are all expected in the Sierra Nevada Mountains (Pagán et al., 2016), which influences both the amount and timing of water transport to southern California. Anticipated rising temperatures, particularly in summer (Cayan et al., 2008), will increase evaporation in reservoirs and viaducts adding additional stress to southern California's water supply.

Water resource management in Southern California is important because the region's growing population requires a dependable fresh water supply year-round for consumption as well as protection from both flood and drought conditions. Understanding the natural hydroclimate variability of southern California is critical to meeting these water resource management obligations. Climate and weather records are key to understanding natural hydroclimate, however, instrumental precipitation records for the region are limited to the past 140 years—too short to realize the full range in hydroclimate conditions. The geologic record can be used to extend the instrumental record if a hydroclimate proxy can be identified. Sediment of terrestrial origin (terrigenous sediment) provides information about the erosion and transportation of rock material. For example, coastal rivers discharge terrigenous sediment into marine basins, and if this sediment is identifiable, well-preserved, and can be applied to a time scale, it can be used to extend the precipitation record back in time and determine the climate variability of the region.

## 1.1 Santa Barbara Basin

Santa Barbara Basin (SBB), located off the coast of southern California (Figure 1.4), preserves flood deposits and layered sediments (Figure 1.5) that record the region's hydroclimate at a yearly resolution. The layered sediments are composed of two-component laminae couplets, a biogenic (originating from organisms) component and a lithogenic (originating from rock) component, that together comprise an annual layer, or varve (Soutar and Crill, 1977; Thunell, 1998; Thunell et al., 1995). The biogenic component is deposited during the spring-summer, when the NPH moves poleward over California, inducing coastal upwelling, bringing nutrients to the photic zone, and stimulating primary production (Lynn and Simpson, 1987; Soutar and Crill, 1977; Thunell, 1998; Thunell et al., 1995). The movement of the NPH toward the equator in winter causes coastal upwelling to diminish and allows storms to enter the region. Precipitation from these storms generates river runoff that transports sediment from river catchments into SBB (Inman and Jenkins, 1999; Nezlin et al., 2005; Nezlin and Stein, 2005; Soutar and Crill, 1977; Thunell, 1998; Thunell et al., 1995; Warrick and Farnsworth, 2009; Warrick and Mertes, 2009). The bottom water in SBB has a low dissolved oxygen concentration, which prohibits macrofauna from colonizing the sediments, preventing bioturbation of the laminae couplets and allowing the sediments to be preserved. High sedimentation rates are the result of enhanced biogenic sediment deposition due to coastal upwelling-induced primary productivity, and high terrigenous sediment flux following precipitation events that results from highly erodible lithologies and active tectonics (Warrick and Mertes, 2009).

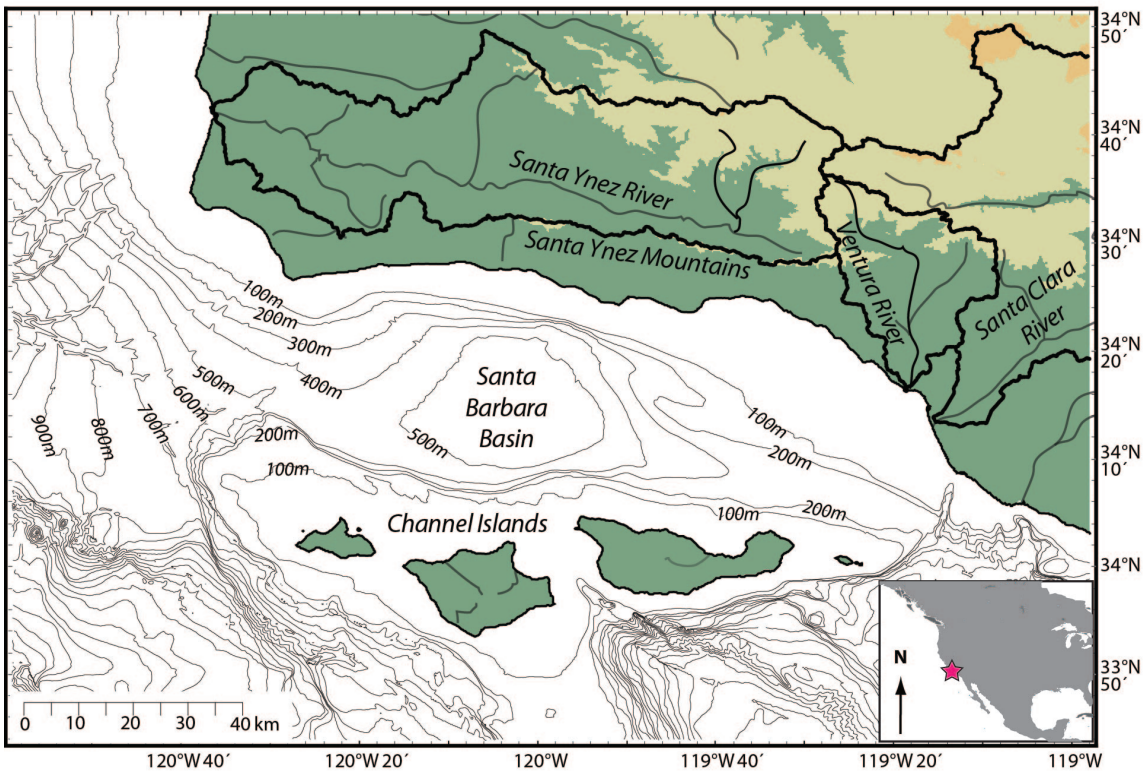


**Figure 1.4.** Map of study area in southern California, including Santa Barbara Basin and local river catchments.

**Figure 1.5.** Image of a typical Santa Barbara Basin sediment core, featuring laminations and thick gray flood deposits. Marked buttons at top of image are spaced in 10 cm increments.

The terrigenous component of SBB sediments is derived from rocks and their weathering products eroded from the catchments of the Santa Clara River, Ventura River, the southern

flanks of the Santa Ynez Mountains, the northern flanks of the Channel Islands, with a minor contribution from the Santa Ynez River (Figure 4) (Fleischer, 1972; Robert, 2004). As rocks are exposed to physical and chemical weathering processes, their constituent minerals break down and are chemically altered into weathering products such as clay minerals. Climate, rock type/parent material, vegetation, topography, and time all play a role in the weathering process (Mitchell and Soga, 2005). Plagioclase feldspars, pyroxenes, and amphiboles are easily chemically weathered, while potassium feldspars and quartz are resistant to weathering (Goldich, 1938). During the chemical weathering process, labile elements such as Ca, Na, Mg, and K are leached by drainage water, while Al, Fe, and Ti are retained (Goldich, 1938). Erodible material in the river catchments is primarily composed of sandstone and shale sedimentary units that contain resistant minerals and relatively immobile elements, while igneous and metamorphosed units located in the Santa Clara and Santa Ynez River catchments, and on Santa Cruz Island contain less resistant minerals and labile elements (Yerkes and Campbell, 2005). As sediments are transported downstream, the less resistant minerals are subject to abrasion due to physical interaction during transport and dissolution as the labile elements are lost from the sediment load. Therefore the mineralogy, geochemistry, and grain size of the lithogenic component of SBB sediments is predictably different from its sediment sources in the catchments, being primarily composed of fine-grained quartz and clay minerals (Fleischer, 1972).

### 1.2 Instrumental methods for determining sediment composition

The composition of the lithogenic sediments in SBB provides important information about from where sediment is eroded, its transportation, and the influence of climate on these processes. Determining where terrigenous sediments are being eroded from, in particular the sediments deposited in flood layers, identifies terrestrial areas that are at-risk to flooding and mass movement. Additionally, if sediment source regions have changed through time due to regional tectonics, global climate, or anthropogenic modification of stream systems, the composition of the lithogenic component will reflect these changes. The presence of terrigenous sediments in marine systems is related to precipitation and river runoff, and therefore can be used to understand hydroclimate regimes and variability in the past. A number of techniques were employed to identify and measure the lithogenic component in the river catchments draining into SBB and in sediment cores from the basin. Mineral composition is determined using X-ray

diffraction (XRD), a technique that takes advantage of the similarity between X-ray wavelengths and the atomic spacing in mineral crystal lattices. During XRD measurements, X-rays are directed towards a sample at a range of different diffraction angles. When the interaction of the X-rays and minerals in the sample produce constructive interference, the diffracted X-rays are detected and a peak in measured intensity is recorded. Constructive interference occurs when the geometry of the incident X-rays and the sample satisfy the Bragg equation ($n\lambda = 2d \sin \theta$; Figure 1.6). The unique crystal structure of each mineral results in a characteristic XRD spectrum, enabling mineral identification.

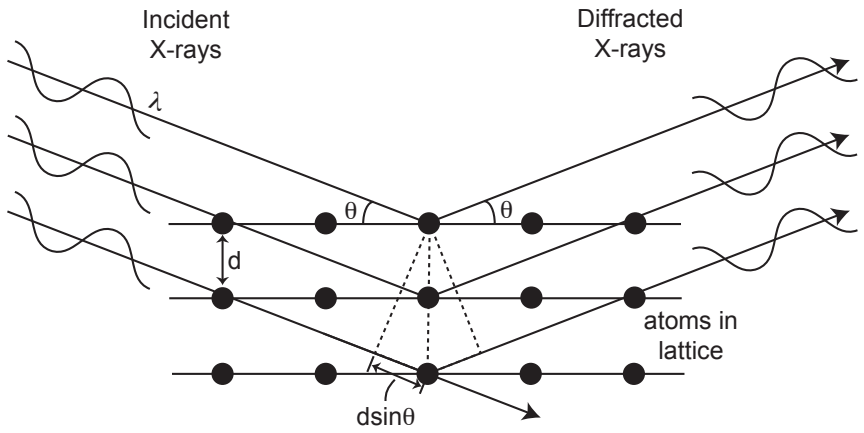


**Figure 1.6.** Diagram illustrating the Bragg equation used in X-ray diffraction.

Elemental composition of SBB sediments is determined using a number of techniques including scanning X-ray fluorescence (XRF), optical emission spectrometry, and mass spectrometry. Scanning XRF is a non-destructive method of obtaining elemental profiles at ultra-high resolution (down to 200 μm) (Croudace et al., 2006). X-ray radiation is used to eject an inner shell electron from an atom, and then an outer shell electron drops to the inner shell to fill-in the vacancy (Figure 1.7). The movement of an electron from an outer shell to an inner shell results in the release of energy as an X-ray photon, also called fluorescence. The amount of energy released during this process is unique to each element, and this is utilized to determine elemental composition via XRF. Although scanning XRF is a semi-quantitative analysis technique, it provides elemental information at 2-7 data points per year in SBB sediments (Hendy et al., 2015)—a resolution unobtainable by any other elemental determinative method. Further, sediment cores contain limited material for destructive analyses of samples, and samples are often split among numerous paleoclimate and paleoceanographic studies. Additionally,

collecting the sediment cores themselves is an expensive and time consuming undertaking, therefore the scanning XRF technique is useful for obtaining elemental information while still preserving the core material.

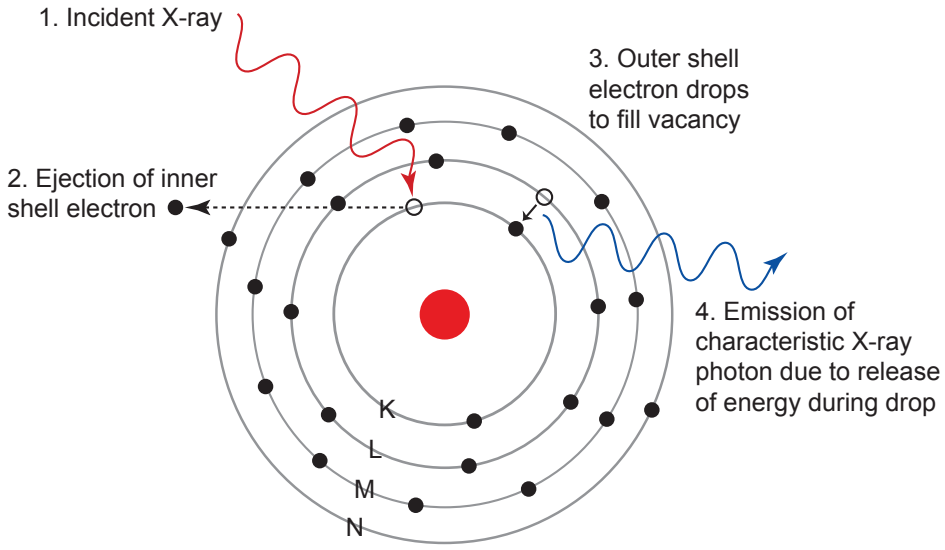


**Figure 1.7.** Cartoon detailing the X-ray fluorescence phenomenon in an atom.

The scanning XRF results are verified using inductively coupled plasma-optical emission spectrometry and inductively coupled plasma-mass spectrometry. These techniques utilize unique and characteristic emission spectra and charge-to-mass ratios, respectively. Spectrometry techniques are beneficial because they are quantitative, but they are destructive and require more sample material, leading to a lower-resolution and an averaging of the elemental composition among several years. These analyses are used to determine the elemental composition of sediments, and the quantitative results produced enable direct comparison to sample mineralogy.

### 1.3 Unraveling SBB lithogenic sediment composition and application to southern California hydroclimate: outline of investigations presented in this dissertation

This dissertation is divided into three data chapters, (Chapters 2-4) and two appendices that contain information that supplements each data chapter, as well as data tables. Chapter 2 provides the groundwork for understanding the transport of the lithogenic component into SBB by mapping the origin of the lithogenic component that is delivered to SBB via streams. Modern

SBB and Holocene flood deposit compositions should reflect catchment sources that were eroded during an extreme weather event. Thus I can identify areas susceptible to flooding which will reduce the societal impact of extreme rain events in southern California. I determined the mineralogy, elemental concentrations, and strontium and neodymium isotopes of numerous stream bed samples and SBB flood layers. Source area composition groups were then characterized using these mineralogical and geochemical results, and compared to the flood layer composition to determine the catchment sources of flood sediments. As a result I was able to identify the provenance of flood layers preserved in SBB sediments.

Chapter 3 (Napier and Hendy) investigates the geochemistry and mineral composition of SBB sediments deposited within the past ~250 years, from before the arrival of Europeans to the heavily modified catchments of the present day. I determine if hydroclimate events and variability are recorded by the lithogenic component, and discern if anthropogenic modifications within the river catchments discharging into SBB have impacted the composition of the lithogenic component. Specifically, I generated semi-quantitative clay mineral concentrations and quantitative elemental concentrations through time, and compared them with precipitation, river flow, climatological indices, and the amount of catchment area blocked by dams.

In Chapter 4, I examined the natural hydroclimate variability of southern California at an annual resolution during the transition from glacial Marine Isotope Stage (MIS) 12 to interglacial MIS 11, also known as Termination V (~424 ka). I reconstructed a precipitation record for this time interval to determine the persistence of El Niño and its impact on California hydroclimate. To do this, I applied a paleoprecipitation proxy developed for annually laminated SBB sediments to well-preserved laminated intervals in sediment cores deposited during Termination V. This proxy utilizes high-resolution scanning XRF counts of elements associated with the lithogenic component, where high counts are associated with increased precipitation and river runoff, and low counts are associated with drought. I then use this precipitation proxy and time series analysis techniques to identify dominant precipitation cycles and drought intervals during this deglacial transition. In Chapter 5, I summarize the major findings of the dissertation, and discuss the applicability of this work and future research directions.

## 1.4 References


Andrews, E.D., Antweiler, R.C., Neiman, P.J., Ralph, F.M., 2004. Influence of ENSO on flood frequency along the California Coast. J. Climate 17, 337-348.

Berg, N., Hall, A., 2015. Increased Interannual Precipitation Extremes over California under Climate Change. J. Climate 28, 6324-6334.

Brown, E.G., Jr., 2017. March 19, 2017 Presidential Disaster Declaration Request Letter, in: California, O.o.t.G.o. (Ed.), p. 6.

California Department of Water Resources, Reservoirs. California Data Exchange Center.

Cayan, D.R., Maurer, E.P., Dettinger, M.D., Tyree, M., Hayhoe, K., 2008. Climate change scenarios for the California region. Clim. Change 87, 21-42.

Cayan, D.R., Redmond, K.T., Riddle, L.G., 1999. ENSO and hydrologic extremes in the Western United States. J. Climate 12, 2881-2893.

Croudace, I.W., Rindby, A., Rothwell, R.G., 2006. ITRAX: description and evaluation of a new multi-function X-ray core scanner. Geol. Soc. London Spec. Publ. 267, 51-63.

Dettinger, M., 2011. Climate Change, Atmospheric Rivers, and Floods in California – A Multimodel Analysis of Storm Frequency and Magnitude Changes1. JAWRA Journal of the American Water Resources Association 47, 514-523.

Dettinger, M.D., Cayan, D.R., Diaz, H.F., Meko, D.M., 1998. North-south precipitation patterns in western North America on interannual-to-decadal timescales. J. Climate 11, 3095-3111.

Dettinger, M.D., Ralph, F.M., Das, T., Neiman, P.J., Cayan, D.R., 2011. Atmospheric Rivers, Floods and the Water Resources of California. Water 3, 445-478.

Fleischer, P., 1972. Mineralogy and sedimentation history, Santa Barbara Basin, California. J. Sed. Res. 42, 49-58.

Goldich, S.S., 1938. A Study in Rock-Weathering. J. Geol. 46, 17-58.

Hendy, I.L., Napier, T.J., Schimmelmann, A., 2015. From extreme rainfall to drought: 250 years of annually resolved sediment deposition in Santa Barbara Basin, California. Quatern. Int. 387, 3-12.

Hoell, A., Hoerling, M., Eischeid, J., Wolter, K., Dole, R., Perlwitz, J., Xu, T., Cheng, L., 2016. Does El Niño intensity matter for California precipitation? GeoRL 43, 819-825.

Inman, D.L., Jenkins, S.A., 1999. Climate change and the episodicity of sediment flux of small California rivers. J. Geol. 107, 251-270.

Los Angeles County Waterworks Districts, 2017. Water Sources, https://dpw.lacounty.gov/wwd/web/YourWater/WaterSources.aspx.

Lu, R., Turco, R.P., Stolzenbach, K., Friedlander, S.K., Xiong, C., Schiff, K., Tiefenthaler, L., Wang, G., 2003. Dry deposition of airborne trace metals on the Los Angeles Basin and adjacent coastal waters. Journal of Geophysical Research: Atmospheres 108, n/a-n/a.

Lynn, R.J., Simpson, J.J., 1987. The California Current system: The seasonal variability of its physical characteristics. J. Geophys. Res. Oceans 92, 12947-12966.

Mitchell, J.K., Soga, K., 2005. Fundamentals of soil behavior, Third ed. John Wiley & Sons, Hoboken, NJ.

Mo, K.C., Higgins, R.W., 1998. Tropical Influences on California Precipitation. J. Climate 11, 412-430.

Napier, T.J., Hendy, I.L., in press. The impact of hydroclimate and dam construction on terrigenous detrital sediment composition in a 250-year Santa Barbara Basin record off southern California. Quatern. Int.

Nezlin, N.P., DiGiacomo, P.M., Stein, E.D., Ackerman, D., 2005. Stormwater runoff plumes observed by SeaWiFS radiometer in the Southern California Bight. Remote Sens. Environ. 98, 494-510.

Nezlin, N.P., Stein, E.D., 2005. Spatial and temporal patterns of remotely-sensed and field-measured rainfall in southern California. Remote Sens. Environ. 96, 228-245.

Pagán, B.R., Ashfaq, M., Rastogi, D., Kendall, D.R., Kao, S.-C., Naz, B.S., Mei, R., Pal, J.S., 2016. Extreme hydrological changes in the southwestern US drive reductions in water supply to Southern California by mid century. Environmental Research Letters 11, 094026.

Peel, M.C., Finlayson, B.L., McMahon, T.A., 2007. Updated world map of the Köppen-Geiger climate classification. HESS 11, 1633.

Robert, C., 2004. Late Quaternary variability of precipitation in Southern California and climatic implications: clay mineral evidence from the Santa Barbara Basin, ODP Site 893. Quatern. Sci. Rev. 23, 1029-1040.

Schonher, T., Nicholson, S.E., 1989. The relationship between California rainfall and ENSO events. J. Climate 2, 1258-1269.

Shields, C.A., Kiehl, J.T., 2016. Atmospheric river landfall-latitude changes in future climate simulations. GeoRL 43, 8775-8782.

Soutar, A., Crill, P.A., 1977. Sedimentation and climatic patterns in the Santa Barbara Basin during the 19th and 20th centuries. Geol. Soc. Am. Bull. 88, 1161-1172.

Sun, X., Renard, B., Thyer, M., Westra, S., Lang, M., 2015. A global analysis of the asymmetric effect of ENSO on extreme precipitation. JHyd 530, 51-65.

Swain, D.L., Horton, D.E., Singh, D., Diffenbaugh, N.S., 2016. Trends in atmospheric patterns conducive to seasonal precipitation and temperature extremes in California. Science Advances 2.

Thunell, R.C., 1998. Particle fluxes in a coastal upwelling zone: sediment trap results from Santa Barbara Basin, California. Deep-Sea Res. Pt. II 45, 1863-1884.

Thunell, R.C., Tappa, E., Anderson, D.M., 1995. Sediment fluxes and varve formation in Santa Barbara Basin, offshore California. Geology 23, 1083-1086.

Warrick, J.A., Farnsworth, K.L., 2009. Sources of sediment to the coastal waters of the Southern California Bight. Geol. Soc. Am. Spec. Pap. 454, 39-52.

Warrick, J.A., Mertes, L.A.K., 2009. Sediment yield from the tectonically active semiarid Western Transverse Ranges of California. Geol. Soc. Am. Bull. 121, 1054-1070.

Yerkes, R.F., Campbell, R.H., 2005. Preliminary Geologic Map of the Los Angeles 30' x 60' Quadrangle, Southern California, USGS Open-File Report 2005-1019, pp. 2-51 p.

# CHAPTER 2

## Identification of onshore sources of Santa Barbara Basin flood deposits and glacial sediments


### Abstract

Southern California is prone to intense precipitation events that result in flooding—events expected to become more extreme and frequent with anthropogenic climate change. Detrital terrestrial sediments preserved in marine basins that contain distinct geochemical identifiers of provenance can be used to identify the on-shore sources of flood deposits. Santa Barbara Basin (SBB), offshore of southern California, contains a continuous Holocene flood record that can provide insights into the frequency and changes in on-shore sources across time for such events. This study characterizes SBB-adjacent sediment sources using mineralogical, elemental, and radiogenic strontium (Sr) and neodymium (Nd) isotopic compositions of stream bed sediments. Modern and Holocene flood deposits and Last Glacial Maximum (LGM) sediment samples collected from SBB sediment cores were similarly analyzed, and compared to the stream bed sediments to provide insight into areas of the catchment that are undergoing rapid denudation, and to elucidate changes in sediment transport into SBB during past eustatic sea level low stands. The Southern Slopes of the Santa Ynez Mountains, drained by the Ventura River and mountain streams, account for ~80% of SBB Holocene flood deposit sediment and together with the Western Santa Clara sub-catchment (Topatopa Mountains), is a primary source of flood sediment. The contribution from the Southern Slopes increased (to ~90%) during the LGM. The Santa Clara River appears to have bypassed SBB during the LGM sea level low stand, but this input loss was compensated by increased sediment flux from the Southern Slopes and the Channel Islands. In sum, the southern slopes of the Santa Ynez and Topatopa Mountains are particularly at-risk to denudation during flooding in southern California.

## 2.1 Introduction

Extreme precipitation events and resulting floods are costly hazards to society (Porter et al., 2011). The U.S. West Coast is prone to extreme events that result in intense precipitation and flooding within a few days. The recent USGS ARkStorm project, modeled after the Great Flood of 1861-62 on the West Coast, has revealed the impacts associated with these extreme rain events including: high winds, severe flooding, landslides, and property, infrastructure, and agriculture loss (Porter et al., 2011). In total, such a storm is estimated to cost state and federal governments ~$700 billion (Porter et al., 2011). The frequency of years with multiple extreme precipitation events impacting the West Coast is expected to increase with anthropogenic climate change (Berg and Hall, 2015; Dettinger, 2011), with notable increases in storm landfall predicted for southern California (Shields and Kiehl, 2016).

The Great Flood of 1861-62 flooded California's Central Valley (Ingram et al., 2013). As severe flooding on this scale has not occurred in California during the modern instrumental period, the ability to assess the risks associated with these rare flood hazards is limited. Detrital terrestrial sediments preserved in marine basins contain geochemical identifiers specific to eroded rock sources (Kovach and Faure, 1977; Nardone and Faure, 1978; Walter et al., 2000) and could be employed to identify the sources of sediment eroded during past floods. Such investigations into flood deposit provenance, accordingly, could then provide insights into areas likely to be at-risk to erosion and property damage during future events.

Offshore of southern California, Santa Barbara Basin (SBB) contains annually laminated sediments that have been widely used in paleoclimatic reconstructions. Although the basin contains a continuous flood record, terrestrial sediment linkages remain poorly resolved (Fleischer, 1972; Robert, 2004; Warrick and Mertes, 2009). The river catchments that discharge sediment into SBB contain compositionally distinct rock types (Critelli et al., 1997; Fan, 1976; Jacobson et al., 2011) that can be used to determine the provenance of SBB flood deposits. Fleischer (1972) compared semi-quantitative clay mineral concentrations from a SBB sediment core to bed-load and suspended load sediment from adjacent streams in order to identify the provenance of SBB flood deposits, and determined the Santa Clara River catchment was likely the primary source of flood sediment. However, Warrick and Mertes (2009) have shown that sediment discharge computed from stream gauge data is greatest along the lithologically weak southern flanks of the Santa Ynez Mountains and Topatopa Mountains, which includes the

southwestern Santa Clara River catchment, the Ventura River catchment, and the southern drainages of the Sana Ynez Mountains (Figure 2.1). Therefore there are two competing hypotheses for the source of SBB flood deposits: 1) the Santa Clara River catchment (Fleischer, 1972; Robert, 2004), or 2) the weak lithologies of the Santa Ynez Mountains' and Topatopa Mountains' southern flanks captured by multiple catchments (Warrick and Mertes, 2009).

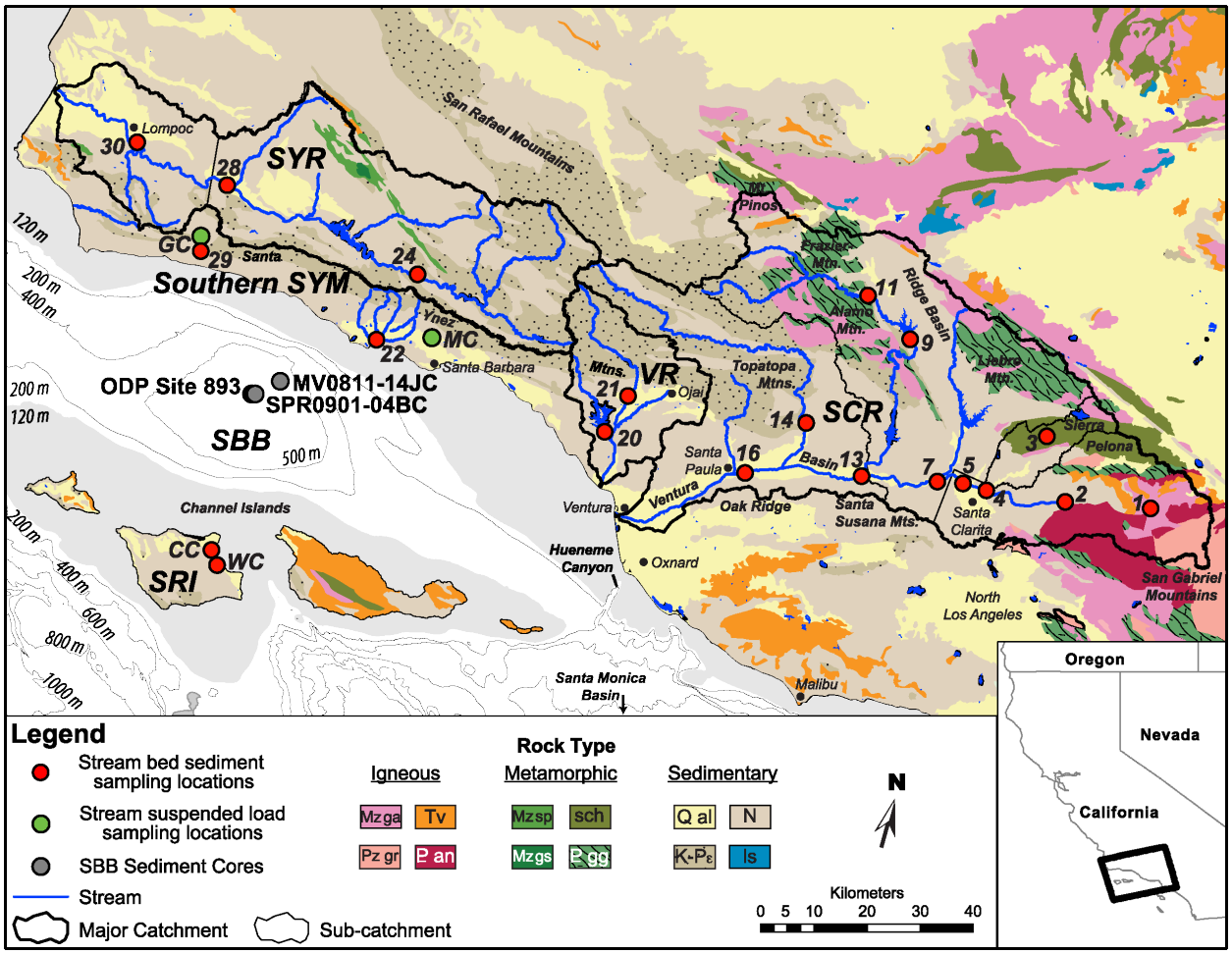


**Figure 2.1.** Simplified geologic map of the study area and sample locations (red and green circles), including Santa Barbara Basin (SBB) and location of sediment cores SPR0901-04BC, MV0811-14JC, and ODP site 893 (gray circles).
Sample location abbreviations: GC–Gaviota Creek, MC–Mission Creek, CC–Cherry Canyon, WC–Water Canyon. River catchments are outlined in black: Santa Ynez River (SYR), Santa Ynez Mountains (SYM), Ventura River (VR), Santa Clara River (SCR), and Santa Rosa Island (SRI). Selected streams are shown by blue lines. Bathymetry contour interval is 200 m; bathymetry ≤120 m is shaded in gray. Rock symbols: Tv–Tertiary volcanics, Mz ga–Mesozoic gabbro, Pz gr–Paleozoic granitoid, P an–Proterozoic anorthosite complex, Mz sp–Mesozoic serpentinite, Mz gs–Mesozoic greenstone, sch–schist, P gg–Proterozoic gneiss and granitoid, Q al–Quaternary alluvium, N–Neogene sandstone, shale, mudstone, and/or conglomerate, K-Pε–Cretaceous through Paleogene sandstone, shale, mudstone, and/or conglomerate, ls–limestone. Geologic data from Ludington et al. (2005). Hydrologic data from the National Hydrology Dataset Plus, Version 2 (McKay, 2012). Bathymetry from Global Multi-Resolution Topography version 2.6 (Ryan et al., 2009).

Sediment sources to SBB have likely not been constant through time. Sedimentation rate increases, coarse grain deposition, and fan progradation in Santa Monica Basin, southeast of SBB, all suggest that the Santa Clara River, and potentially also the Ventura River, bypassed SBB during the sea level low stand of the Last Glacial Maximum (LGM; 26.5-19.0 ka, Clark et al., 2009) (Normark et al., 2006). However sedimentation rates in SBB during the LGM did not change appreciably to account for this significant input loss (Hendy et al., 2002; Hill et al., 2006). Taken together, these studies suggest two possibilities. If the source of sediments deposited did not change between the Holocene and the LGM, then our understanding of modern sedimentation is incomplete, as the Santa Clara River cannot then be the dominant sediment source to SBB. However if the Santa Clara River is the predominant sediment source to SBB, then another source(s) replaced Santa Clara River sediment that bypassed the basin during the LGM sea level lowstand.

This study employs mineralogical and geochemical characterizations of SBB flood and LGM deposits, and catchment sediments to identify the provenance of eroded material. Stream bed sediment samples were collected from the catchments that discharge sediment into SBB, and modern and Holocene flood deposits and LGM sediments were collected from SBB sediment cores. These samples are analyzed and compared in order to understand changes in sediment transport during past global sea level stands and flood events so that areas subject to flooding risk can be identified.

## 2.2 Background

Santa Barbara Basin is bounded by the Santa Ynez Mountains to the north, the Channel Islands to the south, and to the east and west by submarine sills (Figure 2.1). The Santa Clara River (SCR), Ventura River (VR), southern Santa Ynez Mountains (southern SYM) drainages, and northern Channel Island drainages discharge into SBB, with potential input from the Santa Ynez River (SYR) through littoral drift. Regional rivers are ephemeral throughout most of the year, with the average annual sediment load discharged in less than 25 days (Warrick and Farnsworth, 2009; Warrick and Mertes, 2009). Precipitation events generate brief, but intense, sediment-laden discharge from the catchments that is dispersed both in the surface ocean and the subsurface via hyperpycnal plumes before deposition in SBB (Thornton, 1984; Thornton, 1986; Warrick and Farnsworth, 2009; Warrick et al., 2008).

Southern California has a semiarid mediterranean climate with cool winters and hot, dry summers that is moderated by the North Pacific High pressure system (Lora et al., 2016). In summer, the high pressure system blocks storm fronts from impacting the region, resulting in diminished precipitation. In winter the North Pacific High moves southwest, allowing storms to enter the region (Lu et al., 2003). Extreme precipitation is associated with atmospheric rivers—long, narrow plumes (<1,000 km wide, > 2,000 km in length) of water vapor in the atmosphere (Dettinger et al., 2011). In the winter of 2016-2017, several atmospheric river events intersecting California produced more than a meter of precipitation, generating flooding and landslides (Rosen, 2017). These extreme precipitation events produce hyperpycnal plumes (Warrick and Milliman, 2003) that deposit clay-rich sediments, which are preserved as gray flood layers in SBB (Fleischer, 1972; Robert, 2004; Schimmelmann et al., 1998; Thornton, 1984). Precipitation from winter storms, including atmospheric rivers, increases the detrital sediment flux to SBB, although the amount of suspended load in the river runoff is influenced by the length of time between rain events; vegetation cover, catchment geology, tectonics, and relief, as well as human modification of the landscape (Inman and Jenkins, 1999; Nezlin and Stein, 2005; Warrick and Mertes, 2009). The western SYR catchment, the Santa Ynez Mountains, the northeastern VR catchment, and the western SCR catchment receive the most precipitation in the study area, while the eastern SCR catchment and the Channel Islands receive the least (Figure 2.2A).

### *2.2.1 Geology of study area*

The study area lies in the Western Transverse Ranges block, which has rotated ~95º clockwise since 16 Ma in response to development of the San Andreas fault system (Figure 2.2B) (Atwater, 1989; Jacobson et al., 2011; Nicholson et al., 1994). This rotation was accompanied by the formation of pull-apart basins, including the Ventura Basin and its offshore extension Santa Barbara Basin, and regional volcanism (Atwater, 1989). The Big Bend in the San Andreas fault causes active transpression in the region, with north-south shortening rates of ~10 mm/yr (Shen et al., 1996). This motion is accommodated by numerous, generally east-west trending, folds and faults in the Transverse Ranges that impact the study area (Figure 2.2B).

The SCR catchment is geologically diverse and drains the western San Gabriel Mountains; the Sierra Pelona schist; Liebre, Alamo, and Frazier Mountains; the Topatopa Mountains; and the northern flanks of the Santa Susana Mountains and Oak Ridge (Figure 2.1).

The SCR catchment is subdivided into four sub-catchments for this study: the Eastern Santa Clara, the Sierra Pelona, the Northern Santa Clara, and the Western Santa Clara (Figure 2.2C). In the Eastern SCR sub-catchment, the western San Gabriel Mountains are a Proterozoic crystalline basement complex (1200 Ma or older, U-Pb zircon geochronology, Barth et al., 1995) composed of gneiss, schist, amphibolite, augen orthogneiss, and an anorthosite complex dated to (Barth and Ehlig, 1988). The crystalline basement is intruded by the Late Triassic Mount Lowe Intrusion that is composed of monzodiorite, and has been assigned an age of 208–220 Ma (Barth and Ehlig, 1988; Barth et al., 1990; Joseph et al., 1982; Silver et al., 1963). The San Gabriel Mountains have been uplifted by the Sierra Madre-Cucamonga thrust fault system and the Santa Susana fault (Figures 2.1 and 2.2B) (Shen et al., 1996), which have estimated slip rates of ~0.3–9.8 mm/yr (Huftile and Yeats, 1996; Petersen and Wesnousky, 1994; Rubin et al., 1998; Tucker and Dolan, 2001) (Table 2.1).

**Table 2.1.** Slip rate estimates for faults in the study area.

| Fault Name | Slip Rate (mm/yr) | Reference |
|---|---|---|
| Big Pine | 2–7 | Peterson and Wesnousky (1994), and therein |
| Hollywood | 0.33–0.75 | Peterson and Wesnousky (1994), and therein |
| Holser | 0–0.4 | Peterson et al. (1996) |
| Malibu Coast | 0.03–0.09 | Peterson and Wesnousky (1994), and therein |
| Mission Ridge/ Arroyo Parida | 0.35–1.27 | Rockwell et al. (1984) |
| Northridge | 0.35–1.7 | Davis and Namson (1994); Dolan et al. (1997); Huftile and Yeats (1996) |
| Oak Ridge | 1.7–12.5 | Huftile and Yeats (1996); Peterson and Wesnousky (1994), and therein |
| Raymond | 0.10–0.22 | Peterson and Wesnousky (1994), and therein |
| Red Mountain | 0.31–7.16 | Huftile and Yeats (1996) |
| San Andreas (Tejon and Cajon Passes) | 16–38 | Peterson and Wesnousky (1994), and therein |
| San Cayetano | 0.85–10.7 | Huftile and Yeats (1996); Peterson and Wesnousky (1994), and therein; Rockwell (1988); |
| San Gabriel | 0.5–1 | Peterson and Wesnousky (1994), and therein |
| Santa Cruz Island | 0.2–0.9 | Wesnousky (1986), and therein |
| Santa Monica | 0.27–5.9 | Davis and Namson (1994); Dolan and Pratt (1997); Peterson and Wesnousky (1994), and therein |
| Santa Rosa Island | 1 | Colson, 1996 |
| Santa Susana | 2.1–9.8 | Huftile and Yeats (1996) |
| Santa Ynez | 0.05–6.7 | Peterson and Wesnousky (1994), and therein |
| Sierra Madre | 0.36–5.0 | Peterson and Wesnousky (1994), and therein; Tucker and Dolan (2001); Rubin et al. (1998) |
| Simi | 0.4–0.9 | Gonzalez and Rockwell (1991); Hitchcock (2001) |
| Ventura | 0.8–2.4 | Peterson and Wesnousky (1994) |

The Sierra Pelona sub-catchment drains the Pelona schist, which falls within the greenstone metamorphic facies and is primarily quartzofeldspathic, but contains trace metabasite,

serpentinite, and talc-actinolite (Jacobson, 1995). The Pelona schist is thought to be composed of trench material and fragments of oceanic crust associated with subduction of the Farallon plate beneath western North America (Jacobson et al., 2011) Metamorphism occurred in the Late Cretaceous or Paleocene and exhumation occurred during the middle Cenozoic or earlier (Haxel and Dillon, 1978; Jacobson et al., 2011).

The Northern Santa Clara sub-catchment includes Liebre Mountain, the Ridge Basin, and the Alamo-Frazier Mountains region. Rocks ranging in composition from quartz monzonite to quartz diorite make up the Liebre Mountain crystalline block, with gneissic inclusions (Crowell, 2003b; Frizzell et al., 1986). The Ridge Basin is composed of Miocene rocks that pass upward from marine to fluvial-deltaic, lacustrine, fluvial and alluvial strata derived from the Alamo-Frazier Mountains area and from granodiorite and sedimentary units located to the northeast (Crowell, 2003a; Link, 2003). The Alamo-Frazier Mountain region contains Proterozoic gneiss, metasedimentary rock units, augen gneiss, anorthositic rocks, and granites (Crowell, 2003b). The uplift of the Liebre Mountain block is associated with the Clearwater fault (Figure 2.2B) (Yan et al., 2005). The Alamo-Frazier Mountains region has been uplifted due to motion along the Big Pine and Pine Mountain faults, the Frazier Mountain thrust, the Dry Creek Thrust, and the Alamo Mountain Thrust (Figure 2.2B). The Big Pine fault slip rate is 2-7 mm/yr (Petersen and Wesnousky, 1994) (Table 2.1); slip rates are not available for the other faults.

Paleocene to Eocene sedimentary units comprise the Topatopa Mountains in the Western Santa Clara sub-catchment. These units are predominantly marine except for the terrestrial Oligocene Sespe Formation (Crowell, 2003b; Yerkes and Campbell, 2005). The Oak Ridge is composed of Oligocene through Holocene sedimentary units that transition from terrestrial to marine in Miocene units and marine to terrestrial in Late Pliocene-Early Pleistocene units (Azor et al., 2002; Yerkes and Campbell, 2005). The northern flanks of the Santa Susana Mountains, which discharge sediment into the SCR, are composed of Miocene through Holocene sedimentary units that transition from marine into terrestrial during the Late Pliocene-Early Pleistocene (Yerkes and Campbell, 2005). The Oak Ridge-Santa Susana Mountains are being formed by ramping on the Oak Ridge and Santa Susana faults (Levi and Yeats, 1993), which are slipping at 1.7-12.5 mm/yr (Huftile and Yeats, 1996; Petersen and Wesnousky, 1994) (Table 2.1). Sedimentary units deposited prior to Neogene rotation were positioned in the forearc basin and received sediment from the Sierran-Peninsular Ranges arc; younger sediments were eroded

from the ranges uplifted during transpression (Jacobson et al., 2011; Wright, 1987). Motion along the San Cayetano and Oak Ridge-Santa Susana faults is closing the Ventura Basin at rates of ~7-25 mm/yr (Donnellan et al., 1993; Huftile and Yeats, 1995; Yeats, 1983).

The VR and southern SYM catchments drain Eocene through Holocene sedimentary units in the Santa Ynez Mountains, which are composed of sandstones, shales, limestones, and conglomerates (Dibblee, 1966). The paleogeography of these sedimentary units is the same as those in the Western Santa Clara, comprising a forearc basin prior to Neogene rotation. These catchments are combined into the Southern Slopes drainage group (Figure 2.2C), which is also lithologically similar to the Western Santa Clara sub-catchment. The Santa Ynez Mountains are associated with uplift along the Santa Ynez fault (Onderdonk, 2005), which slips at 0.05–6.7 mm/yr (Petersen and Wesnousky, 1994) (Table 2.1).

The SYR catchment drains the northern flanks of the Santa Ynez Mountains and southern San Rafael Mountains. This catchment is divided into the Eastern and Western Santa Ynez sub-catchments (Figure 2.2C) in this work. The Eastern Santa Ynez sub-catchment drains the Late Jurassic-Cretaceous Franciscan Formation that contains sandstone, chert, schist, and greenstone (Dibblee, 1988). Cretaceous through Miocene sandstones, limestones, shales, and diatomite are exposed in the Eastern and Western Santa Ynez sub-catchments (Dibblee, 1988). Units in the sub-catchments are also associated with deposition in the Sierran-Peninsular Ranges forearc basin (Jacobson et al., 2011).

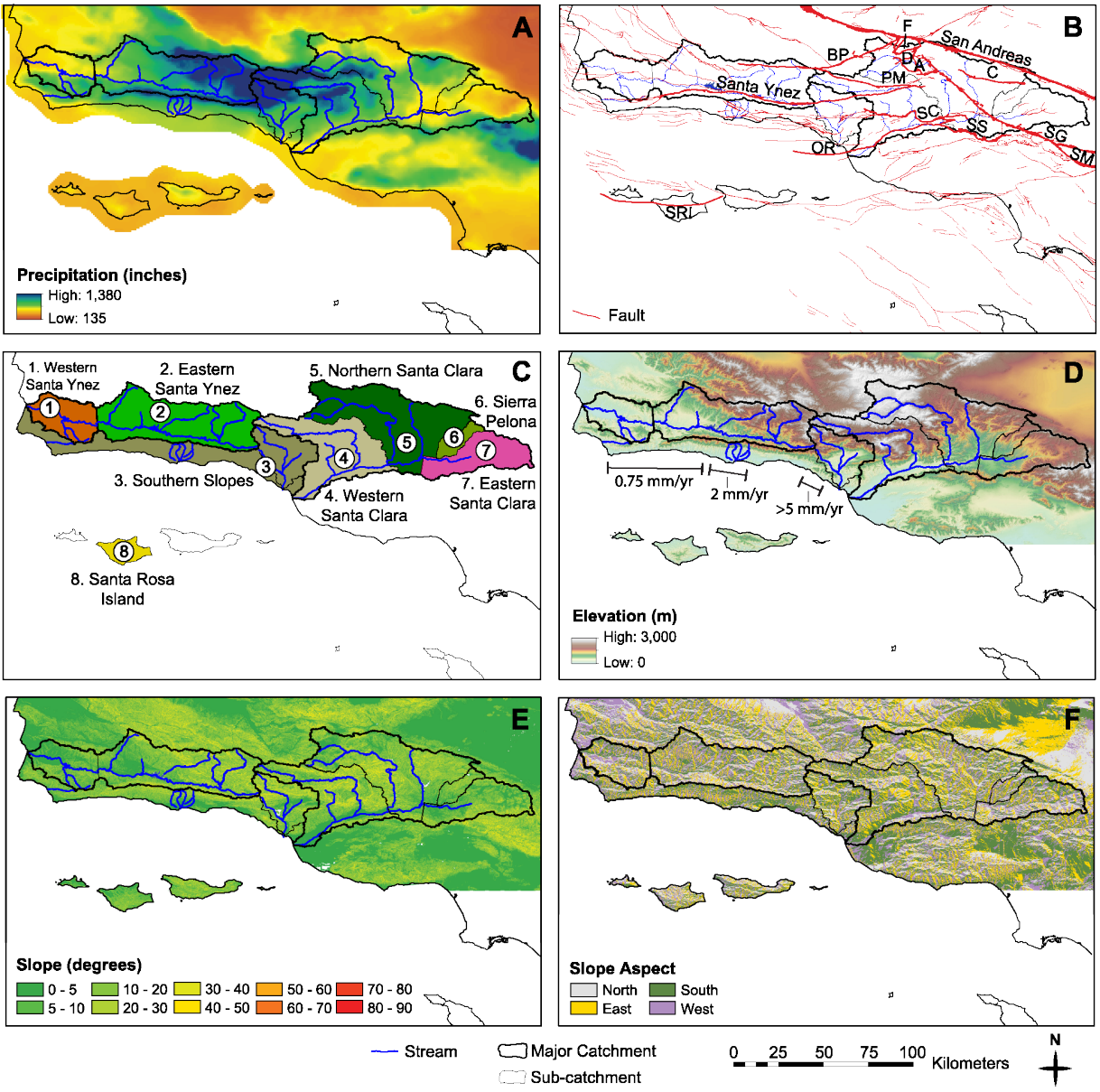


**Figure 2.2.** Geographic attributes of study area.
A. 30-year (1981-2010) annual normal precipitation, data from PRISM Climate Group Oregon State University (2015). B. Faults active in the Quaternary (faults mentioned in text are denoted by thick red lines). BP–Big Pine fault, F–Frazier Mountain thrust, D–Dry Creek thrust, A–Alamo Mountain thrust, PM–Pine Mountain fault, C–Clearwater fault, OR–Oak Ridge fault, SC–San Cayetano fault, SS–Santa Susana fault, SG–San Gabriel fault, SM–Sierra Madre fault, SRI–Santa Rosa Island fault. Data from U. S. Geological Survey and California Geological Survey (2017). C. Division of hydrologic sub-catchments used in this study. D. Elevation, with uplift rates from Duvall et al. (2004) and therein. E. Slope angle. F. Slope aspect (north = 315–360º and 0–45º, east = 45–135º, south = 315–225º, west = 225–315º). Hydrologic data from the National Hydrology Dataset Plus, Version 2 (McKay, 2012).

Exposed units on northern Santa Rosa Island (SRI), one of the Channel Islands, range in age from Oligocene to Holocene. The northern SRI rock types include marine sandstones, shales, siliceous shales, volcaniclastics, conglomerates, and tuffs (Weaver, 1969). The volcanic units are dated to 19-17 Ma, are basaltic in composition, and are associated with Miocene extension

(Luyendyk et al., 1998). The Santa Rosa Island fault (Figure 2.2B) slips at a rate of ~1 mm/yr (Table 2.1) (Colson, 1996).

*2.2.2 Influences on sediment transport*

Sediment transport and yield are functions of precipitation, surface erodibility, and topography, which themselves are intricately influenced by geology and tectonics. Soil slippage and sediment flux are driven primarily by precipitation intensity in the study area (Lavé and Burbank, 2004). High elevations are associated with higher annual average precipitation, including the spine of the Santa Ynez Mountains, the Eastern Santa Ynez, and the northwestern VR and Western Santa Clara catchments (Figures 2.2A and 2.2D). Mass movements tend to occur during and after intense precipitation, such as during atmospheric river events. In between precipitation events, erosion occurs as dry ravel that is stored in stream channels (Lavé and Burbank, 2004). There is a variable temporal delay between sediment production on the hillslopes and sediment export by streams during and after precipitation events (Lavé and Burbank, 2004).

Surface erosion is related to lithology (rock type, rock strength), uplift, vegetation, soil moisture, and wildfire history. The highest sediment yields in the region are associated with the weak Oligocene-Quaternary marine units and fast uplift rates, which co-occur on the southern flanks of the Santa Ynez Mountains and Topatopa Mountains (Duvall et al., 2004; Warrick and Mertes, 2009). Vegetation also plays an important role, as plant cover protects soil from detaching and mobilizing during precipitation events (Osterkamp et al., 2012). Soils become more mobile and erodible during precipitation events, as clay minerals are able to sorb water to their surfaces and become fluidized; however during dry periods clays become progressively more immobile as soil moisture decreases (Napier and Hendy, in press). Wildfires also influence sediment yield because they remove vegetation cover, decreasing root strength and making the exposed soil prone to erosion during precipitation events (Lavé and Burbank, 2004).

Earthquakes generate slope failures and loose sediment in the study area that can be transported downstream during subsequent precipitation events. The 1994 Northridge earthquake triggered over 11,000 landslides, most of which occurred in the Santa Susana Mountains and the mountains just north of the SCR (Harp and Jibson, 1996), resulting in considerable unconsolidated sediment within the SCR catchment. The landslides primarily occurred in weakly

lithified late Miocene through Pleistocene clastic units that have been subjected to folding and faulting, and thus have low rock strength (Harp and Jibson, 1996). These units are easily erodible and form steep slopes that are susceptible to failure. In the study area, slopes range from relatively flat in the SCR valley, to nearly vertical in the mountainous areas (Figure 2.2E, although the low resolution of the figure prevents recognition of the very steep slopes). Slope aspect is diverse in the study area due to the mountainous terrain (Figure 2.2F).

The Santa Clara River contributes sediment to both SBB and Santa Monica Basin in the present-day, with finer grain sizes deposited in SBB and coarse-grains deposited in Santa Monica Basin via the eastward flowing Santa Barbara littoral cell and Hueneme Canyon (Figure 2.1) (Normark et al., 2006; Romans et al., 2009). However, during the LGM sea level low stand, the Santa Clara River bypassed SBB. Lowering of the Santa Clara River base-level due to the LGM eustatic sea level low stand led to a steep river gradient, and caused the Santa Clara River mouth to migrate south and discharge directly into Santa Monica Basin via the Hueneme submarine canyon (Normark et al., 2006).

## 2.3 Methods

### *2.3.1 Sample collection and preparation*

Bed sediment, suspended load, and marine sediment core samples were analyzed in this study. Twenty stream bed sediment samples were collected in March 2015 from 18 locations (L) in the mainland catchments, and four Santa Rosa Island (SRI) stream bed samples (Cherry Canyon [CC1, CC2] and Water Canyon [WC1, WC2]) were collected in May 2016 (Figure 2.1, Table 2.2). Streams were not flowing during bed load sediment sample collection due to drought, which precluded collection of suspended load. Two suspended load samples were obtained after a rainstorm in April 2016 from Mission Creek (MC) and Gaviota Creek (GC) in the SYM catchment (Figure 2.1, Table 2.2). Water and suspended sediment were collected from the flowing streams using submerged bottles, and the sediment was recovered by oven-drying. Two 1-cm-thick samples were collected from gray flood layer deposits in SBB marine sediment core SPR0901-04BC (34º 16.895’ N, 120º 02.489’ W, 588 m water depth; 04BC) at depth intervals 38-39 cm and 59-60 cm, which correspond to A.D. 1861-1862 and A.D. 1761 (Hendy et al., 2015). One 2-cm-thick sample was collected from a gray layer in core MV0811-14JC (34º 16.906’ N, 120º 02.162’ W, 582 m water depth; 14JC, located in section 1 at a depth interval of

16-18 cm depth below core top, which has been radiocarbon dated to 1912 Cal yr BP (Du et al., *in prep*). Two samples were collected from ODP Site 893A (34º 17.25' N, 120º 02.2' W, 576.5 m water depth; ODP), core 004H, section 05W in depth intervals 103-105 and 141-143 cm, which correspond to LGM sediment (Hendy et al., 2002).

During sample collection, rock types and grain sizes observed in the stream beds were consistent with the geology of the locality (Table 2.2). Notably, at L3, we observed mica schist and greenstone. At L4 the bedload contained fragments of gneiss, granite, basalt, chlorite, phyllite, titanomagnetite, and tuff with clast size ranging from gravel to clay. Granite and gneiss boulders were observed at L11 and also at L9 and L13 with the addition of sandstone. Stream bed clasts at L14 in Sespe Creek were composed of gneiss, basalt, granite, red and tan sandstones, and red conglomerate, ranging in size from clay to boulders. At L16 the grain size ranged from clay to gravel, and clasts were composed of gneiss, granite, and sandstone. In the VR catchment at L21, grain sizes ranged from sand to boulder, and clasts were composed of sandstone, conglomerate, granite, and breccia. At L20 we observed sandstone, chert, granite, and diatomite. The bed load sediment samples from the SYM catchment were collected near the littoral zone; L22 was collected in the Goleta Slough, while L29 was collected just upstream of Gaviota Beach. Notable rock types observed at the SYR locations (L24, L28, and L30) include diatomite, chert, sandstone, limestone, serpentinite, and greenstone.

In preparation for quantitative X-ray diffraction (XRD), elemental composition, and radiogenic isotope analyses, samples were oven-dried (40-50 ºC) and weighed. Samples were then split using the quartering method (ASTM C702/C702M). Bulk sample splits were prepared using a jaw crusher, then powdered using a shatterbox. The remaining sample splits were wet-sieved using standard 0.250 and 0.063 mm mesh sieves to separate the sand (63–250 μm) and clay and silt (<63 μm) grain size fractions to represent bed load and suspended load components, respectively. Each grain size fraction was then dried, weighed, and powdered. The sand size fraction was powdered using a shatterbox, while the <63 μm size fraction was powdered using an agate mortar and pestle. Suspended load and sediment core samples were dried, weighed, and powdered.

**Table 2.2.** Description of sampling locations.

| Location | | Latitude | Longitude | Stream Name | Sample Type | Sampling Notes |
|---|---|---|---|---|---|---|
| ***SCR*** | 1 | N 34º27'23.1" | W 118º11'48.6" | Santa Clara R. | bed sediment | |
| | 2 | N 34º25'44.5" | W 118º21'16.9" | Santa Clara R. | bed sediment | |
| | 3 | N 34º33'13.4" | W 118º24'53.2" | Bouquet Creek | bed sediment | |
| | 4 | N 34º25'26.5" | W 118º28'59.0" | Santa Clara R. | bed sediment | Grain size ranges from clay to 50 cm in diameter. Bedload contains fragments of (sub-rounded) gneiss, white and pink granite, basalt, chlorite, phyllite, tuff, sandstone grading into phyllite |
| | 5 | N 34º25'33.5" | W 118º34'45.7" | Santa Clara R. | bed sediment | Grain size ranges same as Loc. 4. Rock fragments same as Loc. 4 plus sandstone. |
| | 7 | N 34º25'05.6" | W 118º39'26.1" | | bed sediment | SCR tributary-Chiquito Canyon. Bedload clasts up to 40 cm in length; up to 300 cm near bridge. Gneiss, granite, sandstone. |
| | 9 | N 34º37'00.6" | W 118º44'42.5" | Piru Creek | bed sediment | Boulders in streambed up to 1 m in length. Rocks in steambed: gneiss, sandstone, granite. |
| | 11 | N 34º42'14.3" | W 118º56'22.5" | Piru Creek | bed sediment | Many boulders in creek (>1 m in length). Granite and gneiss. |
| | 13 | N 34º23'40.7" | W 118º47'57.7" | Santa Clara R. | bed sediment | Grain size ranges from clay/silt up to boulders 1 m in length. Rock types: Granite, gneiss, conglomerate, sandstone. Well-rounded to sub-rounded |
| | 14 | N 34º26'40.3" | W 118º55'37.3" | Sespe Creek | bed sediment | Grain size ranges from clay/silt up to 1.5 m boulders. Gneiss, andesite, red sandstone (Sespe Fm.), tan sandstone, granite, red conglomerate. Rounded to sub-angular. |
| | 16 | N 34º21'22.1" | W 119º02'06.2" | Santa Clara R. | bed sediment | Sandstone, gneiss, granite. Clast size clay/silt up to 40 cm. |
| ***VR*** | 20 | N 34º25'28.0" | W 119º18'08.2" | Coyote Creek | bed sediment | Bedload sample collected just above weir. Clasts are sub-rounded to rounded; range in size from silt/sand to 70 cm. Sandstones, chert, granite/diorite, limestone/diatomite. |
| | 21 | N 34º25'05.8" | W 119º49'33.4" | Ventura River | bed sediment | Clasts sub-angular to well-rounded. Grain size is sand up to boulders ~ <2 m in length. Sandstones, granite, conglomerate, breccia. All boulders are sandstone. |
| ***SYM*** | 22 | N 34º32'43.7" | W 119º47'30.1" | Goleta Slough | bed sediment | |
| | 29 | N 34º40'11.1" | W 120º26'43.1" | Gaviota Creek | bed sediment | Gaviota Beach. Possible influence of SB littoral cell. Mouth of creek closed-off from ocean. Sandstone, chert. |
| | GC | | | Gaviota Creek | suspended load | |
| | MC | N 34º24’45.3" | W 119º41’15.0 | Mission Creek | suspended load | |

| | | | | | |
|---|---|---|---|---|---|
| ***SYR*** | 24 | N 34º32'43.7" | W 119º47'30.1" | bed sediment | Bedload samples collected above and below weir; also collected bedload mud. Clasts in bedload range from mud to ~1 m. Rocks: diatomite/limestone, chert, sandstone, serpentinite, greenstone. |
| | 28 | N 34º28'16.9" | W 120º13'36.5" | bed sediment | Grain size: sand. Rounded to sub-rounded. Rocks: sandstone, diatomite, limestone (fossiliferous), granite, tuff, greenstone, serpentinite, chert, siltstone. |
| | 30 | N 34º40'40.5" | W 120º25'29.8" | bed sediment | Clasts range from clay/mud to ~200 mm. Well-rounded to sub-angular. Sandstone, diatomite, chert, greenstone (few), serpentinite (few) |
| ***SRI*** | WC1 | N 33º59'22.2" | W 120º02'54.96" | bed sediment | Water Canyon |
| | WC2 | N 33º59'35.64" | W 120º02'26.88" | bed sediment | Water Canyon |
| | CC1 | N 34º00'28.08" | W 120º03'3.48" | bed sediment | Cherry Canyon |
| | CC2 | N 34º00'31.38" | W 120º03'0.54" | bed sediment | Cherry Canyon |

*2.3.2 X-Ray diffraction analysis*

Quantitative XRD measurements were completed on the sample sand size fraction, and on the <63 μm size fraction of the furthest downstream bed sediment samples in each catchment (L16, L20, L20, WC1, CC1). Samples were prepared as randomly oriented powder mounts and continuously scanned in 2θ-θ scanning mode from 2-80º 2θ using a Rigaku Ultima IV diffratometer with Cu-Kα radiation (40 kV voltage and 44 mA current). Device scan parameters were set up as follows: scan step = 0.02º, scan speed = 0.3º $min^{-1}$, divergence slit = 0.5º, divergence H.L. slit = 10 mm, scattering slit = 0.5º, and recording slit = 0.15 mm.

Quantitative mineral phase analysis was determined using the Rietveld refinement program BGMN (Bergmann and Taut, 2005) via the graphical user interphase Profex (Doebelin and Kleeberg, 2015). BGMN calculates theoretical mineral peak profiles from the diffratometer configuration. The theoretical peak profiles are then compared with the measured profiles; mineral structures are then optimized in Profex based on the difference between the theoretical and measured profiles. Optimization occurs automatically via adjustments to mineral unit cell dimensions and weight fractions, and other mineral parameters (i.e., crystallite size, micro-strain, and texture/preferred orientation) can be manually released for refinement of the peak profiles (Doebelin and Kleeberg, 2015). For simplicity, identified minerals are presented by phase (e.g., plagioclase) as opposed to specific mineral component (e.g., albite).

*2.3.3 Determination of elemental composition*

Major, minor, and trace elemental compositions were determined by ALS Laboratories in Vancouver, Canada using inductively coupled plasma-atomic emission spectroscopy and inductively coupled plasma-mass spectrometry. Sample splits were obtained from the powdered, <63 μm size fraction of the bed sediment samples, except for L4 and L11 samples, where due to insufficient <63 μm size fraction for measurement, the bulk sample was analyzed. Bulk sample splits were also analyzed from the powdered SBB sediment core samples. Samples were digested using nitric, perchloric, hydrochloric, and hydrofluoric acids at ALS Laboratories. The maximum standard error of measurements of laboratory standards GBM908-10 and MRGeo08 (Appendix A, Table A.1) for selected elements are as follows: Al = ±0.19 % (MRGeo08), Ca = ±0.05 % (GBM908-10), Fe = ±0.07 % (MRGeo08), Ga = ±0.3 ppm (GBM908-10 and MRGeo08), In = ±0.005 ppm (MRGeo08), K = ±0.05 % (MRGeo08), Mg = ±0.03 % (MRGeo08), Na = ±0.03 %

(GBM908-10 and MRGeo08), Nb = ±0.5 ppm (MRGeo08), Rb = ±8 ppm (MRGeo08), Sr = ±5 ppm (MRGeo08), Ga = ±0.04 ppm (MRGeo08), Ti: = ± 0.009 % (GBM908-10 and MRGeo08), and Y = ±0.3 ppm (GBM908-10).

Rare earth element (REE) and isotopic compositions were assessed on powdered sample splits from the <63 μm size fraction of bed sediment samples and on bulk SBB sediment core samples at the University of New Hampshire. Briefly, powdered sample splits from the <63 μm size fraction of bed sediment samples and from the bulk sediment core samples were digested into mixed HF and $HNO_3$, then dissolved in HCl to destroy resulting fluorides. Solutions were subsequently split for trace element and isotopic studies. Sub-aliquots of these digested samples were analyzed for REE compositions on the Nu Instruments AttoM high-resolution inductively coupled plasma mass spectrometer. Analytical precision and accuracy were assessed through the determination of REE concentrations in international laboratory standards JA-1 and BCR-2 (Appendix A, Table A.2). The maximum measurement error, according to measurement of the standards is as follows: La = 2.4 % (BRC-2), Ce = 1.7 % (BRC-2), Pr = 1.9 % (BRC-2), Nd = 1.8 % (JA-1), Sm = 0.8 % (JA-1), Eu = 1.5 % (BCR-2), Gd = 4.1 % (BCR-2), Dy = 1.0 % (JA-1), Er = 0.4 % (BCR-2), and Yb = 0.9 % (JA-1).

*2.3.4 Isotope analysis*

Isotopic compositions were determined at the University of New Hampshire following procedures adapted from Bryce et al. (2005) for the strontium (Sr) isotopic analyses and Gombiner et al. (2016) for the neodymium (Nd) isotope analyses. Sample Sr was separated from the aliquot of the digested solution for isotope work using standard ion chromatographic procedures employing Eichrom Sr spec resin. Strontium-rich salts were then digested in dilute nitric acid and measured on the Nu plasma II-ES multicollector inductively coupled plasma mass spectrometer at the University of New Hampshire following procedures outlined in Konter and Storm (2014). The average measured value of $^{87}Sr/^{86}Sr$ in NIST SRM 987 (n=123) was 0.710248±0.000016 (2σ). Total procedural Sr blanks were < 200 pg, insignificant for the amount of sample processed in these experiments.

Samples for Nd isotopic analysis were prepared following Gombiner et al. (2016). Briefly, Nd was separated from the matrix solution using a three-column process. Most major elements were first eluted in dilute HCl on Ag 50 x 4 ion chromatographic exchange columns,

and the rare earth elements (REEs) and iron were removed from the cation exchange column with 6 N HCl. The resulting solution was loaded onto a 400 μl column containing Eichrom TRU-Spec resin to separate the REEs from any remaining matrix. These elutions, once dried down were then loaded onto a Ln-Spec column where Nd was separated from the other REEs in dilute HCl. Isotopic measurements were made on the Nu plasma II-ES multicollector inductively coupled plasma mass spectrometer at the University of New Hampshire using a desolvating nebulizer to introduce the solution into the mass spectrometer. Instrumental mass fractionation was corrected relative to $^{146}Nd/^{144}Nd = 0.7219$ using an exponential law. The JNDi standard (Tanaka et al., 2000) gave $^{143}Nd/^{144}Nd = 0.512115 \pm 0.000015$ ($2\sigma$; n = 110). Reported sample $^{143}Nd/^{144}Nd$ is converted to the $\varepsilon_{Nd}$ notation, where $\varepsilon_{Nd}$ is the deviation of the measured sample $^{143}Nd/^{144}Nd$ from that of the average of chrondritic meteorites (representative of the bulk earth), in parts per $10^4$ (DePaolo and Wasserburg, 1976). Total procedural Nd blanks were < 100 pg, insignificant for the abundant sample processed in these experiments.

## 2.4 Results

### *2.4.1 Mineralogy*

In general, the mineralogy of all samples is dominated by plagioclase, quartz, and smectite (Figures 2.3-2.4; Table 2.3). In the SCR catchment, plagioclase is present at all sample locations, but its content is greatest at L1, L2, L4, and L5 (>50%) in the Eastern Santa Clara sub-catchment (Figure 2.3; Table 2.3). Quartz and potassium feldspars are in relatively low abundance (<16%) in this sub-catchment, but their proportion increases downstream as plagioclase content decreases. Amphibole, pyroxene, and olivine are present in the L1 and L2 samples, but not downstream. All sample locations within the SCR catchment contain smectite of varying concentration. Kaolinite was identified in samples from L3, L14, and L16-1 in the <63 μm grain size fraction. Chlorite is also present at L1 and L3, and at L16 the <63 μm size fractions contain ~4% chlorite (Table 2.3). The Sierra Pelona sample contains epidote and dolomite, which were not identified in samples collected in the other SCR sub-catchments. Muscovite and titanite were also identified at L3 and at L16 in the <63 μm grain size fraction. The sample from L11 on Piru Creek above the Pyramid Lake reservoir and dam is composed primarily of quartz, plagioclase, potassium feldspar, and smectite (Figure 2.3; Table 2.3). Below the Pyramid Lake reservoir and dam, the L9 sample is dominated by smectite, and also contains

plagioclase, potassium feldspar, quartz, and zeolite (Figure 2.3; Table 2.3). The two bulk samples from L16 are very similar in mineralogic composition and quantity. However, the two <63 μm grain size subsamples from L16 indicate some heterogeneity, with 16-1 containing titanite, kaolinite, and calcite, and having twice the smectite content as 16-2 (~32% compared to ~16%), but half as much muscovite as 16-2 (~3% compared to ~7%) (Table 2.3).

Samples collected from Southern Slopes group have varied mineral abundances. The VR catchment samples are primarily composed of plagioclase, potassium feldspar, quartz, and smectite, with minor calcite (Figure 2.4). The bulk sample from L20 also contains muscovite and the clay minerals illite (1-4%) and kaolinite (2-5%) (Table 2.3). The L20 <63 μm sub-sample contains a greater proportion of clay minerals, muscovite, and calcite compared to the bulk sample, at the expense of quartz and plagioclase (Figure 2.4; Table 2.3). The mineralogy of each sample from the southern SYM catchment is unique (Figure 2.4). Plagioclase, potassium feldspar, quartz, and smectite are present in all samples, but their abundances are inconsistent. Illite is present in the L22 sample (~8%) and the Gaviota Creek (GC) suspended load sample (~10%), and both suspended load samples contain chlorite (1-4%) (Table 2.3). Calcite comprises a considerable proportion of the GC suspended load sample (~30%).

The SYR catchment samples also have variable mineral compositions that are not resolved by the sub-catchment division (Figure 2.4). The two samples from L24 both contain abundant plagioclase, quartz, and smectite (~75% when mineral abundances are combined), as well as calcite and chlorite (Table 2.3). Sample 24-1, collected from mud includes pumpellyite, epidote, serpentine, and the clay mineral kaolinite, minerals not identified in sample 24-2. Further downstream the mineralogy at L28 is dominated by quartz, plagioclase and smectite (~85%, combined), and contains potassium feldspar. Samples from L30 in the Eastern Santa Ynez sub-catchment also contain plagioclase, potassium feldspar, quartz, and smectite. Amorphous silica was identified in the bulk sample from L30, while the <63 μm size fraction subsample from this location contains pyroxene, kaolinite, illite, and muscovite. Quartz dominated the bulk sample composition of L30 (nearly 50%), and clay mineral content increases in the <63 μm size fraction (Figure 2.4; Table 2.3).

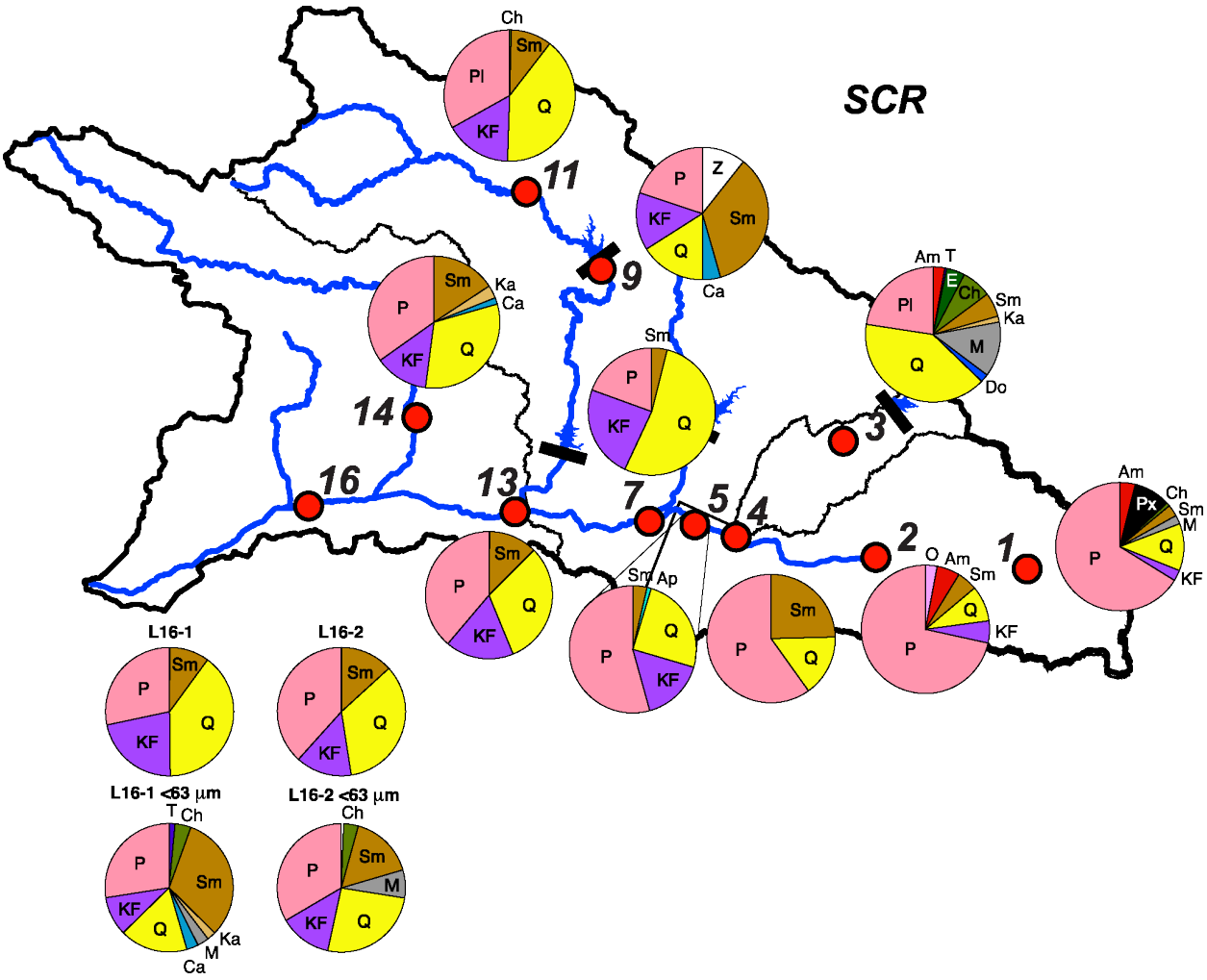


**Figure 2.3.** Mineral abundances for the Santa Clara River (SCR) catchment bulk stream bed sediment samples, and the <63 µm grain size fraction for samples from locations (L) 16-1 and 16-2.
Catchment and sub-catchments are outlined in black. Selected streams are shown by blue lines. Selected dams are show by black bars. Mineral group abbreviations: Pl–plagioclase, KF–potassium feldspar, Q–quartz, Ca–calcite, Do–dolomite, Ap–apatite, M–muscovite, Ka–kaolinite, Sm–smectite, Z–zeolite, Ch–chlorite, E–epidote, T–titanite, Px–pyroxene, Am–amphibole, O–olivine. Hydrologic data from the National Hydrology Dataset Plus, Version 2 (McKay, 2012).

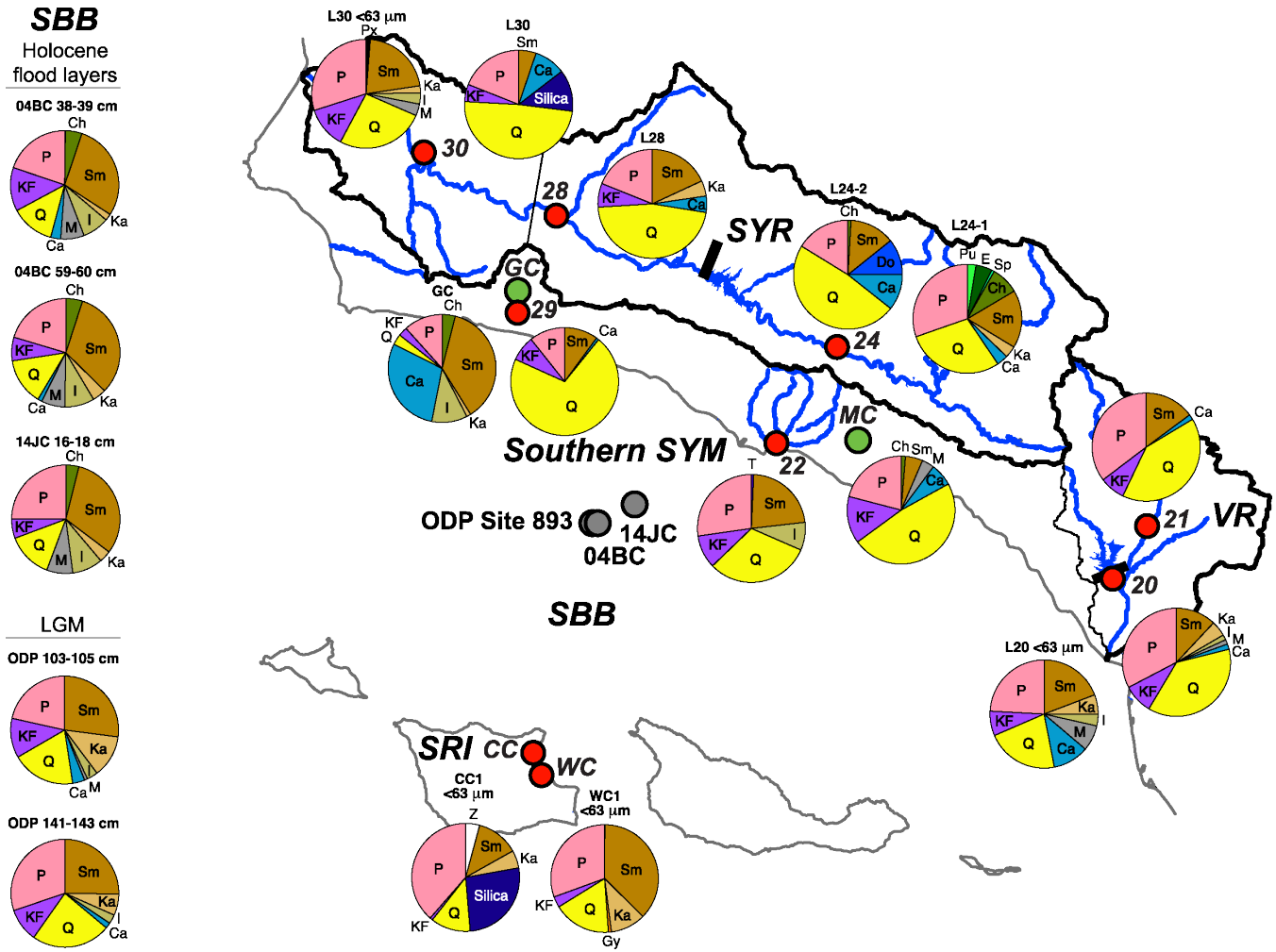


**Figure 2.4.** Mineral abundances in the bulk and the <63 μm grain size fraction stream bed sediment samples (red circles), the stream suspended load samples (green circles) from the Ventura River (VR), Santa Ynez River (SYR), and Santa Ynez Mountains (SYM), and Santa Rosa Island (SRI) catchments. Mineral abundances in the bulk samples from Santa Barbara Basin (SBB) sediment cores (gray circles), SPR0901-04BC (04BC), MV0811-14JC (14JC), and ODP Site 893A are shown on left side of figure. Sample abbreviations: L–location, GC–Gaviota Creek, MC–Mission Creek, CC–Cherry Canyon, WC–Water Canyon, LGM–last glacial maximum. Catchment and sub-catchments are outlined in black. Selected streams are shown by blue lines. Selected dams are show by black bars. Mineral group abbreviations: Pl–plagioclase, KF–potassium feldspar, Q–quartz, silica, Ca–calcite, Do–dolomite, Gy-gypsum, M–muscovite, I–illite, Ka–kaolinite, Sm–smectite, Z–zeolite, Ch–chlorite, Sp–serpentine, E–epidote, Pu–pumpellyite, Px–pyroxene. Hydrologic data from the National Hydrology Dataset Plus, Version 2 (McKay, 2012).

**Table 2.3.** Mineral phase abundances of bed sediment, suspended load, and sediment core samples.

| Mineral Phase | Sample and Phase Abundance (%) | | | | | | | | | | | | | | | | | | |
|---|---|---|---|---|---|---|---|---|---|---|---|---|---|---|---|---|---|---|---|
| | *Santa Clara River catchment* | | | | | | | | | | | | | | *Santa Ynez River catchment* | | | | |
| | L1 | L2 | L4 | L5 | L3 | L7 | L9 | L11 | L13 | L14 | L16-1 | L16-2 | L16-1 <63 µm | L16-2 <63 µm | L24-1 | L24-2 | L28 | L30 | L30 <63 µm |
| Plagioclase | 66 | 72 | 60 | 54 | 23 | 19 | 20 | 33 | 39 | 35 | 28 | 38 | 27 | 33 | 30 | 16 | 19 | 19 | 30 |
| Potassium Feldspar | 3 | 6 | | 16 | | 24 | 14 | 16 | 17 | 13 | 22 | 14 | 10 | 13 | | | 7 | 5 | 12 |
| Quartz | 12 | 9 | 16 | 25 | 40 | 53 | 16 | 40 | 31 | 32 | 40 | 34 | 17 | 26 | 29 | 48 | 46 | 49 | 26 |
| Silica | | | | | | | | | | | | | | | | | | 12 | |
| Calcite | | | | | | | 4 | | | 2 | | | 3 | | 3 | 11 | 5 | 9 | |
| Dolomite | | | | | 2 | | | | | | | | | | | 11 | | | |
| Apatite | | | | 1 | | | | | | | | | | | | | | | |
| Gypsum | | | | | | | | | | | | | | | | | | | |
| Muscovite | 2 | | | | 13 | | | | | | | | 3 | 7 | | | | | 3 |
| Illite | | | | | | | | | | | | | | | | | | | 3 |
| Kaolinite | | | | | 1 | | | | | 3 | | | 2 | | 3 | | 5 | | 2 |
| Smectite | 3 | 5 | 25 | 4 | 6 | 4 | 35 | 10 | 12 | 16 | 10 | 13 | 32 | 16 | 17 | 13 | 18 | 5 | 21 |
| Zeolite | | | | | | | 11 | | | | | | | | | | | | |
| Chlorite | 1 | | | | 7 | | | | | | | | 4 | 4 | 8 | 1 | | | |
| Serpentine | | | | | | | | | | | | | | | 1 | | | | |
| Epidote | | | | | 4 | | | | | | | | | | 5 | | | | |
| Pumpellyite | | | | | | | | | | | | | | | 3 | | | | |
| Titanite | | | | | | | | | | | | | 1 | | | | | | |
| Pyroxene | 9 | | | | | | | | | | | | | | | | | | 1 |
| Amphibole | 4 | 6 | | | 3 | | | | | | | | | | | | | | |
| Olivine | | 3 | | | | | | | | | | | | | | | | | |
| Total | 100 | 100 | 100 | 100 | 100 | 100 | 100 | 100 | 100 | 100 | 100 | 100 | 100 | 99 | 100 | 100 | 100 | 100 | 100 |

**Table 2.3** (*continued*). Mineral phase abundances of bed sediment, suspended load, and sediment core samples.

| Mineral Phase | Sample and Phase Abundance (%) | | | | | | | | | | | | | |
|---|---|---|---|---|---|---|---|---|---|---|---|---|---|---|
| | *Southern Slopes* | | | | | | | *Santa Rosa Is.* | | *SBB Holocene* | | | *SBB LGM* | |
| | L21 | L20 | L20 <63 μm | L22 | L29 | GC | MC | CC1 <63 μm | WC1 <63 μm | 04BC 38-39 cm | 04BC 59-60 cm | 14JC 16-18 cm | ODP 103-105 cm | ODP 141-143 cm |
| Plagioclase | 35 | 33 | 24 | 27 | 11 | 12 | 21 | 39 | 31 | 19 | 20 | 25 | 22 | 30 |
| Potassium Feldspar | 8 | 9 | 7 | 10 | 8 | 3 | 14 | 1 | 3 | 13 | 7 | 6 | 12 | 10 |
| Quartz | 41 | 37 | 22 | 31 | 71 | 3 | 48 | 12 | 17 | 13 | 14 | 14 | 19 | 24 |
| Silica | | | | | | | | 27 | | | | | | |
| Calcite | 2 | 2 | 11 | | 1 | 29 | 7 | | | 3 | 1 | | 4 | 2 |
| Dolomite | | | | | | | | | | | | | | |
| Apatite | | | | | | | | | | | | | | |
| Gypsum | | | | | | | | | 1 | | | | | |
| Muscovite | | 1 | 8 | | | | 4 | | | 7 | 7 | 8 | 1 | |
| Illite | | 2 | 4 | 8 | | 11 | | | | 8 | 9 | 9 | 3 | 3 |
| Kaolinite | | 5 | 6 | | | 1 | | 5 | 11 | 2 | 4 | 4 | 13 | 6 |
| Smectite | 15 | 12 | 19 | 23 | 10 | 37 | 5 | 13 | 37 | 29 | 32 | 31 | 27 | 25 |
| Zeolite | | | | | | | | 4 | | | | | | |
| Chlorite | | | | | | 4 | 1 | | | 5 | 5 | 4 | | |
| Serpentine | | | | | | | | | | | | | | |
| Epidote | | | | | | | | | | | | | | |
| Pumpellyite | | | | | | | | | | | | | | |
| Titanite | | | | 1 | | | | | | | | | | |
| Pyroxene | | | | | | | | | | | | | | |
| Amphibole | | | | | | | | | | | | | | |
| Olivine | | | | | | | | | | | | | | |
| Total | 100 | 100 | 100 | 100 | 100 | 100 | 100 | 100 | 100 | 100 | 100 | 100 | 100 | 100 |

Minerals identified in the SRI samples are generally consistent, but their proportions differ markedly between samples. Plagioclase and quartz comprise ~50% the <63 μm sub-samples from SRI (Figure 2.4; Table 2.3). Clay minerals are also in considerable abundance with smectite ranging from 10-30% and kaolinite from 5-11% in abundance. However, sample CC1 contains zeolite and abundant amorphous silica (~26%), which were not identified in WC1.

The SBB Holocene flood layers have nearly identical mineral content, with slight differences in the abundances (Figure 2.4; Table 2.3). All flood layers contain about 40-45% plagioclase, potassium feldspar, and quartz, combined. Clay minerals comprise 45-50% of the flood layers, with smectite dominating (~30%), followed by illite (~9%), chlorite (~4-5%), and kaolinite (2-4%) (Table 2.3). Calcite and muscovite are also present. The mineral composition of the two SBB samples deposited during the LGM is very similar, both between those two samples and compared to the Holocene flood layer samples (Figure 2.4). Plagioclase, quartz, and smectite are in the greatest abundance (~50-60%, combined), followed by potassium feldspar and kaolinite (Table 2.3). Illite, muscovite, and calcite are minor constituents of the LGM samples. Notably, chlorite is absent in the LGM samples.

*2.4.2 Elemental composition*

In general, the elemental concentrations of the SBB Holocene and LGM samples fall within the ranges of the catchment samples (Table 2.4; analytical errors presented in Tables A.1 and A.2). Among the catchments, sample elemental concentrations are fairly consistent and indistinct, however some sample locations yielded concentrations for certain elements outside the 2σ range of all samples. Sample L4 (Eastern Santa Clara sub-catchment) contains unusually high Ti concentrations (1.815%). Sample L29 from the Southern Slopes has the highest Na concentrations (7.94%), and samples from L2 and L4, collected within the Eastern Santa Clara sub-catchment, both yielded very high Sr concentrations (818 ppm and 896 ppm, respectively) (Table 2.4).

Bivariate correlation analysis of major elements revealed significant positive relationships between Al and Fe, Al and Ti, Fe and Mg, and Fe and Ti ($p<0.01$; sample n=27, or n=26 for Ti correlations) (Figure 2.5). Samples with individual elemental concentrations that exceeded the 2σ range of all samples were considered outliers and excluded from the correlation analysis for certain elements (see above; e.g., L4 was excluded from Ti correlation).

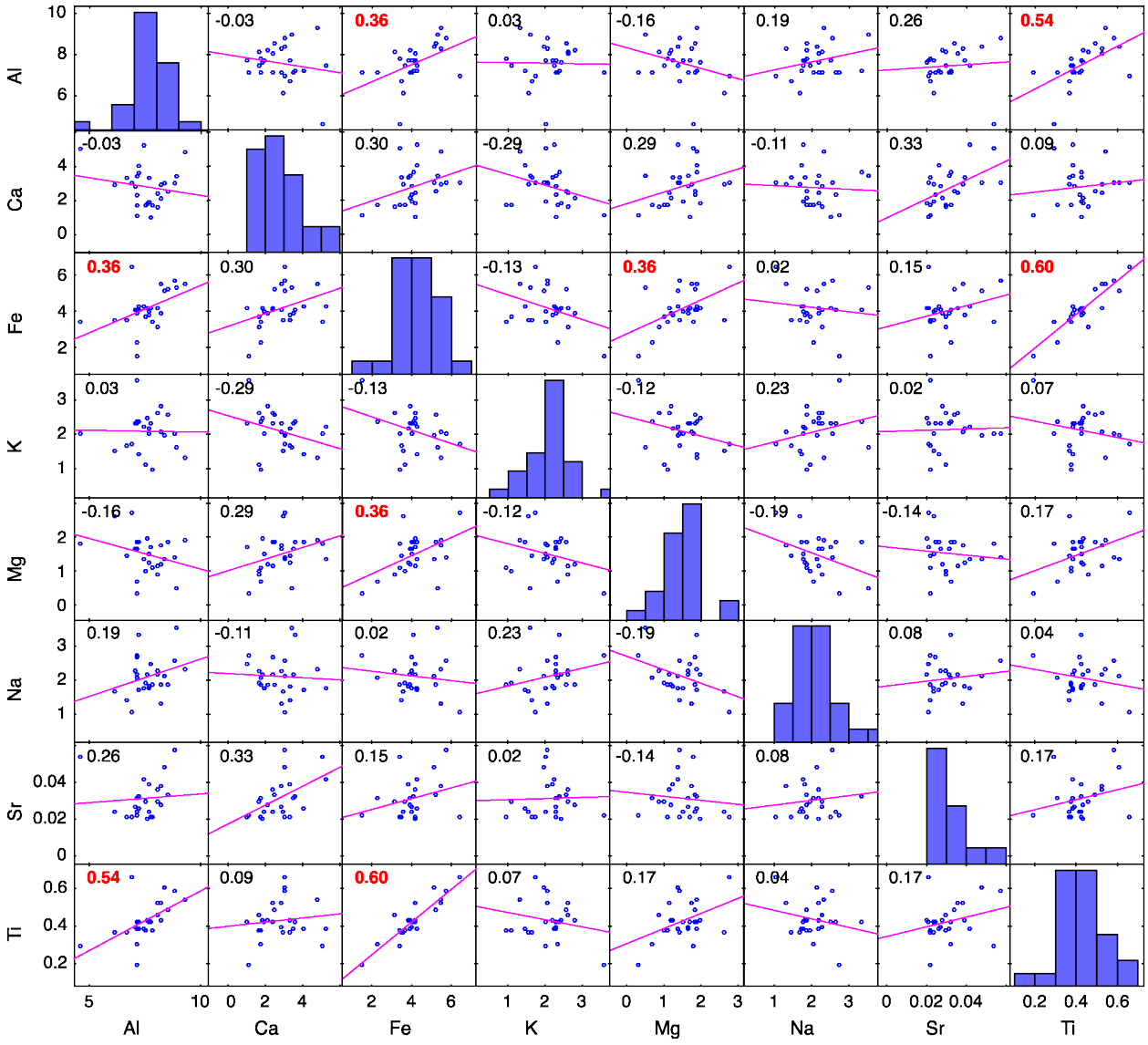


**Figure 2.5.** Major element correlation matrix and elemental histograms.
Correlation lines in pink. Kendall's rank correlation coefficients displayed in the top left of each correlation plot; red text indicated significant correlation. All stream bed sediment and sediment core samples (n=27) were used in correlation plots except for sample L4 in the Ti plots, L29 in the Na plots, and L2 and L4 in the Sr plots, as the respective elemental concentrations in those samples were greater than the 2σ range of all the samples (n=27).

The Rb/Sr values of the SBB samples range from 0.4-0.6 (Table 2.4). The Sierra Pelona sub-catchment sample has a Rb/Sr value of 0.44. The Northern Santa Clara, Eastern Santa Clara, Southern Slopes, and Eastern and Western Santa Ynez sub-catchments all have average Rb/Sr values between 0.30 and 0.35. The Eastern Santa Clara and the SRI sub-catchments have much lower average Rb/Sr values, 0.09 and 0.19, respectively.

Rare earth elemental concentrations were normalized to Post-Archean average Australian shale (PAAS) (McLennan, 1989), which represents Middle Proterozoic–Mesozoic clastic

sediments derived from weathered continental crust (Nance and Taylor, 1976). All samples generally display homogenous and flat PAAS-normalized REE patterns that are either at unity or below (Figure 2.6). Most samples contain a slight positive Eu anomaly, with the exceptions of L2 and L30, which contain large positive Eu anomalies, and CC1, which does not bear an Eu anomaly. The SBB 14JC 16-18 cm sample also contains a positive Ce anomaly that is not present in the REE patterns of the other samples.

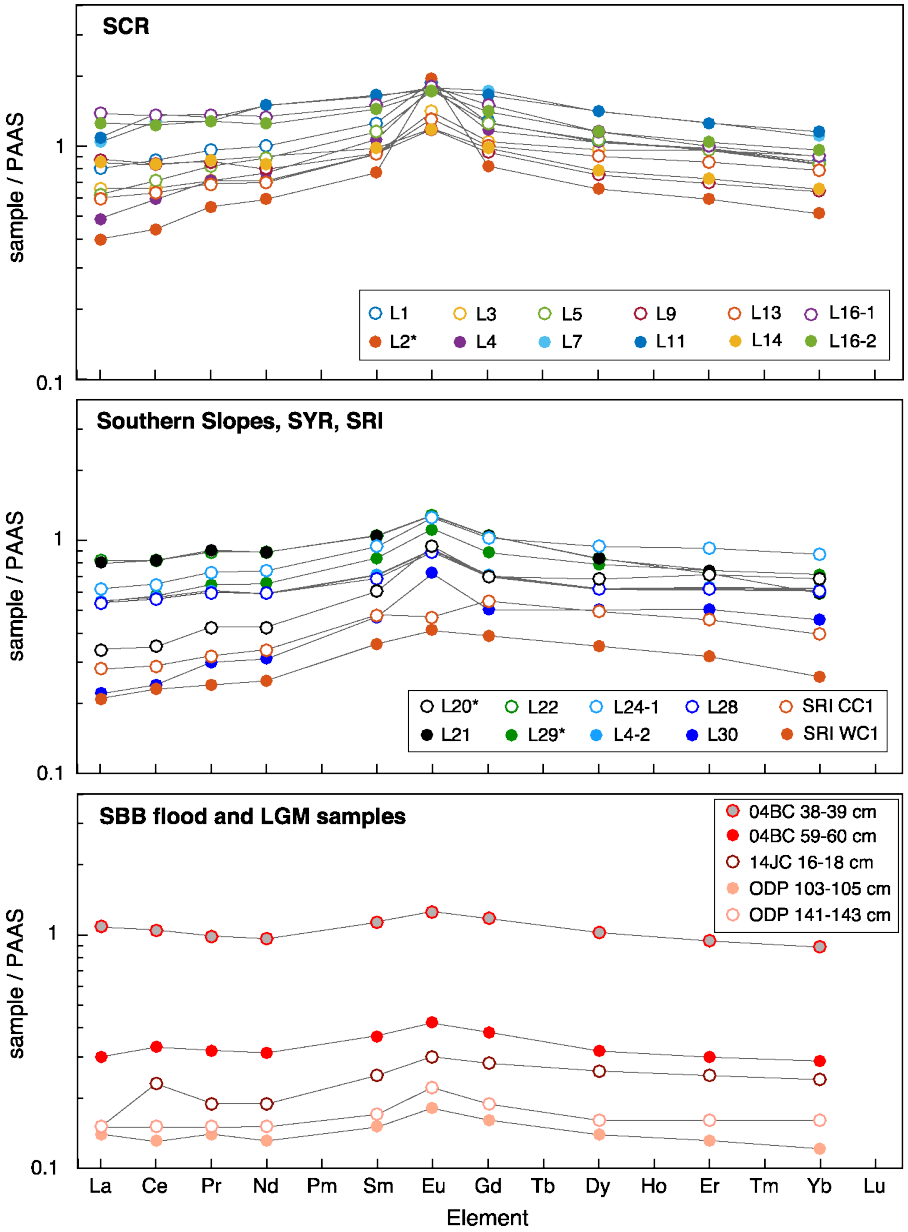


**Figure 2.6.** Shale-normalized (PAAS; McLennan, 1989) REE patterns for stream bed sediment samples and sediment core samples.
Asterisks denote averaging of results from multiple analyses of a sample. SCR–Santa Clara River catchment, VR–Ventura River catchment, SRI–Santa Rosa Island, SYR–Santa Ynez River catchment, SBB–Santa Barbara Basin, LGM–last glacial maximum.

**Table 2.4.** Sample elemental compositions.

| Element | Sample and Concentration | | | | | | | | | | | |
|---|---|---|---|---|---|---|---|---|---|---|---|---|
| | *Santa Clara River catchment* | | | | | | | | | | | |
| | L1 | L2 | L4 | L5 | L3 | L7 | L9 | L11 | L13 | L14 | L16-1 | L16-2 |
| *Major (%)* | | | *Bulk* | | | | | *Bulk* | | | | |
| Al | 8.81 | 9.31 | 8.92 | 8.38 | 6.93 | 8.07 | 8.50 | 7.16 | 8.25 | 8.22 | 7.70 | 8.09 |
| Ca | 2.99 | 4.83 | 3.42 | 2.99 | 3.00 | 2.39 | 2.52 | 1.12 | 2.89 | 2.08 | 3.31 | 1.64 |
| Fe | 5.72 | 5.44 | 5.28 | 5.12 | 6.41 | 4.14 | 5.20 | 1.48 | 5.50 | 3.89 | 3.79 | 3.16 |
| K | 2.04 | 1.31 | 1.62 | 1.95 | 1.74 | 2.60 | 2.56 | 3.60 | 2.08 | 2.80 | 2.19 | 2.60 |
| Mg | 1.41 | 1.89 | 0.50 | 1.36 | 2.74 | 1.14 | 1.85 | 0.31 | 1.75 | 1.20 | 1.24 | 0.87 |
| Na | 2.57 | 2.34 | 3.52 | 2.12 | 1.05 | 2.19 | 1.87 | 2.74 | 1.33 | 1.86 | 1.83 | 2.27 |
| Ti | 0.582 | 0.537 | 1.815 | 0.607 | 0.661 | 0.523 | 0.488 | 0.195 | 0.525 | 0.435 | 0.427 | 0.455 |
| *Minor (ppm)* | | | | | | | | | | | | |
| Rb | 55.6 | 18.8 | 31.3 | 78.0 | 93.0 | 112.0 | 111.0 | 124.0 | 102.5 | 122.0 | 75.4 | 125.5 |
| Sr | 576 | 818 | 896 | 480 | 209 | 357 | 338 | 220 | 384 | 280 | 394 | 295 |
| *REE (ppm)* | | *Average* | *<63 μm* | | | | | *<63 μm* | | | | |
| La | 30.6 | 15.1 | 18.7 | 23.7 | 25.3 | 39.6 | 33.4 | 41.5 | 23.0 | 32.3 | 52.5 | 47.9 |
| Ce | 69.3 | 35.4 | 46.8 | 56.9 | 52.8 | 101.4 | 66.9 | 109.3 | 50.4 | 66.2 | 107.3 | 97.7 |
| Pr | 8.5 | 4.8 | 6.2 | 7.3 | 6.3 | 11.3 | 7.6 | 11.8 | 6.1 | 7.7 | 12.1 | 11.3 |
| Nd | 34.0 | 20.0 | 26.4 | 30.0 | 24.1 | 45.5 | 27.6 | 50.5 | 23.7 | 28.5 | 44.9 | 42.0 |
| Sm | 6.9 | 4.3 | 5.9 | 6.4 | 5.2 | 9.1 | 5.3 | 9.1 | 5.1 | 5.4 | 8.4 | 8.0 |
| Eu | 2.0 | 2.1 | 1.9 | 1.9 | 1.5 | 1.9 | 1.3 | 1.9 | 1.4 | 1.3 | 1.9 | 1.9 |
| Gd | 6.0 | 3.8 | 5.5 | 5.8 | 4.9 | 8.1 | 4.4 | 7.8 | 4.7 | 4.6 | 6.9 | 6.6 |
| Dy | 4.9 | 3.1 | 4.9 | 5.0 | 4.6 | 6.6 | 3.5 | 6.6 | 4.2 | 3.7 | 5.4 | 5.4 |
| Er | 2.8 | 1.7 | 2.8 | 2.7 | 2.8 | 3.5 | 2.0 | 3.6 | 2.4 | 2.1 | 2.9 | 3.0 |
| Yb | 2.5 | 1.5 | 2.4 | 2.3 | 2.5 | 3.1 | 1.8 | 3.2 | 2.2 | 1.9 | 2.6 | 2.7 |
| *Ratios* | | | *<63 μm* | | | | | *<63 μm* | | | | |
| $^{1}La_N/Yb_N$ | 8.30 | 6.92 | 5.21 | 6.87 | 6.74 | 8.56 | 12.38 | 8.61 | 6.94 | 11.75 | 13.75 | 11.76 |
| Rb/Sr | 0.10 | 0.02 | | 0.16 | 0.44 | 0.31 | 0.33 | | 0.27 | 0.44 | 0.19 | 0.43 |
| $^{87}Sr/^{86}Sr$ | 0.707174 | 0.704731 | 0.706754 | 0.708172 | 0.710028 | 0.716059 | 0.713235 | 0.715875 | 0.710542 | 0.713884 | 0.712012 | 0.714334 |
| Sm/Nd | 0.2035 | 0.2143 | 0.2249 | 0.2123 | 0.2148 | 0.2006 | 0.1905 | 0.1809 | 0.2145 | 0.1908 | 0.1868 | 0.1897 |
| $^{143}Nd/^{144}Nd$ | 0.512146 | 0.512255 | | 0.512122 | 0.512266 | 0.511933 | 0.512032 | 0.511960 | 0.512089 | 0.512050 | 0.512019 | 0.512033 |
| $\varepsilon_{Nd}$ | -9.6 | -7.5 | | -10.1 | -7.3 | -13.8 | -11.8 | -13.2 | -10.7 | -11.5 | -12.1 | -11.8 |

[1]La and Yb have been normalized to average chondrite values (Boynton, 1984).

**Table 2.4** (*continued*). Sample elemental compositions.

| Element | Sample and Concentration | | | | | | | |
|---|---|---|---|---|---|---|---|---|
| | ***Southern Slopes*** | | | | ***Santa Ynez River catchment*** | | | |
| | L20 | L21 | L22 | L29 | L24-1 | L24-2 | L28 | L30 |
| *Major (%)* | | | | | | | | |
| Al | 7.42 | 7.67 | 7.72 | 4.62 | 7.21 | 6.7 | 6.14 | 7.13 |
| Ca | 5.25 | 1.92 | 1.01 | 5.03 | 4.09 | 3.29 | 2.98 | 1.73 |
| Fe | 4.29 | 4 | 4.16 | 3.4 | 4.26 | 3.52 | 3.53 | 2.29 |
| K | 2.24 | 2 | 2.31 | 2.03 | 1.44 | 1.65 | 1.54 | 2.35 |
| Mg | 1.35 | 1.51 | 1.69 | 1.81 | 1.88 | 1.44 | 2.62 | 0.69 |
| Na | 1.77 | 1.75 | 2.49 | 7.94 | 1.72 | 1.43 | 1.69 | 2.06 |
| Ti | 0.381 | 0.426 | 0.424 | 0.294 | 0.386 | 0.365 | 0.363 | 0.305 |
| *Minor (ppm)* | | | | | | | | |
| Rb | 116.0 | 84.9 | 117.5 | 87.1 | 62.3 | 74.2 | 72.7 | 110.5 |
| Sr | 419 | 238 | 210 | 538 | 258 | 216 | 239 | 319 |
| *REE (ppm)* | *Average* | | | *Average* | | | | |
| La | 31.0 | 15.5 | 26.1 | 20.7 | 10.7 | 15.3 | 23.6 | 8.2 |
| Ce | 65.1 | 39.1 | 52.7 | 44.8 | 24.8 | 30.8 | 51.8 | 19.3 |
| Pr | 7.9 | 5.1 | 6.3 | 5.4 | 3.5 | 4.0 | 6.5 | 2.7 |
| Nd | 30.1 | 20.6 | 23.5 | 20.0 | 14.2 | 14.6 | 25.1 | 10.6 |
| Sm | 5.8 | 4.7 | 4.7 | 3.9 | 3.5 | 3.2 | 5.2 | 2.6 |
| Eu | 1.4 | 1.2 | 1.2 | 1.0 | 1.0 | 1.0 | 1.4 | 0.8 |
| Gd | 4.9 | 4.2 | 4.1 | 3.3 | 3.5 | 3.0 | 4.8 | 2.4 |
| Dy | 3.9 | 3.8 | 3.5 | 2.9 | 3.6 | 2.8 | 4.4 | 2.4 |
| Er | 2.1 | 2.2 | 2.1 | 1.8 | 2.2 | 1.8 | 2.6 | 1.4 |
| Yb | 1.7 | 2.1 | 1.9 | 1.7 | 2.1 | 1.7 | 2.5 | 1.3 |
| *Ratios* | | | | | | | | |
| $^{1}La_N/Yb_N$ | 12.38 | 4.96 | 9.38 | 8.00 | 3.36 | 5.96 | 6.39 | 4.29 |
| Rb/Sr | 0.28 | 0.36 | 0.56 | 0.16 | 0.24 | 0.34 | 0.30 | 0.35 |
| $^{87}Sr/^{86}Sr$ | 0.711948 | 0.713200 | 0.712883 | 0.710425 | 0.709190 | 0.710416 | 0.710563 | 0.711692 |
| Sm/Nd | 0.1939 | 0.2268 | 0.1978 | 0.1941 | 0.2458 | 0.2206 | 0.2088 | 0.2469 |
| $^{143}Nd/^{144}Nd$ | 0.512079 | 0.512157 | 0.512153 | 0.512143 | 0.512472 | 0.512323 | 0.512242 | 0.512137 |
| $\varepsilon_{Nd}$ | -10.9 | -9.4 | -9.5 | -9.7 | -3.2 | -6.2 | -7.7 | -9.8 |

[1]La and Yb have been normalized to average chondrite values (Boynton, 1984).

**Table 2.4** (*continued*). Sample elemental compositions.

| Element | Sample and Concentration | | | | | | | | |
|---|---|---|---|---|---|---|---|---|---|
| | ***Santa Rosa Island*** | | | | ***SBB Holocene*** | | | ***SBB LGM*** | |
| | CC1 | CC1 sand | WC1 | WC1 sand | 04BC 38-39 cm bulk | 04BC 59-60 cm bulk | 14JC 16-18 cm bulk | ODP 103-105 cm bulk | ODP 141-143 cm bulk |
| *Major (%)* | | | | | | | | | |
| Al | 7.49 | | 7.80 | | 7.19 | 7.12 | 7.63 | 7.12 | 7.08 |
| Ca | 1.69 | | 1.75 | | 3.62 | 2.37 | 1.86 | 3.48 | 2.82 |
| Fe | 3.67 | | 3.44 | | 4.09 | 4.04 | 4.16 | 3.90 | 4.02 |
| K | 1.10 | | 0.97 | | 2.39 | 2.30 | 2.45 | 2.30 | 2.31 |
| Mg | 1.00 | | 1.11 | | 1.87 | 1.85 | 1.98 | 1.66 | 1.63 |
| Na | 1.94 | | 1.85 | | 3.34 | 2.66 | 2.19 | 2.20 | 2.29 |
| Ti | 0.374 | | 0.372 | | 0.422 | 0.419 | 0.430 | 0.384 | 0.390 |
| *Minor (ppm)* | | | | | | | | | |
| Rb | 50.5 | | 42.6 | | 134.0 | 128.5 | 141.0 | 127.5 | 124.0 |
| Sr | 292 | | 216 | | 325 | 243 | 204 | 315 | 269 |
| *REE (ppm)* | | | | | | | | | |
| La | 10.5 | | 7.8 | | 41.0 | 11.6 | 5.8 | 5.2 | 5.6 |
| Ce | 23.4 | | 18.5 | | 83.6 | 26.2 | 17.9 | 10.5 | 11.6 |
| Pr | 2.8 | | 2.1 | | 8.8 | 2.8 | 1.7 | 1.2 | 1.3 |
| Nd | 11.5 | | 8.5 | | 32.5 | 10.5 | 6.6 | 4.4 | 5.0 |
| Sm | 2.7 | | 2.0 | | 6.3 | 2.0 | 1.4 | 0.8 | 0.9 |
| Eu | 0.5 | | 0.4 | | 1.4 | 0.5 | 0.3 | 0.2 | 0.2 |
| Gd | 2.6 | | 1.8 | | 5.5 | 1.8 | 1.3 | 0.7 | 0.9 |
| Dy | 2.3 | | 1.6 | | 4.8 | 1.5 | 1.2 | 0.6 | 0.8 |
| Er | 1.3 | | 0.9 | | 2.7 | 0.8 | 0.7 | 0.4 | 0.4 |
| Yb | 1.1 | | 0.7 | | 2.5 | 0.8 | 0.7 | 0.3 | 0.4 |
| *Ratios* | | | | | | | | | |
| $^{1}La_N/Yb_N$ | 6.32 | 4.45 | 7.16 | 5.08 | 10.95 | 9.69 | 5.77 | 10.21 | 8.50 |
| Rb/Sr | 0.17 | | 0.20 | | 0.41 | 0.53 | 0.69 | 0.40 | 0.46 |
| $^{87}Sr/^{86}Sr$ | 0.707577 | 0.705290 | | 0.706667 | 0.711794 | 0.712400 | 0.713350 | 0.711273 | 0.711704 |
| Sm/Nd | 0.2322 | | 0.2319 | | 0.1944 | 0.1942 | 0.2155 | 0.1916 | 0.1906 |
| $^{143}Nd/^{144}Nd$ | 0.512626 | 0.512750 | 0.512585 | 0.512667 | 0.512086 | 0.512102 | 0.512109 | 0.512126 | 0.512123 |
| $\varepsilon_{Nd}$ | -0.2 | | -1.0 | | -10.8 | -10.4 | -10.3 | -10.0 | -10.0 |

[1]La and Yb have been normalized to average chondrite values (Boynton, 1984).

The SBB samples have consistent, non-normalized Sm/Nd values between 0.1906 and 0.1944, except for the 14JC 16-18 cm Holocene flood sample, which has a higher ratio of 0.2155 (Table 2.4). The sub-catchment average Sm/Nd values range from 0.1809 to 0.2469. The $La_N/Yb_N$ of the samples, where the subscript N denotes normalization to average chondrite concentrations from Boynton (1984), are variable with a large range of 3.36-13.75 (Table 2.4). Samples from the SYR catchment have lower $La_N/Yb_N$ between 3.36 and 6.39, and the SRI samples have $La_N/Yb_N$ ratios between 4.45 and 7.16. The remaining samples range from 4.96 to 13.75 (Table 2.4).

Principal component analysis (PCA) was used to deconvolve influences on major element composition (Table 2.5). Iron and Ti have the highest loadings in the first principal component (PC1). The second principal component (PC2) has strong positive loadings for Mg, and strong negative loadings for Na, K, and Al. Samples from L4, L11, and L29 were not included in the major element PCA due to very high concentrations of Ti (L4) and Na (L29), and low concentrations of Fe (L11). Further, bed sediment samples from L4 and L11 are bulk samples, as opposed to <63 μm subsamples for the other bed sediment samples, therefore they were also excluded to remove grain size influences. The sub-catchments plot in distinct areas within the major element principal component space. The Eastern Santa Clara River samples have high PC1 values and low PC2 values (Figure 2.7). The Pelona Schist has high PC1 and PC2 values. The Eastern Santa Ynez sub-catchment samples are centered in PC1, but have high PC2 values. Santa Rosa Island samples have slightly more negative PC1 values that separate them from the Southern Slopes and the SBB samples. The Holocene flood samples plot within the Southern Slopes field, while the LGM samples plot slightly closer to the SRI samples (Figure 2.7).

**Table 2.5.** Major element principal component analysis loadings.

| Variable | Loading[1] | |
|---|---|---|
| | PC1 | PC2 |
| Al | 0.29 | **-0.56** |
| Ca | 0.29 | 0.25 |
| Fe | **0.61** | -0.04 |
| K | -0.10 | **-0.46** |
| Mg | 0.36 | **0.41** |
| Na | -0.14 | **-0.44** |
| Ti | **0.55** | -0.24 |
| Variance | 36% | 25% |

[1]Bolded values indicate that a variable has a higher loading than would be expected if each variable were independent of one another. Loadings were bolded if their value was greater than the square root of (1/n), where n = the number of elements used in the principal component analysis.

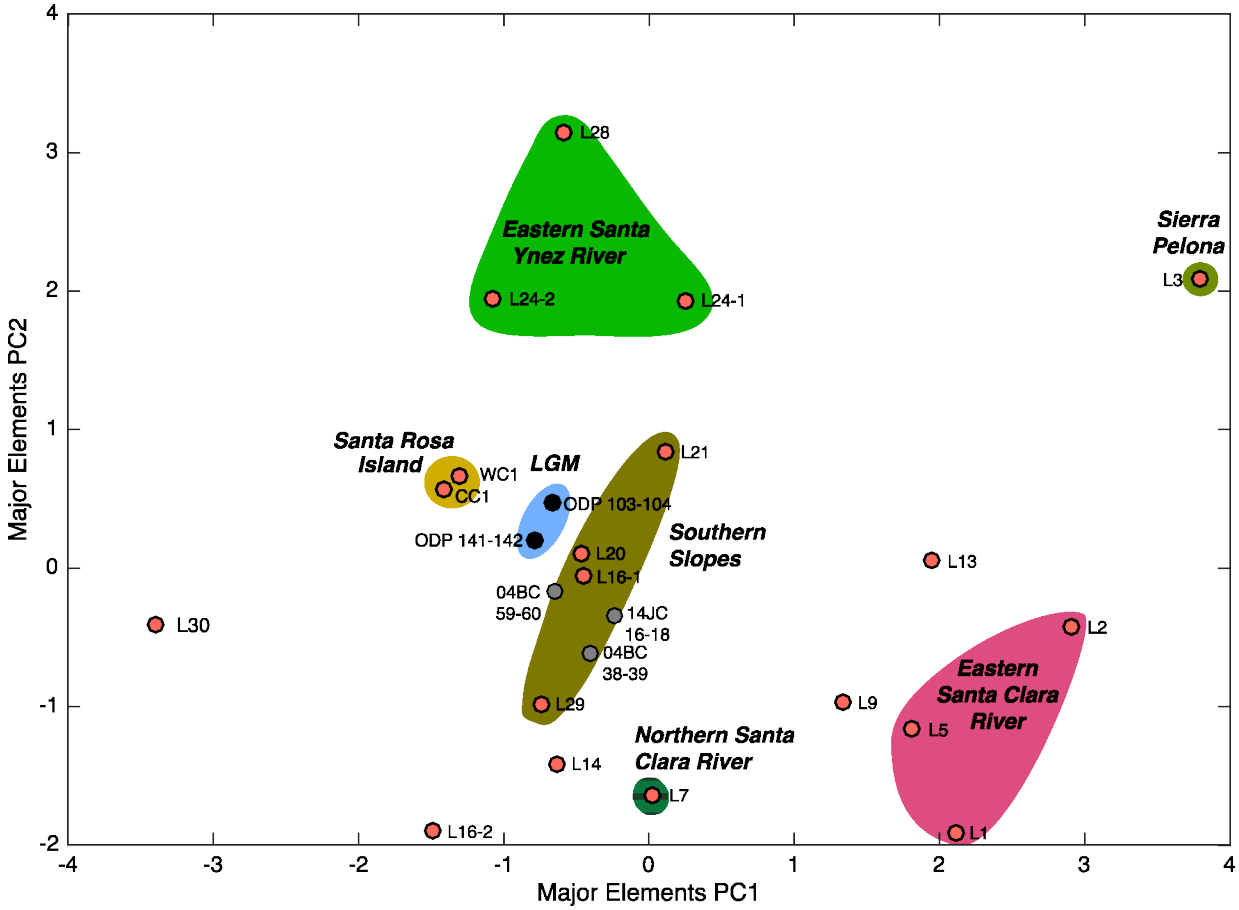


**Figure 2.7.** The <63 μm grain size fraction of stream bed sediment (black circles) and bulk sediment core samples (flood deposits [red circles] and last glacial maximum sediment [pink circles]) plotted along the first (PC1) and second (PC2) major element principal components (Table 2.5).
Samples L4 and L11 were excluded from the analysis. Composition groups are shaded and reflect locations in Figures 2.1 and 2.2C. SRI–Santa Rosa Island.

*2.4.3 Isotopes*

The catchment and SBB samples have variable $^{87}Sr/^{86}Sr$ values (Figure 2.8; Table 2.4). The SCR samples have a wide range of $^{87}Sr/^{86}Sr$, from 0.716059 in the L7 sample to 0.704731 in the L2 sample. Samples from the Eastern Santa Clara sub-catchment have the lowest $^{87}Sr/^{86}Sr$ values of the SCR catchment, while the samples from the Northern Santa Clara River have the highest $^{87}Sr/^{86}Sr$ values. Samples collected from sub-catchments that drain the southern Santa Ynez Mountains (Western Santa Clara and Southern Slopes) fall between ~0.710 and ~0.714 in $^{87}Sr/^{86}Sr$ values, as do the SBB samples.

The catchment and SBB samples also have variable $\varepsilon_{Nd}$ values, ranging from -14 to +2.2 (Figure 2.8; Table 2.4). The SRI samples have the most positive $\varepsilon_{Nd}$ values, from ~0 to +2. Samples from the Eastern Santa Ynez sub-catchment range from -7.7 to -3.2 in $\varepsilon_{Nd}$. The Eastern Santa Clara sub-catchment samples range from -10.1 to -7.5 in $\varepsilon_{Nd}$. The Northern Santa Clara sub-catchment samples have the most negative $\varepsilon_{Nd}$ values, from ~ -14 to -13. Samples collected from the Southern Slopes region and SBB have $\varepsilon_{Nd}$ values between -12.1 and -9.4. The LGM SBB samples are slightly depleted in $\varepsilon_{Nd}$ compared to the Holocene flood samples.

The Sr and Nd isotopic compositions of the bed sediment samples are generally not consistent with previous work in the study area (Table 2.6). The Eastern Santa Clara sub-catchment samples overlap slightly with the $^{87}Sr/^{86}Sr$ range of the Mendenhall Gneiss, which crops out in the San Gabriel Mountains (Barth et al., 1995). The $^{87}Sr/^{86}Sr$ value of gneiss collected near the Bouquet Reservoir (Kistler et al., 1973), located just north of the Sierra Pelona schist, is similar to the L3 Sr isotopic result. The Liebre Mountain and Mt. Pinos radiogenic Sr and Nd isotopic values determined by Kistler et al. (1973) are much lower than the measured values of bed sediment samples collected downstream from those sources (Tables 2.4 and 2.6; Figures 2.1 and 2.8). The SRI stream bed sediment samples bear Sr isotopic values that are similar to the basaltic andesite rocks from the Tranquillon Volcanics (Cole and Basu, 1995), located just south of the SYR mouth, and are also similar to whole rock samples from the Willows Plutonic Complex on Santa Cruz Island (Hammond Gordon and Weigland, 1994), located just east of SRI (Tables 2.4 and 2.6; Figures 2.1 and 2.8). The SBB samples have $\varepsilon_{Nd}$ values that are similar to samples from core ODP 893A, collected from the SBB (Murphy and Thomas, 2010). The Southern Slopes and SBB samples compare well with the global average Sr and Nd isotopic compostion of river sediment (Figure 2.8) (Goldstein and Jacobsen, 1988).

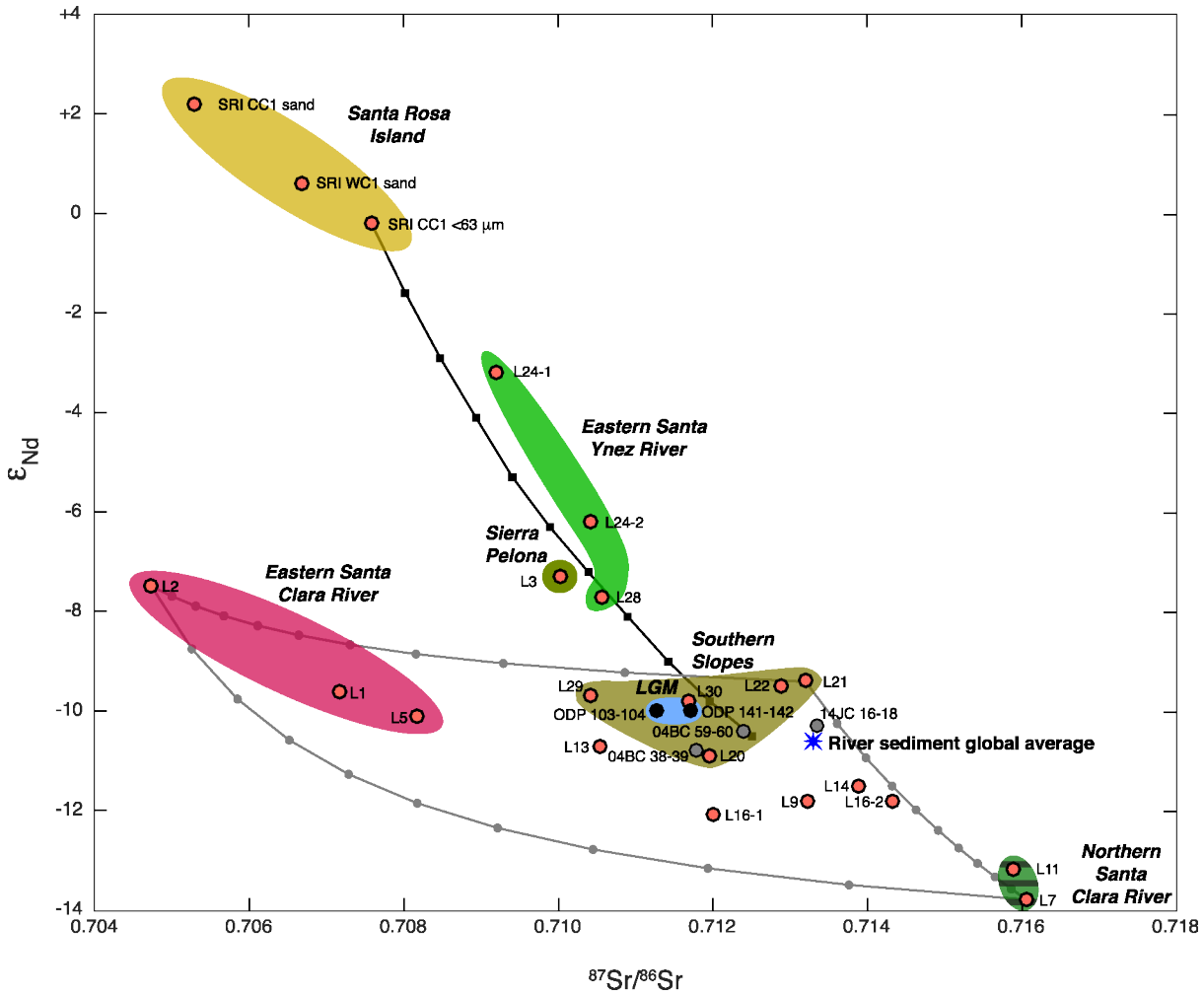


**Figure 2.8.** Isotopic composition of the <63 μm grain size fraction of stream bed sediment (black circles) and bulk sediment core samples (flood deposits [red circles] and last glacial maximum sediment [pink circles]). Mixing lines are marked with 10% increments of binary mixtures between end-member pairs. Two sand size (63-250 μm) Santa Rosa Island (SRI) samples are also plotted. The blue star denotes the Sr and Nd isotopic compositions of average global river water (Goldstein and Jacobsen, 1988). Composition groups are shaded and reflect locations in Figures 2.1 and 2.2C.

**Table 2.6.** Strontium and Neodymium isotopic results from source localities within the study area.

| Locality | Rock Type | $^{87}Sr/^{86}Sr_{(0)}$ * | $^{143}Nd/^{144}Nd_{(0)}$ | $\varepsilon_{Nd(0)}$ ** | Reference |
|---|---|---|---|---|---|
| Mendenhall Gneiss | mafic granulites | 0.70717 | | | Barth et al. (1995) |
| Mendenhall Gneiss | mafic granulites | 0.70569 | | | Barth et al. (1995) |
| Mendenhall Gneiss | mafic granulites | 0.70779 | | | Barth et al. (1995) |
| Mendenhall Gneiss | mafic granulites | 0.71587 | | | Barth et al. (1995) |
| Mendenhall Gneiss | mafic granulites | 0.70618 | | | Barth et al. (1995) |
| Mendenhall Gneiss | mafic granulites | 0.70466 | | | Barth et al. (1995) |
| Mendenhall Gneiss | mafic granulites | 0.70567 | | | Barth et al. (1995) |
| Mendenhall Gneiss | mafic granulites | 0.70827 | | | Barth et al. (1995) |
| Mendenhall Gneiss | augen gneiss | 0.71815 | | | Barth et al. (1995) |
| Mendenhall Gneiss | augen gneiss | 0.70943 | | | Barth et al. (1995) |
| Mendenhall Gneiss | felsic gneiss | 0.70892 | | | Barth et al. (1995) |
| Mendenhall Gneiss | felsic gneiss | 0.71088 | | | Barth et al. (1995) |
| Mendenhall Gneiss | felsic gneiss | 0.73774 | | | Barth et al. (1995) |
| Mendenhall Gneiss | felsic gneiss | 0.72480 | | | Barth et al. (1995) |
| Mendenhall Gneiss | felsic gneiss | 0.70694 | | | Barth et al. (1995) |
| Mendenhall Gneiss | felsic gneiss | 0.75602 | | | Barth et al. (1995) |
| Mendenhall Gneiss | aluminous gneiss | 0.74607 | | | Barth et al. (1995) |
| Mendenhall Gneiss | aluminous gneiss | 0.74636 | | | Barth et al. (1995) |
| Bouquet Reservoir | gneiss | 0.7099 | | | Kistler et al. (1973) |
| Liebre Mountain | granitic | 0.7095 | | | Kistler et al. (1973) |
| Mt. Pinos | gneiss | 0.7168 | | | Kistler et al. (1973) |
| Mt. Pinos | - | 0.7092 | | | Kistler et al. (1973) |
| Mt. Pinos | - | 0.7136 | | | Kistler et al. (1973) |
| Mt. Pinos | amphibolite | | 0.511735 | -17.6 | Bennett and DePaolo (1987) |
| Mt. Pinos | pelitic schist | | 0.510731 | -37.2 | Bennett and DePaolo (1987) |
| Mt. Pinos | augen gneiss | | 0.510830 | -35.3 | Bennett and DePaolo (1987) |
| Tranquillon volcanics | rhyolite | 0.710617 | 0.512738 | 2.0 | Cole and Basu (1995) |
| Tranquillon volcanics | rhyolite | 0.710729 | 0.512727 | 1.7 | Cole and Basu (1995) |
| Tranquillon volcanics | rhyolite | 0.712017 | 0.512759 | 2.4 | Cole and Basu (1995) |
| Tranquillon volcanics | basaltic andesite | 0.704033 | 0.512867 | 4.5 | Cole and Basu (1995) |
| Tranquillon volcanics | basaltic andesite | 0.704125 | 0.512943 | 5.9 | Cole and Basu (1995) |
| Santa Cruz Island, WPC | whole rock | 0.70372 | | | Hammond Gordon and Weigland (2004) |
| Santa Cruz Island, WPC | whole rock | 0.70357 | | | Hammond Gordon and Weigland (2004) |
| Santa Cruz Island, WPC | whole rock | 0.70370 | | | Hammond Gordon and Weigland (2004) |
| Santa Cruz Island, WPC | whole rock | 0.70343 | | | Hammond Gordon and Weigland (2004) |
| Santa Cruz Island, WPC | whole rock | 0.70367 | | | Hammond Gordon and Weigland (2004) |
| Santa Cruz Island, WPC | whole rock | 0.70352 | | | Hammond Gordon and Weigland (2004) |
| Sediment core ODP 893A | silicate >63 μm | | 0.5120376 | -11.7 | Murphy and Thomas (2010) |
| Sediment core ODP 893A | silicate >63 μm | | 0.5120269 | -11.9 | Murphy and Thomas (2010) |
| Sediment core ODP 893A | silicate >63 μm | | 0.5120236 | -12.0 | Murphy and Thomas (2010) |
| Sediment core ODP 893A | silicate >63 μm | | 0.5120318 | -11.8 | Murphy and Thomas (2010) |

*Subscript (0) denotes present-day measurement.
**$^{143}Nd/^{144}Nd_{CHUR} = 0.512638$
WPC –Willows Plutonic Complex

## 2.5 Discussion

The composition of the river bed samples primarily reflects the adjacent geology, and therefore detrital sediments from the river catchments can be used for provenance work. In addition to adjacent geology, river bed samples reflect upstream geology, transformation by physical and chemical weathering, differential erosion rates of source rocks, and sediment transport processes that sort and mix the sediment. Processes that influence sample composition will be discussed first, before geochemically characterizing distinct drainage basins that may be

prospective source areas, and finally the provenance of the Holocene flood deposits and LGM sediments deposited in SBB will be demonstrated.

*2.5.1 Influences on river sediment composition*

The primary controls on sample mineralogy and geochemical composition are the adjacent and upstream lithologic units. Most of the units in the study area have undergone sedimentary recycling, and thus contain relict influences of weathering and associated loss/retention of mobile/immobile elements, as well as of sedimentary grain size sorting that are reflected in their composition. The modern stream bed samples are also subjected to weathering and grain size sorting during their transport downstream. Additionally sample compositions are influenced locations within the study area that have high erosion rates will and proportionately contribute more sediment to the bed load.

Adjacent lithologies are clearly reflected in sample mineral composition. Amphibole and pyroxene in the Eastern Santa Clara sub-catchment samples are likely sourced from the adjacent amphibolite and augen orthogneiss in the Proterozoic crystalline basement complex, while the abundant plagioclase is from the anorthosite complex (Critelli et al., 1997; Fan, 1976) (Figures 2.1 and 2.3). The L3 sample mineralogy is reflective of the metamorphic Sierra Pelona Schist, that bears minerals associated with the greenschist metamorphic facies including epidote, chlorite, and muscovite. The mineralogy of sample L24-1 represents a metamorphic assemblage, that of the Franciscan Formation and its associated greenstones, including serpentinite. Additionally the SYR bed sediment mineralogy is influenced by amorphous silica from chert and diatomite, and calcite from limestone in the uplifted marine sediments of the catchment (Figure 2.4). Samples collected from the SRI, Northern Santa Clara, and Western Santa Clara sub-catchments and the Southern Slopes region have mineralogies typical of clastic sedimentary lithologies, with high proportions of quartz, feldspar, clay minerals, and minor calcite. The high calcite in the GC suspended load sample can be attributed to sampling near a carbonate bed associated with the Miocene Monterey Shale (Dibblee Jr, 1981).

The decrease in plagioclase downstream along the SCR with increased distance from the anorthosite complex is the result of numerous compounding processes. First, sediment yield decreases as distance from the source increases (Parsons et al., 2006). Further, plagioclase is susceptible to physical and chemical weathering, which leads to its degradation downstream and

also during sediment recycling. Finally, dilution by other minerals also plays an important role. The fastest fault slips rates (Table 2.1) and greatest sediment yield occur in the Western Santa Clara sub-catchment and the Southern Slopes region (Figure 2.2B). The young sedimentary units in this area are derived from older, local sedimentary units, and thus are composed of more resistant quartz and potassium feldspar. These factors all contribute to the decline in plagioclase abundance downstream, as well as declining amphibole and pyroxene. In addition these factors also explain the increased abundances of quartz, potassium feldspar, and clay minerals, which are the stable products of chemical weathering.

Sedimentary sorting is another important parameter influencing mineral composition. Dense minerals, such at titanomagnetite tend to fall out of suspension and become concentrated in the bedload, therefore their abundances decrease downstream. Conversely clay minerals tend to remain in suspension and therefore increase in abundance downstream. Additionally, anthropogenic influences on mineral composition are also observed. The large changes in mineral abundances between L11 and L9, both collected from Piru Creek, are reflective of sampling above and below a dam, which prevents larger, denser grains from moving downstream, thus the L9 sample contains abundant clay mineral smectite (Figure 2.3).

Sample elemental compositions reflect the sample mineralogy and rock type observations. The sample from L4 (Eastern Santa Clara) contains abundant Ti, which can be associated with the titanomagnetite observed during sample collection. Samples with high plagioclase abundance also contain high concentrations of Ca and Na, and samples with abundant potassium feldspar contain high concentrations of K. The high concentrations of Na and Ca in the L29 sample indicate substantial influence of seawater and the nearshore environment. Strongly correlated Fe, Ti, and Mg may manifest the presence of titanomagnitite in the samples, as observed at L4, and/or other mafic minerals.

The behavior of elements in earth surface environments can also explain elemental relationships. During chemical weathering of minerals, the behavior of elements causes them to either be retained in the mineral products (e.g., clay minerals) or to be lost. For example, Ti and Al are relatively immobile elements, and their correlation could be the result of this property. Conversely, Ca and Sr are mobile and are removed during mineral disintegration.

The Rb/Sr and Sm/Nd sample values are typical of the upstream lithologies, but are also heavily leveraged by the sample mineralogy. In general, the sample Sm/Nd values are similar to

the average upper continental crust value of 0.18 (Taylor and McLennan, 1981). Samples from the Eastern Santa Clara sub-catchment (L1, L2, L4) have low Rb/Sr that can be attributed to abundant plagioclase, which has low Rb and high Sr concentrations. The Sm/Nd values of the Eastern Santa Clara samples are similar to intermediate plutonic rocks (0.215, Faure and Mensing), consistent with the lithologies of the Western San Gabriel Mountains. The Sierra Pelona sample (L3) Rb/Sr matches that of average shales (~0.47, Turekian and Wedepohl, 1961) and its Sm/Nd value is similar to sandstone (0.227, Faure and Mensing, 2005), consistent with its arc trench sediment proto-lithology. The Rb/Sr of samples from the Northern and Eastern Santa Clara, the Southern Slopes, and the Eastern and Western Santa Ynez sub-catchments falls between high-Ca granitic and shale Rb/Sr values (~0.25–0.47, Turekian and Wedephol, 1961), consistent with recycled sedimentary units and the anothorsite source in the Eastern Santa Clara sub-catchment. The Sm/Nd values of these sub-catchments also aligns with shale and sandstone sources, except for the Northern Santa Clara sub-catchment, where samples bear Sm/Nd values that are similar to granite (0.188, Faure and Mensing, 2005). The low Rb/Sr of sample L29 may be due to high quartz abundance. The SRI samples also have low Rb/Sr, and this could be attributed to abundant amorphous silica, quartz, and smectite. The SRI samples bear Sm/Nd values that are similar to sandstone (Table 2.4). The SBB samples yielded Rb/Sr and Sm/Nd values that are typical of shales, as expected for fine-grained, clastic marine sediments. Differences between the river bed sediment Sr and Nd isotopic values (Table 2.4) and published isotopic results (Table 2.6) from sources within the study area can be attributed to mixing of the myriad igneous and sedimentary sources during sediment transport.

The PAAS-normalized REE patterns of the stream bed and SBB sediment core samples are lower than or close to unity, indicating typical shale composition, but also that some samples have undergone more intense weathering than PAAS (Jin et al., 2006). The Eu enrichments match the observed high plagioclase feldspar content (Nance and Taylor, 1977). Positive Ce anomaly in the SBB 14JC 16-18 cm sample may indicate the presence of Fe- and Mn-oxyhydroxides, known to scavenge Ce (Masuzawa et al., 1989). The sampled 14JC flood deposit is particularly thick (5 cm), compared to the 04BC flood deposits (≤1.5 cm in thickness; Napier and Hendy, in press). Additionally, SBB flood deposits are clay-rich and have low permeability. Thus the thick, impermeable flood deposit in 14JC may have escaped exposure to typical SBB reducing conditions via the “coffin lid” effect, preventing degradation (Schimmelmann, 2012)

and allowing the Fe- and Mn-oxyhydroxides to remain intact and resulting in a positive Ce anomaly for this sample. The chondrite-normalized $La_N/Yb_N$ sample values are generally typical of sandstones and shales, but the lower ratios of the SYR and SRI catchments reflect sediment mixing with the metamorphic and volcanic units in those catchments (Condie, 1993).

The PCA results suggest that the greatest variability in major element content is related to the dichotomy between mafic and felsic compositions (Figure 2.7). Sample locations in the Eastern Santa Clara sub-catchment are associated with increased PC1 (high loadings for Fe and Ti), indicating a mafic composition, but also with lower PC2 values (driven by higher Na and Al; Tables 2.4-2.5), which is attributable to the high plagioclase feldspar content. The Sierra Pelona sample is mafic on both PC axes, with high Fe, Ti, and Mg (higher PC2 values). Samples associated with the Eastern Santa Ynez sub-catchment are mafic on the PC2 axis (high Mg), but are slightly felsic on the PC1 axis, which could reflect mixing of the sedimentary rocks with the greenstone metamorphic units of the Franciscan Formation. Samples collected from the Southern Slopes are slightly negative in PC1, but range from felsic to slightly mafic along PC2.

*2.5.2 Characterization of source areas*

The above geochemical analyses, in particular the PCA and the isotopic results, distinguished six composition groups and potential source areas:

1. The Eastern Santa Clara sub-catchment (samples L1, L2, L4, L5) is characterized by mafic major element PC1 (Fe-Ti-rich) and felsic major element PC2 (Na-K-Al-rich) (Figure 2.7; Table 2.5), $^{87}Sr/^{86}Sr$ values ranging from 0.704-0.708, and $\varepsilon_{Nd}$ values between -7 and -10, consistent with derivation from an ancient mafic crustal source (e.g., San Gabriel Mountains anorthosite complex) (Barth et al., 1995) (Figure 2.8; Table 2.4).
2. The Sierra Pelona sub-catchment sample (L3) is mafic in PC1 and PC2 (Figure 2.7; Table 2.5), with $^{87}Sr/^{86}Sr$ of ~0.710 and an $\varepsilon_{Nd}$ value of -7.3.
3. The Northern Santa Clara sub-catchment (L7, L11) sample composition is relatively felsic (Figure 2.7; Table 2.5), and bears $^{87}Sr/^{86}Sr \sim 0.716$ and $\varepsilon_{Nd}$ values between -13 and -14 (Figure 2.8; Table 2.4).
4. The Southern Slopes and Western Santa Clara sub-catchment are compositionally similar. The southern flanks of the Santa Ynez Mountains are drained by the Southern

Slopes catchment and the southern flanks of the Topatopa Mountains are drained by the Western Santa Clara sub-catchment (Figures 2.1 and 2.2C). Allowing the Southern Slopes samples (L20, L21, L22, and L29) to define the Santa Ynez Mountains group composition, suggests this group is slightly felsic in composition, and bears $^{87}Sr/^{86}Sr$ values between 0.710 and 0.715 and $\varepsilon_{Nd}$ between -9 and -12 (Figure 2.8; Table 2.4). Expanding to include the Western Santa Clara sub-catchment (L9, L13, L14, L16, L20, L21, L22, L29, L30) and thus the Topatopa Mountains, results in a composition that is slightly felsic (negative PC2; Figure 2.7), with $^{87}Sr/^{86}Sr$ values ranging between ~0.710-0.715, and $\varepsilon_{Nd}$ between ~ -9 and -12 (Figure 2.8, Table 2.4), similar to the global average of river sediments (Goldstein and Jacobsen, 1988).

5. The Eastern Santa Ynez sub-catchment is defined by samples from L24 and L28. Group sample composition is slightly mafic as indicated by higher PC2 values (Mg-rich; Figure 2.7; Table 2.5). Sample $^{87}Sr/^{86}Sr$ values range between ~0.709–0.711, and $\varepsilon_{Nd}$ ranges from -9 to -3 (Figure 2.8; Table 2.4).
6. The SRI group composition is slightly felsic (Figure 2.7), with $^{87}Sr/^{86}Sr$ ranging from ~0.705–0.708, and from ~0 to +2 in $\varepsilon_{Nd}$, reflective of sedimentary mixing with the young (Miocene) volcanics (Weaver, 1969) (Figure 2.8; Table 2.4).

*2.5.3 Provenance of the SBB Holocene flood layer samples*

The SBB flood deposit samples deviate slightly from the glacial samples in mineralogy, PCA results, and radiogenic isotope values, suggesting differences in SBB sediment source between the LGM and the Holocene/modern. The PCA and radiogenic isotope results indicate that the Eastern Santa Ynez and SRI sub-catchments are not major contributors to SBB sediments (Figures 2.7-2.8). Mineralogy is remarkably similar among the Holocene flood layer samples from SBB, suggesting that sources of flood deposit sediment are consistent (Figure 2.4). The flood layers each contain 4-5% chlorite, similar to the amount in the L16 <63 μm subsamples from the Western Santa Clara sub-catchment (Figure 2.3; Table 2.3). This indicates that the Western Santa Clara is a major contributor of flood sediment, consistent with previous work (Fleischer, 1972). Some chlorite was also identified in the GC and MC suspended sediment samples from the Southern Slopes; therefore this region is probably also a source of flood deposit sediment. Illite and kaolinite, present in the flood layer samples, are likely sourced from

the Southern Slopes. The higher proportions of clay minerals in the flood layers as compared to the <63 μm river bed sediment subsamples can be attributed enrichment of smaller grain sizes in SBB sediments as larger, denser grains (e.g., quartz, feldspar, titanomagnetite) settle out during transit from their sources to the marine basin >10 km offshore.

In terms of the PCA, the SBB samples are generally most similar in values to the Southern Slopes composition group, as defined by samples L20, L21, L22, and L29 (Figure 2.7). Strontium and Nd isotope results are consistent with the PCA work, and reveal an even tighter correspondence between the Southern Slopes source area and the SBB flood deposit samples. Estimation of provenance sources using the Sr-Nd mixing lines suggests the Southern Slopes provide ~80% of flood deposit sediment, the Eastern Santa Clara sub-catchment contributes <10%, and the Northern Santa Clara sub-catchment contributes ~10-20% (Figure 2.8). The primary sources of SBB Holocene flood layer sediment are the sedimentary units of the Southern Slopes region, and the Western Santa Clara sub-catchment, which contributes chlorite to the flood deposits. Streams with the highest sediment loads in the Southern Slopes region drain young Pliocene-Quaternary sedimentary rocks, and these are located in the eastern Santa Ynez Mountains, which have uplift rates >5 mm/yr (Duvall et al., 2004). The easily erodible rocks, together with higher slip rates, lead to increased sediment discharge (Warrick and Mertes, 2009). The river sediment load increases during flood events, and the easily erodible sediment in the Southern Slopes region and Western Santa Clara sub-catchment (southern flanks of the Santa Ynez Mountains and Topatopa Mountains) is transported and deposited in SBB as a flood layer.

### *2.5.4 Provenance of the SBB LGM samples*

Comparison of the LGM samples from ODP core 893A with the Holocene flood layer samples from SPR0901-04BC and MV0811-14JC reveal a potential SBB sediment source change between the low sea level stand of the last glacial and the Holocene sea level high stand. The LGM samples do not contain chlorite, and illite and muscovite abundances are much lower than the flood samples, while the kaolinite abundance is higher (Figure 2.4; Table 2.3). The absence of chlorite can be interpreted as a loss of sediment influx from the Western Santa Clara sub-catchment, while less muscovite in the LGM samples could indicate that the VR catchment contributed less sediment to SBB during the sea level low stand. The increase in kaolinite abundance in the LGM samples suggests that the SRI catchment contribution to SBB sediments

increased during the low stand, and perhaps sediment flux from the Channel Islands as a whole was higher at this time. The LGM samples are slightly less mafic along major element PC1 (Fe-Ti-rich) and slightly more mafic along the major element PC2 (Mg), plotting closer to the SRI samples as compared to the flood deposit samples (Figure 2.7). The LGM samples also plot within the radiogenic Sr-Nd composition of the Southern Slopes group, but are more depleted in $\varepsilon_{Nd}$ compared to the SBB Holocene flood deposits (Figure 2.8).

The LGM samples contain greater proportions of plagioclase, potassium feldspar, and quartz as compared to the Holocene flood layer samples, which may be caused by increased grain size in the LGM samples. Eustatic sea level is estimated to have been ~120 m lower than the modern sea level during the LGM (Figure 2.1), and therefore the distance from the coastline to SBB was reduced, leading to less settling out of the larger grain sizes during sub-aerial marine transit. Alternatively, bioturbation of LGM sediments could have mixed in larger grain sizes deposited by downslope processes.

The mineralogical and geochemical data indicate that the Southern Slopes were a prominent source of SBB sediments during the last glacial sea level low stand, with potential increased sediment flux from SRI and the Channel Islands as a whole. Strontium-Nd mixing model estimates suggest the Southern Slopes contributed ~90% of sediment to SBB during the LGM, while the Eastern Santa Clara and Northern Santa Clara sub-catchments contributed <10% (Figure 2.8). Consistent with the observations of Normark et al. (2006), the results presented here indicate that the SCR did not discharge into SBB during the LGM, and that the VR may have bypassed SBB as well. The river systems of the Santa Ynez Mountains west of the VR catchment and of the Channel Islands are restricted, and could not have bypassed SBB during the LGM. The consistency in sedimentation rates between the LGM and Holocene (Hendy et al., 2002; Hill et al., 2006), despite the loss of SCR input, must then be attributed to increased denudation of the Santa Ynez Mountains west of the VR catchment and of the Channel Islands during the glacial. Based on estimates from bimodal Sr-Nd mixing between the <63 μm SRI sample and the Holocene flood deposit average, the Channel Islands' sediment contribution to SBB was ~10% greater during the LGM sea level low stand than during the Holocene high stand (Figure 2.8). Increased erosion and incision associated with the LGM sea level lowstand has been observed in the upstream areas of SRI (Schumann et al., 2016). Late Pleistocene alluvium was entirely eroded from the SRI valleys during the LGM lowstand (Schumann et al., 2016),

which would have generated increased sediment flux from northern SRI drainages into SBB. The Santa Ynez Mountains likely also experienced similar upstream erosion and incision, and increased sediment flux to SBB during the LGM. Increased contribution from the Santa Ynez Mountains and SRI (Channel Islands) to SBB during the LGM is consistent with greater compositional similarity between the SBB LGM samples and the Southern Slopes and SRI composition groups, and with less influence from the SCR catchment source groups.

## 2.6 Conclusion

Detrital sediments deposited in marine basins provide insight into onshore areas at-risk to flooding when the provenance of those sediments can be determined. Six distinct composition groups were identified using the stream bed sample PCA and Sr and Nd isotope results, which represent potential SBB sediment source areas. These are: 1. the Eastern Santa Clara sub-catchment, 2. the Northern Santa Clara sub-catchment, 3. the Southern Slopes and Western Santa Clara sub-catchment group, 4. the Eastern Santa Ynez sub-catchment, and 5. SRI.

Similarities in Sr and Nd radiogenic isotopic compositions, PC1 and PC2 values, and chlorite concentrations between the SBB flood deposits and the Southern Slopes and Western Santa Clara sub-catchment samples (L16), suggest these sub-catchments are major contributors of flood deposit sediment. The Southern Slopes account for ~80% of flood deposit sediment, while the Eastern Santa Clara sub-catchment contributes <10%, and the Northern Santa Clara sub-catchment supplies ~10%. The results of this work indicate that both hypotheses are correct for Holocene flood deposits, i.e., the Western Santa Clara River catchment is a primary source of sediment, consistent with Fleischer (1972), and the weak lithologies of the Santa Ynez Mountains (Southern Slopes units, derived from sedimentary recycling of older units within the study area) are also a major sediment source, consistent with Warrick and Mertes (2009). Therefore the Santa Ynez Mountains and Topatopa Mountains region, identified here as the Western Santa Clara sub-catchment and the Southern Slopes, is particularly at-risk to denudation during flood events, which are expected to become more frequent.

Mineralogical and geochemical evidence suggests the Southern Slopes were the primary source of sediment (~90%) to SBB during the LGM. Absence of chlorite, and increased kaolinite suggests loss of the SCR as a sediment source and increased contribution for the SRI catchment, respectively. The SCR bypassed the SBB during the LGM sea level lowstand (Normark et al.,

2006), however SBB sedimentation rates were unperturbed (Hendy et al., 2002; Hill et al., 2006). This is attributed to increased sediment flux from the Santa Ynez Mountains (Southern Slopes) and SRI (and possibly the Channel Islands as a whole) to SBB during the LGM, as indicated by the Sr-Nd mixing lines and the major elemental composition of the SBB LGM samples.

## 2.7 References


Atwater, T., 1989. Plate tectonic history of the northeast Pacific and western North America, in: Winterer, E.L., Hussong, D.M., Decker, R.W. (Eds.), The Geology of North America. Geological Society of America, Boulder, Colorado, pp. 21-72.

Azor, A., Keller, E.A., Yeats, R.S., 2002. Geomorphic indicators of active fold growth: South Mountain–Oak Ridge anticline, Ventura basin, southern California. Geol. Soc. Am. Bull. 114, 745-753.

Barth, A.P., Ehlig, P.L., 1988. Geochemistry and petrogenesis of the marginal zone of the Mount Lowe Intrusion, central San Gabriel Mountains, California. CoMP 100, 192-204.

Barth, A.P., Tosdal, R.M., Wooden, J.L., 1990. A petrologic comparison of Triassic plutonism in the San Gabriel and Mule Mountains, Southern California. Journal of Geophysical Research-Solid Earth and Planets 95, 20075.

Barth, A.P., Wooden, J.L., Tosda, R.M., Morrison, J., Dawson, D.L., Hernly, B.M., 1995. Origin of gneisses in the aureole of the San Gabriel anorthosite complex and implications for the Proterozoic crustal evolution of southern California. Tecto 14, 736.

Berg, N., Hall, A., 2015. Increased Interannual Precipitation Extremes over California under Climate Change. J. Climate 28, 6324-6334.

Bergmann, J., Taut, T., 2005. Rietveld Analysis Progam BGMN, Dresden, Germany.

Boynton, W.V., 1984. Cosmochemistry of the rare earth elements: meteorite studies, in: Henderson, P. (Ed.), Rare Earth Element Geochemistry. Elsevier, Amsterdam, pp. 63-114.

Bryce, J.G., DePaolo, D.J., Lassiter, J.C., 2005. Geochemical structure of the Hawaiian plume: Sr, Nd, and Os isotopes in the 2.8 km HSDP-2 section of Mauna Kea volcano. Geochemistry Geophysics Geosystems 6.

Clark, P.U., Dyke, A.S., Shakun, J.D., Carlson, A.E., Clark, J., Wohlfarth, B., Mitrovica, J.X., Hostetler, S.W., McCabe, A.M., 2009. The Last Glacial Maximum. Sci 325, 710.

Cole, R.B., Basu, A.R., 1995. Nd-Sr isotopic geochemistry and tectonics of ridge subduction and middle Cenozoic volcanism in western California. Geol. Soc. Am. Bull. 107, 167-179.

Colson, K., 1996. Neotectonics of the left-lateral Santa Rosa Island Fault, Western Transverse Ranges, Southern California, Geology. San Diego State Univesity, p. 110.

Condie, K.C., 1993. Chemical composition and evolution of the upper continental crust: Contrasting results from surface samples and shales. ChGeo 104, 1-37.

Critelli, S., Le Pera, E., Ingersoll, R., 1997. The effects of source lithology, transport, deposition and sampling scale on the composition of southern California sand. Sedimentology 44, 653-671.

Crowell, J.C., 2003a. Introduction to geology of Ridge Basin, southern California, in: Crowell, J.C. (Ed.), Evolution of the Ridge Basin, Southern California: An interplay of sedimentation and tectonics. Geological Society of America, Boulder, Colorado, pp. 1-15.

Crowell, J.C., 2003b. Overview of rocks bordering Ridge Basin, southern California. Geol. Soc. Am. Spec. Pap. 367, 89-112.

Davis, T.L., Namson, J.S., 1994. A balanced cross-section of the 1994 Northridge earthquake, southern California. Nature 372, 167.

DePaolo, D.J., Wasserburg, G.J., 1976. Nd isotopic variations and petrogenetic models. GeoRL 3, 249-252.

Dettinger, M., 2011. Climate Change, Atmospheric Rivers, and Floods in California – A Multimodel Analysis of Storm Frequency and Magnitude Changes1. JAWRA Journal of the American Water Resources Association 47, 514-523.

Dettinger, M.D., Ralph, F.M., Das, T., Neiman, P.J., Cayan, D.R., 2011. Atmospheric Rivers, Floods and the Water Resources of California. Water 3, 445-478.

Dibblee Jr, T.W., 1981. Geologic map of the Gaviota quadrangle, California, Open-File Report, - ed.

Dibblee, T.W., 1966. Geology of the central Santa Ynez Mountains, Santa Barbara County, California, San Francisco.

Dibblee, T.W., Jr., 1988. Geology of the Ventura Basin Area, in: Link, M.H. (Ed.), Ventura Basin: Geologic Introduction and Field Trip Guidebook. Pacific Section American Association of Petroleum Geologists and Los Angeles Basin Geological Society, Los Angeles, pp. 6-17.

Doebelin, N., Kleeberg, R., 2015. Profex: a graphical user interface for the Rietveld refinement program BGMN. JApCr 48, 1573-1580.

Dolan, J.F., Pratt, T.L., 1997. High‐resolution seismic reflection profiling of the Santa Monica Fault Zone, west Los Angeles, California. GeoRL 24, 2051.

Dolan, J.F., Sieh, K., Rockwell, T.K., Guptill, P., Miller, G., 1997. Active tectonics, paleoseismology, and seismic hazards of the Hollywood fault, northern Los Angeles basin, California. GSA Bulletin 109, 1595.

Donnellan, A., Hager, B.H., King, R.W., 1993. Discrepancy between geological and geodetic deformation rates in the Ventura basin. Nature 366, 333-336.

Du, Xiaojing, Hendy, I.L., Schimmelmann, A., *in preparation for submission to Marine Geology*. Revised 9000-year stratigraphy for Santa Barbara Basin sediment offshore of Southern California.

Duvall, A., Kirby, E., Burbank, D., 2004. Tectonic and lithologic controls on bedrock channel profiles and processes in coastal California. Journal of Geophysical Research: Earth Surface 109, n/a-n/a.

Fan, P.-F., 1976. Recent silts in the Santa Clara river drainage basin, southern California; a mineralogical investigation of their origin and evolution. J. Sed. Res. 46, 803-812.

Faure, G., Mensing, T.M., 2005. Isotopes: principles and applications, Third ed. Wiley, Hoboken, N.J.

Fleischer, P., 1972. Mineralogy and sedimentation history, Santa Barbara Basin, California. J. Sed. Res. 42, 49-58.

Frizzell, V.A., Mattinson, J.M., Matti, J.C., 1986. Distinctive Triassic megaporphyritic monzogranite: Evidence for only 160 km offset along the San Andreas Fault, southern California. Journal of Geophysical Research: Solid Earth 91, 14080-14088.

Goldstein, S.J., Jacobsen, S.B., 1988. Nd and Sr isotopic systematics of river water suspended material: implications for crustal evolution. Earth Planet. Sci. Lett. 87, 249-265.

Gombiner, J.H., Hemming, S.R., Hendy, I.L., Bryce, J.G., Blichert-Toft, J., 2016. Isotopic and elemental evidence for Scabland Flood sediments offshore Vancouver Island. Quatern. Sci. Rev. 139, 129-137.

Gonzalez, T., Rockwell, T.K., 1991. Holocene activity of the Springville Fault in Camarillo, Transverse Ranges, Southern California; Preliminary observations, in: Blake, T.F., Larson, R.A. (Eds.), Engineering Geology along the Simi-Santa Rose Fault System and Adjacent Areas, Simi Valley to Camarillo, Ventura County, California; Field Trip Guidebook of the 1991 Annual Field Trip. Association of Engineering Geologists, Southern California Section, pp. 369-383.

Hammond Gordon, J., Weigland, P.W., 1994. A slice of immature arc rocks marooned on Santa Cruz Island, California, in: Halvorson, W.L., Maender, G.J. (Eds.), The Fourth California Islands Symposium: Update on the Status of Resources. Santa Barbara Museum of Natural History, pp. 235-243.

Harp, E.L., Jibson, R.W., 1996. Landslides triggered by the 1994 Northridge, California, earthquake. Bull. Seismol. Soc. Am. 86, S319.

Haxel, G.B., Dillon, J.T., 1978. The Pelona-Orocopia Schist and Vincent-Chocolate Mountain thrust system, southern California, in: Howell, D.G., McDougall, K.A. (Eds.), Mesozoic Paleogeography of the Western United States. Society for Sedimentary Geology, Pacific Section, Los Angeles, pp. 453-469.

Hendy, I.L., Kennett, J.P., Roark, E.B., Ingram, B.L., 2002. Apparent synchroneity of submillennial scale climate events between Greenland and Santa Barbara Basin, California from 30–10 ka. Quatern. Sci. Rev. 21, 1167-1184.

Hendy, I.L., Napier, T.J., Schimmelmann, A., 2015. From extreme rainfall to drought: 250 years of annually resolved sediment deposition in Santa Barbara Basin, California. Quatern. Int. 387, 3-12.

Hill, T.M., Kennett, J.P., Pak, D.K., Behl, R.J., Robert, C., Beaufort, L., 2006. Pre-Bølling warming in Santa Barbara Basin, California: surface and intermediate water records of early deglacial warmth. Quatern. Sci. Rev. 25, 2835-2845.

Hitchcock, C.S., Lindvall, S.C., Treiman, J.A., Weaver, K.D., Jelms, J.G., Lettis, W.R., 2001. Paleoseismic investigation of the Simi fault, Ventura County, California, Final Technical Report. National Earthquake Hazards Reduction Program.

Huftile, G.J., Yeats, R.S., 1995. Convergence rates across a displacement transfer zone in the western Transverse Ranges, Ventura basin, California. Journal of Geophysical Research: Solid Earth 100, 2043-2067.

Huftile, G.J., Yeats, R.S., 1996. Deformation rates across the placerita (Northridge M(w)=6.7 aftershock zone) and Hopper Canyon segments of the western transverse ranges deformation belt. Bull. Seismol. Soc. Am. 86, S3.

Ingram, B.L., Frances, M.-R., Sandra, L.P., 2013. The West without Water. University Of California Press, US.

Inman, D.L., Jenkins, S.A., 1999. Climate change and the episodicity of sediment flux of small California rivers. J. Geol. 107, 251-270.

Jacobson, C.E., 1995. Qualitative thermobarometry of inverted metamorphism in the Pelona and Rand Schists, southern California, using calciferous amphibole in mafic schist. Journal of Metamorphic Geology 13, 79-92.

Jacobson, C.E., Grove, M., Pedrick, J.N., Barth, A.P., Marsaglia, K.M., Gehrels, G.E., Nourse, J.A., 2011. Late Cretaceous-early Cenozoic tectonic evolution of the southern California margin inferred from provenance of trench and forearc sediments. Geol. Soc. Am. Bull. 123, 485-506.

Jin, Z., Li, F., Cao, J., Wang, S., Yu, J., 2006. Geochemistry of Daihai Lake sediments, Inner Mongolia, north China: Implications for provenance, sedimentary sorting, and catchment weathering. Geomorphology 80, 147-163.

Joseph, S.E., Criscione, J.J., Davis, T.E., Ehlig, P.L., 1982. The Lowe igneous pluton, in: Fife, D.L., Minch, J.A. (Eds.), Geology and mineral wealth of the California Transverse Ranges. Mason Hill, pp. 307-309.

Kistler, R.W., Peterman, Z.E., Ross, D.C., Gottfried, D., 1973. Strontium isotopes and the San Andreas Fault, Conference on Tectonic Problems of the San Andreas Fault System. Stanford University, Stanford University, pp. 339-347.

Konter, J.G., Storm, L.P., 2014. High precision 87Sr/86Sr measurements by MC-ICP-MS, simultaneously solving for Kr interferences and mass-based fractionation. ChGeo 385, 26-34.

Kovach, J., Faure, G., 1977. Sources and abundance of volcanogenic sediment in piston cores from the ross sea, Antarctica. N. Z. J. Geol. Geophys. 20, 1017-1026.

Lavé, J., Burbank, D., 2004. Denudation processes and rates in the Transverse Ranges, southern California: Erosional response of a transitional landscape to external and anthropogenic forcing. J. Geophys. Res. Earth Surf. 109, F01006.

Levi, S., Yeats, R.S., 1993. Paleomagnetic constraints on the initiation of uplift on the Santa Susana Fault, Western Transverse Ranges, California. Tecto 12, 688-702.

Link, M.H., 2003. Depositional systems and sedimentary facies of the Miocene-Pliocene Ridge Basin Group, Ridge Basin, Southern California, in: Crowell, J.C. (Ed.), Evolution of Ridge Basin, southern California: An interplay of sedimentation and tectonics. Geological Society of America, Boulder, Colorado, pp. 17-87.

Lora, J.M., Mitchell, J.L., Tripati, A.E., 2016. Abrupt reorganization of North Pacific and western North American climate during the last deglaciation. GeoRL 43, 11,796-711,804.

Lu, R., Turco, R.P., Stolzenbach, K., Friedlander, S.K., Xiong, C., Schiff, K., Tiefenthaler, L., Wang, G., 2003. Dry deposition of airborne trace metals on the Los Angeles Basin and adjacent coastal waters. Journal of Geophysical Research: Atmospheres 108, n/a-n/a.

Ludington, S., Moring, B.C., Miller, R.J., Flynn, K.S., Stone, P.A., Bedford, D.R., 2005. Preliminary integrated databases for the United States - Western States: California, Nevada, Arizona, and Washington. U.S. Geological Survey, Reston, Virginia, USA.

Luyendyk, B.P., Gans, P.B., Kamerling, M.J., 1998. 40Ar/39Ar geochronology of southern California Neogene volcanism, in: Weigand, P.W. (Ed.), Contributions to the Geology of the Northern Channel Islands, Southern California. Pacific Section of the American Association of Petroleum Geologists, Bakersfield, California, pp. 9-35.

Marshall, S.T., Funning, G.J., Owen, S.E., 2013. Fault slip rates and interseismic deformation in the western Transverse Ranges, California. Journal of Geophysical Research: Solid Earth 118, 4511-4534.

Masuzawa, T., Masuzawa, T., Koyama, M., Koyama, M., 1989. Settling particles with positive Ce anomalies from the Japan Sea. GeoRL 16, 503.

McKay, L.B., T.; Dewald, T.; Johnston, J.; Moore, R.; Rea, A., 2012. NHDPlus Version 2.

McLennan, S.M., 1989. Rare earth elements in sedimentary rocks; influence of provenance and sedimentary processes. Reviews in Mineralogy and Geochemistry 21, 169-200.

Murphy, D.P., Thomas, D.J., 2010. The negligible role of intermediate water circulation in stadial–interstadial oxygenation variations along the southern California margin: Evidence from Nd isotopes. Quatern. Sci. Rev. 29, 2442-2450.

Nance, W.B., Taylor, S.R., 1976. Rare earth element patterns and crustal evolution—I. Australian post-Archean sedimentary rocks. Geochim. Cosmochim. Acta 40, 1539-1551.

Nance, W.B., Taylor, S.R., 1977. Rare earth element patterns and crustal evolution—II. Archean sedimentary rocks from Kalgoorlie, Australia. Geochim. Cosmochim. Acta 41, 225-231.

Napier, T.J., Hendy, I.L., The impact of hydroclimate and dam construction on terrigenous detrital sediment composition in a 250-year Santa Barbara Basin record off southern California. Quatern. Int.

Nardone, C.D., Faure, G., 1978. A study of sedimentation at DSHP Hole 379A, Black Sea, based on the isotopic composition of strontium, in: Ross, D.A., Neprochnov, Y.P. (Eds.), Initial reports of the Deep Sea Drilling Project. U.S. Government Printing Office, Washington, D.C., pp. 607-615.

Nezlin, N.P., Stein, E.D., 2005. Spatial and temporal patterns of remotely-sensed and field-measured rainfall in southern California. Remote Sens. Environ. 96, 228-245.

Nicholson, C., Sorlien, C.C., Atwater, T., Crowell, J.C., Luyendyk, B.P., 1994. Microplate capture, rotation of the western Transverse Ranges, and initiation of the San Andreas transform as a low-angle fault system. Geology 22, 491-495.

Normark, W.R., Piper, D.J.W., Sliter, R.A.Y., 2006. Sea-level and tectonic control of middle to late Pleistocene turbidite systems in Santa Monica Basin, offshore California. Sedimentology 53, 867.

Onderdonk, N.W., 2005. Structures that accommodated differential vertical axis rotation of the western Transverse Ranges, California. Tecto 24, n/a-n/a.

Osterkamp, W.R., Hupp, C.R., Stoffel, M., 2012. The interactions between vegetation and erosion: new directions for research at the interface of ecology and geomorphology. Earth Surf. Proc. Land. 37, 23-36.

Parsons, A.J., Brazier, R.E., Wainwright, J., Powell, D.M., 2006. Scale relationships in hillslope runoff and erosion. Earth Surf. Proc. Land. 31, 1384-1393.

Petersen, M.D., 1996. Probabilistic seismic hazard assessment for the state of California.

Petersen, M.D., Wesnousky, S.G., 1994. Fault slip rates and earthquake histories for active faults in southern California. Bull. Seismol. Soc. Am. 84, 1608.

Porter, K., Wein, A., Alpers, C., Baez, A., Barnard, P., Carter, J., Corsi, A., Costner, J., Cox, D., Das, T., Dettinger, M., Done, J., Eadie, C., Eymann, M., Ferris, J., Gunturi, P., Hughes, M., Jarrett, R., Johnson, L., Dam Le-Griffin, H., Mitchell, D., Morman, S., Neiman, P., Olsen, A., Perry, S., Plumlee, G., Ralph, M., Reynolds, D., Rose, A., Schaefer, K., Serakos, J., Siembieda, W., Stock, J., Strong, D., Sue Wing, I., Tang, A., Thomas, P., Topping, K., Wills, C., Jones, L., 2011. Overview of the ARkStorm scenario. U.S. Geological Survey, p. 183 p.

PRISM Climate Group Oregon State University, 2015. 30-yr normal precipitation: annual.

Robert, C., 2004. Late Quaternary variability of precipitation in Southern California and climatic implications: clay mineral evidence from the Santa Barbara Basin, ODP Site 893. Quatern. Sci. Rev. 23, 1029-1040.

Rockwell, T., 1988. Neotectonics of the San Cayetano fault, Transverse Ranges, California. GSA Bulletin 100, 500.

Rockwell, T.K., Keller, E.A., Clark, M.N., Johnson, D.L., 1984. Chronology and rates of faulting of Ventura River terraces, California. Bull. Geol. Soc. Am. 95, 1466.

Romans, B.W., Normark, W.R., McGann, M.M., Covault, J.A., Graham, S.A., 2009. Coarse-grained sediment delivery and distribution in the Holocene Santa Monica Basin, California: Implications for evaluating source-to-sink flux at millennial time scales. Geol. Soc. Am. Bull. 121, 1394-1408.

Rosen, J., 2017. California rain puts spotlight on atmospheric rivers, Sci. AAAS.

Rubin, C.M., Lindvall, S.C., Rockwell, T.K., 1998. Evidence for Large Earthquakes in Metropolitan Los Angeles. Sci 281, 398.

Ryan, W.B.F., Carbotte, S.M., Coplan, J.O., O'Hara, S., Melkonian, A., Arko, R., Weissel, R.A., Ferrini, V., Goodwillie, A., Nitsche, F., Bonczkowski, J., Zemsky, R., 2009. Global Multi-Resolution Topography synthesis. Geochem. Geophys. Geosyst. 10, Q03014.

Schimmelmann, A., 2012. The "coffin lid" effect: flood layers and turbidites in Santa Barbara Basin affect diagenesis of organic matter in underlying varved sediment, in: Besonen, M.R. (Ed.), Second Workshop of the PAGES Varves Working Group, Program and Abstracts, 17-19 March, 2011, Corpus Christi, Texas, USA, pp. 83-86.

Schimmelmann, A., Zhao, M., Harvey, C.C., Lange, C.B., 1998. A large California flood and correlative global climatic events 400 years ago. Quatern. Res. 49, 51-61.

Schumann, R.R., Pigati, J.S., McGeehin, J.P., 2016. Fluvial system response to late Pleistocene-Holocene sea-level change on Santa Rosa Island, Channel Islands National Park, California. Geomorphology 268, 322-340.

Shen, Z.-K., Jackson, D.D., Ge, B.X., 1996. Crustal deformation across and beyond the Los Angeles basin from geodetic measurements. Journal of Geophysical Research: Solid Earth 101, 27957-27980.

Shields, C.A., Kiehl, J.T., 2016. Atmospheric river landfall-latitude changes in future climate simulations. GeoRL 43, 8775-8782.

Silver, L.T., McKinney, C.R., Deutsch, S., Bolinger, J., 1963. Precambrian Age Determinations in the Western San Gabriel Mountains, California. J. Geol. 71, 196.

Tanaka, T., Togashi, S., Kamioka, H., Amakawa, H., Kagami, H., Hamamoto, T., Yuhara, M., Orihashi, Y., Yoneda, S., Shimizu, H., Kunimaru, T., Takahashi, K., Yanagi, T., Nakano, T., Fujimaki, H., Shinjo, R., Asahara, Y., Tanimizu, M., Dragusanu, C., 2000. JNdi-1: a neodymium isotopic reference in consistency with LaJolla neodymium. ChGeo 168, 279-281.

Taylor, S.R., McLennan, S.M., 1981. The origin and evolution of the Earth's continental crust - The composition and evolution of the continental crust: rare earth element evidence from sedimentary rocks. Philosophical Transactions of the Royal Society of London. Series A, Mathematical and Physical Sciences 301, 381-399.

Thornton, S.E., 1984. Basin model for hemipelagic sedimentation in a tectonically active continental margin: Santa Barbara Basin, California Continental Borderland. Geol. Soc. London Spec. Publ. 15, 377-394.

Thornton, S.E., 1986. Origin of mass flow sedimentary structures in hemipelagic basin deposits: Santa Barbara Basin, California Borderland. Geo-Mar. Lett. 6, 15-19.

Tucker, A.Z., Dolan, J.F., 2001. Paleoseismologic Evidence for a >8 Ka Age of the Most Recent Surface Rupture on the Eastern Sierra Madre Fault, Northern Los Angeles Metropolitan Region, California. Bull. Seismol. Soc. Am. 91, 232.

Turekian, K.K., Wedepohl, K.H., 1961. Distribution of the elements in some major units of the Earth's crust. Geol. Soc. Am. Bull. 72, 175-192.

U. S. Geological Survey, California Geological Survey, 2017. Quaternary fault and fold database for the United States, in: U. S. Geological Survey, California Geological Survey (Eds.). U. S. Geological Survey.

Walter, H.J., Hegner, E., Diekmann, B., Kuhn, G., Rutgers van der loeff, M.M., 2000. Provenance and transport of terrigenous sediment in the south Atlantic Ocean and their

relations to glacial and interglacial cycles: Nd and Sr isotopic evidence. Geochim. Cosmochim. Acta 64, 3813-3827.

Warrick, J.A., Farnsworth, K.L., 2009. Sources of sediment to the coastal waters of the Southern California Bight. Geol. Soc. Am. Spec. Pap. 454, 39-52.

Warrick, J.A., Mertes, L.A.K., 2009. Sediment yield from the tectonically active semiarid Western Transverse Ranges of California. Geol. Soc. Am. Bull. 121, 1054-1070.

Warrick, J.A., Milliman, J.D., 2003. Hyperpycnal sediment discharge from semiarid southern California rivers: Implications for coastal sediment budgets. Geology 31, 781-784.

Warrick, J.A., Xu, J., Noble, M.A., Lee, H.J., 2008. Rapid formation of hyperpycnal sediment gravity currents offshore of a semi-arid California river. Cont. Shelf Res. 28, 991-1009.

Weaver, D.W., 1969. Geology of the Northern Channel Islands, n.p.

Wesnousky, S.G., 1986. Earthquakes, quaternary faults, and seismic hazard in California. Journal of Geophysical Research: Solid Earth 91, 12587-12631.

Wright, T., 1987. Geologic evolution of the petroleum basins of southern California, in: Wright, T., Heck, R. (Eds.), Petroleum geology of soastal Southern California. American Association of Petroleum Geologists, Pacific Section, Ventura, California, pp. 1-20.

Yan, Z., Clayton, R.W., Saleeby, J., 2005. Seismic refraction evidence for steep faults cutting highly attenuated continental basement in the central Transverse ranges, California. GeoJI 160, 651-666.

Yeats, R.S., 1983. Large-scale Quaternary detachments in Ventura Basin, southern California. Journal of Geophysical Research: Solid Earth 88, 569-583.

Yerkes, R.F., Campbell, R.H., 2005. Preliminary Geologic Map of the Los Angeles 30' x 60' Quadrangle, Southern California, USGS Open-File Report 2005-1019, pp. 2-51 p.

# CHAPTER 3

## The impact of hydroclimate and dam construction on terrigenous detrital sediment composition in a 250-year Santa Barbara Basin record off southern California


### Abstract

The recurrence and magnitude of southern California hydroclimate extremes are poorly resolved due to the relatively short duration (<140 years) of modern instrumental precipitation and stream gauge records. Terrigenous detrital sediments are often used to reconstruct long-term hydroclimate changes as precipitation increases river runoff and sediment transport into nearby basins. Here we assess the potential of elemental and mineralogical sediment composition from Santa Barbara Basin (SBB, California) box core SPR0901-04BC, a ~250 year record, as a proxy for precipitation and/or river runoff. Additionally we explore the impact of anthropogenic modification of rivers on sediment composition. Potassium and Ti concentrations and kaolinite + chlorite abundances are significantly correlated with regional precipitation. Transfer function modeling demonstrates that precipitation alone predicts Ti concentration variability well, but not clay mineral abundances. However, when dam construction within catchments draining into SBB is included, kaolinite + chlorite abundances can be modeled. We propose kaolinite + chlorite and illite sources in the upper reaches of catchments are trapped behind dams, while smectite sources in lower catchment areas are unimpeded and continue to be deposited in the basin. Linear correlations and model results suggest detrital elemental concentrations are more suitable for precipitation and river runoff reconstruction than clay mineral composition. Correlations observed between sediment composition and precipitation demonstrate the potential for marine sediment proxies to extend weather and climate records beyond the instrumental record, however anthropogenic land use modification, specifically damming, must be considered.

## 3.1 Introduction

Increased frequency of hydroclimate extremes such as droughts and floods, their physical impacts on the landscape, and related water availability for growing human populations are economically concerning aspects of climate change. The recurrence and magnitude of such events are poorly resolved in part due to relatively short modern instrumental records (<250 years globally; <140 years in southern California), and the uncertainties associated with these events in the sedimentary record. The ability to determine the frequency and character of these events can aid in emergency preparedness and water resource management, if they can be identified in a well-dated sedimentary record and tied to sediment composition.

Southern California is prone to hydroclimate extremes. Drought is a normal, recurrent feature of California's Mediterranean climate (Peel et al., 2007), yet the potential for heavy winter precipitation exists through 'atmospheric rivers' and intense Pacific storm fronts (Browning and Pardoe, 1973; Nezlin and Stein, 2005). Intense precipitation events erode and transport sediment, generating enhanced terrigenous sediment fluxes to nearshore marine basins via flood plumes. When this terrigenous detrital sediment (hereafter referred to as detrital sediment) is preserved in continuous deposits, a sedimentary record of these events is created (Fleischer, 1972; Hein et al., 2003; Inman and Jenkins, 1999; Robert, 2004; Soutar and Crill, 1977; Stein, 1995; Thunell, 1998; Thunell et al., 1995; Warrick and Farnsworth, 2009b), which can enable paleoclimate reconstructions of flood and drought events and extend the instrumental record.

The Santa Barbara Basin (SBB, California) is ideally positioned to preserve such sedimentary deposits. It is located close to an actively uplifting region, has a two-component (biogenic versus detrital) sediment input, and a high sediment flux that together produce a high-resolution sediment record, while low bottom-water oxygen concentrations prevent bioturbation from smoothing annual sediment variations (Fleischer, 1972; Soutar and Crill, 1977; Thunell, 1998; Thunell et al., 1995; Warrick and Farnsworth, 2009b; Warrick and Mertes, 2009). Flood deposits have been identified in SBB sediments, including the Great Flood of 1861-62 (Hendy et al., 2015) and a well-defined sequence of flood events occurring with a frequency of ~200 years (Schimmelmann et al., 2003).

The composition of detrital sediment is often used to determine many aspects of paleoclimate as well as provenance (e.g., Ergin et al., 2007; Mishra et al., 2015). Climate reconstructions that exploit the high-resolution stratigraphy of SBB have used clay minerals to identify catchment source and classify deposition event type (Fleischer, 1972; Hein et al., 2003; Schimmelmann et al., 1998; Stein, 1995), while clay mineral composition has been used as a precipitation proxy (Robert, 2004). Specifically, smectite has been associated with detrital fluvial input from the Santa Clara River catchment (Fleischer, 1972), and kaolinite and illite with fluvial suspended loads from the Ventura River, Santa Ynez River, and Santa Ynez Mountain catchments (Figure 3.1; Fleischer, 1972; Robert, 2004; Stein, 1995). Flood deposits within SBB sediments are classified using clay mineral composition by identifying gray layers containing relatively low chlorite and high smectite concentrations (>18%) (Fleischer, 1972; Robert, 2004; Schimmelmann et al., 1998; Stein, 1995). This flood layer classification is solely based on the clay mineral composition of fluvial suspended loads collected during the 1969 floods in southern California and the associated flood deposit found in SBB (Fleischer, 1972).

Geochemical analyses of sediments provide additional insights into paleoclimate regimes (e.g., Heymann et al., 2013). Elemental abundance determined by non-destructive scanning X-Ray fluorescence (XRF) is used to reconstruct precipitation variability on annual timescales (Haug et al., 2003; Lamy et al., 2001; Tierney et al., 2005). Using this method Hendy et al. (2015) observed annual variability in elemental counts in SBB sediments that could be correlated to interannual and decadal climate regimes. The first principle component of the counts was associated with elements found in detrital sediment, and high loadings of those elements coincided with historically significant precipitation events. Hendy et al. (2015) concluded that scanning XRF detrital elemental counts can be used as a proxy to track precipitation-driven river runoff in SBB, however, this proxy assumes that the geochemical composition of transported sediments remains constant through time. This assumption may not be valid as climate influences the intensity of physical and chemical weathering, and chemical weathering in turn alters sediment mineralogy and the geochemical composition of detrital sediment (Bahlburg and Dobrzinski, 2011; Fedo et al., 1995; Passchier and Krissek, 2008). Thus weathering indices, developed from the elemental composition of sediments, are also used to study paleoclimate (Nesbitt and Young, 1982; Passchier et al., 2013; Sheldon et al., 2002). Progressive chemical weathering removes labile elements and produces minerals that are more stable under surface

conditions; therefore weathering indices normalize the most mobile elements (e.g., $Na^{+}$, $K^{+}$, $Ca^{2+}$) to the least (e.g., $Al^{3+}$, $Ti^{4+}$) (Bahlburg and Dobrzinski, 2011; Fedo et al., 1995; Nesbitt and Young, 1982).

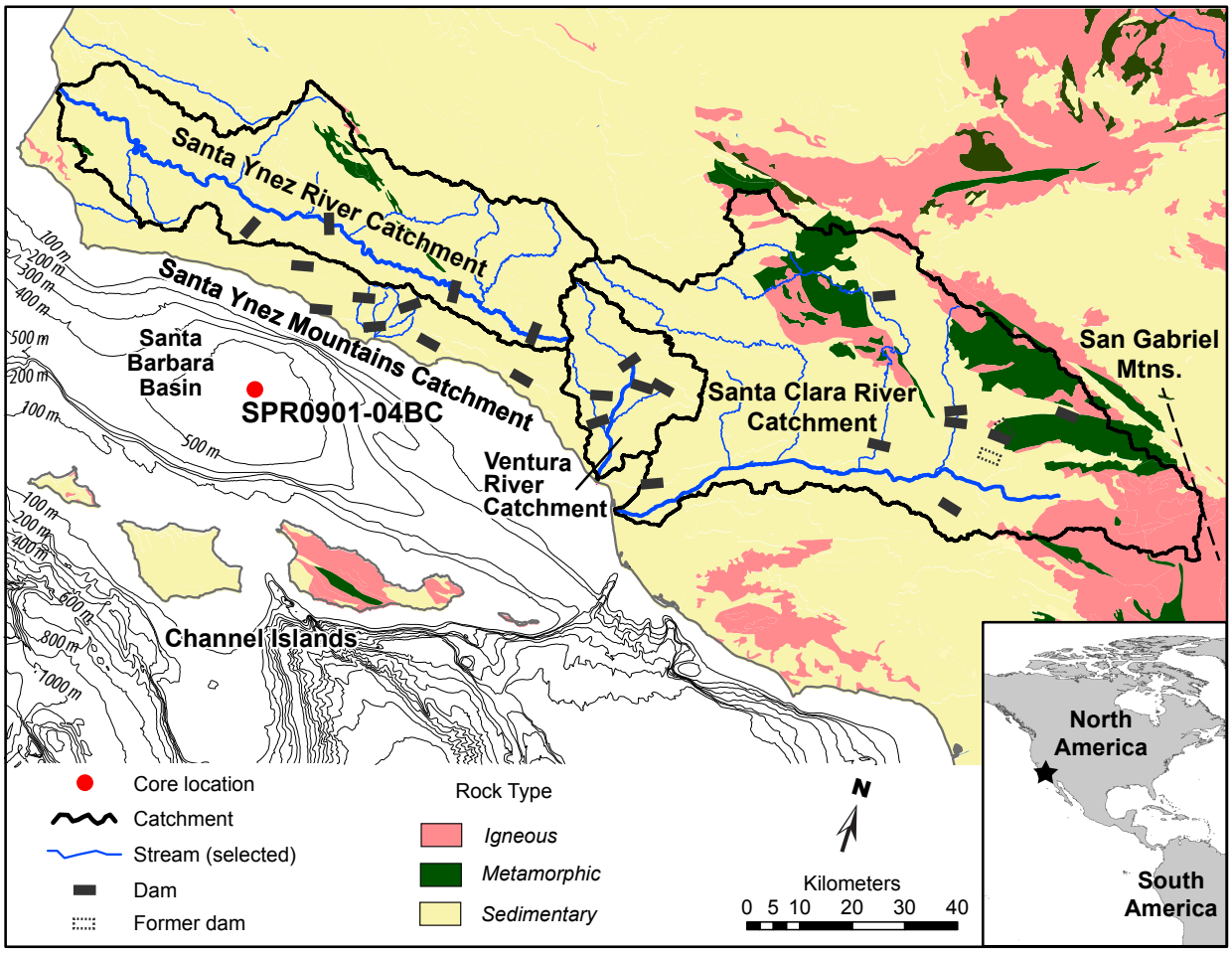


**Figure 3.1.** Geologic map of study area, including Santa Barbara Basin and location of box core SPR0901-04BC, and dams within river catchments that discharge sediment into Santa Barbara Basin.
River catchments are outlined in black. Selected rivers are shown by blue lines; main stem of river indicated by thick blue line. Bathymetry contour interval is 100 m. The star in the inset figure denotes the study location. Geologic data from Ludington et al. (2005). Dam information from California Dept. of Water Resources, Division of Safety of Dams [*California Jurisdictional Dams, http://www.water.ca.gov/damsafety/damlisting/index.cfm, accessed February 2015*]. Hydrologic data from the National Hydrology Dataset Plus, Version 2 (McKay et al., 2012). Bathymetry from Global Multi-Resolution Topography version 2.6 (Ryan et al., 2009).

Anthropogenic modifications within catchments, such as urbanization, industrial agriculture, and damming, can both increase and decrease sediment flux within catchments (Brownlie and Taylor, 1981; Chang et al., 2015; Dai et al., 2008; Huang et al., in press; Lavé and Burbank, 2004; Li et al., in press; Wang et al., 2012; Warrick and Farnsworth, 2009b; Warrick et al., 2012; Willis and Griggs, 2003; Xu, 2009, 2011), which in turn alters the detrital sediment

composition and flux to SBB. Since the detrital fraction of SBB sediments is used as a paleoclimate proxy, it is important to understand how the detrital sediment composition is impacted by such modifications, especially since the paleoclimate proxies stem from modern observations (e.g., Fleischer, 1972, Robert, 2004, Schimmelmann et al., 1998). The objectives of this paper are (1) to use sediment compositional data from box core SPR0901-04BC to evaluate the degree to which hydroclimate events (floods and droughts) and climate variability are recorded in sediment cores of the Santa Barbara Basin, (2) to compare the detrital elemental concentrations with clay mineral composition to determine how well each behaves as a precipitation and/or river runoff proxy (Fleischer, 1972; Hendy et al., 2015; Robert, 2004; Schimmelmann et al., 1998; Stein, 1995), and (3) to discern if anthropogenic modifications of the regional catchments have impacted the composition of SBB sediments.

### 3.2 Regional setting

The Santa Barbara Basin (SBB) is located in the Southern California Bight and is bounded by the Santa Ynez Mountains, the Channel Islands, and submarine sills (Figure 3.1). Laminations in SBB sediments are produced from two distinct sediment sources that seasonally vary in flux. Biogenic sediment flux is greatest in spring/summer during coastal upwelling produced by the seasonal northward movement of the North Pacific High, while detrital sediment flux largely occurs in winter due to precipitation events associated with low pressure systems steered out of the northwest Pacific Ocean (Inman and Jenkins, 1999; Lynn and Simpson, 1987; Nezlin et al., 2005; Nezlin and Stein, 2005; Soutar and Crill, 1977; Thunell, 1998; Thunell et al., 1995; Warrick and Farnsworth, 2009b; Warrick et al., 2008). The Mediterranean climate of California (Peel et al., 2007) is associated with hydroclimate extremes–either intense precipitation events (flood) or no precipitation (droughts) (Dettinger et al., 2011; Lavé and Burbank, 2004). Mean annual precipitation ranges from 30-70 cm due to the influence of elevation and orography (Andrews et al., 2004; Nezlin et al., 2005; Nezlin and Stein, 2005; Warrick and Mertes, 2009). Shifts in hydroclimate extremes are related to interannual climate variability. The Pacific Decadal Oscillation (PDO) and El Niño-Southern Oscillation (ENSO) climate patterns increase precipitation in southern California during their respective positive phases (positive PDO, El Niño) (Andrews et al., 2004; Cayan et al., 1999; Dettinger et al., 1998; Inman and Jenkins, 1999; Mantua et al., 1997; Mo and Higgins, 1998; Nezlin and Stein, 2005;

Schonher and Nicholson, 1989). PDO regimes persist for 20-30 years, influencing interannual climate over decadal time scales, while ENSO events are 6-18 months in duration, and as such impact both annual and interannual climate (Mantua and Hare, 2002). In southern California, precipitation events that exceed the 90$^{th}$ percentile are more likely to occur during an El Niño phase (Cayan et al., 1999; Warrick and Milliman, 2003). Through precipitation PDO and ENSO directly influence river suspended load, with increased (decreased) river sediment flux to SBB during wet (dry) periods associated with positive PDO, El Niño (negative PDO, La Niña) (Inman and Jenkins, 1999; Nezlin and Stein, 2005; Soutar and Crill, 1977; Warrick and Farnsworth, 2009b).

The Santa Clara River catchment is the primary source of detrital sediment to SBB (Fleischer, 1972; Hein et al., 2003; Kolpack and Drake, 1984; Nezlin et al., 2005; Robert, 2004; Stein, 1995; Warrick and Milliman, 2003), and contains metamorphic, igneous, and sedimentary rock units (Yerkes and Campbell, 2005). The Ventura and Santa Ynez rivers and the Santa Ynez Mountain catchments primarily drain sedimentary rock units (Figure 3.1). River discharge is episodic, with long periods of low or no flow and brief periods (<25 days) of high discharge (Warrick and Farnsworth, 2009b; Warrick and Mertes, 2009; Warrick and Milliman, 2003). River sediment flux is related to precipitation events (Warrick and Mertes, 2009; Warrick and Milliman, 2003), which quickly generate discharge from the smaller Santa Ynez Mountain catchments, followed by sediment flux from the larger Ventura and Santa Clara rivers, and finally the Santa Ynez River (Nezlin et al., 2005; Warrick et al., 2008).

Nearly half of discharged sediment is transported to the continental shelf in hyperpycnal plumes, bypassing the eastward-flowing Santa Barbara littoral cell (Romans et al., 2009; Warrick et al., 2008). The remaining sediment is delivered to the shelf by floc formation (clumping of fine-grained particles) and settling of buoyant plume sediment (Warrick and Farnsworth, 2009a; Warrick et al., 2008). Resuspension of fluvial sediment on the shelf by storm waves and subsequent surface current transport and settling, and mass movement processes on basin-slopes carry the material downslope to SBB (Thornton, 1984; Thornton, 1986; Warrick and Farnsworth, 2009a; Warrick et al., 2008). Mudflows dominate mass movements and can be recognized in core sediment by minor folds and faulting at the sequence base, convolution of bedding, and dewatering pipe and dish structures at the top of the sequence (Thornton, 1986). Sediment fluxes into SBB can vary temporally and spatially within river catchments as a function of climate,

lithology, and land modification (Inman and Jenkins, 1999; Soutar and Crill, 1977; Warrick and Mertes, 2009). Event precipitation amounts and storm intensity in particular control sediment flux. Extreme precipitation events produce flood deposits that are preserved as gray layers in SBB (Fleischer, 1972; Robert, 2004; Schimmelmann et al., 1998; Stein, 1995; Thornton, 1984), thus the thickness of flood layers in SBB has been attributed to the magnitude of the precipitation events (Soutar and Crill, 1977; Warrick and Farnsworth, 2009b).

### 3.3 Materials and methods

Box core SPR0901-04BC (04BC) was collected in SBB in January 2009 (34º 16.895' N, 120º 02.489' W, 588 m water depth, 67 cm length). The core contains two distinct gray layers associated with extreme flood events (1861-62, 0.7 cm thickness; 1761, 1.5 cm thickness; Hendy et al., 2015), and one massive olive layer (1809-42) associated with a turbidite from the 1812 Santa Barbara, California earthquake (Stover and Coffman, 1993) and the subsequent *Macoma* event identified as a rare oxygenation event in central SBB that is indicated by the presence of the burrowing bivalves *Macoma leptonoidea* (Schimmelmann et al., 1992). In spring 2013 the core was sampled in contiguous 1 cm increments to generate bulk sample. Core shrinkage due to drying during storage reduced the core length by 5 cm, resulting in collection of 62 total samples. Samples were freeze-dried, then powdered to <75 μm.

Core 04BC was correlated to previous SBB sediment cores using distinctive changes in sedimentary fabric identified by X-radiographs, core photographs, and porosity (Schimmelmann et al., 1992). The SBB cores used in the Schimmelmann et al. (1992) were dated using varve counts (Soutar and Crill, 1977), $^{210}$Pb radiometric dating (Koide et al., 1972), and excess $^{55}$Fe associated with fallout from nuclear weapons testing in the early 1960s (Krishnaswami et al., 1973). Initial age assignments were based on distinctive changes in sedimentary fabric caused by the strong El Niño events of 1941, 1957, 1983, and 1997 (error ± ~2 years), some of which were observed as they occurred by temporally consecutive SBB coring expeditions beginning in the late 1960s (Soutar and Isaacs, 1969). The distinctive sedimentary fabric changes visually correlate with scanning X-ray fluorescence elemental counts, therefore the elemental detrital component (PC1; Al, Fe, K, Rb, Si, Ti) of scanning XRF for 04BC (Hendy et al., 2015) was used to further refine the existing age model (Schimmelmann et al., 1992) by matching the peaks and troughs of PC1 with the positive and negative PDO phases using *Analyseries* software (Paillard

et al., 1996), as PC1 increases (decreases) during positive (negative) PDO phases (Hendy et al., 2015). Each 1 cm sample analyzed in this contribution records ~2-7 years, and we estimate the age model error to be ±2 years (Schimmelmann et al., 1992). As varve counting as a dating technique accumulates error, we anticipate the error in the age model increases downcore.

*3.3.1 Quantitative elemental analyses*

ALS Laboratories in Vancouver, Canada determined elemental concentrations in each powdered bulk sample. Samples were digested with nitric, perchloric, hydrofluoric, and hydrochloric acids. Concentrations of major, minor, and trace elements were determined by inductively coupled plasma-mass spectrometry (ICP-MS) and inductively coupled plasma-atomic emission spectroscopy (ICP-AES). The standard error of measurements of standards GBM908-10 and MRGeo08 for selected elements are as follows: sodium (Na): 1 st. err. = ±0.03 %; magnesium (Mg): 1 st. err. = ±0.02 %; aluminum (Al): 1 st. err. = ±0.05 and ±0.12 %, respectively; potassium (K): 1 st. err. = ±0.04 and ±0.05 % respectively; calcium (Ca): 1 st. err. = ±0.05 and ±0.04 %, respectively; titanium (Ti): = ± 0.01 %; manganese (Mn): 1 st. err. = ±8.48 and ±8.51 ppm; respectively, and iron (Fe): 1 st. err. = ±0.05 and ±0.07 %, respectively.

Sample enrichment factors (EFs) were calculated using the concentrations of each element and average shale elemental concentrations (Turekian and Wedepohl, 1961):

$$EF = (\text{element X/Ti})_{\text{sample}}/(\text{element X/Ti})_{\text{average shale}}$$

The chemical index of alteration (CIA Index) was calculated for each sample using molar proportions (Nesbitt and Young, 1982):

$$\text{CIA Index} = [Al_2O_3/(Al_2O_3 + CaO^* + Na_2O + K_2O)] \times 100$$

The CIA Index measures the removal of labile elements (Na, Ca, K) relative to Al during weathering. Calcium is corrected to include only silicate-derived Ca (CaO*, Ca*) (Fedo et al., 1995; Nesbitt and Young, 1982). For the Ca correction in this study, all carbonate in the bulk samples was assumed to be calcium carbonate, as the amount of phosphorous derived from apatite was not determined. High CIA Index values indicate the sediment has undergone more chemical weathering (Fedo et al., 1995; Nesbitt and Young, 1982).

*3.3.2 X-Ray diffraction sample preparation*

Bulk sediment from each sample was prepared as a randomly oriented powder mount and continuously scanned from 2-70º 2θ using a Rigaku Ultima IV theta-theta diffractometer (Cu Kα radiation, 40 kV, 44 mA, 0.02º step size, 1.00º/min scan speed; Rigaku Corporation, Tokyo, Japan). The clay size fraction (<2 μm) was separated by centrifugation using Stokes' Law techniques. Samples were mixed with deionized water to produce slurries, which were mounted on glass slides and air-dried to produce oriented samples so that basal plane (the plane parallel to the clay mineral structural layers; *hkl=00l*) reflections are enhanced above background intensity (Moore and Reynolds, 1997; Solum et al., 2005). Clay size fraction samples were scanned twice, once air-dried and again after ethylene glycol solvation for at least 24 hours, using a Scintag LT-801 theta-theta diffractometer (Cu Kα radiation, 40 kV, 30 mA, 0.02º step size, 0.02º/min scan speed; Scintag Inc., Cupertino, California, USA). Ethylene glycol was used to identify swelling clays (e.g., smectite), which are able to expand and contract their structures perpendicular to the basal plane by exchanging the cations located between basal structural layers (Moore and Reynolds, 1997). Air-dried samples were scanned from 2-50º 2θ; ethylene glycol solvated samples were scanned from 2-20º 2θ.

Clay mineral peak area is a function of crystal thickness, particle size, mixed layering, and mineral abundance in a mixture (Moore and Reynolds, 1997). Clay mineral peak areas were calculated for the basal reflections of smectite (001; the diffraction peak that occurs at the smallest 2θ diffraction angle), illite (001), and the overlapping kaolinite (001) + chlorite (002; the diffraction peak that occurs at the second smallest 2θ diffraction angle) peaks (hereafter K+C) for each sample using the ethylene glycol solvated sample diffractogram. Peak heights above background and peak widths at half-height were determined for each peak using the MacDiff program (Petschick, 2010); the product of these values determined peak area, which was used to calculate mineral abundance (Moore and Reynolds, 1997). Increases in clay mineral peak area indicate greater mineral abundance.

*3.3.3 Data Analyses*

Statistical correlation between detrital sediment and monthly climate and precipitation, daily Ventura River discharge, a mean ENSO Index, and a mean PDO Index, require that a summed precipitation dataset and a summed Ventura River discharge dataset be created to match

the sediment core age model (see Appendix B). The Ventura River discharge (USGS gauge 11118500) was used, as it is the only continuous river discharge record in the study area. The mean, median, skewness, and kurtosis were determined for all variables. Variables were mathematically transformed prior to bivariate linear analysis if their skewness or kurtosis values fell outside the range of ± 3, resulting in a more normal distribution for bivariate linear analysis. The original data and transformed data, along with the skewness and kurtosis values, are presented in SI Tables 1, 2, and 4. Statistical analyses were carried out using the IBM *SPSS Statistics for Macintosh (Version 22.0)* software.

A dataset of dams was created incorporating the year dams in each catchment filled and the percentage of catchment area dammed. Dam location and catchment area information were obtained from the U.S. Bureau of Reclamation (http://www.usbr.gov/projects/dams.jsp#Initial_B), StreamStats (Version 3; http://water.usgs.gov/osw/streamstats/california.html), and the California Division of Safety of Dams (http://www.water.ca.gov/damsafety/damlisting/index.cfm). The mean percentage of total catchment area dammed was calculated for each individual catchment, and the SBB catchment area as a whole (Santa Clara, Ventura, and Santa Ynez rivers and Santa Ynez Mountain catchments combined; total SBB catchment area), for each corresponding age model time interval. The individual catchment areas for the Santa Clara, Ventura, and Santa Ynez river catchments were calculated using StreamStats, and the area for the Santa Ynez Mountain catchments was determined by Willis and Griggs (2003).

Bivariate linear analysis was conducted between each detrital sediment, climate, weather, and dam variable. Pearson product-moment correlation coefficients were calculated, and the significance for each correlation was determined using Fisher transformation and 95% confidence limits, which is based solely on the number of samples in the dataset (Hazen et al., 2013). Transfer function models were developed for detrital sediment, weather, and dam variables that showed significant linear correlation. Numerator and denominator transfer functions were used in the models so that past values of the independent weather and dam variables could be used to predict current values of the dependent detrital sediment variables. The numerator transfer function specifies which previous values of the independent series are used to predict current values in the dependent series; a numerator order of one specifies that the value of the independent time series one time period in the past, along with the current value, are

used to predict the current value of the dependent series (IBM, 2012). The denominator transfer function identifies which previous values of the independent series–in this case the values are the deviation from the series mean–are used to predict current values in the dependent series. Similarly a denominator order of one specifies that the deviation of the independent time series one time period in the past, along with the current deviation, are used to predict the current value of the dependent series (IBM, 2012). Respective models were created for each detrital sediment variable based on the percent of total SBB catchment area dammed, summed daily precipitation, and summed daily precipitation combined with the percent of total SBB catchment area dammed. Goodness of model fit was determined using the normalized Bayesian Information Criterion (BIC), which considers the goodness-of-fit, the number of observations, and the total number of parameters in the model. Penalties are added as the number of parameters in the model increases. Smaller BIC values indicate a better model fit according to the BIC calculation (Schwarz, 1978).

## 3.4 Results

Data analyzed in this paper is available in the complementary Appendix B (Appendix B Tables B.1-6).

### *3.4.1 Elemental analyses*

Detrital elemental concentrations in the bulk sediment samples, as determined by ICP-MS and -AES (e.g. Al, Ca*, Fe, K, and Ti), are variable among hydroclimate events (Figure 3.3A-H). The gray layers, which are the result of the historical 1861-62 and 1761 flood deposits, are associated with the highest detrital elemental concentrations, except for Ca* and Na. Samples associated with floods that did not produce gray layers also yield high elemental concentrations for Al, Fe, K, Mg, Mn, and Ti. Detrital elemental concentrations are generally more elevated in samples associated with recent floods (1969, 1980), than samples associated with recent El Niño events, but Na and Ca* show the opposite trend. Elemental concentrations are neither consistently high during El Niño events, nor consistently low during droughts (Figure 3.2A-H). Within samples associated with droughts, elemental concentrations generally decrease, but not to the lowest values in the core. Sodium and Ca* concentrations oppose the trends observed for the other detrital elements, with the lowest values for Na and Ca* elements in the gray layer samples, while the concentrations for the other detrital elements are elevated in gray layer samples (Figure 3.2A-H). Sediment with the highest CIA index values corresponds to wet

hydroclimate events, including floods, and the most recent El Niño event, while samples corresponding to intervals of drought have the lowest CIA Index values (Figure 3.2I). Gray flood layers and the 1980 flood sediments contain the highest CIA Index values (Figure 3.2I).

Most detrital elements investigated are not enriched compared to average shale values (EFs <3), except Na with EFs ranging between ~30-60 (Figure 3.3). EF values, except for K, are lowest in the gray layers, but increase in the samples associated with less intense floods. Elemental EFs are variable among El Niño events and droughts. The EFs for Ca*, Mg, Na, and K increase in the three samples at the top of the core (Figure 3.3), so correspondingly the CIA index decreases (Figure 3.2I).

*3.4.2 Mineralogy*

Bulk mineralogy is invariant downcore, with no apparent differences in mineral composition among samples associated with different depositional events (i.e., gray layers, olive layer, wet and dry years). Most peaks in the bulk diffractograms are attributable to quartz, feldspar, muscovite, calcite, and halite (Figure 3.4), consistent with previous SBB sediment studies (Fleischer, 1972; Hein et al., 2003; Robert, 2004; Stein, 1995) and soil mineralogy analyses in the catchments that discharge into SBB (Harden et al., 1986; Kerr et al., 1971; McFadden, 1988). Smectite, illite, kaolinite, and chlorite clay minerals were identified in the <2 μm fraction (Figure 3.5). The two samples from the 1761 gray layer flood event generate the highest intensities and sharpest peaks for all clay minerals. Samples associated with wet years and dry years overlap in peak intensities (Figure 3.5).

Smectite (001), illite (001), and kaolinite (001) + chlorite (002) peak areas vary throughout the core. Smectite peak areas range from 80-269 CPS-deg 2θ (Figure 3.6A-D). Illite peak areas range from 75-208 CPS-deg 2θ (Figure 3.6A-B, E-F), and the K+C peak area ranges from 21-118 CPS-deg 2θ (Figure 3.6C-F). The greatest clay mineral peak areas occur in gray flood layer sediments. Clay mineral peak areas are nearly always greater in samples associated with El Niño events as compared to the recent flood deposits (1969, 1980); the only exception is smaller smectite peak areas in the sample associated with the 1972-73 El Niño than the 1980 flood (Figure 3.7A-C). Droughts and El Niño events are associated with variable clay mineral concentrations (Figure 3.6).

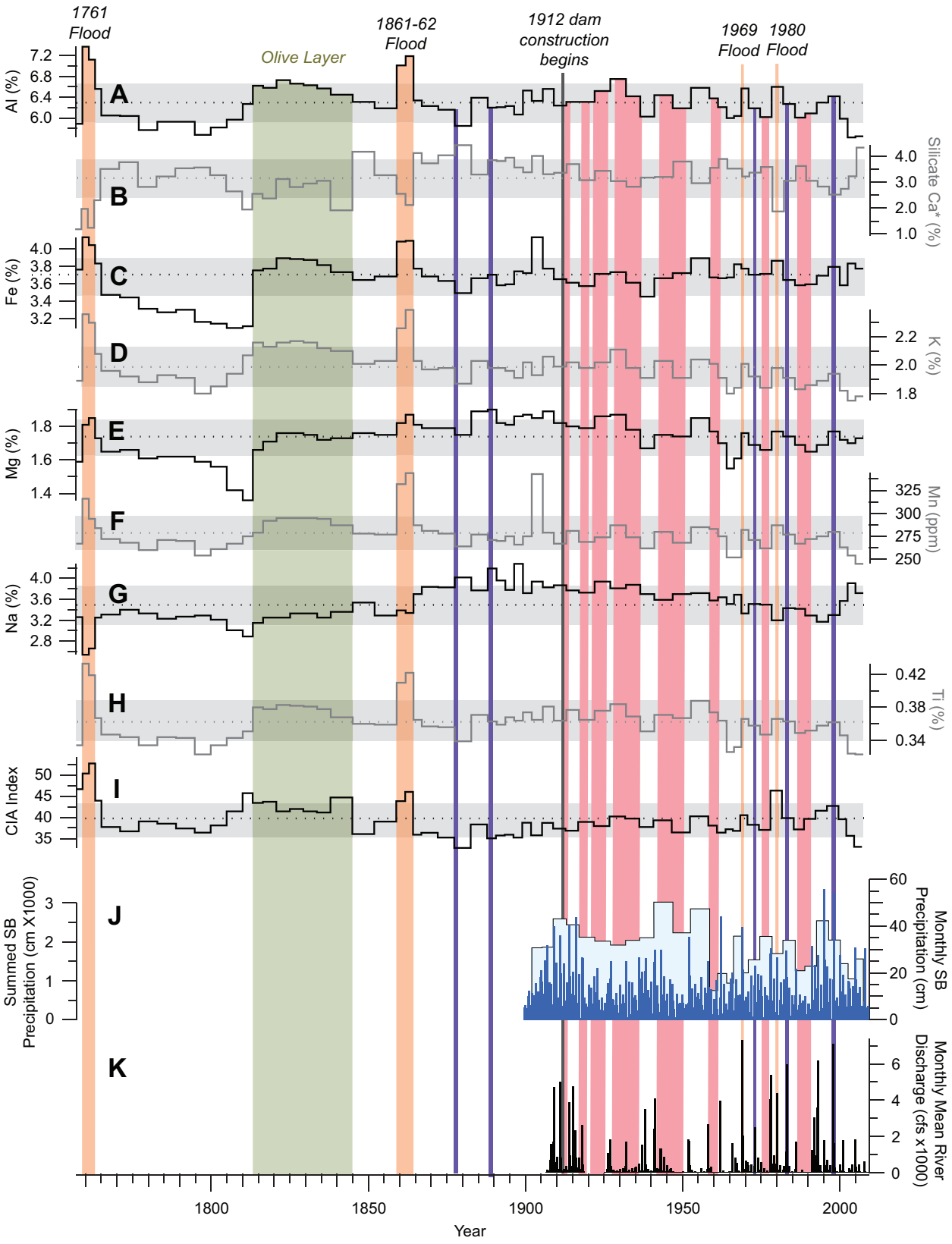


**Figure 3.2.** Comparison of bulk sediment detrital elemental concentrations and Chemical Index of Alteration (CIA) values for SPR0901-04BC samples.

**Figure 3.2 (*continued*). A.** aluminum (Al), **B.** silicate calcium (Ca*) **C.** iron (Fe), **D.** potassium (K), **E.** magnesium (Mg), **F.** manganese (Mn), **G.** sodium (Na), **H.** titanium (Ti), **I.** Chemical Index of Alteration (CIA index), **J.** monthly Santa Barbara, CA precipitation (dark blue lines) and summed monthly precipitation within each sample time span (light blue shading), and **K.** Monthly mean river discharge for the Santa Clara (USGS site number 11114000), Ventura (USGS site number 11118500), and Santa Ynez rivers (USGS site number 11133500); for individual hydrographs see SI Figure 1. Elemental mean denoted by dashed lines, and shaded envelope represents ±1 standard deviation. The bioturbated olive layer is denoted with green shading. Floods are identified with an orange bar; thick orange bars denote floods that are associated with gray layers in core SPR0901-04BC sediment. Recent droughts identified by pink shading. El Niños with a sea surface temperature anomaly greater than 2ºC are identified with a violet bar (data from Center for Ocean-Atmosphere Prediction Studies (COAPS), Florida State University, ENSO Index according to Japan Meteorological Agency (JMA) sea surface temperature anomalies (SSTA) (1868-present): http://coaps.fsu.edu/jma). Precipitation data from County of Santa Barbara Public Works Water Resources Division, site: Santa Barbara Downtown, http://www.countyofsb.org/pwd/pwwater.aspx?id=3786#Top; River discharge data from USGS Water Data, http://waterdata.usgs.gov/nwis/inventory. Historical flood and drought information from Paulson et al. (1991).

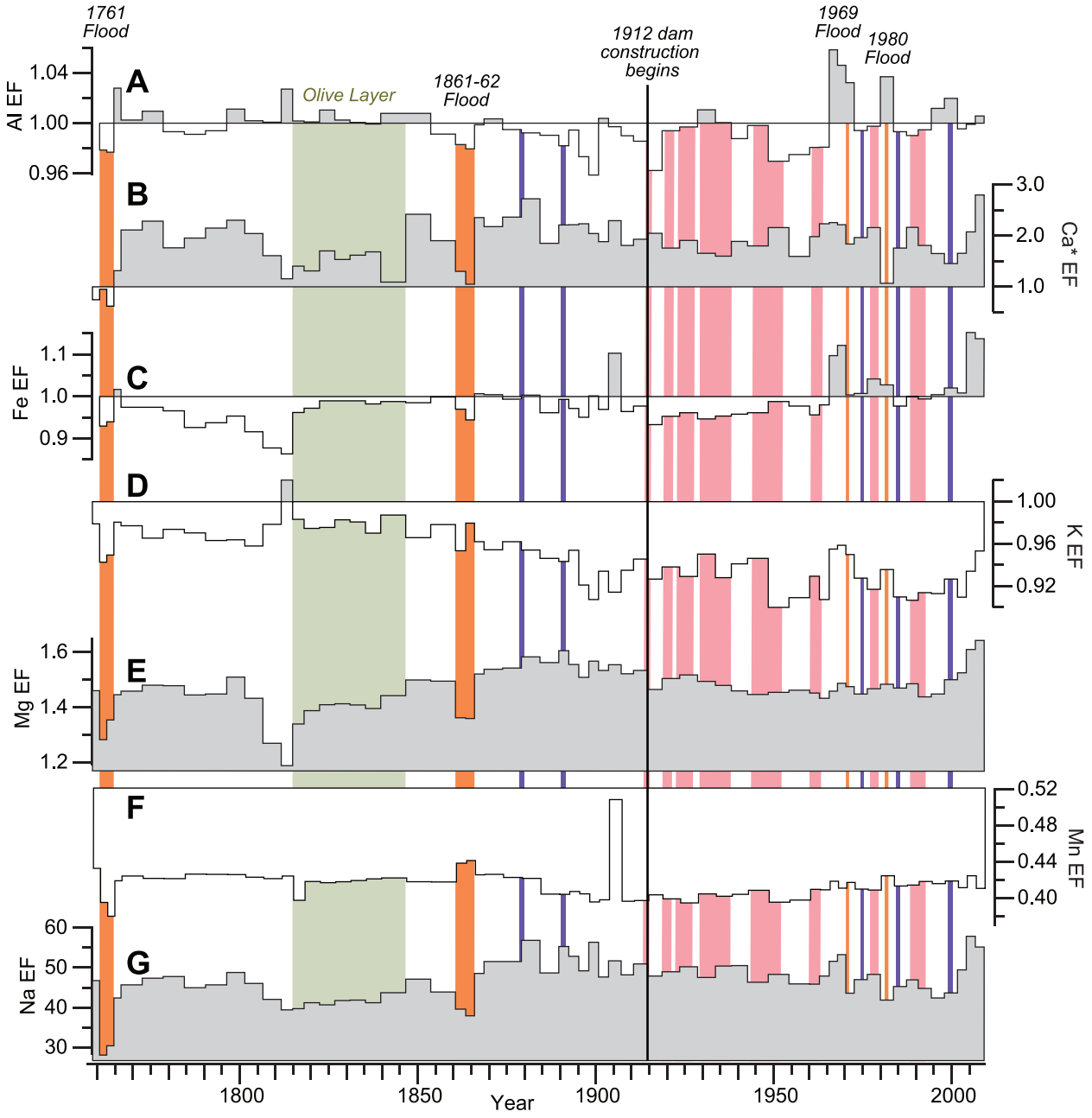


**Figure 3.3.** Elemental enrichment factors (EFs) in SPR0901-04BC samples.
**A.** aluminium (Al), **B.** silicate calcium (Ca*), **C.** iron (Fe), **D.** potassium (K), **E.** magnesium (Mg), **F.** manganese (Mn), **G.** sodium (Na). Gray shading represents enrichment factors > 1, while white shading represents enrichment factor <1. The bioturbated olive layer is denoted with green shading. Floods are identified with an orange bar; thick orange bars denote floods that are associated with gray layers in core SPR0901-04BC sediment. Recent droughts identified by pink shading. El Niños with a sea surface temperature anomaly greater than 2ºC are identified with a violet bar (data from Center for Ocean-Atmosphere Prediction Studies (COAPS), Florida State University, ENSO Index according to Japan Meteorological Agency (JMA) sea surface temperature anomalies (SSTA) (1868-present): http://coaps.fsu.edu/jma).

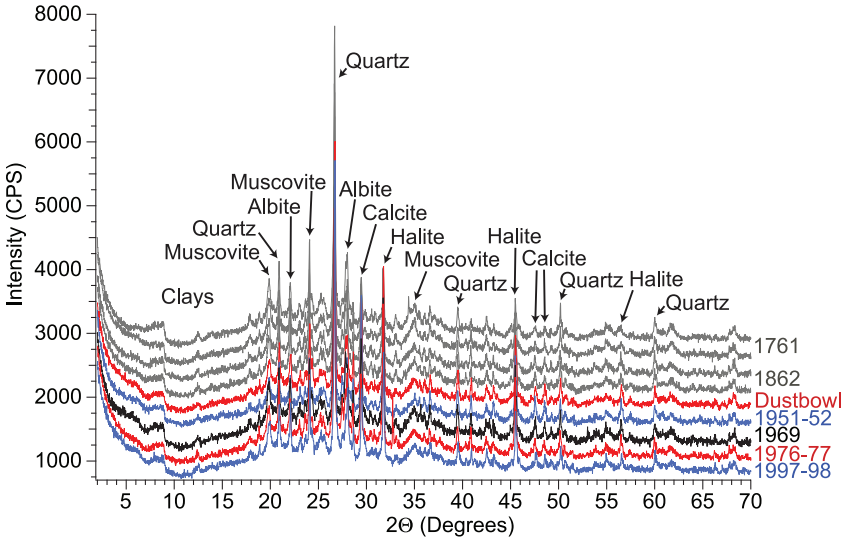


**Figure 3.4.** Typical bulk sediment sample diffractograms and mineralogy.
Gray layer flood event sample diffractograms in gray, diffractograms for samples that contain an El Niño event in blue, and diffractograms for samples associated with droughts in red. Each sample is labeled with the corresponding event. Diffractograms have been offset for clarity.

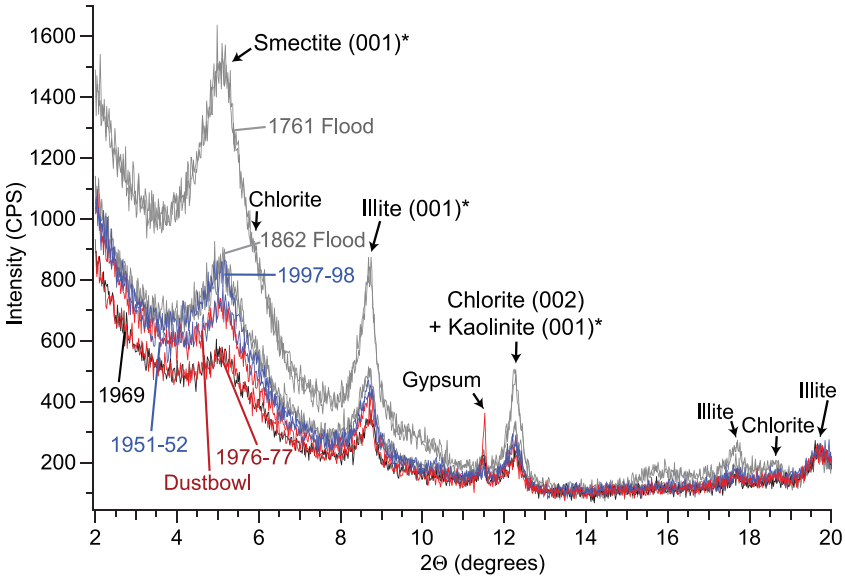


**Figure 3.5.** Selected sample clay size fraction (<2 μm) diffractograms after ethylene glycol solvation.
Samples and coloring as in Figure 3.4. Asterisks indicate mineral peaks used in peak area calculations.
Diffractograms have not been offset.

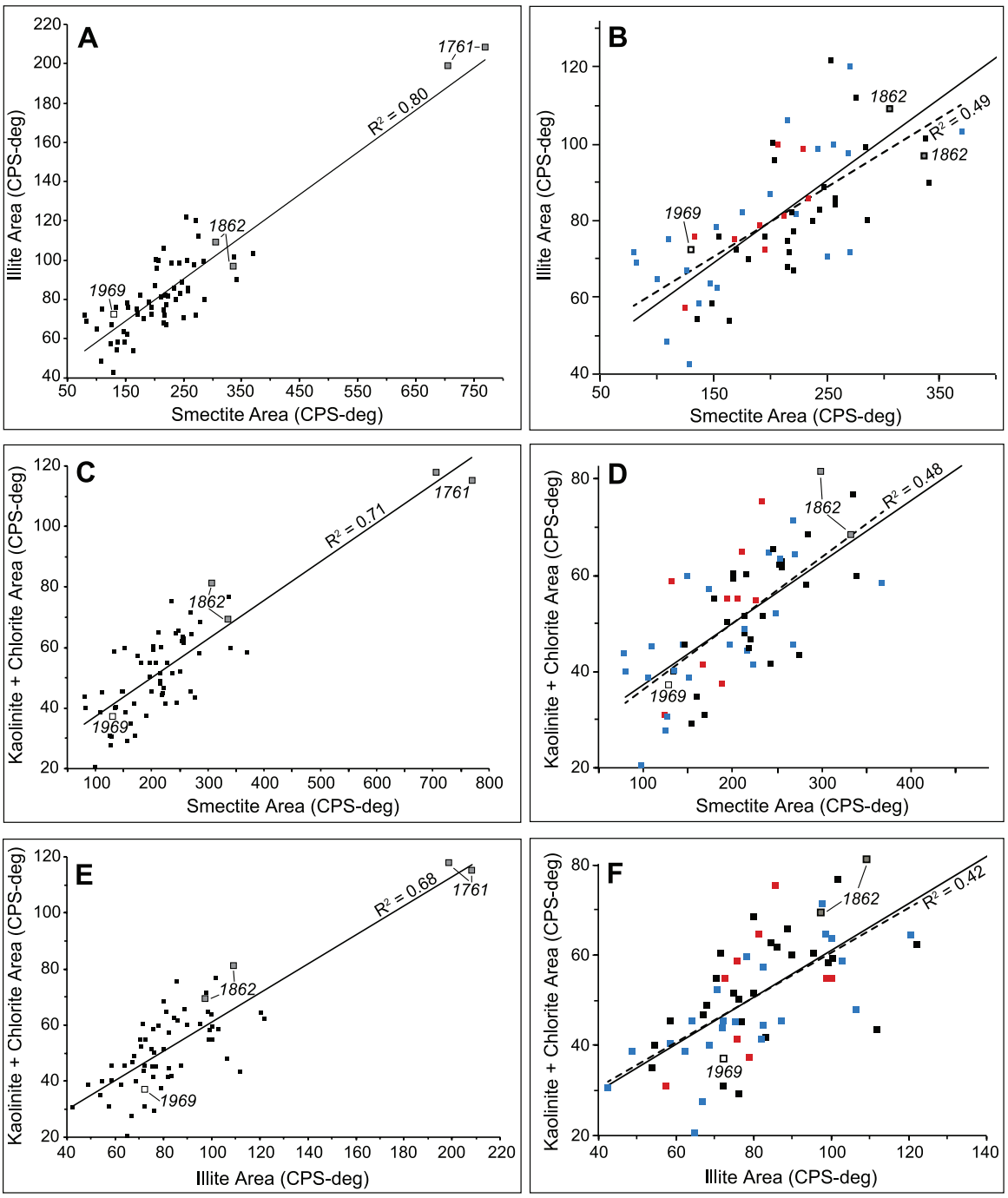


**Figure 3.6.** Clay mineral peak area comparisons.
**A**. Illite (001) peak areas versus smectite (001, ethylene glycol solvated) peak areas; all degrees are in 2Θ units. Black linear best-fit line ($R^2 = 0.80$) includes all samples (n = 62). Samples from gray layers colored gray with a black border. Sample that includes the 1969 flood sediment colored white with a black border. **B**. As in A, except 1761 gray layer samples excluded. Dashed best-fit line ($R^2 = 0.49$) excludes two samples (n = 60). Gray layer samples and 1969 sample as in A, samples that contain an El Niño event in blue, and samples associated with drought in red. When a sample captured both drought and an El Niño event, the sample was colored blue. **C**. Kaolinite (001) + chlorite (002) peak areas versus smectite (001) peak areas for all samples. Coloring as in A. **D**. As in C, except 1761 gray layer samples excluded. Coloring and sample number as in B.

**Figure 3.6 (*continued*). E**. Kaolinite (001) + chlorite (002) peak areas versus illite (001) peak areas for all samples. Coloring as in A. **F**. As in E, except 1761 gray layer samples excluded. Coloring and sample number as in B.

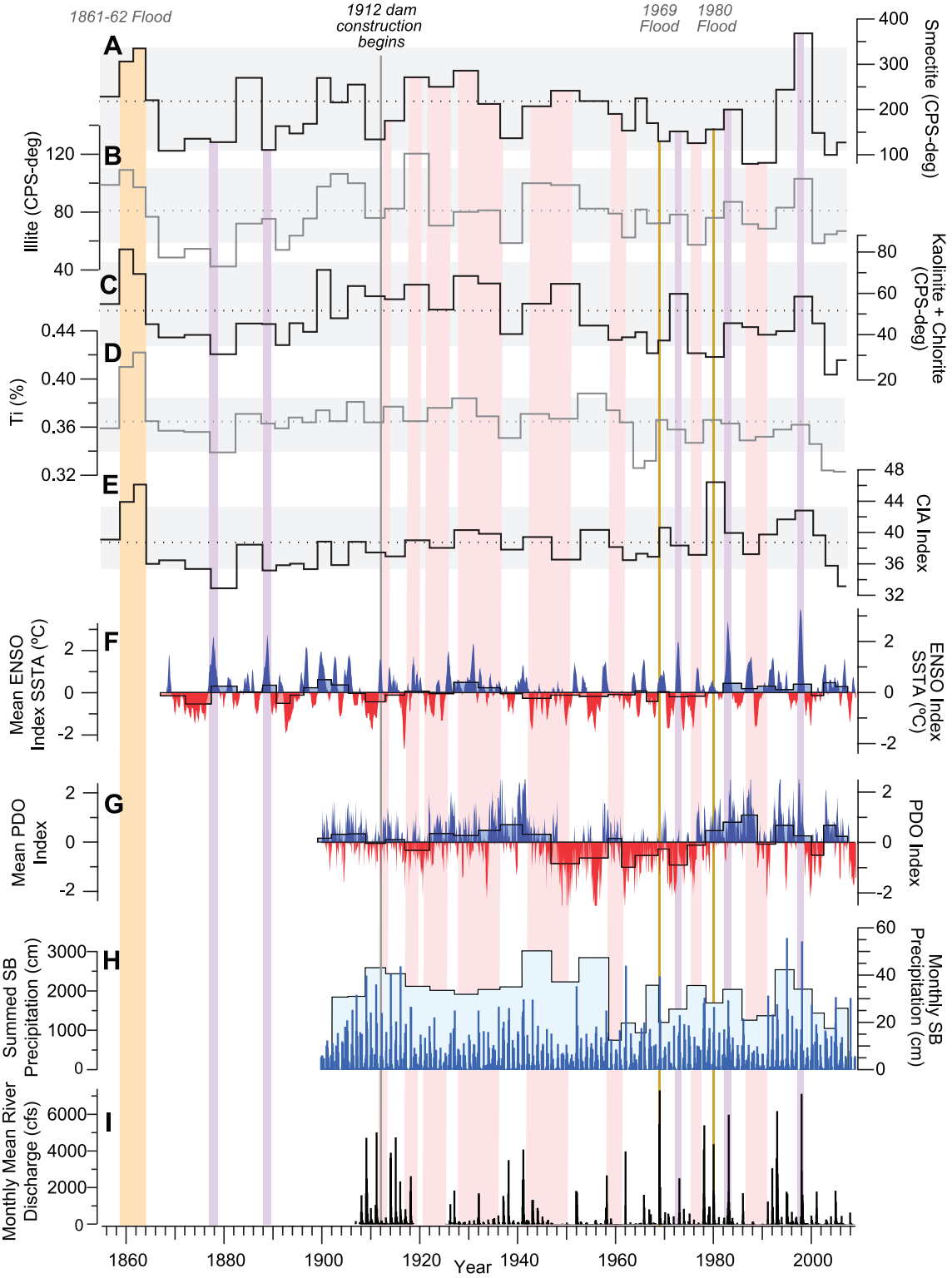


**Figure 3.7.** Comparison of clay mineral peak area, titanium concentrations, and CIA Index (weathering) variations in SPR0901-04BC to hydroclimate aspects.

**Figure 3.7 (*continued*). A.** smectite (001, ethylene glycol solvated), **B.** illite (001), and **C.** kaolinite (001) + chlorite (002) peak areas; **D.** titanium, **E.** chemical index of alteration (CIA Index), **F.** El Niño-Southern Oscillation (ENSO) Index (dark blue and red) and mean ENSO Index value for each sample time span (light blue and red bars), **G.** Pacific Decadal Oscillation (PDO) Index (dark blue and red) and mean PDO Index value for each sample time span (light blue and red bars), and **H.** Santa Barbara, CA monthly precipitation record (dark blue bars) and summed monthly precipitation within each sample time span (light blue shading), and **I.** Monthly mean river discharge for the Santa Clara (USGS site number 11114000), Ventura (USGS site number 11118500), and Santa Ynez Rivers (USGS site number 11133500); for individual hydrographs see SI Figure 1. Bars and shading as in Figure 2. Data sources are located in the Figure 2 caption.

### *3.4.3 Statistical Analyses*

Bivariate correlation analysis among all samples (n=62) reveals significant correlations among many detrital sediment variables (Table 3.1). Most detrital elements are significantly positively correlated with one another (e.g., Al with K, K with Fe, Ti with K). However Ca* and Na are significantly negatively correlated with every detrital element except for each other, and Na is significantly positively correlated with Mg (Table 3.1). Most detrital elements are significantly correlated with each clay mineral, except Mg, and Fe is not significantly correlated with K+C. Silicate Ca and Na are negatively correlated with each clay mineral. Clay mineral peak areas are significantly positively correlated with one another (Table 3.1, Figure 3.6). The sediment CIA values are significantly positively correlated with Fe, Mn, Ti, smectite, illite, and K+C, but there is no correlation with Mg (Table 3.1). Correlations were not determined between the CIA values and Al, Ca*, K, or Na, as these elements are used in calculating the CIA values. Few significant relationships exist between the detrital sediment variables and climate (ENSO and PDO; Table 3.1). No correlations were found for any detrital sediment variable and mean ENSO, PDO, or Ventura River discharge. While there are positive correlations between precipitation and many detrital elements (Al, K, Mg, Ti) and all detrital clay minerals, only K, Ti, and K+C have a significant correlation with precipitation (Table 3.1).

The dam dataset begins in 1912 with the Dry Canyon dam in the Santa Clara River catchment (State of California Dept. of Water Resources, 2014). Many detrital sediment variables are correlated with the extent of dammed area within each individual catchment and within the combined catchments (Table 3.1). The percent of dammed area within the total SBB catchment is significantly negatively correlated with Al, K, Mg, Na, Ti, illite, and K+C (Table 3.1). There is little difference in the correlations among the individual catchments and the total SBB catchment area; notably, there is no significant correlation between illite and the percent of

catchment area dammed in the Santa Ynez Mountain catchments, or between Al and the percent of dammed Santa Ynez River catchment (Table 3.1).

The significant relationships between detrital variables are similar when correlating samples for the time period prior to the first dam built in 1912 (n=36; Table 3.2), and over the entire record (n=62; Table 3.1); only the correlation between Fe and K+C differs (Tables 3.1-2). However, for the variables for which significant correlations exist, the relationship is generally stronger for the pre-damming (1760-1912) data (Table 3.2) than for the entire dataset (Table 3.1). There is a loss of significant correlation between many variables in the after-damming dataset (1912-2009; Table 3.3). For example, Fe has no significant relationship with any variable in the after-damming dataset (Table 3.3), while in the pre-damming dataset, Fe has a significant relationship with nine other variables (Table 3.2). Only Mg and smectite, and Mg and K+C, have a significant relationship in the after-damming dataset (Table 3.3), while in the pre-damming dataset they are not significantly correlated (Table 3.2).

**Table 3.1.** Bivariate correlation analysis results summary for all core data. Pearson product-moment correlation coefficients.

| Variable | Al | Ca* | Fe | K | Mg | Mn† | Na | Ti | Smectite | Illite | Kaolinite + Chlorite | CIA | n |
|---|---|---|---|---|---|---|---|---|---|---|---|---|---|
| *Sediment* | | | | | | | | | | | | | |
| Al | | | | | | | | | | | | | 62 |
| Ca* | **-0.482** | | | | | | | | | | | | 62 |
| Fe | **0.678** | -0.218 | | | | | | | | | | | 62 |
| K | **0.925** | **-0.496** | **0.527** | | | | | | | | | | 62 |
| Mg | **0.524** | 0.163 | **0.663** | **0.406** | | | | | | | | | 62 |
| Mn† | **0.809**† | **-0.333**† | **0.632**† | **0.796**† | **0.449**† | | | | | | | | 62 |
| Na | **-0.316** | **0.666** | 0.050 | **-0.378** | **0.491** | -0.233† | | | | | | | 62 |
| Ti | **0.958** | **-0.397** | **0.652** | **0.915** | **0.608** | **0.807**† | -0.221 | | | | | | 62 |
| Smectite† | **0.635**† | **-0.555**† | **0.254**† | **0.394**† | 0.084† | **0.470**† | **-0.541**† | **0.585**† | | | | | 62 |
| Illite† | **0.663**† | **-0.540**† | **0.433**† | **0.645**† | 0.162† | **0.527**† | **-0.544**† | **0.642**† | **0.795**† | | | | 62 |
| Kaolinite + Chlorite† | **0.646**† | **-0.507**† | 0.222† | **0.709**† | 0.169† | **0.501**† | **-0.488**† | **0.656**† | **0.786**† | **0.780**† | | | 62 |
| CIA | – | – | **0.345** | – | -0.058 | **0.507**† | – | **0.594** | **0.682**† | **0.679**† | **0.634**† | | 62 |
| *Climate* | | | | | | | | | | | | | |
| Mean ENSO | 0.015 | -0.160 | 0.182 | -0.125 | 0.131 | 0.139† | -0.017 | -0.026 | 0.231 | 0.292 | 0.143 | 0.120 | 37 |
| Mean PDO | 0.012 | -0.220 | -0.061 | 0.019 | 0.189 | 0.136† | -0.043 | -0.005 | -0.032 | 0.009 | -0.114 | 0.163 | 28 |
| Summed Precipitation | 0.343 | -0.165 | 0.025 | **0.417** | 0.349 | 0.163† | 0.161 | **0.422** | 0.361 | 0.360 | **0.421** | 0.177 | 28 |
| Summed Ventura River Discharge | 0.177 | -0.200 | -0.068 | 0.184 | 0.123 | 0.173† | -0.334 | 0.159 | 0.234 | 0.323 | 0.052 | 0.269 | 22 |
| *Anthropogenic* | | | | | | | | | | | | | |
| Percent of Total SBB Catchment Area dammed | **-0.413** | -0.102 | 0.284 | **-0.648** | **-0.581** | -0.236† | **-0.669** | **-0.546** | -0.349 | **-0.426** | **-0.710** | 0.117 | 27 |
| Percent of SCR Catchment Area Dammed | **-0.443** | -0.111 | 0.263 | **-0.663** | **-0.555** | -0.306† | **-0.676** | **-0.561** | -0.372 | **-0.411** | **-0.702** | 0.115 | 27 |
| Percent of VR Catchment Area Dammed | **-0.426** | -0.012 | 0.303 | **-0.653** | **0.612** | -0.323† | **-0.663** | **-0.555** | -0.355 | **-0.385** | **-0.693** | 0.054 | 27 |
| Percent of SYM Catchment Area Dammed | **-0.453** | -0.222 | 0.198 | **-0.658** | **-0.440** | -0.220† | **-0.652** | **-0.524** | -0.303 | -0.285 | **-0.601** | 0.178 | 27 |
| Percent of SYR Catchment Area Dammed | -0.326 | -0.104 | 0.294 | **-0.570** | **-0.575** | -0.192† | **-0.608** | **-0.476** | -0.280 | **-0.434** | **-0.592** | 0.128 | 27 |

*Note:*
[†]Transformed data used in correlation analysis, refer to Supporting Information.
Bolded correlations are statistically significant; p-value < 0.05.
Ca* = Silicate calcium
Abbreviations: CIA = Chemical Index of Alteration; ENSO = El Nino Southern Oscillation; PDO = Pacific Decadal Oscillation; SBB = Santa Barbara Basin; SCR = Santa Clara River; VR = Ventura River; SYM = Santa Ynez Mountains; SYR = Santa Ynez River.

**Table 3.2. Before damming (prior to 1912): Bivariate correlation analysis results summary. Pearson product-moment correlation coefficients.**

| Variable | Al | Ca* | Fe | K | Mg | Mn | Na | Ti | Smectite† | Illite† | Kaolinite + Chlorite† | n |
|---|---|---|---|---|---|---|---|---|---|---|---|---|
| Al | | | | | | | | | | | | 36 |
| Ca* | **-0.471** | | | | | | | | | | | 36 |
| Fe | **0.843** | -0.321 | | | | | | | | | | 36 |
| K | **0.978** | **-0.550** | **0.792** | | | | | | | | | 36 |
| Mg | **0.497** | 0.231 | **0.747** | **0.389** | | | | | | | | 36 |
| Mn | **0.892** | **-0.411** | **0.777** | **0.913** | **0.425** | | | | | | | 36 |
| Na | **-0.373** | **0.714** | -0.026 | **-0.449** | **0.495** | -0.294 | | | | | | 36 |
| Ti | **0.980** | **-0.430** | **0.853** | **0.954** | **0.576** | **0.884** | -0.295 | | | | | 36 |
| Smectite† | **0.681** | **-0.648** | **0.430** | **0.670** | 0.094 | **0.466** | **-0.717** | **0.673** | | | | 36 |
| Illite† | **0.714** | **-0.626** | **0.520** | **0.712** | 0.158 | **0.515** | **-0.690** | **0.724** | **0.931** | | | 36 |
| Kaolinite + Chlorite† | **0.534** | **-0.653** | **0.485** | **0.693** | 0.120 | **0.547** | **-0.706** | **0.685** | **0.894** | **0.895** | | 36 |
| CIA | – | – | **0.467** | – | -0.104 | **0.574** | – | **0.632** | **0.808** | **0.791** | **0.799** | 36 |

*Note:*
†Transformed data used in correlation analysis, refer to Supporting Information.
Bolded correlations are statistically significant; p-value < 0.05.
Underlined values designate correlations whose (non)significance changes after damming.
Ca* = Silicate calcium
CIA = Chemical Index of Alteration

**Table 3.3.** After damming (after 1912): Bivariate correlation analysis results summary. Pearson product-moment correlation coefficients.

| Variable | Al | Ca* | Fe | K | Mg | Mn | Na | Ti | Smectite | Illite | Kaolinite + Chlorite | n |
|---|---|---|---|---|---|---|---|---|---|---|---|---|
| Al | | | | | | | | | | | | 26 |
| Ca* | **-0.487** | | | | | | | | | | | 26 |
| Fe | 0.172 | -0.146 | | | | | | | | | | 26 |
| K | **0.919** | -0.279 | 0.044 | | | | | | | | | 26 |
| Mg | **0.664** | -0.220 | 0.178 | **0.788** | | | | | | | | 26 |
| Mn | **0.897** | **-0.497** | 0.103 | **0.835** | **0.643** | | | | | | | 26 |
| Na | -0.113 | **0.409** | -0.069 | 0.167 | 0.379 | -0.251 | | | | | | 26 |
| Ti | **0.890** | -0.289 | -0.011 | **0.928** | **0.781** | **0.905** | 0.077 | | | | | 26 |
| Smectite | **0.551** | -0.291 | 0.170 | **0.471** | **0.397** | 0.373 | 0.043 | **0.442** | | | | 26 |
| Illite | **0.453** | -0.209 | 0.035 | **0.411** | 0.308 | 0.337 | -0.052 | **0.388** | **0.708** | | | 26 |
| Kaolinite + Chlorite | **0.534** | -0.104 | -0.322 | **0.598** | **0.501** | **0.408** | 0.271 | **0.613** | **0.595** | **0.622** | | 26 |
| CIA | | | 0.201 | | 0.273 | **0.696** | | **0.466** | 0.366 | 0.286 | 0.154 | 26 |

*Note:*
Bolded correlations are statistically significant; p-value < 0.05.
Underlined values designate correlations whose (non)significance changes before damming.
Ca* = Silicate calcium
CIA = Chemical Index of Alteration

Potassium, Ti, and K+C have significant positive correlations with both summed precipitation and the percent of total SBB catchment area dammed (Table 3.1), however, transfer function models were only created for K+C and Ti. These datasets were chosen because K+C is the only clay with a significant correlation with precipitation, while Ti has a stronger relationship with precipitation than K, is less reactive, and is commonly used to estimate terrigenous detrital abundance in sediments (Wei et al., 2003). Model fit statistics are available in Table 3.4, and the best-fit models for each model category (precipitation and/or dammed catchment area) are shown in Figure 3.8. All models captured the observed long-term decreasing K+C abundance from the early 1900s through the early 2000s (Figure 3.8), however, only the summed monthly precipitation model reconstructed the increased K+C abundance from 1960 to 2000 (Figure 3.8C). The model combining both summed precipitation and dammed catchment area had the highest $R^2$-value among the K+C models, however no model captured the variability in the observed K+C abundance (Figure 3.8). The model using the dammed catchment area to predict Ti concentrations did not fit the data based on the $R^2$-value (Figure 3.8A). The best-fit models (Table 3.4) for both the summed precipitation, and the combined summed precipitation and dammed catchment area are able to reconstruct the magnitude of the Ti concentration variability (Figure 3.8D, F), however the $R^2$-value indicates the model using only summed monthly precipitation closely fits observed Ti concentrations (Figure 3.8).

**Table 3.4.** Transfer function model fit statistics.

| [a]Model | [b]Transfer Function | Stationary $R^2$ | Root Mean Square Error | Mean Absolute Percentage Error | Mean Absolute Error | [c]Normalized BIC |
|---|---|---|---|---|---|---|
| Kaolinite + Chlorite | | | | | | |
| *Total SBB Catchment Area Dammed* | | | | | | |
| 1 (A) | None | 0.47 | 9.70 | 18.19 | 7.45 | **4.78** |
| *Summed Monthly Precipitation* | | | | | | |
| 2 | None | 0.18 | 12.07 | 23.18 | 9.52 | 5.22 |
| 3 | Num = 1 | 0.31 | 11.50 | 21.52 | 8.81 | 5.25 |
| 4 | Num =2 | 0.37 | 11.11 | 19.78 | 8.07 | 5.32 |
| 5 (C) | Denom = 1 | 0.34 | 11.29 | 20.70 | 8.63 | **5.21** |
| 6 | Denom = 2 | 0.37 | 11.13 | 19.84 | 8.15 | 5.32 |
| *Summed Monthly Precipitation + Total SBB Catchment Area Dammed* | | | | | | |
| 7 (E) | None | 0.48 | 9.80 | 18.13 | 7.50 | **4.92** |
| 8 | Num = 1 | 0.54 | 9.64 | 18.04 | 7.38 | 5.02 |
| 9 | Num = 2 | 0.52 | 9.92 | 17.84 | 7.26 | 5.22 |
| 10 | Denom = 1 | 0.52 | 9.77 | 18.01 | 7.42 | 5.05 |
| 11 | Denom = 2 | 0.57 | 9.36 | 17.43 | 7.24 | 5.10 |
| Titanium | | | | | | |
| *Total SBB Catchment Area Dammed* | | | | | | |
| 1 (B) | None | 0.29 | 0.02 | 3.22 | 0.01 | **-8.17** |
| *Summed Monthly Precipitation* | | | | | | |
| 2 | None | 0.18 | 0.02 | 3.45 | 0.01 | -8.02 |
| 3 | Num = 1 | 0.43 | 0.01 | 3.11 | 0.01 | -8.18 |
| 4 (D) | Num =2 | 0.58 | 0.01 | 2.53 | 0.01 | **-8.33** |
| 5 | Denom = 1 | 0.48 | 0.01 | 2.94 | 0.01 | -8.27 |
| 6 | Denom = 2 | 0.55 | 0.01 | 2.63 | 0.01 | -8.26 |
| *Summed Monthly Precipitation + Total SBB Catchment Area Dammed* | | | | | | |
| 7 | None | 0.32 | 0.02 | 3.17 | 0.01 | -8.06 |
| 8 | Num = 1 | 0.48 | 0.01 | 3.09 | 0.01 | -8.10 |
| 9 (F) | Num = 2 | 0.59 | 0.01 | 2.55 | 0.01 | **-8.17** |
| 10 | Denom = 1 | 0.49 | 0.01 | 2.99 | 0.01 | -8.12 |
| 11 | Denom = 2 | 0.56 | 0.01 | 2.65 | 0.01 | -8.10 |

Note:

[a]Letter in parentheses refers to panel in Figure 8.

[b]Transfer functions used in the models. None: no transfer function used. Num = 1: Numerator transfer function of 1. Num = 2: Numerator transfer function of 2. Denom = 1: Denominator transfer function of 1. Denom = 2: Denominator transfer function of 2. Please refer to the Methods for a detailed description of the transfer functions.

[c]Normalized Bayesian Information Criterion. Bolded, underlined values indicate the best-fit model.

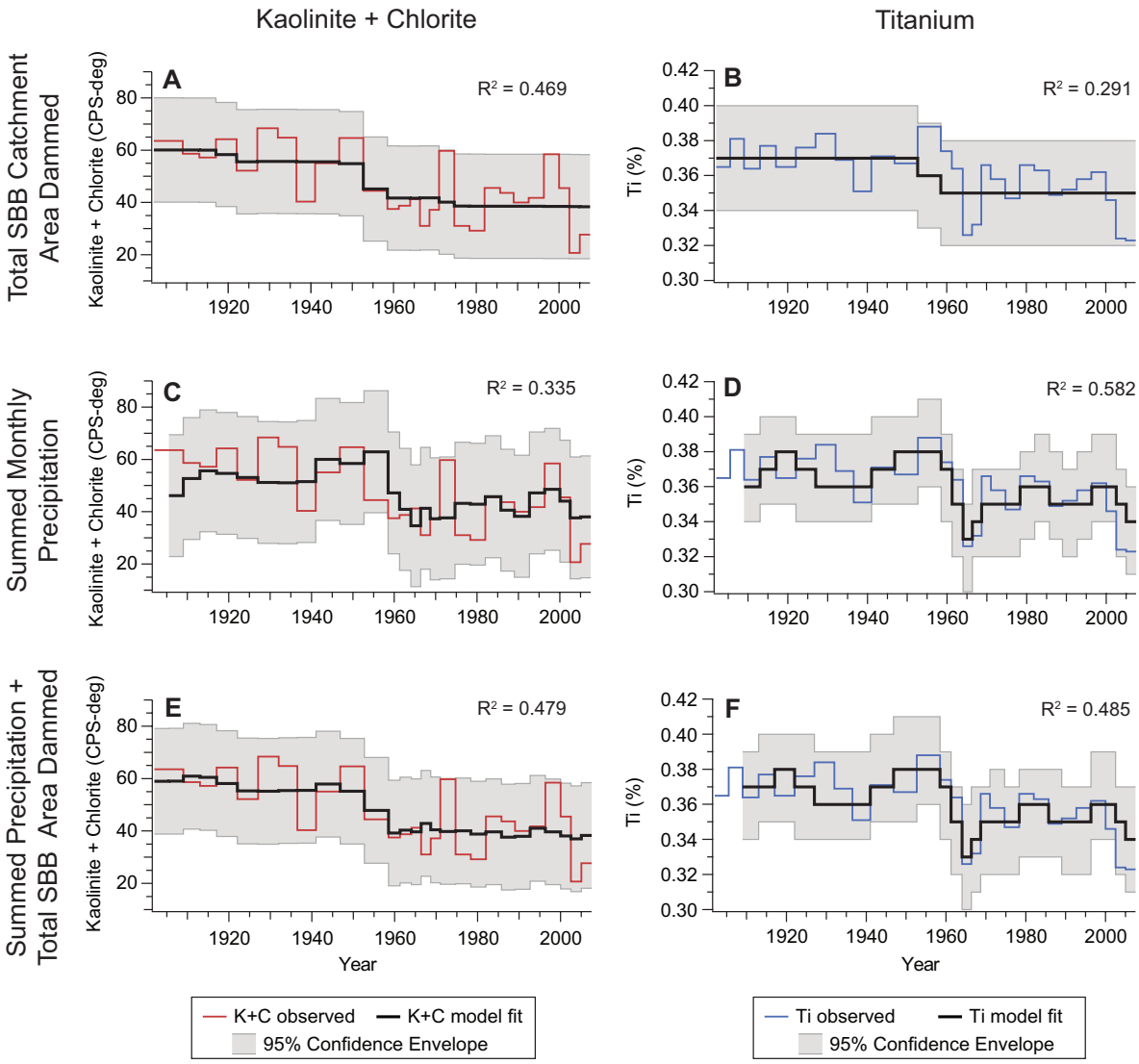


**Figure 3.8.** Transfer function model results.
Modeled Kaolinite + Chlorite (K+C) abundances for various predictor variables in the left column, and modeled Titanium (Ti) concentrations in the right column. Observed K+C abundances in red, observed Ti concentrations in blue, model fit of K+C abundances and Ti concentrations in black, and 95% model confidence envelope in gray. **A.** Model results for K+C abundances as influenced by the mean percent of total Santa Barbara Basin (SBB) catchment area blocked by dams for each respective sample time period. **B.** Model results for Ti concentrations as influenced by the mean percent of total SBB catchment area blocked by dams for each respective sample time period. **C.** Model results for K+C concentrations as influenced by the total summed monthly precipitation in Santa Barbara, CA (SB) for each respective sample time period; transfer function (TF) of one in the numerator order used so the model uses the summed precipitation values for one time period in the past and the current modeled time period to predict K+C abundances. **D.** Model results for Ti concentrations as influenced by the total summed monthly SB precipitation for each respective sample time period; TF of two in the numerator order used so the model uses the summed precipitation values for two and one time periods in the past, and the current modeled time period to predict Ti concentrations. **E.** Model results for K+C abundances as influenced by the total summed monthly SB precipitation and the mean percent of total SBB catchment area blocked by dams for each respective sample time period. **F.** Model results for Ti concentrations as influenced by the total summed monthly SB precipitation and the mean percent of total SBB catchment area blocked by dams for each respective sample time period; TF of two in the numerator order used so the model uses the summed precipitation values for two and one time periods in the past, and the current modeled time period, in addition to dammed area in order to predict Ti concentrations.

## 3.5 Discussion

### *3.5.1 Climate signals in modern detrital sediments*

Detrital sediment composition in SBB over the last 250 years generally records increased terrigenous flux in response to individual precipitation events, strong El Niño events, and extreme floods that produce gray layer deposits. This agrees with previous studies reporting that sediment discharge in the Transverse Ranges is a function of rainfall and is influenced by event intensity and magnitude (Soutar and Crill, 1977; Warrick and Farnsworth, 2009b). There is no consistency in the magnitude of the detrital component response to floods or El Niño events, however (Figure 3.7). For example, the clay mineral abundances, as indicated by peak area, do not increase during either the 1969 or the 1980 floods, but increase during the most recent El Niño events (Figure 3.7). The detrital element concentrations, excluding Ca* and Na, increase significantly during all floods, but only slightly during the most recent El Niño events (Figures 3.2, 3.7). It is not clear why clay mineral concentrations are more elevated during El Niño events than flood events as compared to the detrital elemental concentrations. These observed differences may be related to transport processes, dam releases, and grain size differences, assuming detrital elements are predominately transported into SBB in a larger grain size fraction than clays. Larger grain sizes may be temporarily deposited within the stream bed, or on the coastal shelf, which causes a delay in the sediment reaching SBB by up to seven years (Soutar and Crill, 1977). The time-lag in detrital sediment reaching SBB due to coastal shelf deposition likely varies and is dependent upon wave regimes (Adams et al., 2008; Warrick et al., 2008) and other factors governing seaward transport.

Climate modes do not appear to control the composition of modern SBB detrital sediments, however, there are components in the detrital fraction that seem to respond to precipitation changes, i.e., K, Ti, and K+C are significantly correlated with summed precipitation (Table 3.1). The modeling fits in this study indicate that precipitation can be used to predict K+C and Ti concentrations in SBB sediments, and the fit is improved when the amount of precipitation during the previous two time intervals (as per the age model: ~4-14 years), is incorporated (Table 3.4, Figure 3.8C, D). Between the two detrital variables, summed

precipitation is a better predictor of Ti than K+C, suggesting that Ti concentration is a more appropriate choice as paleoprecipitation proxy than clay mineral concentrations.

Processes operating on geologic timescales (>11 kyr; e.g., weathering) may not be applicable to paleoclimate investigations over shorter timescales. Robert (2004) used the relative enrichment of smectite to illite (S/I) to identify periods of intensified precipitation and riverine flux for the past 160 ka, assuming a greater smectite flux from the Santa Clara River during flood events. Following this assumption during the last 250 years, intervals of higher precipitation, such as El Niños and floods, should demonstrate similar S/I enrichment, yet, our data do not support this. Smectite and illite relative abundances are positively correlated and the samples associated with wet intervals do not fall below the best fit line in Figure 6B, suggesting the S/I ratio is not a proxy for rainfall on annual to decadal time scales. Further, all clay mineral abundances are strongly positively correlated with each other (Figure 3.6), including those in gray layer sediments where the kaolinite (001) + chlorite (002) peak area increases alongside smectite and illite (Figure 3.6), contrary to previous observations (Fleischer, 1972; Schimmelmann et al., 1998; Stein, 1995). As weathering processes that lead to differential clay formation are unlikely to change on historical timescales, and the weathering index values for this sediment core are fairly consistent (Figure 3.2I), we suggest erosion and sediment transport during and following precipitation events are the likely processes controlling detrital clay composition in recent SBB sediments.

### *3.5.2 Anthropogenic impacts on the composition of the modern detrital fraction*

Pre-anthropogenic sediment yield in the Transverse Ranges was primarily a function of tectonics and lithology, but presently anthropogenic landscape modification plays an important role (Downs et al., 2013; Warrick and Mertes, 2009). Human modification of river catchments has occurred over the last 250 years including: damming of rivers entering the basin, increased wildfire frequency, and changes in vegetation cover alongside expansion of intensive agricultural practices and urbanization (Downs et al., 2013; Warrick et al., 2012; Warrick and Rubin, 2007). Deep-rooted chaparral vegetation was gradually replaced by shallow-rooted grass after the founding of the California missions in the late 1700s to support livestock – an important element for mission community subsistence and as a result the missionary practice of fire suppression (Burcham, 1957; Ejarque et al., 2015). Land development continued during the Rancho period

when secularization of the missions established large land grants for sheep and cattle farming, with a cattle boom from 1850-60 in response to the California Gold Rush (Burcham, 1957). The decline in cattle ranching occurred following cattle deaths during the flood of 1861-62 and the subsequent severe drought, which led to the expansion of intensive agricultural practices (Burcham, 1957). Many of these land use changes occurred during deposition of the massive olive layer (1809-1835), a turbidite associated with the 1812 earthquake (Stover and Coffman, 1993), which sits below the oxygenated bottom water event indicated by the *Macoma* layer (1835-1842) (Schimmelmann et al., 1992). Sedimentary disturbances during this interval make identifying a single process responsible for driving compositional changes in SBB detrital sediments difficult.

With agricultural practices already established in the region by the late 19$^{th}$ century, other anthropogenic impacts on the detrital composition and flux into SBB should be considered. During the 20$^{th}$ century population growth in southern California led to the need to control water resources (Willis and Griggs, 2003). Regional river management began in 1912 with dam construction, and increasingly more ambitious water projects continued through to the 1970s (Willis and Griggs, 2003). The resulting dam impoundment within catchments draining into SBB has resulted in sediment loss over the past ~90 years (Downs et al., 2013; Slagel and Griggs, 2008; Warrick and Farnsworth, 2009b; Williams, 1979; Willis and Griggs, 2003). Many detrital variables have a significant negative correlation with the percent of catchment area that is dammed in the study area (Table 1), suggesting that dams trap sediments containing these elements (Al, K, Mg, Na, Ti) and clay minerals (illite, K+C), thus preventing their transport into SBB. This relationship is consistent with observed reductions in sediment discharge in the study area due to dam impoundment (Downs et al., 2013; Slagel and Griggs, 2008; Warrick and Farnsworth, 2009b; Williams, 1979; Willis and Griggs, 2003).

Not every clay mineral variable is correlated with dams, which may reflect mineral compositional differences between sediment source areas. All clay minerals are negatively correlated with dammed catchment area, but the impact of damming on each mineral is disproportionate – K+C is more affected than illite, and smectite is the least impacted (Table 3.1). Kaolinite + chlorite has a strong significant negative correlation with both the percent of catchment area dammed individually, and with the total SBB catchment area, while illite has moderate negative correlations in each catchment except the Santa Ynez Mountains. Finally

smectite has no significant correlation with the percent of catchment area dammed indicating dam construction has no impact on this clay mineral (Table 3.1). We posit that kaolinite is eroded from the upper reaches in each catchment, but is trapped by dams during sediment transport downstream and illite is eroded from the mid-reaches, where less sediment is trapped behind dams (Figure 3.9). Smectite is eroded from the lower reaches of the catchments where few dams impede sediment transport downstream (Figure 3.9). Robert (2004) hypothesized similar clay mineral sources for SBB sediments with K+C and illite eroded from the mountains (upper and mid-reaches in each catchment), and smectite from the low relief areas. Furthermore we suggest the relationship between detrital clay minerals and catchment dammed area will not remain constant through time if sediment is able to bypass these impeding structures. Dams may release water during significant precipitation events when reservoir water levels are high, which allows the suspended load to continue traveling downstream. However, when the frequency or magnitude of precipitation events is not sufficient to overfill reservoirs, dams remain closed, allowing the suspended load (including clay minerals) to settle out as sediment in the reservoirs.

### *3.5.3 The detrital signal in gray layers*

Anthropogenic impacts in regional catchments have altered the detrital clay mineral and elemental composition and flux of the fluvial sediment load delivered to SBB (Tables 3.2-3.3; Warrick and Farnsworth, 2009b). Interpretations of pre-anthropogenically modified sediment based on modern observations in this region must account for these alterations. The 1969 SBB flood deposit, and the river bedload and suspended-load samples collected in the study area by Fleischer (1972) characterized the Santa Clara River as the predominant source of flood sediment. However, the 1969 flood would have been impacted by the anthropogenic influences on sediment composition in the catchments. Therefore it may not be appropriate to use the clay composition of the 1969 flood deposit in SBB as a simple classification for prehistoric SBB flood layers.

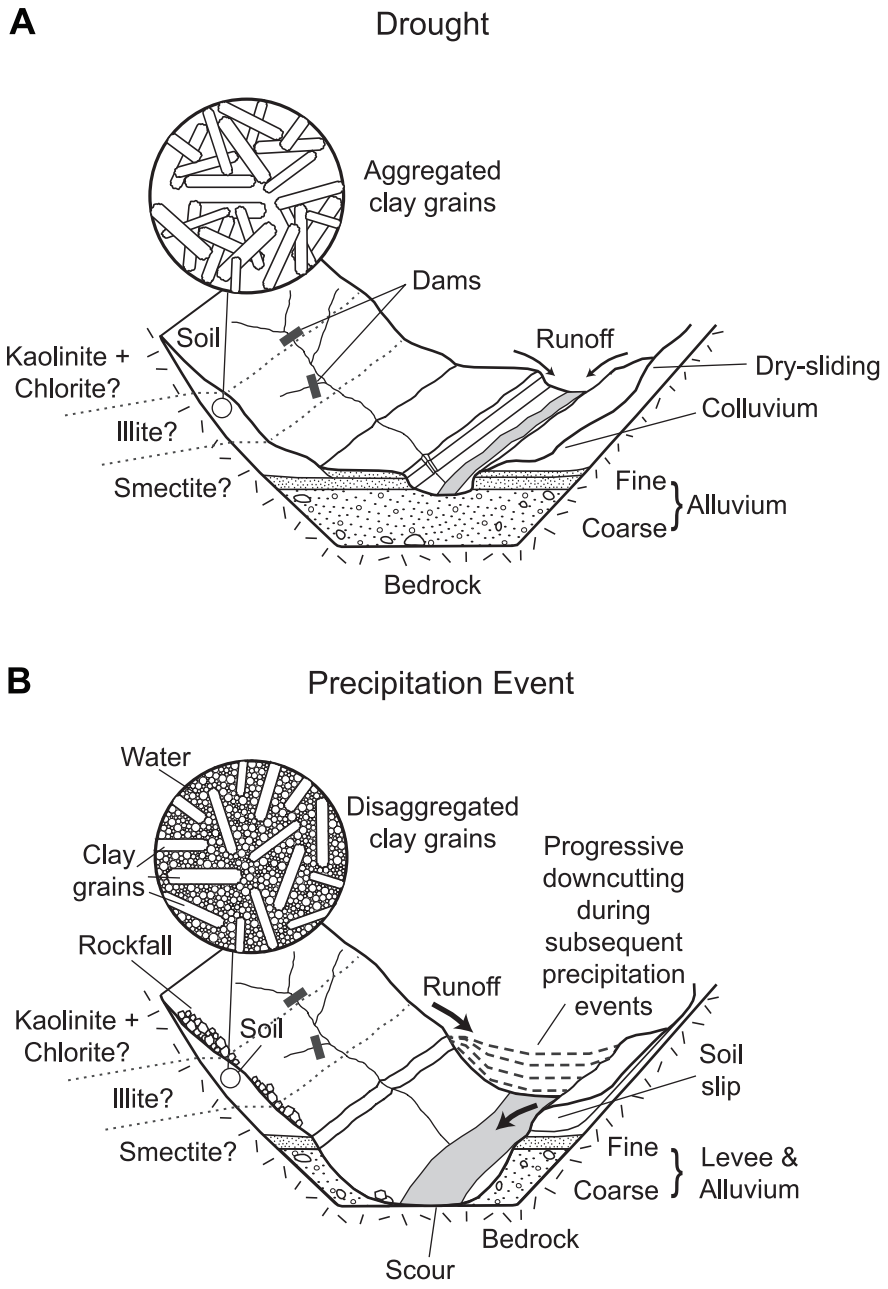


**Figure 3.9.** Stream channel profile and landscape erosion during (A) drought and (B) precipitation events. Clay mineral grain interactions are inset. Adapted from Scott and Williams (1978).

*3.5.4 Precipitation and sediment transport*

Precipitation events in southern California correlate with the PDO and ENSO climate modes (Andrews et al., 2004; Cayan et al., 1999; Dettinger et al., 1998; Mantua et al., 1997; Mo and Higgins, 1998; Schonher and Nicholson, 1989), leading to increased river runoff and therefore sediment flux into SBB (Inman and Jenkins, 1999; Warrick and Farnsworth, 2009b)

(Figure 3.7). However the detrital elements and clay minerals in this study do not correlate with the PDO or ENSO (Table 3.1). The lack of correlation with the climate modes may be a result of the multiple year averaging (2-7 years) of the bulk sediment sampling for ICP-MS and -AES analyses and/or the relative contribution of non-detrital components. Yet detrital variables have positive correlations with precipitation (Table 3.1).

All the clay minerals increase in abundance as total summed precipitation increases (although only K+C has a significant relationship; Table 3.1). This may be attributable to the generation of eroded clay minerals during precipitation events, which is related to the ability of clay minerals to sorb water to their surfaces. During dry periods and droughts, soil clay minerals lose sorbed water (Velde, 1992) and aggregate to become less mobile (Figure 3.9A), but during precipitation events soil aggregates disintegrate, allowing clay particles to become fluidized and erode (Figure 3.9B) (Bryan, 2000). We posit that during precipitation events in the Transverse Ranges, clays are able to sorb water, becoming more mobile and erodible (Grabowski et al., 2011; Velde, 1992), and are transported downstream to be deposited in SBB, while during dry periods soil moisture decreases (White et al., 2005), and clays become progressively more immobile in the catchments (Figure 3.9 inset). Thus clay mineral abundances increase in SBB sediments during intervals associated with frequent precipitation events, and decrease during droughts (Figure 3.7).

The correlations that exist between precipitation and the detrital variables (Table 3.1) validate the use of detrital sediment clay mineral abundances and element concentrations in paleoprecipitation reconstructions. Such reconstructions enable precipitation event frequency analysis on longer timescales (e.g., millennial; Romans et al., 2009) in a region that is well known for vulnerability to both extreme precipitation events and drought. Further, these results demonstrate that high-resolution elemental analysis of similar laminated marine sediments found on the margins of many continents [e.g., North America (Cowan et al., 1997; Dean and Kemp, 2004; Sancetta, 1995), South America (Hughen et al., 1996), Africa (Pokras and Winter, 1987; Seeberg-Elverfeldt et al., 2005), Europe (Haenssler et al., 2013; Wohlfarth et al., 1998), and Asia (Lückge et al., 2002)] should also accurately capture paleoprecipitation variability.

*3.5.5 Sediment transport effects on the detrital signal*

Variations in elemental EFs suggest the contribution of sediment from different provenance sources varies among individual precipitation events and hydroclimate regimes. Similar Ca* and Na EF trends suggest the presence of plagioclase feldspars, indicating sediment sourced from the eastern Santa Clara River catchment (Yerkes and Campbell, 2005). This input is likely diluted by downstream sources, causing inverse Ca* and Na concentrations to other detrital elements (Figure 3.2). This is corroborated by a greater proportion of quartz, potassium feldspar, and sedimentary lithics, and decreasing plagioclase and metamorphic lithics downstream in the Santa Clara River (Critelli et al., 1997; Fan, 1976), which reflects both source lithology change as sediment transport progresses downriver, and preferential destruction of plagioclase. The opposing trends in Ca* and Na EFs compared to the weathering indices also support this interpretation (Figures 3.2I and 3.3B, G). Gray layer samples have the lowest EF values, while EF values increase in samples associated with smaller floods, (Figure 3.3). This may indicate differential erosive response to less intense precipitation events from certain source areas, while during extreme events, such as floods that produce gray layers, sediment contribution may be more uniform.

Weathering and transportation processes selectively break down weaker minerals, and transport more resistant minerals and smaller grain sizes into SBB. Suspended sediment loads can vary spatially and temporally within catchments (Downs et al., 2013; Inman and Jenkins, 1999; Warrick and Farnsworth, 2009b; Warrick and Mertes, 2009), which can affect the abundance and integration of minerals/elements within the river sediment flux into SBB. The attenuation of the provenance signal during stream transport makes sediment source area difficult to identify in detrital sediment. The detrital component of SBB sediments is also influenced by nearshore wave dynamics and biogeochemical processes (e.g., redox) during sediment transport and deposition, which can modify the precipitation and runoff signal, and the sediment source properties prior to deposition in SBB (Koiter et al., 2013). These processes may explain the lack of correlation between precipitation and elements such as Ca* and Na due to weathering and dilution during transport, and Fe and Mn due to redox changes after deposition in SBB.

## 3.6 Conclusions

The high-resolution Santa Barbara Basin sediment record has long been used to reconstruct paleoclimate change, and even captures extreme weather events such as floods and drought. Here we show that on historical timescales the detrital fraction in SPR0901-04BC is influenced both by precipitation events and anthropogenic land use change that impact sediment erosion, integration, and flux. Linear correlation and transfer function modeling results suggest the concentration of Ti may be the most suitable precipitation proxy in the SBB catchment area. Deviations between detrital element variations, such as Ca* and Na versus Al and K, may record sediment source or changes in sediment generation and integration downstream, however additional research, including provenance investigations, is needed to test this hypothesis. The inconsistent response of detrital variables to precipitation events may relate to the differing roles of sediment source and transport within the catchments, differential weathering, and grain size.

Comparisons made between historical and geologic timescales must consider anthropogenic modifications alongside additional factors that influence the detrital sediment flux (e.g., sea level changes and tectonics). Correlation of many of the detrital variables analyzed in this study with the percent of total catchment area dammed suggests trapping of sediment behind dams influences the composition of detrital sediment input into SBB. The dams, therefore, likely bias the composition of the suspended load to elements/clay minerals associated with the lower, undammed reaches of the local catchments. To interpret changes in the components of detrital sediment, a better understanding of the processes that create and modify this fraction, including provenance, rock weathering, erosion, stream transport, and anthropogenic modifications, is necessary. With these considerations, the detrital signal can be used to determine paleoprecipitation event and hydroclimate regime frequencies and predict future variability– information that is crucial to water resource management, environmental management, and hazard mitigation planning.

## 3.7 References

Adams, P.N., Inman, D.L., Graham, N.E., 2008. Southern California Deep-Water Wave Climate: Characterization and Application to Coastal Processes. J. Coast. Res. 24, 1022-1035.

Andrews, E.D., Antweiler, R.C., Neiman, P.J., Ralph, F.M., 2004. Influence of ENSO on flood frequency along the California Coast. J. Climate 17, 337-348.

Bahlburg, H., Dobrzinski, N., 2011. Chapter 6 A review of the Chemical Index of Alteration (CIA) and its application to the study of Neoproterozoic glacial deposits and climate transitions. Geological Society, London, Memoirs 36, 81-92.

Browning, K.A., Pardoe, C.W., 1973. Structure of low-level jet streams ahead of mid-latitude cold fronts. Q. J. Roy. Meteorol. Soc. 99, 619-638.

Brownlie, W.R., Taylor, B.D., 1981. Sediment management for Southern California mountains, coastal plains and shoreline; Part C, coastal sediment delivery by major rivers in southern California. Environmental Quality Laboratory, California Institute of Technology, Pasadena, p. 314.

Bryan, R.B., 2000. Soil erodibility and processes of water erosion on hillslope. Geomorphology 32, 385-415.

Burcham, L.T., 1957. California range land. Division of Forestry, Dept. of National Resources, State of California, Sacramento.

Cayan, D.R., Redmond, K.T., Riddle, L.G., 1999. ENSO and hydrologic extremes in the Western United States. J. Climate 12, 2881-2893.

Chang, J., Wang, Y., Istanbulluoglu, E., Bai, T., Huang, Q., Yang, D., Huang, S., 2015. Impact of climate change and human activities on runoff in the Weihe River Basin, China. Quatern. Int. 380–381, 169-179.

Cowan, E.A., Cai, J., Powell, R.D., Clark, J.D., Pitcher, J.N., 1997. Temperate glacimarine varves; an example from Disenchantment Bay, Southern Alaska. J. Sed. Res. 67, 536-549.

Critelli, S., Le Pera, E., Ingersoll, R., 1997. The effects of source lithology, transport, deposition and sampling scale on the composition of southern California sand. Sedimentology 44, 653-671.

Dai, S.B., Lu, X.X., Yang, S.L., Cai, A.M., 2008. A preliminary estimate of human and natural contributions to the decline in sediment flux from the Yangtze River to the East China Sea. Quatern. Int. 186, 43-54.

Dean, J.M., Kemp, A.E.S., 2004. A 2100 year BP record of the Pacific Decadal Oscillation, El Niño Southern Oscillation and Quasi-Biennial Oscillation in marine production and fluvial input from Saanich Inlet, British Columbia. Palaeogeogr., Palaeoclimatol., Palaeoecol. 213, 207-229.

Dettinger, M.D., Cayan, D.R., Diaz, H.F., Meko, D.M., 1998. North-south precipitation patterns in western North America on interannual-to-decadal timescales. J. Climate 11, 3095-3111.

Dettinger, M.D., Ralph, F.M., Das, T., Neiman, P.J., Cayan, D.R., 2011. Atmospheric Rivers, Floods and the Water Resources of California. Water 3, 445-478.

Downs, P.W., Dusterhoff, S.R., Sears, W.A., 2013. Reach-scale channel sensitivity to multiple human activities and natural events: Lower Santa Clara River, California, USA. Geomorphology 189, 121-134.

Ejarque, A., Anderson, R.S., Simms, A.R., and Gentry, B.J., 2015, Prehistoric fires and the shaping of colonial transported landscapes in southern California: A paleoenvironmental study at Dune Pond, Santa Barbara County. Quatern. Sci. Rev. 112, 181-196.

Ergin, M., Kadir, S., Keskin, Ş., Turhan-Akyüz, N., Yaşar, D., 2007. Late Quaternary climate and sea-level changes recorded in sediment composition off the Büyük Menderes River delta (eastern Aegean Sea, Turkey). Quatern. Int. 167–168, 162-176.

Fan, P.-F., 1976. Recent silts in the Santa Clara river drainage basin, southern California; a mineralogical investigation of their origin and evolution. J. Sed. Res. 46, 803-812.

Fedo, C.M., Nesbitt, H.W., Young, G.M., 1995. Unraveling the effects of potassium metasomatism in sedimentary rocks and paleosols, with implications for paleoweathering conditions and provenance. Geology 23, 921-924.

Fleischer, P., 1972. Mineralogy and sedimentation history, Santa Barbara Basin, California. Journal of Sedimentary Research 42, 49-58.

Grabowski, R.C., Droppo, I.G., Wharton, G., 2011. Erodibility of cohesive sediment: The importance of sediment properties. Earth-Sci. Rev. 105, 101-120.

Haenssler, E., Nadeau, M.-J., Vött, A., Unkel, I., 2013. Natural and human induced environmental changes preserved in a Holocene sediment sequence from the Etoliko Lagoon, Greece: New evidence from geochemical proxies. Quatern. Int. 308–309, 89-104.

Harden, J.W., Sarna-Wojcicki, A.M., Dembroff, G.R., 1986. Soils developed on coastal and fluvial terraces near Ventura, California. U.S. G.P.O., p. 34.

Haug, G.H., Günther, D., Peterson, L.C., Sigman, D.M., Hughen, K.A., Aeschlimann, B., 2003. Climate and the collapse of Maya civilization. Sci 299, 1731-1735.

Hazen, R.M., Sverjensky, D.A., Azzolini, D., Bish, D.L., Elmore, S.C., Hinnov, L., Milliken, R.E., 2013. Clay mineral evolution. AmMin 98, 2007-2029.

Hein, J.R., Dowling, J.S., Schuetze, A., Lee, H.J., 2003. Clay-mineral suites, sources, and inferred dispersal routes: Southern California continental shelf. Marine Environmental Research 56, 79-102.

Hendy, I.L., Napier, T.J., Schimmelmann, A., 2015. From extreme rainfall to drought: 250 years of annually resolved sediment deposition in Santa Barbara Basin, California. Quatern. Int. 387, 3-12.

Heymann, C., Nelle, O., Dörfler, W., Zagana, H., Nowaczyk, N., Xue, J., Unkel, I., 2013. Late Glacial to mid-Holocene palaeoclimate development of Southern Greece inferred from the sediment sequence of Lake Stymphalia (NE-Peloponnese). Quatern. Int. 302, 42-60.

Huang, S., Huang, Q., Chang, J., Leng, G., Chen, Y., in press. Variations in precipitation and runoff from a multivariate perspective in the Wei River Basin, China. Quatern. Int.

Hughen, K.A., Overpeck, J.T., Peterson, L.C., Anderson, R.F., 1996. The nature of varved sedimentation in the Cariaco Basin, Venezuela, and its palaeoclimatic significance. Geol. Soc. London Spec. Publ. 116, 171-183.

IBM, 2012. Transfer functions in custom ARIMA models, SPSS Statistics 21.0.0.

Inman, D.L., Jenkins, S.A., 1999. Climate change and the episodicity of sediment flux of small California rivers. J. Geol. 107, 251-270.

Kerr, P.F., Stroud, R.A., Drew, I.M., 1971. Clay mobility in landslides, Ventura, California. American Association of Petroleum Geologists Bulletin. 55, 267-291.

Koide, M., Soutar, A., Goldberg, E.D., 1972. Marine geochronology with 210Pb. Earth Planet. Sci. Lett. 14, 442-446.

Koiter, A.J., Owens, P.N., Petticrew, E.L., Lobb, D.A., 2013. The behavioural characteristics of sediment properties and their implications for sediment fingerprinting as an approach for identifying sediment sources in river basins. Earth-Science Reviews 125, 24-42.

Kolpack, R.L., Drake, D.E., 1984. Transport of clays in the eastern part of santa barbara channel, California. Geo-Mar. Lett. 4, 191-196.

Krishnaswami, S., Lal, D., Amin, B.S., Soutar, A., 1973. Geochronological studies in Santa Barbara Basin: 55Fe as a unique tracer for particulate settling. Limnology and Oceanography 18, 763-770.

Lamy, F., Hebbeln, D., Röhl, U., Wefer, G., 2001. Holocene rainfall variability in southern Chile: a marine record of latitudinal shifts of the Southern Westerlies. Earth and Planetary Science Letters 185, 369-382.

Lavé, J., Burbank, D., 2004. Denudation processes and rates in the Transverse Ranges, southern California: Erosional response of a transitional landscape to external and anthropogenic forcing. J. Geophys. Res. Earth Surf. 109, F01006.

Li, S., Dai, Z., Mei, X., Huang, H., Wei, W., Gao, J., in press. Dramatic variations in water discharge and sediment load from Nanliu River (China) to the Beibu Gulf during 1960s–2013. Quatern. Int.

Lückge, A., Reinhardt, L., Andruleit, H., Doose-Rolinski, H., von Rad, U., Schulz, H., Treppke, U., 2002. Formation of varve-like laminae off Pakistan: decoding 5 years of sedimentation. Geol. Soc. London Spec. Publ. 195, 421-431.

Ludington, S., Moring, B.C., Miller, R.J., Flynn, K.S., Stone, P.A., Bedford, D.R., 2005. Preliminary integrated databases for the United States - Western States: California, Nevada, Arizona, and Washington. U.S. Geological Survey, Reston, Virginia, USA.

Lynn, R.J., Simpson, J.J., 1987. The California Current system: The seasonal variability of its physical characteristics. Journal of Geophysical Research: Oceans 92, 12947-12966.

Mantua, N.J., Hare, S.R., 2002. The Pacific Decadal Oscillation. Journal of Oceanography 58, 35-44.

Mantua, N.J., Hare, S.R., Zhang, Y., 1997. A Pacific interdecadal climate oscillation with impacts on salmon production. Bulletin of the American Meteorological Society 78, 1069-1079.

McFadden, L.D., 1988. Climatic influences on rates and processes of soil development in Quaternary deposits of southern California. Geol. Soc. Am. Spec. Pap. 216, 153-178.

McKay, L.; Bondelid, T.; Dewald, T.; Johnston, J.; Moore, R.; Rea, A., 2012. NHDPlus Version 2.

Mishra, P.K., Anoop, A., Schettler, G., Prasad, S., Jehangir, A., Menzel, P., Naumann, R., Yousuf, A.R., Basavaiah, N., Deenadayalan, K., Wiesner, M.G., Gaye, B., 2015. Reconstructed late Quaternary hydrological changes from Lake Tso Moriri, NW Himalaya. Quatern. Int. 371, 76-86.

Mo, K.C., Higgins, R.W., 1998. Tropical Influences on California Precipitation. J. Climate 11, 412-430.

Moore, D.M., Reynolds, R.C., 1997. X-ray diffraction and the identification and analysis of clay minerals. Oxford University Press, Oxford.

Nesbitt, H.W., Young, G.M., 1982. Early Proterozoic climates and plate motions inferred from major element chemistry of lutites. Nature 299, 715-717.

Nezlin, N.P., DiGiacomo, P.M., Stein, E.D., Ackerman, D., 2005. Stormwater runoff plumes observed by SeaWiFS radiometer in the Southern California Bight. Remote Sens. Environ. 98, 494-510.

Nezlin, N.P., Stein, E.D., 2005. Spatial and temporal patterns of remotely-sensed and field-measured rainfall in southern California. Remote Sens. Environ. 96, 228-245.

Paillard, D., Labeyrie, L., Yiou, P., 1996. Macintosh Program performs time-series analysis. Eos, Transactions American Geophysical Union 77, 379-379.

Passchier, S., Bohaty, S.M., Jiménez‐Espejo, F., Pross, J., Röhl, U., Flierdt, T., Escutia, C., Brinkhuis, H., 2013. Early Eocene to middle Miocene cooling and aridification of East Antarctica. Geochemistry, Geophysics, Geosystems 14, 1399-1410.

Passchier, S., Krissek, L.A., 2008. Oligocene–Miocene Antarctic continental weathering record and paleoclimatic implications, Cape Roberts drilling Project, Ross Sea, Antarctica. Palaeogeogr., Palaeoclimatol., Palaeoecol. 260, 30-40.

Paulson, R.W., Chase, E.B., Roberts, R.S., Moody, D.W., 1991. National water summary 1988-89: hydrologic events and floods and droughts, Water Supply Paper. U. S. Government Printing Office, Washington, D.C., pp. 601-601.

Peel, M.C., Finlayson, B.L., McMahon, T.A., 2007. Updated world map of the Köppen-Geiger climate classification. HESS 11, 1633.

Petschick, R., 2010. MacDiff 4.2.6.

Pokras, E.M., Winter, A., 1987. Variability of Holocene diatom assemblages in laminated sediments near Walvis Bay, southwest Africa. Mar. Geol. 76, 185-194.

Robert, C., 2004. Late Quaternary variability of precipitation in Southern California and climatic implications: clay mineral evidence from the Santa Barbara Basin, ODP Site 893. Quaternary Science Reviews 23, 1029-1040.

Romans, B.W., Normark, W.R., McGann, M.M., Covault, J.A., Graham, S.A., 2009. Coarse-grained sediment delivery and distribution in the Holocene Santa Monica Basin, California: Implications for evaluating source-to-sink flux at millennial time scales. Geol. Soc. Am. Bull. 121, 1394-1408.

Ryan, W.B.F., Carbotte, S.M., Coplan, J.O., O'Hara, S., Melkonian, A., Arko, R., Weissel, R.A., Ferrini, V., Goodwillie, A., Nitsche, F., Bonczkowski, J., Zemsky, R., 2009. Global Multi-Resolution Topography synthesis. Geochem. Geophys. Geosyst. 10, Q03014.

Sancetta, C., 1995. Diatoms in the Gulf of California: Seasonal flux patterns and the sediment record for the last 15,000 years. Paleoceanography 10, 67-84.

Schimmelmann, A., Lange, C.B., Berger, W.H., Simon, A., Burke, S.K., Dunbar, R.B., 1992. Extreme climatic conditions recorded in Santa Barbara Basin laminated sediments: the 1835–1840 Macoma event. Marine Geology 106, 279-299.

Schimmelmann, A., Lange, C.B., Meggers, B.J., 2003. Palaeoclimatic and archaeological evidence for a similar to 200-yr recurrence of floods and droughts linking California, Mesoamerica and South America over the past 2000 years. Holocene 13, 763-778.

Schimmelmann, A., Zhao, M., Harvey, C.C., Lange, C.B., 1998. A large California flood and correlative global climatic events 400 years ago. Quaternary Research 49, 51-61.

Schonher, T., Nicholson, S.E., 1989. The relationship between California rainfall and ENSO events. Journal of Climate 2, 1258-1269.

Schwarz, G., 1978. Estimating the Dimension of a Model. The Annals of Statistics 6, 461-464.

Scott, K.M., Williams, R.P., 1978. Erosion and sediment yields in the Transverse Ranges, southern California. U.S. Government Print Office, p. 38.

Seeberg-Elverfeldt, I.A., Lange, C.B., Pätzold, J., Kuhn, G., 2005. Laminae type and possible mechanisms for the formation of laminated sediments in the Shaban Deep, northern Red Sea. Ocean Science 1, 113-126.

Sheldon, N.D., Retallack, G.J., Tanaka, S., 2002. Geochemical climofunctions from North American soils and application to paleosols across the Eocene-Oligocene Boundary in Oregon. J. Geol. 110, 687-696.

Slagel, M.J., Griggs, G.B., 2008. Cumulative losses of sand to the California coast by dam impoundment. Journal of Coastal Research 24, 571-584.

Solum, J.G., van der Pluijm, B.A., Peacor, D.R., 2005. Neocrystallization, fabrics and age of clay minerals from an exposure of the Moab Fault, Utah. Journal of Structural Geology 27, 1563-1576.

Soutar, A., Crill, P.A., 1977. Sedimentation and climatic patterns in the Santa Barbara Basin during the 19th and 20th centuries. Geol. Soc. Am. Bull. 88, 1161-1172.

Soutar, A., Isaacs, J.D., 1969. History of fish populations inferred from fish scales in anaerobic sedimends off California, California Cooperative Oceanic Fisheries Investigations Reports 13, pp. 63-70.

State of California Department of Water Resources, 2014. Dams within the jurisdiction of the State of California.

Stein, R., 1995. Clay and bulk mineralogy of Late Quaternary sediments at Site 893, Santa Barbara Basin, in: Kennett, J.P., Baldauf, J.G., Lyle, M. (Eds.), Proceedings of the Ocean Drilling Program, Scientific Results. Ocean Drilling Program, College Station, TX, pp. 89-102.

Stover, C.W., Coffman, J.L., 1993. Seismicity of the United States, 1568-1989 (Revised), in: Survey, U.S.G. (Ed.). United States Government Printing Office, Washington, D.C., p. 418 p.

Thornton, S.E., 1984. Basin model for hemipelagic sedimentation in a tectonically active continental margin: Santa Barbara Basin, California Continental Borderland. Geological Society, London, Special Publications 15, 377-394.

Thornton, S.E., 1986. Origin of mass flow sedimentary structures in hemipelagic basin deposits: Santa Barbara Basin, California Borderland. Geo-Marine Letters 6, 15-19.

Thunell, R.C., 1998. Particle fluxes in a coastal upwelling zone: sediment trap results from Santa Barbara Basin, California. Deep-Sea Research Part II 45, 1863-1884.

Thunell, R.C., Tappa, E., Anderson, D.M., 1995. Sediment fluxes and varve formation in Santa Barbara Basin, offshore California. Geology 23, 1083-1086.

Tierney, J., Giosan, L., Donnelly, J.P., Shuman, B., 2005. The use of Scanning XRF technology in terrestrial paleoclimatology and paleohydrology. Eos Transactions, American Geophysical Union Fall Meeting Supplemental 86, Abstract PP14B-02.

Turekian, K.K., Wedepohl, K.H., 1961. Distribution of the elements in some major units of the Earth's crust. Geol. Soc. Am. Bull. 72, 175-192.

Velde, B., 1992. Introduction to clay minerals: chemistry, origins, uses, and environmental significance. Chapman & Hall, London ; New York.

Wang, S., Yan, M., Yan, Y., Shi, C., He, L., 2012. Contributions of climate change and human activities to the changes in runoff increment in different sections of the Yellow River. Quatern. Int. 282, 66-77.

Warrick, J.A., Farnsworth, K.L., 2009a. Dispersal of river sediment in the Southern California Bight. Geol. Soc. Am. Spec. Pap. 454, 53-67.

Warrick, J.A., Farnsworth, K.L., 2009b. Sources of sediment to the coastal waters of the Southern California Bight. Geological Society of America Special Papers 454, 39-52.

Warrick, J.A., Hatten, J.A., Pasternack, G.B., Gray, A.B., Goni, M.A., Wheatcroft, R.A., 2012. The effects of wildfire on the sediment yield of a coastal California watershed. Geol. Soc. Am. Bull. 124, 1130-1146.

Warrick, J.A., Mertes, L.A.K., 2009. Sediment yield from the tectonically active semiarid Western Transverse Ranges of California. Geological Society of America Bulletin 121, 1054-1070.

Warrick, J.A., Milliman, J.D., 2003. Hyperpycnal sediment discharge from semiarid southern California rivers: Implications for coastal sediment budgets. Geology 31, 781-784.

Warrick, J.A., Rubin, D.M., 2007. Suspended-sediment rating curve response to urbanization and wildfire, Santa Ana River, California. Journal of Geophysical Research: Earth Surface 112, F02018.

Warrick, J.A., Xu, J., Noble, M.A., Lee, H.J., 2008. Rapid formation of hyperpycnal sediment gravity currents offshore of a semi-arid California river. Continental Shelf Research 28, 991-1009.

Wei, G., Liu, Y., Li, X., Shao, L., Liang, X., 2003. Climatic impact on Al, K, Sc and Ti in marine sediments: Evidence from ODP site 1144, South China Sea. GeocJ 37, 593-602.

White, A.F., Schulz, M.S., Vivit, D.V., Blum, A.E., Stonestrom, D.A., Harden, J.W., 2005. Chemical weathering rates of a soil chronosequence on granitic alluvium: III.

Hydrochemical evolution and contemporary solute fluxes and rates. Geochimica et Cosmochimica Acta 69, 1975-1996.

Williams, R.P., 1979. Sediment discharge in the Santa Clara River Basin, Ventura and Los Angeles Counties, California, Water-Resources Investigations Report, - ed, p. 51.

Willis, Cope M., Griggs, Gary B., 2003. Reductions in fluvial sediment discharge by coastal dams in California and implications for beach sustainability. Journal of Geology 111, 167-182.

Wohlfarth, B., Holmquist, B., Cato, I., Linderson, H., 1998. The climatic significance of clastic varves in the Ångermanälven Estuary, northern Sweden, AD 1860 to 1950. Holocene 8, 521-534.

Xu, J., 2009. Plausible causes of temporal variation in suspended sediment concentration in the upper Changjiang River and major tributaries during the second half of the 20th century. Quatern. Int. 208, 85-92.

Xu, J., 2011. Variation in annual runoff of the Wudinghe River as influenced by climate change and human activity. Quaternary International 244, 230-237.

Yerkes, R.F., Campbell, R.H., 2005. Preliminary Geologic Map of the Los Angeles 30' x 60' Quadrangle, Southern California, USGS Open-File Report 2005-1019, pp. 2-51 p.

# CHAPTER 4

## Southern California hydroclimate during deglacial Termination V (~430-420 ka): The persistence of drought, flooding, and interannual precipitation variability


### Abstract

The hydroclimate of southern California fluctuates between extreme precipitation and drought. Effective water resource management requires knowledge of the natural hydroclimate variability of southern California and its response to climate warming. Sedimentary archives of past variability in hydroclimate can provide a long-term context that complements modern records. Pristine laminated Santa Barbara Basin (SBB) sediment cores MV0508-33JPC, -21JPC, and -29JPC were recovered from a truncated anticline and dated to Termination V ($T_V$) at ~420 ka, the transition from glacial Marine Isotope Stage (MIS) 12 to warm interglacial MIS 11. Foraminiferal $\delta^{18}O$ variations in these cores record centennial-scale abrupt climate change during $T_V$ that are coherent with known North Atlantic rapid warming events. A paleoprecipitation proxy for laminated intervals of MV0508-33JPC was developed using the first principal component of scanning XRF elemental counts (PC1) that has high loadings for siliciclastic sediment-associated elements K, Ti, and Si. Twentieth century laminated sedimentary couplets in SBB sediments have been identified as annual varves, therefore the $T_V$ laminations identified in PC1 were annually tuned. Extreme flooding and decadal-to-centennial droughts were identified in the PC1 southern California $T_V$ paleoprecipitation reconstruction, similar to modern and Holocene climate records. Time series analysis of the paleoprecipitation reconstruction reveals El Niño-Southern Oscillation (ENSO)-like (2-7 year) periodicities in southern California hydroclimate that coincided with intervals of increased precipitation, while this cyclicity was absent during the droughts. Drought conditions may be the result of atmospheric reorganization involving poleward or zonal expansion of the subtropical dry zone through the North Pacific High pressure system as climate warmed. Although similar decadal-scale precipitation variability has been associated with a Pacific Decadal Oscillation, newly observed centennial-scale

variability has not yet been detected in the limited duration of modern instrumental records. This paleoprecipitation reconstruction indicates that present day southern California precipitation patterns—including extreme flooding, extended drought, and interannual influence similar to ENSO—are highly persistent through time in warm climate intervals since the mid-Pleistocene.

### 4.1 Introduction

The El Niño-Southern Oscillation (ENSO) is robustly coupled with interannual precipitation variability in the Pacific Basin and across the globe (Ropelewski and Halpert, 1987), and alternates between El Niño (warm), neutral, or La Niña (cool) phases that occur every 2-7 years (Ayling et al., 2015). In southern California, El Niño events are associated with increased precipitation (Andrews et al., 2004; Cayan et al., 1999; Dettinger et al., 1998; Hoell et al., 2016; Mo and Higgins, 1998; Schonher and Nicholson, 1989), and with a greater probability of extreme precipitation events (Cayan et al., 1999; Sun et al., 2015). California has a highly variable hydroclimate, alternating between flooding and drought. Annual precipitation totals rely on a small number of reservoir-filling intense precipitation events, creating difficulties in balancing water resource management with flood management (Dettinger et al., 2011; Warrick and Farnsworth, 2009b). Hence it is important to understand natural precipitation variability to improve the management of water resources in California.

The observational ENSO index is limited to the past ~150 years (Rayner et al., 2003), but paleoclimate archives that record ENSO events can lengthen the ENSO index to provide additional targets for climate model testing. Extreme El Niño and La Niña events are expected to become more frequent under future greenhouse warming, however climate models have difficulty producing realistic simulations of ENSO, leading to uncertainties in the modeling projections (Cai et al., 2015a; Cai et al., 2015b). Furthermore, investigating periods of warming in the past provides insights into the relationship between ENSO and forcing changes, and the natural variability of ENSO without anthropogenic forcing influences. Marine Isotope Stage (MIS) 11 is considered to be a close analogue to the present Holocene interglacial due to similar orbital insolation configuration and atmospheric $CO_2$ concentrations similar to pre-industrial levels (Loutre and Berger, 2003) making this interglacial interval a relevant choice for examining interannual precipitation variability that is comparable to modern ENSO. Capturing the response of interannual hydroclimate variability to warming during one of the largest deglacial events,

Termination V ($T_V$) may lead to better understanding of how ENSO will respond to future warming.

Termination V, the transition from glacial MIS 12 to interglacial MIS 11 around 424 ka was one of the largest deglaciations of the Pleistocene, with a benthic foraminiferal $\delta^{18}O$ shift of 1.97‰ VPDB (Lisiecki and Raymo, 2005). The initial deglaciation phase occurred during the first MIS 11 insolation maximum and sea level rapidly rose 50-60 m over 5 kyr (Rohling et al., 2010). Climate fluctuations observed in marine and continental MIS 12 and 11 paleoclimate records (Candy et al., 2014) are similar to those recorded in the most recent glacial-interglacial cycle, Termination I ($T_I$). Marine cores from the North Atlantic and the Iberian Margin document ice-rafting events during MIS 12 and $T_V$, as well as millennial and (inter)stadial-type temperature oscillations during $T_V$ and MIS 11 (Oppo et al., 1998; Rodrigues et al., 2011; Voelker et al., 2010). A lacustrine record from the Sulmona basin in Italy indicates an increasing precipitation trend through $T_V$ and MIS 11 (Regattieri et al., 2016). In the American Southwest, the strength of the North American Monsoon generally increased during warm substages of MIS 11 (a, c, and e; Prokopenko et al., 2001), and decreased during the cool substages (b and d) (Cisneros-Dozal et al., 2014; Fawcett et al., 2011). However, this region also experienced episodes of drought spanning centuries to millennia during the warmest phase of MIS 11 and during much of MIS 12; these have been attributed to a combination of less winter precipitation (as mid-latitude Westerlies shifted poleward), and reductions in summer precipitation (Fawcett et al., 2011).

The interannual hydroclimate variability of $T_V$ is difficult to reconstruct because very few annual-resolution archives exist. Ice cores and typical marine sediment cores that record this time period have low resolution that precludes interannual climate investigations. Centennial-scale climate oscillations within the ENSO bandwidth have been observed in annually laminated lacustrine sediment from Germany (Koutsodendris et al., 2011; Koutsodendris et al., 2012). In the western equatorial Pacific Ocean, a region strongly influenced by ENSO, MIS 11 sea surface temperatures were the warmest of the last 450 ka, and the transition from cold MIS 12 sea surface temperatures to warm MIS 11 temperatures occurred before ice volume changes (Lea et al., 2003). Decreased ENSO frequency was observed in Papua New Guinea during MIS 11, however this study was temporally limited to the 35-year lifetime of a clam (Ayling et al., 2015).

Santa Barbara Basin (SBB), located offshore of southern California, preserves a varved annual archive that records modern and Holocene hydroclimate variability (Hendy et al., 2013;

Hendy et al., 2015; Schimmelmann et al., 2013; Schimmelmann et al., 1990; Schimmelmann et al., 1992; Schimmelmann et al., 2006; Schimmelmann et al., 1998; Soutar and Crill, 1977). A suite of cores recovered from a truncated anticline in the Santa Barbara Channel revealed preserved laminated sediments deposited through several glacial terminations during the Quaternary, including $T_V$ (Afshar, 2011; Behl et al., 2005; Behl et al., 2007; Dean et al., 2015; Hopkins et al., 2006; Marshall, 2012; White et al., 2013), that show promise as high-resolution paleoclimate archives.

This study investigates the natural hydroclimate variability of southern California during $T_V$, targeting variability associated with the ENSO bandwidth, using a paleoprecipitation proxy developed for the annually laminated sediments in SBB (Hendy et al., 2015). Annual resolution scanning XRF elemental counts record high counts of siliciclastic sediment-associated elements in the preserved annual laminations that are associated with precipitation and river runoff into the Santa Barbara Channel. Drought intervals are indicated by generally low counts of the same elements (Figure C.1). These elemental variations have been used to identify 20$^{th}$ century ENSO events in SBB sediments (Hendy et al., 2015), indicating their utility in the examination of interannual hydroclimate variability. The first principal component of the scanning XRF counts is used to generate a paleoprecipitation proxy for laminated intervals of SBB sediment core MV0508-33JPC. Time series analysis is applied to identify dominant cyclicities in southern California hydroclimate during the transition from a cool glacial to a warm interglacial climate during $T_V$ (~430-420 ka).

**4.2 Background**

Southern California has a mediterranean climate with cool, wet winters and warm, dry summers. The positions of the Aleutian Low and North Pacific High pressure systems control moisture transport into western North America (Lora et al., 2016). In winter the high pressure system is displaced southwest, which enables storms to bring moisture to California (Lu et al., 2003). The region's hydroclimate typically varies between two precipitation extremes, resulting in either flooding or drought (Dettinger et al., 2011). Variations in hydroclimate extremes have been linked to interannual and interdecadal climate oscillations. El Niño (La Niña) events in southern California are associated with increased (decreased) precipitation (Mo and Higgins, 1998; Venrick, 2012). Santa Barbara, California receives increased precipitation two months

after an El Niño event has reached peak conditions, as indicated by the Oceanic Niño Index (ONI) (Figure 4.1), which measures deviations sea surface temperatures within the Niño 3.4 region (5ºN–5ºS, 170ºW–120ºW) (see Appendix C). The regional hydroclimate is further influenced by decadal climate variability as precipitation events during El Niño occur more frequently during the positive phase of the Pacific Decadal Oscillation (PDO) (Verdon and Franks, 2006). Additionally extreme precipitation in California is associated with atmospheric rivers (ARs), which are narrow plumes (<1000 km wide and >2000 km in length) of tropically sourced atmospheric water vapor (Dettinger et al., 2011). These ARs result in intense precipitation events that are responsible for up to half of California's total precipitation (Dettinger et al., 2011). In southern California, ARs are responsible for a larger-than-average fraction of precipitation during El Niño events and in the positive PDO phase (Dettinger et al., 2011).

The semi-enclosed SBB is located within the southern California Bight (Figure 4.2). Sediment deposited in the SBB is derived from two primary sources. Coastal upwelling occurs in spring-summer and induces increased primary productivity and biogenic sediment deposition. Precipitation generally occurs in the winter and stimulates river runoff into the basin and deposition of terrestrial siliciclastic sediment. These two sediment components are seasonal, and their alternate deposition leads to laminated sedimentary deposits in SBB. Active local tectonics combined with the seasonally-enhanced biogenic deposition result in very high sedimentation rates in the basin, with an average sedimentation rate of 102.2 cm/kyr over the past million years (Behl et al., 2007). Below the submarine sill depth, the waters in SBB are oxygen-depleted (Behl and Kennett, 1996). Restricted bottom water flow in SBB and low bottom water dissolved oxygen concentrations limit bioturbation of sediments below ~300 m water depth (Moffitt et al., 2014), leading to preservation of the laminations. The laminations preserved in SBB sediments have been designated as varves, i.e., couplets of two distinct sediment lamina deposited within a single year (Soutar and Crill, 1977).

Non-laminated or massive sediments indicate oxic waters entered the basin and allowed macrofauna to bioturbate the sediments. During cool climatic intervals such as the Last Glacial Maximum (MIS 2) and Younger Dryas, the OMZ was better ventilated and bioturbation prevented preservation of laminations in SBB sediments (Moffitt et al., 2014). Abrupt shifts between bioturbated and laminated sediments have been linked to rapid climate change events

(Behl and Kennett, 1996), notably the Bølling-Allerød (Moffitt et al., 2014) during Termination I ($T_I$, the LGM to Holocene deglacial transition) and the warm Dansgaard-Oeschger events of MIS 3 (Hendy and Kennett, 1999).

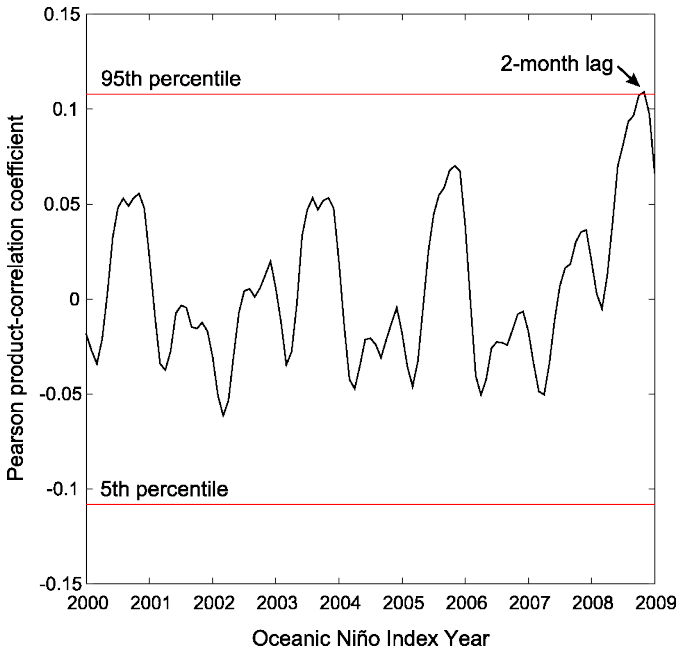


**Figure 4.1.** Running cross-correlation (black line) of downtown Santa Barbara, California precipitation with the Oceanic Niño Index (ONI) over October 1899 to January 2009.
The precipitation record was shifted back in time at monthly steps and correlated with the stationary ONI. The Pearson product-correlation coefficient was calculated between the two series at each step. The precipitation record and the ONI were analyzed as monthly series. The lower 5$^{th}$ and upper 95$^{th}$ percentiles of the distribution of all values are indicated with red lines. The highest correlation coefficient, which exceeds the 95$^{th}$ percentile, was obtained by shifting precipitation back in time by two months. ONI data from Rayner et al. (2003); precipitation data from County of Santa Barbara Public Works Water Resources Division, site: Santa Barbara Downtown, http://cosb.countyofsb.org/pwd/pwwater.aspx?id=3786.

The Southern California Bight region is tectonically active as a transpression margin, associated with the Big Bend in the San Andreas Fault. Sediment cores in this study were collected from an active anticline structure known as the Mid-Channel Trend (MCT). Erosion of the surface of this anticline during glacial low sea level stands has enabled coring access to Pleistocene strata. The MCT has developed since $T_V$ such that the paleobathymetry of SBB differed from the modern. Sediment accumulation was limited to the eastern SBB during $T_V$, which gradually filled (Marshall, 2012). During this time, the MCT grew and propagated westward, leading to decreased sedimentation on the structure and erosion in some locations (Marshall, 2012). The paleobathymetry of SBB and the MCT in particular during $T_V$ is difficult to estimate due to the influence of regional tectonics at this localized scale. Additionally during

MIS 12, global sea level was estimated to be ~195 m lower, and rose through the deglaciation of $T_V$. A paleoceanographic study of $T_{VII}$ (~630 ka) from a nearby sediment core estimated the paleo-water depth during deposition was 300-500 m (Dean et al., 2015). The quality of lamination preservation during $T_I$ in SBB at 300 m water depth (Moffitt et al., 2014) is similar to the $T_V$ cores and supports an estimated paleodepth of >300 m.

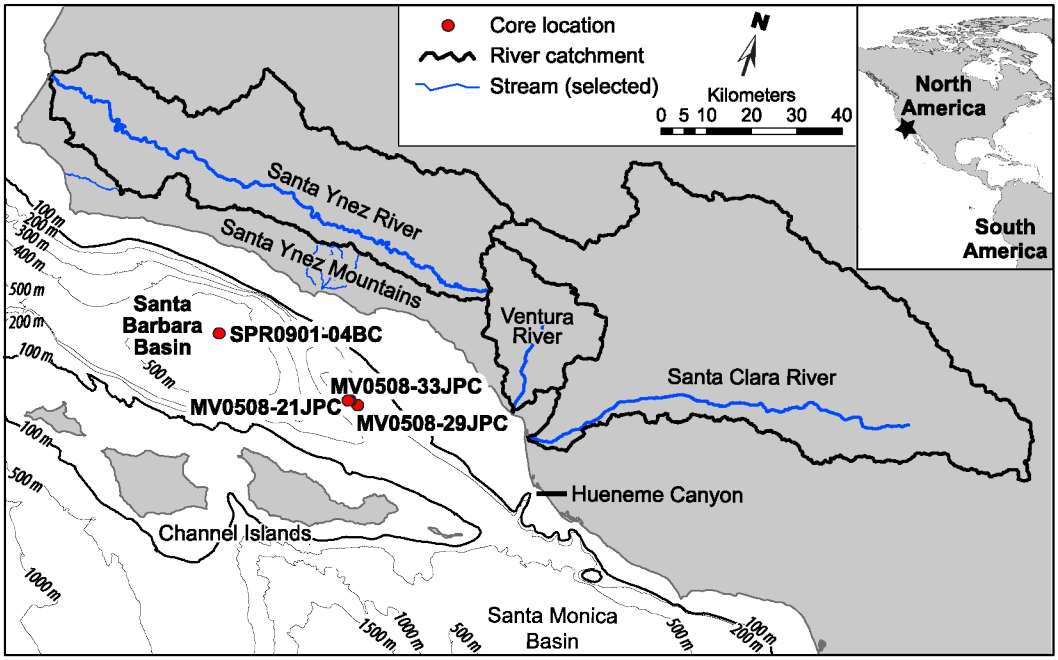


**Figure 4.2.** Location of core sites (red circles) in Santa Barbara Channel, southern California. River catchments are outlined in black and selected streams and rivers are shown by blue lines. Bathymetry contour interval is every 100 m within the channel and every 500 m south of the Channel Islands. Bathymetry is plotted from Global Multi-Resolution Topography, version 2.6 (Ryan et al., 2009).

## 4.3 Materials and Methods

### *4.3.1 Sediment Cores*

Jumbo piston sediment cores MV0508-33JPC (N 34º 13.2701', W 119º 41.6644', 147 m water depth; 33JPC), MV0508-21JPC (N 34º 13.257', W 119º 41.63', 142 m water depth; 21JPC), and MV0508-29JPC (N 34º 13.2525', W 119º 41.5954', 142 m water depth; 29JPC) were collected from the MCT in SBB (Figure 4.2) (Hopkins et al., 2006). Sediment core SPR0901-04BC (34º 16.895' N, 120º 02.489' W, 588 m water depth; 04BC) was collected in the central SBB. The distinctly laminated box core 04BC, 67 cm in length, was used to examine the

uppermost 42 cm spanning the time period A.D. 1870-2009 for direct comparison with the instrumental ONI.

Laminated intervals were identified using core fabric observed in high-resolution images and scanning XRF data. Core 33JPC (~410 cm core length) contains dark, olive gray silty to sandy clay. Four distinctly laminated intervals with three massive, bioturbated intervals are observed with a few prominent gray layers that range in thickness from <1 cm to >2.5 cm. Depths and durations of these stratigraphic intervals are presented in Table 4.1 and Figure 4.4. Core 21JPC (~323 cm core length) also contains dark olive gray silty clay. Two laminated intervals and two massive, bioturbated intervals were identified (Table 4.1). Prominent gray layers occur throughout the core and range in thickness from <1 cm to 2 cm. Laminated interval C in 21JPC overlaps with laminated interval C in 33JPC, but 21JPC contains a lapse in the scanning XRF data in this interval. Core 29JPC (~273 cm core length) contains mostly massive dark, olive gray silty to sandy clay. One distinct laminated interval is visible between 3.70 cm and 87.92 cm, which overlaps with the laminated D intervals of 33JPC and 21JPC. The remainder of the core is bioturbated. Prominent gray layers range in thickness from ~0.5 cm to <3 cm.

**Table 4.1.** Stratigraphic description of sediment cores MV0508-33JPC, -21JPC, and -29JPC.

| Core | Poorly-preserved Laminated Interval Depths (cm) | Well-Preserved Laminated Interval Depths (cm) | Bioturbated Interval Depths (cm) | Core Gap or Unconsolidated Sediment Depths (cm) |
|---|---|---|---|---|
| 33JPC | 0.00 – 5.98 | A 6.00 – 48.78 | 48.80 – 66.18 | |
| | | B 66.20 – 105.30 | 105.32 – 119.06 | |
| | | C 119.08 – 256.44 | 256.46 – 293.98 | |
| | | D 294.00 – 409.78 | | |
| 21JPC | | C 7.80 – 21.86[1]<br>23.36 – 107.98 | 108.00 – 146.40 | 0.00 – 7.78 |
| | | D 146.42 – 272.48 | 272.50 – 322.68 | |
| 29JPC | | D 3.70 – 87.92 | 87.94 – 273.14 | 0.00 – 3.69 |

[1]Lapse in scanning XRF data from 21.88-23.24 cm.

*4.3.2 Bulk Elemental Analyses*

In-situ bulk elemental composition of all cores was determined using an ITRAX X-ray Fluorescence (XRF) Core Scanner (Cox Analytical Instruments) at the Large Lakes Observatory at the University of Minnesota Duluth. All cores were scanned at 0.02 cm resolution with an 8 s count time for core 04BC and a 16 s count time for 33JPC, 21JPC, and 29JPC, using a Cr X-ray tube with a current of 30 kV and a voltage of 20 mA. Raw scanning XRF data were reprocessed using proprietary Q-Spec 8.6.0 software to optimize peak fitting. Elements used in this study are Si, S, K, Ca, Ti, Fe, and Br. Counts were normalized to coherent scattering to account for count offsets between cores (see Appendix C). Bromine was smoothed after normalization to coherent scattering using a 3-point moving average in 04BC and a 2-point moving average in 33JPC, 21JPC, and 29JPC. Cores 33JPC, 21JPC, and 29JPC were sampled at 10 cm intervals and analyzed using ICP-MS and ICP-AES to determine absolute elemental concentrations, which were used to verify scanning XRF results. The details of sampling and analyses for the absolute elemental concentrations are presented in Appendix C.

*4.3.3 Principal component analysis and correlation*

Scanning XRF Si, S, K, Ca, Ti, Fe, and Br counts were standardized to a zero mean and unit variance, then input into principal component analysis of each core using Analyseries (version 2.0.8) (Paillard et al., 1996). These elements were selected because they have relatively high signal-to-noise ratios. Each $T_V$ core was analyzed separately as each captures sediment deposited at different times during the deglacial in different depositional environments. The siliciclastic component was consistently associated with the first principal component (PC1, Table 4.2), and is used in subsequent time series analyses. I note that Br has a relatively high loading in the PC1 of 33JPC (Table 4.2), however Br has very low count rates in section 3 of core 33JPC (<200 counts per 16 s), resulting in low signal-to-noise ratio. Therefore I do not believe the high loading for Br in the PC1 of core 33JPC is meaningful, and conclude that the PC1 of this core represents siliciclastic sediment.

Cores 33JPC, 21JPC, and 29JPC were coarsely stratigraphically correlated using seismic stratigraphy; distinctive intercalations of massive sediment, laminations, and gray layers; and multisensor track density (Behl et al., 2005; Behl et al., 2007; Escobedo, 2009; Hopkins et al., 2006; Hopkins, 2006; Marshall, 2012). I refined stratigraphic correlations using PC1 in well-

preserved, laminated portions of the sediment cores (Appendix C Figures C.3-C.6). Core 33JPC was used as the reference core during correlation. Core 29JPC was rescaled onto the 33JPC depth scale in order to create a consistent composite depth for the correlations. A composite PC1 record was created by splicing the standardized, detrended PC1 of the entire 33JPC core (laminated and bioturbated intervals, 0.14-370.20 cm) to the standardized, detrended PC1 of the laminated interval of 29JPC. Further details of the correlation procedure are presented in Appendix C.

**Table 4.2.** First principal component (PC1) elemental loadings of laminated portions and total variance explained by PC1 for each core.

| Variable[1] | Loading[2] | | | |
|---|---|---|---|---|
| | 04BC PC1 | 33JPC PC1 | 21JPC PC1 | 29JPC PC1 |
| K | **0.47** | **0.53** | **0.55** | **0.55** |
| Ti | **0.46** | **0.53** | **0.51** | **0.54** |
| Si[3] | **0.45** | **0.51** | **0.47** | **0.44** |
| Fe | 0.35 | 0.16 | **0.44** | 0.29 |
| Ca | 0.26 | -0.04 | 0.14 | -0.02 |
| Br | -0.28 | 0.37 | 0.08 | -0.32 |
| S | -0.31 | -0.10 | 0.06 | -0.13 |
| % Variance | 62 | 41 | 43 | 38 |

[1]Each variable has been normalized to coherent scattering. Br has been smoothed using a 3-point moving average in core 04BC and a 2-point moving average in cores 33JPC, 21JPC, and 29JPC. Each element was then standardized prior to the principal component analysis.

[2]Bolded values indicate that a variable has a higher loading than would be expected if each variable were independent of one another. Loadings were bolded if their value was greater than the square root of (1/n), where n = the number of elements used in the principal component analysis.

[3]The Si XRF data in core 29JPC section 1 and section 2 were standardized independently to correct the Si offset in section 2.

### *4.3.4 Stable Isotopes*

Ten cc samples of sediment from high carbonate intervals in 33JPC, 21JPC, and 29JPC were wet-sieved over >63 μm sieves. One to ten specimens of benthic foraminiferal *Uvigerina* and *Bolivina* species, and 2-16 specimens of *Neogloboquadrina pachyderma* (mixed) and *Globigerina bulloides* were picked from the >150 μm size fraction and cleaned following standard procedures. Stable isotope analyses were performed on a ThermoFisher MAT123 stable isotope ratio mass spectrometer coupled to a GasBench-II peripheral in continuous flow mode at

the University of South Florida College of Marine Science Stable Isotope Biochemistry Lab. Measurement followed standard procedures (Burman et al., 2005; Duhr and Hilkert, 2004; Evans et al., 2016; Revesz and Landwehr, 2002; Spötl, 2011; Spötl and Vennemann, 2003), and laboratory reference materials (TSF-1 $\delta^{18}O$ = -2.20 ± 0.06‰, Borba $\delta^{18}O$ = -6.15 ± 0.09‰, LECO $\delta^{18}O$ = -20.68 ± 0.16‰, all calibrated to certified reference materials NBS 19, NBS 18, and LSVEC) were used to normalize measurements to the Vienna Pee Dee Belemnite (VPDB) scale. All oxygen isotope results are reported in the standard delta (δ) notation as per mil relative to the VPDB standard.

*4.3.5 Age Models*

The age model for the Holocene box core 04BC is reported in Hendy et al. (2015). Seismic stratigraphy sequence boundaries, correlated with industry wells in SBB provide initial $T_V$ age estimates for 21JC, 29JC, and 33JC (Hopkins et al., 2006; Marshall, 2012). Methods for the MIS boundary chronostratigraphic framework applied to the suite of cores collected during the 2005 *R/V Melville* SBB cruise are detailed in White et al. (2013). Benthic and planktonic foraminiferal $\delta^{18}O$ values derived from 33JPC, 21JPC, and 29JPC were placed in the composite depth scale (see section 4.3.4). The composite $\delta^{18}O$ record was compared to the LR04 global benthic $\delta^{18}O$ foraminifera stack (Lisiecki and Raymo, 2005) and to the sub-millennial benthic foraminifera $\delta^{18}O$ record of Iberian Margin sediment core MD03-2699 (Voelker et al., 2010) to refine the ages of each core at $T_V$.

Finally, using an annual tuning method, floating annual age models were created for the laminated intervals of each core with the assumption that each maximum PC1 peak is a single year, as observed in the modern SBB sediments (Hülsemann and Emery, 1961). Each gray layer deposit was also interpreted as a single event representing one year. Each PC1 data series was centered to a mean value of zero; the annual cycles were isolated using a Taner bandpass filter in Matlab with the script *tanerfilter.m* (Kodama and Hinnov, 2015) (Appendix C). The bandpass filter frequencies were uniquely determined for each laminated interval. The sediment core depth of each maximum in the bandpassed PC1 series was then identified in Matlab using the script *maxima.m* (Appendix C). Since it is assumed that each maximum represents one year, the total number of maxima in the series represents the total number of years in each respective laminated interval. The depth scale was then converted to a time scale using the Matlab script

*depthtotime.m* (Appendix C). The time series analysis methods require the time series to have a uniform time step, where the spacing between each data point is consistent, however, the thicknesses of each year, and therefore the time steps between each year are variable. To remedy this each PC1 series was interpolated to a uniform time step equal to the mean time step of the entire PC1 series. I determined the error of the floating annual tuning age model method by comparing the absolute and varve chronology of 04BC with the annually-tuned age model for core 04BC, and by comparing the independent floating annually-tuned age models of the laminated intervals of 33JPC, 21JPC, and 29JPC that are well-correlated and well-preserved. Uncertainties in the annual tuning are discussed in section 4.5.3.

*4.3.6 Time Series Analysis*

Each PC1 time series was pre-whitened by removing a LOESS-smoothed curve from each series. The LOESS-smoothed curve was computed using Matlab's *smooth.m* using a sliding window set to half the length of the series. Power spectra were computed for each annually tuned, pre-whitened PC1 series using the multi-taper method with *pmtm.m*. I used red noise hypothesis testing to identify statistically significant frequencies. The classical red noise of each PC1 series was determined with *Rednoise.m* (Kodama and Hinnov, 2015). Prior to red noise hypothesis testing the annual frequency was estimated and removed from each series using the Matlab script *deharm.m* (Appendix C) so that it would not be included in the hypothesis testing and modeled as noise. Evolutionary power spectra were created for each PC1 series using the Matlab script *evofftnew.m* (Appendix C) with a sliding window and a time step equal to the mean time step used during creation of the annual age model. The 1-year period was removed from the 04BC PC1 series prior to computation of its evolutionary power spectrum for comparison with the ONI, but no periodicities were removed from the $T_V$ cores prior to the computation of the evolutionary power spectra.

A power spectrum for the ONI was estimated to compare with the precipitation-driven river runoff record from SBB. Monthly sea surface temperatures from the Niño 3.4 region (Rayner et al., 2003) were obtained from the U.S. NOAA ESRL Physical Sciences Division webpage (http://www.esrl.noaa.gov/psd/gcos_wgsp/Timeseries/Nino34/index.html, accessed 11 July 2017). The ONI was then calculated according to the standard procedure (Lindsey, 2013). The half-year periodicity was removed from the series prior to red noise hypothesis testing. An

evolutionary power spectrum was also created for the ONI series using a sliding 10-year window and a monthly time step. No periodicities were removed prior to computation of the evolutionary power spectrum.

## 4.4 Results

### *4.4.1 Test of annual tuning method of the 20$^{th}$ century*

A test of the Taner bandpass filter annual tuning method, and the identification of the ENSO signal in SBB sediments was conducted using PC1 from 04BC and compared to the instrumental ONI record. The annual tuning method generated 149 years in the upper 44 cm of 04BC compared to 139 years estimated using the established age model (Hendy et al., 2015), an overestimation of 10 years or 7%. The instrumental ONI record is characterized by significant periodicities ranging from ~2-6 years (Figure 4.3, ii). Over the same time period, the PC1 in 04BC is characterized by similar interannual periodicities that fall within and near the ~2-6-year ONI periodicity range, specifically: 5.3, 3.5, 2.4, 2.3 and 2.1 (Figure 4.3, i). PC1 signal strength varies over time, with strong periodicities occurring from years 5-10 (~A.D. 2005.5-2001), 20-30 (~A.D. 1993.5-1981.5), 55-70 (~A.D. 1959-1945), 110-120 (~A.D. 1905-1897.5), and 130-145 (~A.D. 1890-1876) (Figure 4.3, iii). Many occurrences of strong periodicities in the PC1 evolutionary power spectrum coincide with similar intervals of strong periodicities in the ONI evolutionary power spectrum (Figure 4.3, iv) around A.D. 1880, 1955, 1980, and 2005. The 04BC PC1 series captures strong, lower frequency ENSO periodicities but not weaker, higher frequency ENSO periodicities (2-3 years) that are by contrast prevalent in the ONI evolutionary power spectrum.

### *4.4.2 Foraminiferal oxygen isotopes in Termination V sediments*

Planktonic and benthic foraminiferal $\delta^{18}O$ values of 1.3-3.1‰ and 2.9-4.2‰, respectively at 450-540 cm composite depth are typical of SBB glacial values. A synchronous positive and negative shift of ~2.3‰ for benthic and 1.2‰ for planktonic $\delta^{18}O$ values occurs between 425 and 450 cm composite depth, respectively (Figure 4.4). Above 450 cm composite depth, the highest $\delta^{18}O$ values (~1.8-2.2‰ planktonic and 3.4-3.2‰ benthic) are generally recorded during bioturbated intervals, while the lowest $\delta^{18}O$ values (~0.2 and 2.5‰, respectively) occur near the bases of laminated intervals C and D (Figure 4.4, iii). There is a long-term increase in $\delta^{18}O$

values of ~1.5‰ in planktonic foraminifera and ~0.6‰ in benthic foraminifera from 425 cm composite depth to the top of the record.

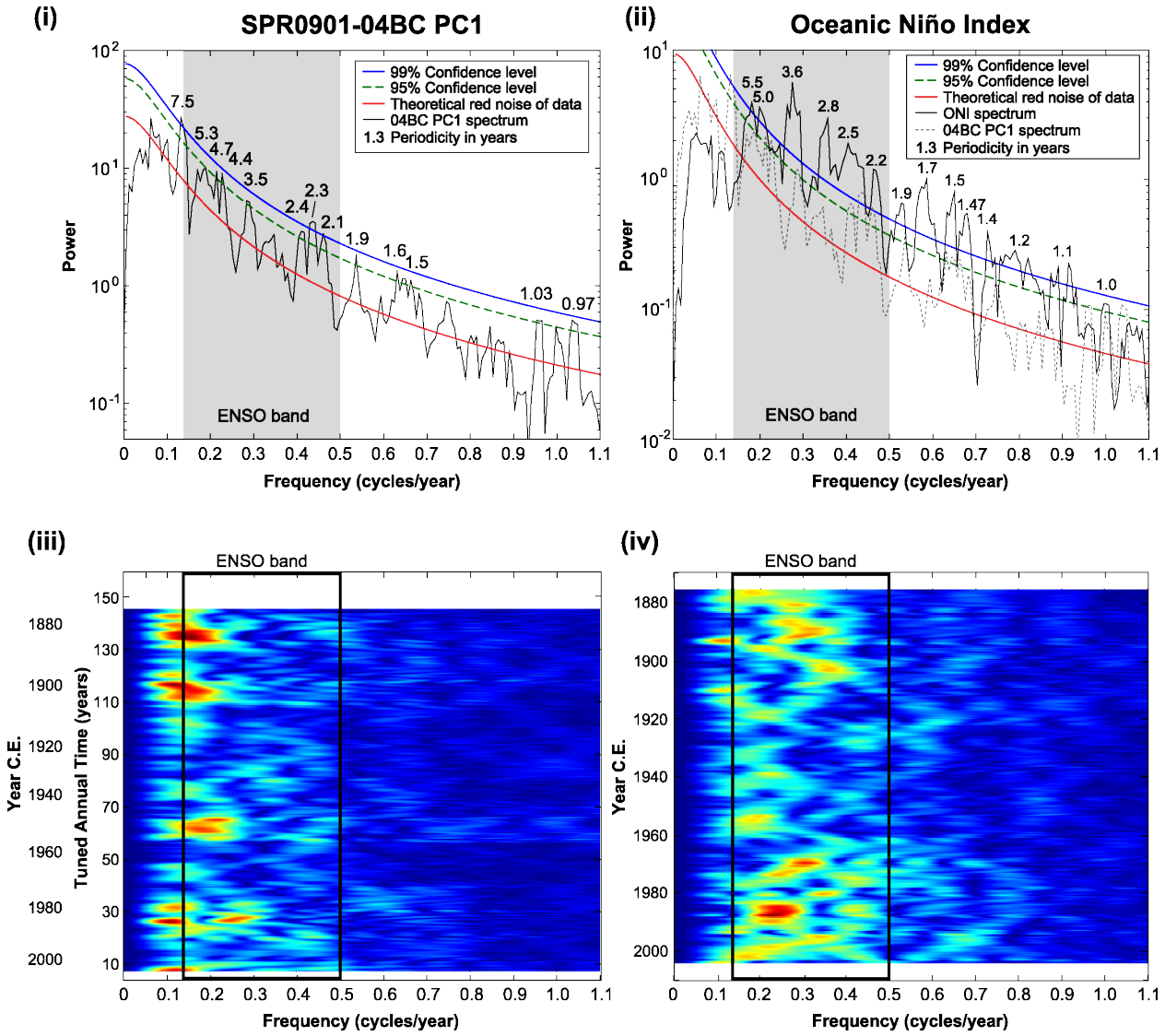


**Figure 4.3.** Annually tuned PC1 time series analysis of core SPR0901-04BC (04BC; left column) compared to the Oceanic Niño Index (ONI; right column) from A.D. 1870 to 2009.
2π Multi-taper Method (MTM) power spectrum of (i) annually tuned, pre-whitened 04BC PC1 time series and (ii) ONI time series (black lines) with the annual frequency removed from the series to allow for red noise hypothesis testing. 95% and 99% confidence levels shown with significant (≥95% confidence level) periodicities labeled. The 04BC PC1 power spectrum is plotted as a gray dotted line in panel ii and has been lined up using the confidence levels, not the power. Evolutionary power spectrum of the (iii) pre-whitened, annually tuned 04BC PC1 and (iv) ONI time series with a 10-year sliding window without removal of the annual frequency. Power is not normalized per spectrum for either series, with the highest power in dark red and the lowest in dark blue. Shaded gray box and black rectangle encompasses and represents the frequency bandwidth range of El Niño-Southern Oscillation (ENSO). The approximate calendar years of the 04BC PC1 time series (Hendy et al., 2015) are shown for comparison with tuned annual time and the ONI record. The ONI was calculated from the Niño 3.4 region monthly sea surface temperature record obtained from the U.S. NOAA ESRL Physical Sciences Division webpage (http://www.esrl.noaa.gov/psd/gcos_wgsp/Timeseries/Nino34/index.html, accessed 11 July 2017).

*4.4.3 Lithogenic components of the Termination V sediments*

The lithogenic input of $T_V$ sediments in SBB is assessed from PC1 of the scanning XRF and quantitative elemental concentrations. While variable, a 40-point moving average of the composite PC1 record is generally low from ~80-105 cm, 120-210 cm, and 320-340 cm (Figure 4.5, iii). Low values of PC1 represent low siliciclastic elemental counts, which are confirmed by the quantitative elemental concentrations. PC1 scores are elevated within gray layers (Figure 4.5, iii-iv), which are found clustered at depths 35-45 cm, 170-180 cm, 210-215 cm, 300-312 cm, 350-355 cm, and 370 cm. The composite PC1 series generally follows the same trends as the quantitative Ti and K concentrations in 33JPC, 21JPC, and 29JPC (Figure C.7), and indicates that the scanning XRF technique accurately captures the variability in elemental composition of the sediment cores.

*4.4.4 Time series analysis of the Pleistocene precipitation proxy*

The annual tuning method consistently resolves the greatest number of years in 33JPC (Appendix C), which contains the best preserved laminations over the length of the core suite. Therefore I have restricted time series analysis to 33JPC as follows.

Laminated interval A annual tuning resulted in 495 years and an average sedimentation rate of 86 cm/kyr. The interval A PC1 series generally remains around zero except for a decrease to -2 around 50 cm (Figure 4.6, i and ii). The annual signal is present throughout interval A, except for years 40-60 (Figure 4.6, iv), with the highest power from ~60-220 and 460-480 years. Strong significant (>95% confidence level) periodicities that fall within the ENSO band range from 2-3-year cycles. Significant interdecadal periodicities of ~18 years also occur in this interval (Figure 4.6, iii). ENSO periodicities are present throughout the record, except for years 40-60, with the most persistent and highest power ENSO band periodicities ranging from 4-7-year cycles and occurring over years 60-250 and 350-380 (Figure 4.6, iii and iv). Shorter ENSO periodicities are stronger and more persistent from year ~420 through year 480.

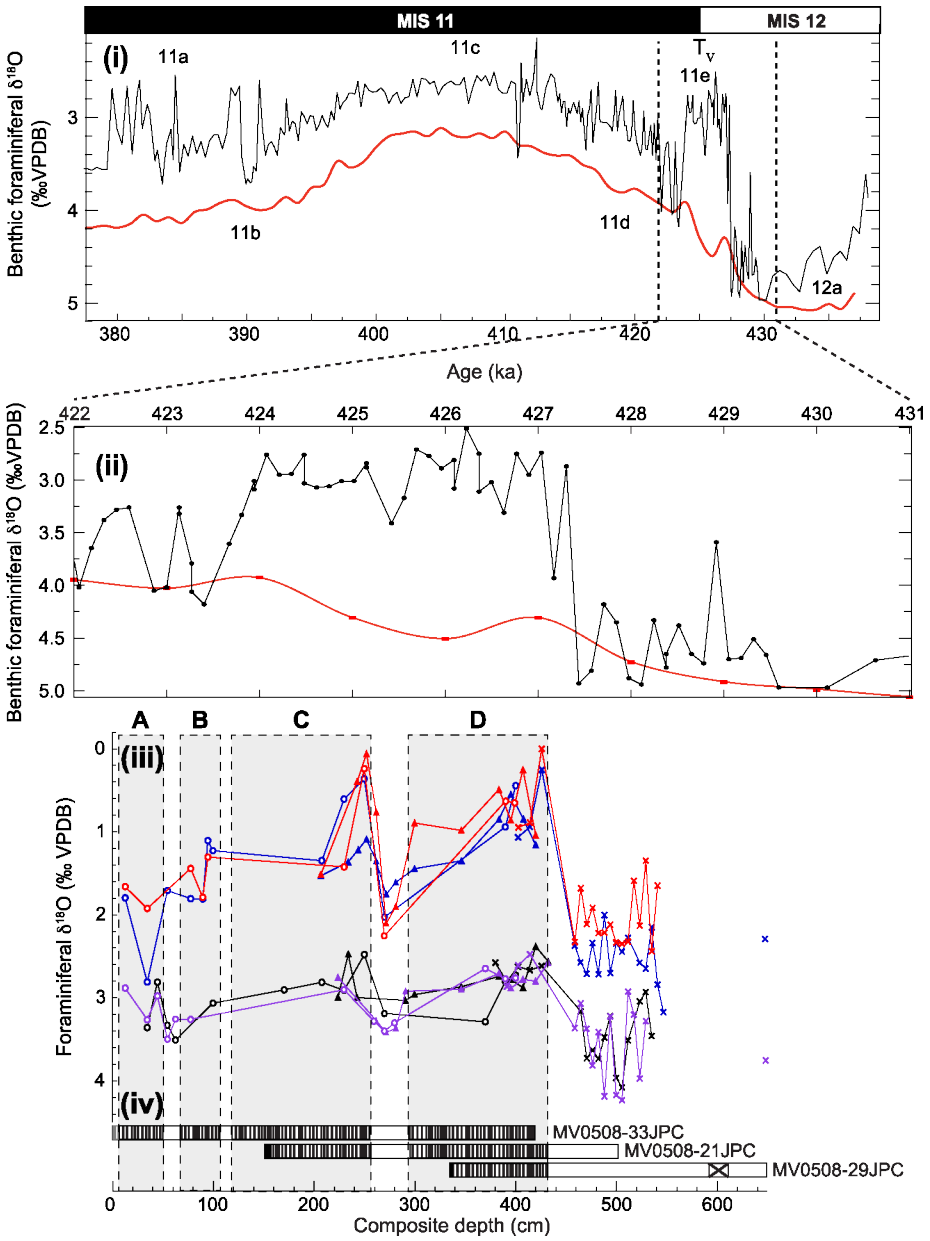


**Figure 4.4.** Oxygen isotope stratigraphy of Termination V ($T_V$) showing estimated age of the core suite. (i) Stratigraphy for the interval from 376 to 438 ka with the global benthic foraminiferal $\delta^{18}O$ stack (‰ VPDB thick red line) (Lisiecki and Raymo, 2005) and the benthic foraminiferal $\delta^{18}O$ record from sediment core MD03-2699 from the Iberian Margin (‰ VPDB, thin black line) (Voelker et al., 2010). (ii) Stratigraphy for the interval from 422 to 431 ka with the global benthic foraminiferal $\delta^{18}O$ stack (thick red line) (Lisiecki and Raymo, 2005) and the benthic foraminiferal $\delta^{18}O$ record from sediment core MD03-2699 from the Iberian Margin (thin black line) (Voelker et al., 2010). (iii) Foraminiferal $\delta^{18}O$ values (‰ VPDB of *G. bulloides* (red line), *N. pachyderma* (mixed) (blue line), *Uvigerina* spp. (violet line) and *Bolivina* spp. (black line) for the suite of cores; MV0508-33JPC (open circles), MV0508-21JPC (solid triangles), and MV0508-29JPC (crosses) against composite core depth. (iv) Sediment core fabric descriptions for each core with banding denoting laminations. Gray shaded boxes represent laminated intervals A-D. Marine Isotope Stage (MIS) and substage nomenclature after Railsback et al. (2015). Termination V identification after Lisiecki and Raymo (2005).

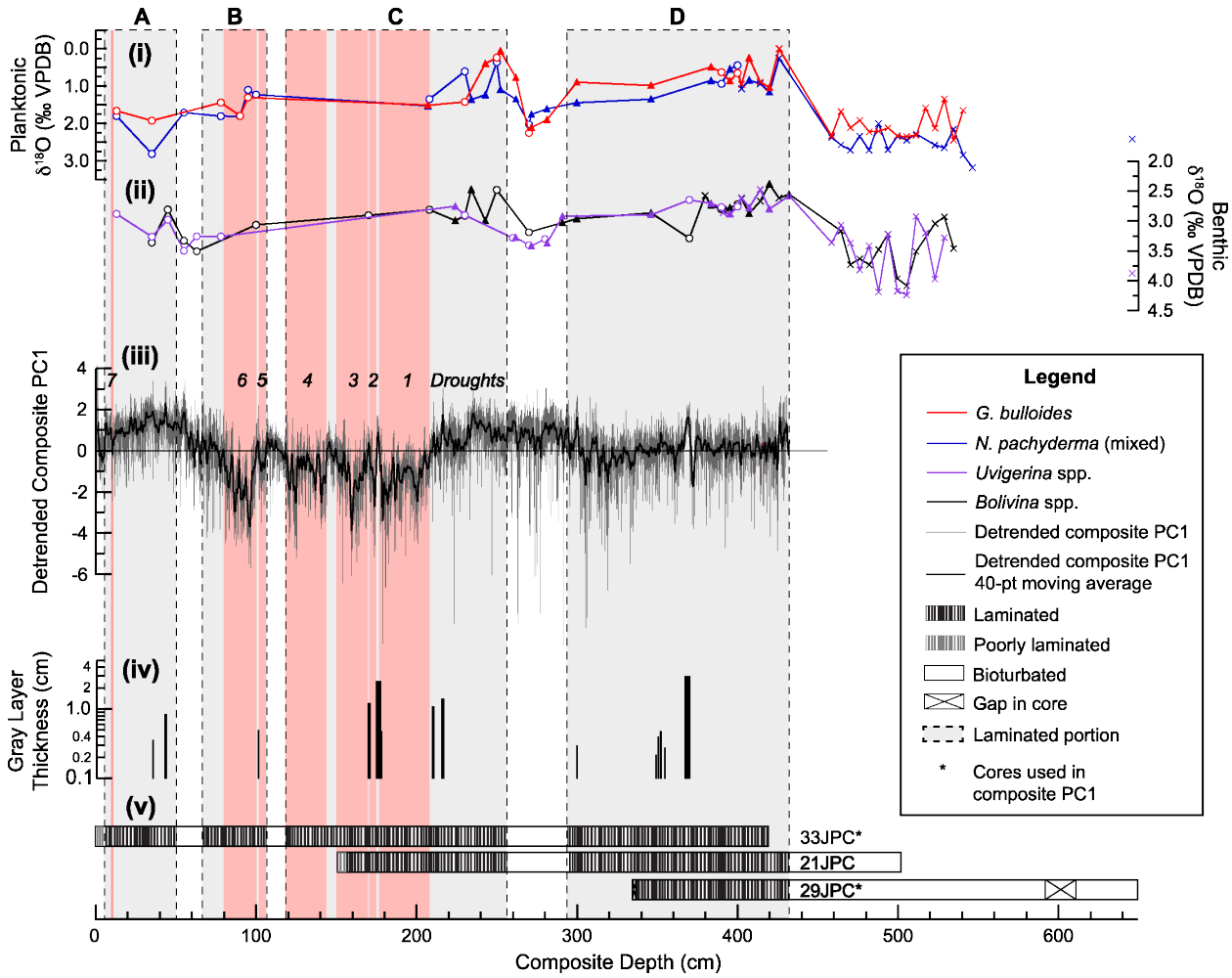


**Figure 4.5.** Foraminiferal $\delta^{18}O$ data (‰ Vienna Peedee belemnite (VPDB)) for the core suite: MV0508-33JPC (open circles), -21JPC (filled triangles), and -29JPC (crosses) against composite core depth. (i) *G. bulloides* (red line) and *N. pachyderma* (mixed) (blue line) (ii) *Uvigerina* spp. (violet line) and *Bolivina* spp. (black line). (iii) Linearly detrended composite (33JPC and 29JPC) PC1 (gray line) with smoothing (black line, 40-point moving average) from scanning XRF elemental counts. (iv) Gray layer thickness and position in sediment core 33JPC. (v) Sediment core fabric descriptions with banding denoting laminations. Gray shaded boxes represent laminated intervals A-D. Red shaded boxes denote periods of drought.

Laminated interval B annual tuning resulted in 430 years with an average sedimentation rate of 91 cm/kyr. The interval B PC1 series drops below zero from years ~150-400 (Figure 4.6, v). The annual signal in interval B has the highest power from years 50-100 and 360-410, but low power in the remainder of the interval (Figure 4.6, viii). Red noise hypothesis testing of the interval B power spectrum reveals significant periodicities within the ENSO band, with 2-3-year periodicities having the greatest significance (Figure 4.6, vii). There are no significant periodicities in the interdecadal band (Figure 4.6, iii). Strong cyclicity within the ENSO band

occurs from years ~25-160, particularly for periodicities between 2.5-7 years, with weaker, infrequent cyclicity from years 160-420 (Figure 4.6, v ii and viii).

Laminated interval C annual tuning resulted in 1,628 years with an average sedimentation rate of 84 cm/kyr. The PC1 series in interval C is below zero from years 0-1000, with many notable negative intervals <-2 (Figure 4.7, i). The annual signal has the highest power from years 325-425 and year 850 through to the end of the interval (Figure 4.7, iv). Periodicities ranging from 2-4.2 years have the most significance within the ENSO band (Figure 4.7, iii), with other significant cycles between 1.1-2- and at 162-year periodicities. Periodicities within the ENSO band have the highest power from years 325-425, 825-950, 1125-1325, and 1375-1500 in interval C (Figure 4.7, iii and iv).

Laminated interval D annual tuning resulted in 1,446 years with an average sedimentation rate of 81 cm/kyr. PC1 values generally remain close to zero except for a drop below -2 around year 125 (Figure 4.7, v). The annual signal maintains a moderate-to-high power throughout interval D (Figure 4.7, viii). Significant periodicities occur within the ENSO band, with the greatest significance in the 2-3.3-year periodicities (Figure 4.7, vii), which remain moderate to strong in power throughout the interval (Figure 4.7, viii). Interval D also contains a significant longer periodicity of 125 years (Figure 4.7, vii).

When combined, the four laminated intervals of 33JPC record a persistent annual signal through interval D (Figure 4.7, vii) that continues into interval C, but loses power around year 800 in interval C (Figure 4.7, iv). The power of the annual signal remains low through the remainder of interval C, but increases in interval B from years 100-50 (Figure 4.6, viii) and maintains moderate-to-high power throughout interval A (Figure 4.6, iv). The strongest periodicities within the ENSO band occur when the annual signal is also strong. Significant ENSO band periodicities persist throughout interval D, but during interval C the ENSO periodicities become notably absent at year 850, and these absences continue through interval B.

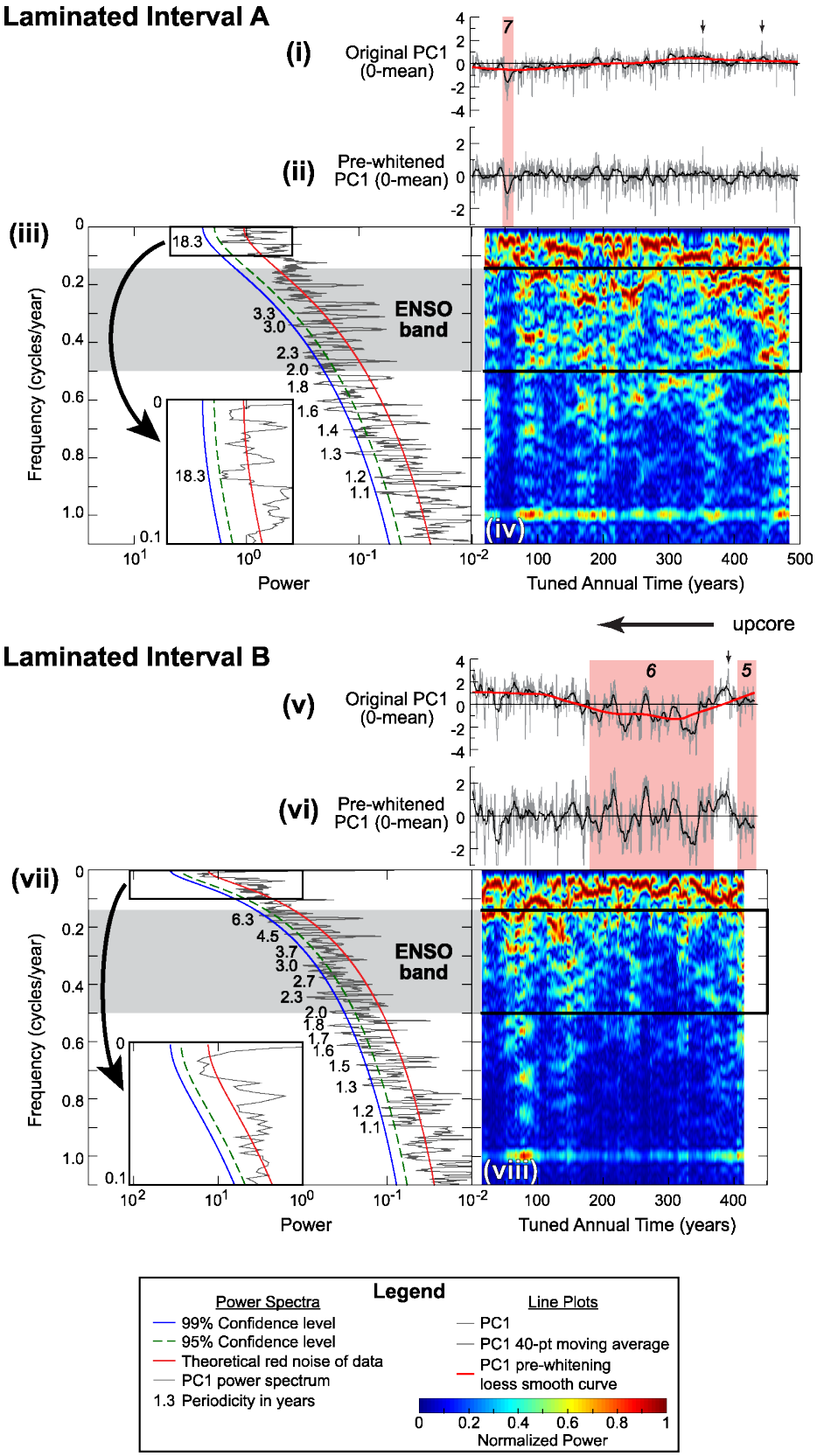


**Figure 4.6.** Comparison of annually tuned time series analyses of core MV0508-33JPC laminated intervals A and B.

**Figure 4.6 (*continued*).** Laminated interval A spans 495 years and laminated interval B spans 430 years: (i and v) Annually tuned PC1 time series (gray line) smoothed with a 40-point moving average (black line) and loess smoothing curve (red line) that is subtracted during pre-whitening. (ii and vi) Pre-whitened annually tuned PC1 time series (gray line) with smoothing (black line), and (iii and vii) 3π and 2π Multi-taper Method (MTM) power spectrum, respectively, of the pre-whitened annually tuned PC1 time series with the annual frequency removed from the series to allow for red noise hypothesis testing. Theoretical red noise of data is indicated by the red line. 95% and 99% confidence levels (blue and green lines) shown in legend with significant (≥95% confidence level) periodicities labeled. The inset expands the graph frequencies of 0-0.1 cycles/year. (iv and viii) Evolutionary power spectrum of the pre-whitened annually tuned PC1 with a 30-year sliding window without removal of the annual frequency. Power is normalized per spectrum, with the highest power in dark red and the lowest in dark blue. Shaded gray box and black rectangle encompass the frequency bandwidth range of El Niño-Southern Oscillation (ENSO). Pink shaded boxes denote periods of drought observed in the composite PC1 record.

**Figure 4.7 (*following page*).** Comparison of annually tuned time series analyses of core MV0508-33JPC laminated intervals C and D. Laminated interval C spans1,628 years and laminated interval D spans 1,446 years: (i and v) Annually tuned PC1 time series (gray line) smoothed with a 40-point moving average (black line) and loess smoothing curve (red line) that is subtracted during pre-whitening. (ii and vi) Pre-whitened annually tuned PC1 time series (gray line) with smoothing (black line), and (iii and vii) 6π Multi-taper Method (MTM) power spectrum of the pre-whitened annually tuned PC1 time series with the annual frequency removed from the series to allow for red noise hypothesis testing. Theoretical red noise of data is indicated by the red line. 95% and 99% confidence levels (blue and green lines) are shown with significant (≥95% confidence level) periodicities labeled. The inset expands the graph frequencies of 0-0.1 cycles/year. (iv and vii) Evolutionary power spectrum of the pre-whitened annually tuned PC1 time series with a 50-year sliding window without removal of the annual frequency. Power is normalized per spectrum, with the highest power in dark red and the lowest in dark blue. Shaded gray box and black rectangle encompass the frequency bandwidth range of El Niño-Southern Oscillation (ENSO). Pink shaded boxes denote periods of drought observed in the composite PC1 record.

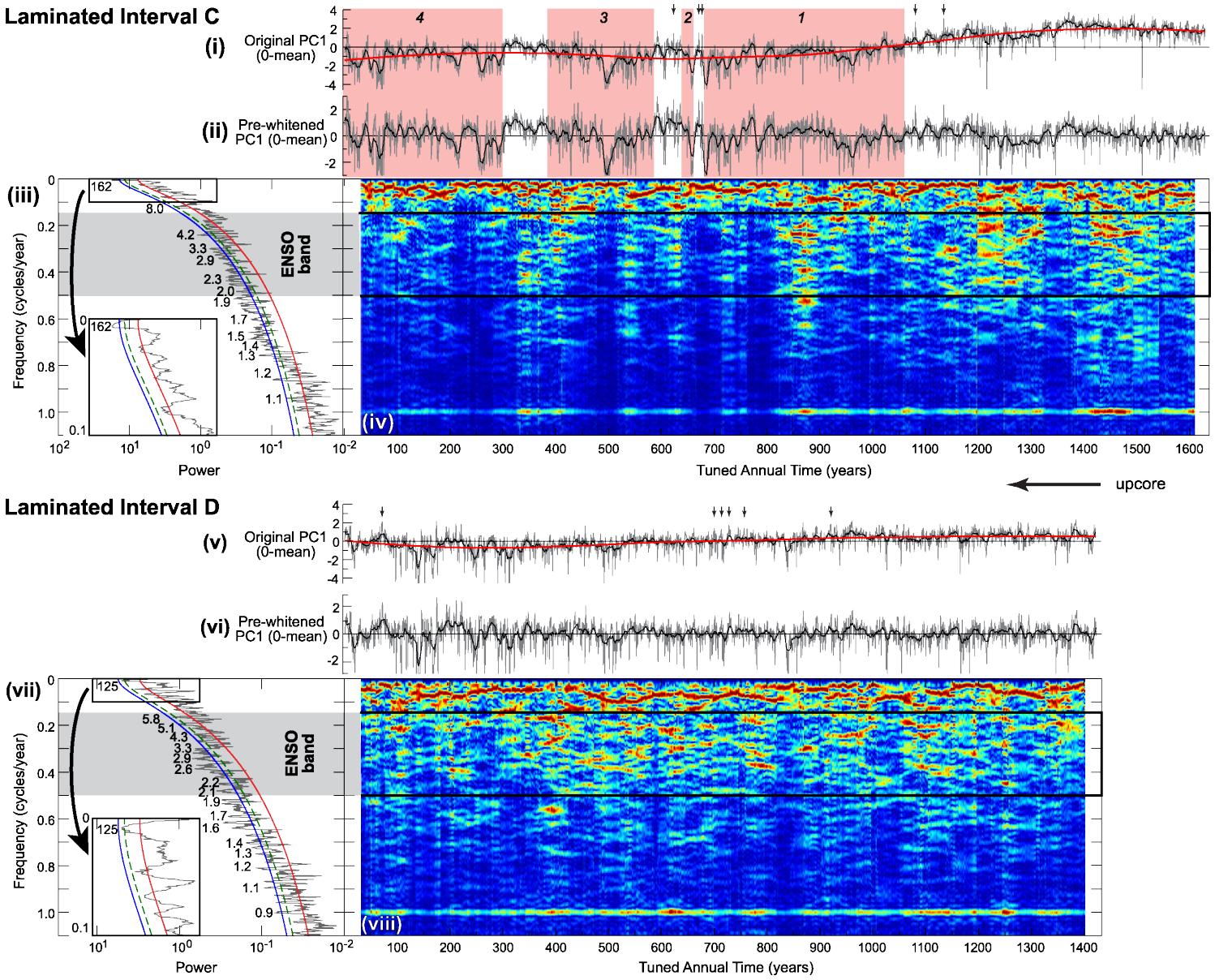


**Figure 4.7.** Comparison of annually tuned time series analyses of core MV0508-33JPC laminated intervals C and D.

## 4.5 Discussion

### *4.5.1 Pleistocene core chronology*

Benthic and planktonic $\delta^{18}O$ results support the SBB seismic stratigraphic boundaries that identify the glacial-interglacial transition between MIS 12 and 11 (Hopkins et al., 2006; Marshall, 2012) indicating that 33JPC, 21JPC, and 29JPC capture $T_V$. During $T_V$, the transition from glacial maximum sea level lowstand to full interglacial highstand occurred over 25 kyr, a longer deglaciation relative to 11 kyr transition associated with $T_I$ (Lambeck and Chappell, 2001; Rohling et al., 2010). The unusual length of the $T_V$ deglacial has been attributed to the two insolation maxima that influenced climate at this time (Rohling et al., 2010). Near-glacial conditions within the bioturbated portion of 29JPC are indicated by $\delta^{18}O$ values in planktonic (~2.3‰) and benthic (~3.6‰) foraminifera (Figure 4.4) during MIS 12, similar to MIS 2 values recorded at ODP site 893 (Hendy and Kennett, 1999, 2000, 2003). This suggests that 29JPC, 21JPC, and 33JPC were deposited during the first, weaker insolation maximum of $T_V$ and the subsequent decline in insolation.

Similar to the Bølling/Allerød and the Younger Dryas during $T_I$, $\delta^{18}O$ variations record centennial-scale abrupt climate changes during $T_V$. The abrupt and large negative shifts in both planktonic and benthic $\delta^{18}O$ prior to laminated intervals D and C suggest rapid warming of SBB waters, and the subsequent positive shifts suggest gradual cooling. Near-glacial conditions were succeeded by abrupt warming at the inception of laminated interval D, as indicated by decreased $\delta^{18}O$ values (~2.1‰ in planktonic and ~1.0‰ in benthic foraminifera; Figure 4.4) occurring over a timespan of ~300-400 years. Subsequent gradual cooling over the next ~1,600 years is indicated by increased planktonic (~1.8‰) and benthic foraminifera (~0.6‰) $\delta^{18}O$ values. Rapid warming occurred again over the next 200-300 years just prior to laminated interval C, with decreases of $\delta^{18}O$ planktonic (~1.6‰) and benthic (~0.7‰) foraminiferal $\delta^{18}O$. This was followed by step-wise cooling through the rest of the record, with increased planktonic $\delta^{18}O$ values (~1.6‰) and benthic values (~0.8‰) over ~2,700 years (Figure 4.4).

The rapid climate change events recorded in SBB $\delta^{18}O$ are likely coincident with events observed in Atlantic Ocean sediment cores. Foraminiferal $\delta^{18}O$ and ice rafted debris records from ODP site 980 in the North Atlantic indicate that two short duration, rapid warming events occurred during $T_V$, which are similar in their relative timing and duration to the SBB events (Oppo et al., 1998). Benthic foraminiferal $\delta^{18}O$ from sediment core MD03-2699 in the eastern

North Atlantic along the Iberian Margin also records abrupt warming during $T_V$ (Voelker et al., 2010). Although the SBB $T_V$ chronology is limited both due to the short sediment record and the absence of absolute age markers, the similarity of these rapid warm events suggests a similar climate coherence between the North Atlantic and North Pacific, as has been observed for MIS 3 (Hendy and Kennett, 1999).

*4.5.2 Influences on PC1*

Precipitation totals in Southern California capture the expression of ENSO and PDO variability and drive river runoff locally (Inman and Jenkins, 1999; Nezlin et al., 2005; Warrick and Farnsworth, 2009b). The elemental composition of SBB sediment can be used as a proxy for river runoff (Hendy et al., 2015) as precipitation events ≥0.25 cm cause sediment plumes in SBB (Nezlin et al., 2005). In the 20$^{th}$ century, increased relative concentration of siliciclastic sediments are associated with wet El Niño years and river runoff into SBB, while decreased siliciclastic sediments are associated with drought (Figure C.1) (Hendy et al., 2015). The first principal component of the XRF elemental data from the $T_V$ cores presented in this study has high loadings for elements K, Ti, and Si, similar to 20$^{th}$ century sediments (Table 4.2) (Hendy et al., 2015). These elements are associated with siliciclastic sediment derived from onshore river catchments. Therefore increased southern California precipitation during $T_V$ is indicated by higher PC1, while decreases mark droughts. Over $T_V$, PC1 records constant precipitation in southern California during interval D, followed by increased precipitation in the beginning of interval C (Figure 4.5iii). PC1 indicates drought conditions in intervals C and B, followed by maximum precipitation and river runoff in interval A. Rapid increases in PC1 are indicative of flooding events.

Although terrigenous lithogenic sediment is the dominant component of sediment flux to SBB, comprising 65-90% of the annual contribution (Thunell et al., 1995), PC1 is also influenced by the biogenic sediment input that is responsible for much of the remaining contribution. However, the same climate phases that drive increases(decreases) in biogenic sedimentation also cause independent decreases(increases) in PC1. For example, during El Niño events reduced coastal upwelling of nutrient-rich water lowers the biogenic contribution to SBB sediments (Kincaid et al., 2000), while at the same time precipitation driven river runoff increases the lithogenic component. Both lead to increased PC1 loading. Nevertheless, dilution

by biogenic sediments cannot drive decreases in PC1 in the laminated intervals of the sediment cores due to the low relative contribution of the biogenic component to SBB sediment flux. Additionally, loading in PC1 is predominantly driven by changes in K, Ti, and Si, elements associated with siliciclastic sediments. In sum, I attribute decreases in PC1 within the laminated intervals to reductions in precipitation.

Over centennial to millennial time scales, changes in siliciclastic sediment input into SBB could also result from other processes that influence the lithogenic sediment flux. During recent glacial lowstands, the Santa Clara River discharged considerable sediment southward into Santa Monica Basin (SMB) via Hueneme Canyon, potentially by-passing SBB altogether, as indicated by high sedimentation rates and turbidite deposition in SMB (Normark et al., 2006; Romans et al., 2009). However prior to MIS 10, seismic stratigraphic evidence suggests that the Anacapa ridge tectonic high, located between the Channel Islands and the mainland, blocked southward sediment deposition into SMB (Normark et al., 2006). Therefore I do not anticipate a change in sedimentation rate or relative decrease in siliciclastic sediment throughout deglacial record of $T_V$, as the Santa Clara River discharged sediment directly into SBB prior to MIS 10.

Bathymetric changes due to eustatic sea level rise during $T_V$ and local tectonics could also affect sediment deposition at the core locations. More accommodation space was created on the widening shelf between the core sites and the mainland as sea level rose that would gradually decrease detrital sedimentation on the MCT. Furthermore, the MCT anticline was growing very gradually over the last ~400 ka (Marshall, 2012), reducing sediment accommodation space and even causing erosion of sediment during sea level lowstands. However, I do not observe any sedimentological indicators of hiatuses in the cores used in this investigation that would indicate substantial syn-depositional local tectonic movement. Therefore bathymetry changes cannot account for declines in siliciclastic sedimentation, which are indicated by rapid and relatively short-lived decreases in PC1.

### *4.5.3 Fidelity of annual tuning method and relative contribution of siliciclastic sediment in SBB as a hydroclimate proxy*

Several criteria need to be met to assess interannual hydroclimate variability. First, a proxy for precipitation is needed that is sampled more frequently than once per year. Second, the age model must be annually resolved to enable determination of sub-decadal frequency

variability. I used a Taner bandpass tuning method to generate a computational, annually-scaled age model on identified annual sedimentary couplets in 20$^{th}$ century laminated SBB sediments (Biondi et al., 1997; Soutar and Crill, 1977). This method of determining a 20$^{th}$ century annual age model produced 10 extra years (7% overestimation) compared to the Hendy et al. (2015) core 04BC age model that employed known sedimentary events. However in a longer duration age model comparison, Schimmelmann et al. (2006) underestimated years in visual varve-counting of X-radiographs of SBB sediment cores by 30% relative to the radiocarbon chronology over 1,550 years (Hendy et al., 2013). This comparison of radiocarbon and varve-counting chronologies in SBB revealed a systematic undercounting of varves that results in the average loss of 1 year in every 3.35 years (Hendy et al., 2013). The loss of the varved signal could result from erosion during downslope movement, loss of one depositional component of the varve, e.g., from suppressed siliciclastic sedimentation during droughts, and/or poor preservation of laminations (Hendy et al., 2013). Thus up to 30% of annual couplets may be undercounted due to influences from depositional processes, climate forcing, and preservation. Therefore I estimate +7% to -30% error in the number of years obtained by the annual tuning method for SBB sediment.

To further assess the accuracy of the annual tuning method, I compared the number of annual years resolved between correlated laminated intervals in the $T_V$ cores (Appendix C), which revealed a 25% maximum discrepancy in number of years obtained by annual tuning (Table C.3, Figure C.8). These discrepancies can be attributed to variable sedimentation rates between the cores sites due to their position relative to river mouths and with bathymetry. For example, the most easterly core, 33JPC, has a higher sedimentation rate, producing thicker individual laminations and more years resolved over the same correlated interval as compared to 21JPC and 29JPC, which have lower sedimentation rates (Section 4.4). Because the resolution of the XRF core scanner is 0.02 cm, this means that at a lower sedimentation rate, thin laminations will be more difficult to measure and the tuning method could fail to count years.

Years missed by the annual tuning method could impact the determination of precipitation recurrence intervals, resulting in higher frequency periodicities. If the missed time is the result of reduced deposition of the siliciclastic component (PC1) during drought, then precipitation events would artificially appear to occur more frequently. Reduced deposition and potentially missing annual couplets are expected to occur only during severe, prolonged

droughts. Furthermore, reduced deposition would not be continuous throughout the drought event. For example, in the historical core 04BC precipitation record, deposition of the siliciclastic component continues to occur through several droughts, although PC1 does decline during these events (Hendy et al., 2015). Importantly, PC1 in 04BC records historical El Niño events that occur during droughts, such as the A.D. 1951-1952 event, therefore I have confidence in the ability of PC1 to record ENSO events, even during drought.

Times series analysis of 04BC PC1 and the ONI (Figure 4.3) demonstrates similar clustering of periodicities (e.g., around 2.3, 3.5, and 5 years). Notable differences between the spectra, particularly at the shorter ENSO periodicities, suggest that PC1 does not record high frequency ENSO variability. This is likely because river runoff requires a threshold rainfall ≥0.25 cm from precipitation events before a sediment plume enters SBB (Nezlin et al., 2005). If El Niño events are not of sufficient strength to influence the eastern Pacific and generate enhanced precipitation in southern California, then they will not be recorded by PC1. Furthermore, sediment deposition occurs during transport through the river catchments and across the continental shelf prior to deposition in SBB, which results in attenuation of river sediment plumes and the PC1 signal (Soutar and Crill, 1977; Warrick and Farnsworth, 2009a). PC1 does appear to capture the strong, longer ENSO periodicities (>3 years) observed in the ONI (Figure 4.3, iii-iv). In sum the ability of the SBB precipitation proxy to capture ENSO and other climate variability is limited to strong El Niño events that have longer recurrence intervals.

### *4.5.4 Southern California hydroclimate during $T_V$*

The records suggest that the hydroclimate of southern California during $T_V$ was variable and influenced by ENSO-like conditions. Similar to the modern and Holocene hydroclimate records (Hendy et al., 2015; Heusser et al., 2015), southern California was susceptible to extreme precipitation events that likely resulted in severe flooding, and to prolonged periods of drought. The hydroclimate similarities between $T_V$ and the Holocene suggest interannual precipitation patterns that impact southern California during warm climate states are persistent and have been since at least $T_V$ during mid-Pleistocene time.

Extreme precipitation events have also been recorded in SBB during the Holocene, notably the historical Great Flood of 1861-1862, which flooded California's Central Valley. These flood events may be the product of series of atmospheric river storms that impact southern

California multiple times within a single year, involving an intense amount of precipitation in a short amount of time. This scenario led to the Great Flood of 1861-62, which is recorded by a ~0.7 cm thick gray layer in SBB sediments (Napier and Hendy, in press). The floods are preserved as thick, fine-grained gray layers within the Holocene SBB sediment record. Analogous thick gray layers within the $T_V$ sediment record (Figure 4.5) indicate that extreme precipitation events are a persistent feature of southern California hydroclimate. The amount of precipitation that generated the $T_V$ flood deposits was likely greater than that which fell during 1861-62, especially in the case of the compacted 3 cm thick flood layer in laminated interval D. The $T_V$ records suggest that these extreme flood events do not have a consistent recurrence interval; instead long periods (>600 years) occur during which flood deposits are absent, and short, 50-60 year periods are observed during which multiple extreme flood events occur (Figures 5-6).

The PC1 reconstruction also indicates that southern California experienced intervals of drought during $T_V$. Seven sustained, decadal-to-centennial droughts, from ~10-380 years in duration, occurred over the ~2,400 years represented by laminated intervals C-A (Figure 4.5). Extended periods of aridity, lasting centuries to millennia, were also recorded in MIS 11e lake deposits in New Mexico, within the American Southwest (Fawcett et al., 2011). These arid intervals have been associated with decreased winter precipitation, as well as reduction in the strength of the North American monsoon leading to less summer precipitation (Cisneros-Dozal et al., 2014; Fawcett et al., 2011).

Multi-decadal droughts also occurred in southern California during the Medieval Climate Anomaly between A.D. 860-1040, 1130-1170, 1290-1310, and 1420-1460 (Heusser et al., 2015). These droughts were 30-180 years in duration, similar in length to the $T_V$ droughts. Dry conditions during the Medieval Climate Anomaly have been recorded by precipitation proxies throughout western and central North America and have been linked to persistent La Niña-like conditions in the Pacific (Graham et al., 2007 and references therein). Such prolonged droughts have not been observed in southern California in the modern instrumental period, however both SBB $T_V$ and Holocene records imply that multi-decadal drought is a natural and persistent climate phenomena in this region.

*4.5.5 Interannual precipitation variability during $T_V$*

Robust precipitation periodicities that fall within the modern ENSO bandwidths are recorded by the precipitation proxy PC1, and suggest that an ENSO-like climate pattern impacted precipitation in southern California during $T_V$. However, the PC1 power spectra suggest ENSO-like precipitation variability was absent from southern California during the seven decadal-to-centennial droughts recorded in laminated intervals C-A (Figures 5-6). The loss of this ENSO band variability could be caused by: 1) persistent La Niña conditions, 2) changes in the spatial pattern or type of interannual El Niño-like event (e.g., conventional eastern tropical Pacific El Niño versus central tropical Pacific warming El Niño pattern (also known as El Niño Modoki/warm-pool El Niño/Date Line El Niño) (Ashok and Yamagata, 2009; Di Lorenzo et al., 2010; Kug et al., 2009; Larkin and Harrison, 2005), 3) loss of interannual climate pattern influence on/communication with southern California precipitation, 4) North Pacific High pressure system moisture blocking, and/or shifting or expansion of the subtropical dry zone.

In the modern climate, La Niña events are coincident with less rainfall and river discharge in southern California (Warrick and Farnsworth, 2009b), and dry conditions in the U.S. southwest (Cole et al., 2002). Therefore it may be that persistent La Niña-like conditions are responsible for the decadal-to-centennial droughts observed in $T_V$. Some climate modeling and reconstruction studies have linked ENSO variability with orbital forcing (primarily precession) (Clement et al., 2001; Clement et al., 1999; Clement et al., 2000; Karamperidou et al., 2015; Koutavas and Joanides, 2012; Liu et al., 2014; Marchitto et al., 2010; Timmermann et al., 2007), however others have not found an orbital link to ENSO reconstructions from fossil corals and mollusks (Carré et al., 2014; Cobb et al., 2013; Emile-Geay et al., 2016). The ENSO band absences observed in $T_V$ are similar in duration to the abrupt and sustained ENSO shutdowns reported by Clement et al. (2001) from 450-400 ka in their modeling study of orbitally-driven ENSO. However, the recurrence interval of the ENSO band absences are dissimilar: absences observed in the SBB $T_V$ record recur every 50-175 years as opposed to the longer duration 11-kyr ENSO recurrence shutdown interval reported by Clement et al. (2001). It is unlikely that orbital forcing triggered the drought intervals and ENSO band absences observed in the SBB record because these precipitation changes occurred much more quickly than orbital forcing cyclicities would allow. Nevertheless I cannot rule out that persistent La Niña conditions caused

these decadal-to-centennial droughts, therefore additional interannual paleoclimate records with ENSO influence are needed from this time to compare with the SBB PC1.

The periods of drought and ENSO band absences could also be related to different types of El Niño-like events and their respective impacts on southern California precipitation. Increased precipitation is more likely to occur during conventional El Niño events in southern California, however the influence of central tropical Pacific El Niño events on southern California precipitation is less pronounced, with a small statistical increase compared to background conditions (Weng et al., 2009; however see Larkin and Harrison (2005)). Perhaps the central tropical Pacific El Niño-like pattern was more prominent during the drought periods observed in SBB during $T_V$, leading to a reduced influence on precipitation in southern California. However if this were the case, I would not necessarily expect prolonged drought conditions, unless the central tropical Pacific El Niño-like pattern was the exclusive interannual phase throughout the drought intervals, with no occurrence of the conventional El Niño-like pattern. The absence of ENSO band variability may have been due to loss of communication between the tropics and southern California, such that ENSO-like events no longer influenced regional precipitation.

Southern California also receives moisture from the northwest Pacific, therefore in order for a drought to occur, moisture must be blocked from this source in addition to reduced influence of tropical events. The dry conditions during $T_V$ could have resulted from the movement of the North Pacific High pressure system into a persistent blocking position, which could have prevented moisture transport from the northwest Pacific into southern California. Through a similar mechanism, a persistent anomalous high ridge over California deflected storms north and prevented precipitation from reaching the southwest coast during the recent 2013-2016 extreme California drought (Swain et al., 2016). The extended duration of the $T_V$ droughts may be indicative of reorganized atmospheric circulation, where the mid-latitude Westerlies were shifted poleward and the subtropical dry zone is expanded, resulting in increased aridity in the American Southwest (Fawcett et al., 2011). While I cannot determine the cause of the $T_V$ droughts in southern California, the most likely explanation of these decadal-to-centennial events is poleward shifting or zonal expansion of the subtropical dry zone and associated North Pacific High pressure system. This reorganization of atmospheric pressure was probably a response to the orbitally-induced warming (Fawcett et al., 2011) that occurred during $T_V$ and

resulting changes in oceanic and atmospheric heat transfer. Additional $T_V$ paleoclimate records with at least decadal resolution are needed to assess this hypothesis.

Intervals of increased precipitation coincide with the presence of ENSO band variability in PC1 (Figures 5-6). More frequent El Niño-like events may therefore have led to increased rainfall in southern California. The power of the ENSO band variability decreases through time, which could indicate that El Niño-like events became less frequent or intense as deglaciation proceeded. The wetter intervals could also be due to increased moisture transport from the tropical eastern Pacific (Lyle et al., 2012), as was invoked to explain the pluvial conditions of the western U.S. during MIS 2. However moisture transport out of the tropical eastern Pacific may be related to El Niño-like events that lead to wet conditions in the southwestern U.S. (Weng et al., 2009).

Significant interdecadal and centennial precipitation periodicities occur throughout $T_V$ (Figures 5-6). The interdecadal precipitation periodicity is similar to the 20$^{th}$ century North Pacific interdecadal climate fluctuations also known as the Pacific Decadal Oscillation (PDO) (Mantua and Hare, 2002; Mantua et al., 1997). The PDO impacts precipitation in southern California by influencing the expression of ENSO phase variability on regional climate (Verdon and Franks, 2006), and interdecadal periodicities observed in the $T_V$ precipitation record may indicate the PDO-like climate pattern is also a persistent feature of the North Pacific. The centennial periodicities are indicative of a longer duration climate phenomena capable of influencing precipitation in southern California. Such a long duration climate pattern cannot yet be observed in the short modern instrumental records and requires further paleoclimate reconstruction to confirm its spatial pattern.

### 4.6 Conclusion

The characteristic features of the modern southern California hydroclimate were also present during $T_V$, despite orbital-forcing changes leading to the deglaciation of MIS 12. Using the PC1 precipitation proxy, Precipitation variability was detected in $T_V$ sediments with frequencies that fall within the modern ENSO cyclicity band. Intervals of increased precipitation in southern California during $T_V$ coincide with the presence of significant ENSO bandwidth frequencies (2-7 year periodicities) in PC1. Therefore more frequent El Niño-like events may have led to increased rainfall in southern California during this climate transition. Reductions in

the power of the ENSO band variability suggest that El Niño-like events became less frequent as deglaciation proceeded or that the ENSO teleconnection with southern California was lost. Low PC1 values indicate seven decadal-to-centennial droughts occurred in southern California during $T_V$, wherein ENSO band precipitation variability was absent. The coincidence of increased (decreased) precipitation and the occurrence (absence) of ENSO band variability in the precipitation record indicates that El Niño-like events influenced southern California hydroclimate during $T_V$, similar to the modern and their frequency decreased as deglaciation proceeded.

Furthermore I demonstrate that severe droughts and floods occurred during this glacial-interglacial transition, and these may be linked to ocean-atmosphere phenomena that are also operating in the modern, such as ENSO and atmospheric rivers. The similarities between this $T_V$ precipitation reconstruction and the southern California hydroclimate conditions of the last 150/1,100 years are significant because they imply extreme flooding and multi-decadal droughts are prominent and recurrent features. While flooding and drought in southern California have been experienced in the modern, the magnitude and duration of precipitation extremes observed in the Tv reconstruction have not. The decadal-to-centennial droughts may have been caused by the effects of natural warming on the poleward extension or zonal expansion of the subtropical dry zone (Fawcett et al., 2011). In particular, the $T_V$ precipitation reconstruction may be indicative of the hydroclimate response in southern California to anthropogenic warming, where both extreme precipitation events and sustained droughts are common. This record of hydroclimate conditions can aid in regional planning for extreme flooding and severe drought in order to mitigate the effects of these events.

### 4.7 References

Afshar, S., 2011. High-resolution windows into abrupt and millennial-scale changes in climate and ocean since the Mid-Pleistocene Transition, Santa Barbara Basin, California, Geological Sciences. California State University, Long Beach, p. 148.

Andrews, E.D., Antweiler, R.C., Neiman, P.J., Ralph, F.M., 2004. Influence of ENSO on flood frequency along the California Coast. J. Climate 17, 337-348.

Ashok, K., Yamagata, T., 2009. Climate change: The El Nino with a difference. Nature 461, 481-484.

Ayling, B.F., Chappell, J., Gagan, M.K., McCulloch, M.T., 2015. ENSO variability during MIS 11 (424–374 ka) from Tridacna gigas at Huon Peninsula, Papua New Guinea. Earth Planet. Sci. Lett. 431, 236.

Behl, R., Kennett, J., Hill, T.M., Pak, D., Schimmelmann, A., Cannariato, K., Team, S., Sorlien, C.C., Hopkins, S.E., 2005. Extending the high-resolution global climate record in Santa Barbara Basin: developing a more continuous composite section from overlapping cores. Eos Transactions American Geophysical Union Fall Meeting Supplemental 86, PP51D-0636.

Behl, R.J., Escobedo, D.K., Kennett, J.P., Nicholson, C., Sorlien, C., 2007. Decadal to million-year sedimentation rates and the ultra-high-resolution marine record from Santa Barbara Basin. Eos Transactions American Geophysical Union Fall Meeting Supplemental 88, PP41C-0677.

Behl, R.J., Kennett, J.P., 1996. Brief interstadial events in the Santa Barbara basin, NE Pacific, during the past 60 kyr. Nature 379, 243-246.

Biondi, F., Lange, C.B., Hughes, M.K., Berger, W.H., 1997. Inter-decadal signals during the last millennium (AD 1117–1992) in the Varve record of Santa Barbara Basin, California. GeoRL 24, 193-196.

Burman, J., Gustafsson, O., Segl, M., Schmitz, B., 2005. A simplified method of preparing phosphoric acid for stable isotope analyses of carbonates. Rapid Commun. Mass Spectrom. 19, 3086-3088.

Cai, W., Santoso, A., Wang, G., Yeh, S.-W., An, S.-I., Cobb, K.M., Collins, M., Guilyardi, E., Jin, F.-F., Kug, J.-S., Lengaigne, M., McPhaden, M.J., Takahashi, K., Timmermann, A., Vecchi, G., Watanabe, M., Wu, L., 2015a. ENSO and greenhouse warming. Nature Clim. Change 5, 849-859.

Cai, W., Wang, G., Santoso, A., McPhaden, M.J., Wu, L., Jin, F.-F., Timmermann, A., Collins, M., Vecchi, G., Lengaigne, M., England, M.H., Dommenget, D., Takahashi, K., Guilyardi, E., 2015b. Increased frequency of extreme La Nina events under greenhouse warming. Nature Clim. Change 5, 132-137.

Candy, I., Schreve, D.C., Sherriff, J., Tye, G.J., 2014. Marine Isotope Stage 11: Palaeoclimates, palaeoenvironments and its role as an analogue for the current interglacial. Earth-Sci. Rev. 128, 18-51.

Carré, M., Sachs, J.P., Purca, S., Schauer, A.J., Braconnot, P., Falcón, R.A., Julien, M., Lavallée, D., 2014. Holocene history of ENSO variance and asymmetry in the eastern tropical Pacific. Sci 345, 1045-1048.

Cayan, D.R., Redmond, K.T., Riddle, L.G., 1999. ENSO and hydrologic extremes in the Western United States. J. Climate 12, 2881-2893.

Cisneros-Dozal, L.M., Huang, Y., Heikoop, J.M., Fawcett, P.J., Fessenden, J., Anderson, R.S., Meyers, P.A., Larson, T., Perkins, G., Toney, J., Werne, J.P., Goff, F., WoldeGabriel, G., Allen, C.D., Berke, M.A., 2014. Assessing the strength of the monsoon during the late Pleistocene in southwestern United States. Quatern. Sci. Rev. 103, 81-90.

Clement, A.C., Cane, M.A., Seager, R., 2001. An Orbitally Driven Tropical Source for Abrupt Climate Change. J. Climate 14, 2369-2375.

Clement, A.C., Seager, R., Cane, M.A., 1999. Orbital controls on the El Niño/Southern Oscillation and the tropical climate. Paleoceanography 14, 441-456.

Clement, A.C., Seager, R., Cane, M.A., 2000. Suppression of El Niño during the Mid-Holocene by changes in the Earth's orbit. Paleoceanography 15, 731-737.

Cobb, K.M., Westphal, N., Sayani, H.R., Watson, J.T., Di Lorenzo, E., Cheng, H., Edwards, R.L., Charles, C.D., 2013. Highly Variable El Niño–Southern Oscillation Throughout the Holocene. Sci 339, 67-70.

Cole, J.E., Overpeck, J.T., Cook, E.R., 2002. Multiyear La Niña events and persistent drought in the contiguous United States. GeoRL 29, 25-21-25-24.

Dean, W.E., Kennett, J.P., Behl, R.J., Nicholson, C., Sorlien, C.C., 2015. Abrupt termination of Marine Isotope Stage 16 (Termination VII) at 631.5 ka in Santa Barbara Basin, California. Paleoceanography 30, 1373-1390.

Dettinger, M.D., Cayan, D.R., Diaz, H.F., Meko, D.M., 1998. North-south precipitation patterns in western North America on interannual-to-decadal timescales. J. Climate 11, 3095-3111.

Dettinger, M.D., Ralph, F.M., Das, T., Neiman, P.J., Cayan, D.R., 2011. Atmospheric Rivers, Floods and the Water Resources of California. Water 3, 445-478.

Di Lorenzo, E., Cobb, K.M., Furtado, J.C., Schneider, N., Anderson, B.T., Bracco, A., Alexander, M.A., Vimont, D.J., 2010. Central Pacific El Nino and decadal climate change in the North Pacific Ocean. Nature Geosci 3, 762-765.

Duhr, A., Hilkert, A.W., 2004. delta O-18 and delta C-13 determination of carbonates using Thermo Scientific GasBench II, Thermo Fisher Scientific Application Note 30050.

Emile-Geay, J., Cobb, K.M., Carre, M., Braconnot, P., Leloup, J., Zhou, Y., Harrison, S.P., Correge, T., McGregor, H.V., Collins, M., Driscoll, R., Elliot, M., Schneider, B., Tudhope, A., 2016. Links between tropical Pacific seasonal, interannual and orbital variability during the Holocene. Nature Geosci 9, 168-173.

Escobedo, D.K., 2009. Extreme erosional events recorded by flood deposits in the Late Quaternary Santa Barbara Basin, Coasta Southern California, Department of Geological Sciences. California State University, Long Beach, p. 101.

Evans, M.N., Selmer, K.J., Breeden, B.T., Lopatka, A.S., Plummer, R.E., 2016. Correction algorithm for online continuous flow δ13C and δ18O carbonate and cellulose stable isotope analyses. Geochem. Geophys. Geosyst. 17, 3580-3588.

Fawcett, P.J., Werne, J.P., Anderson, R.S., Heikoop, J.M., Brown, E.T., Berke, M.A., Smith, S.J., Goff, F., Donohoo-Hurley, L., Cisneros-Dozal, L.M., Schouten, S., Sinninghe Damste, J.S., Huang, Y., Toney, J., Fessenden, J., WoldeGabriel, G., Atudorei, V., Geissman, J.W., Allen, C.D., 2011. Extended megadroughts in the southwestern United States during Pleistocene interglacials. Nature 470, 518-521.

Graham, N.E., Hughes, M.K., Ammann, C.M., Cobb, K.M., Hoerling, M.P., Kennett, D.J., Kennett, J.P., Rein, B., Stott, L., Wigand, P.E., Xu, T., 2007. Tropical Pacific – mid-latitude teleconnections in medieval times. Clim. Change 83, 241-285.

Hendy, I.L., Dunn, L., Schimmelmann, A., Pak, D.K., 2013. Resolving varve and radiocarbon chronology differences during the last 2000 years in the Santa Barbara Basin sedimentary record, California. Quatern. Int. 310, 155-168.

Hendy, I.L., Kennett, J.P., 1999. Latest Quaternary North Pacific surface-water responses imply atmosphere-driven climate instability. Geology 27, 291-294.

Hendy, I.L., Kennett, J.P., 2000. Dansgaard-Oeschger Cycles and the California Current System: Planktonic foraminiferal response to rapid climate change in Santa Barbara Basin, Ocean Drilling Program Hole 893A. Paleoceanography 15, 30.

Hendy, I.L., Kennett, J.P., 2003. Tropical forcing of North Pacific intermediate water distribution during Late Quaternary rapid climate change? Quatern. Sci. Rev. 22, 673.

Hendy, I.L., Napier, T.J., Schimmelmann, A., 2015. From extreme rainfall to drought: 250 years of annually resolved sediment deposition in Santa Barbara Basin, California. Quatern. Int. 387, 3-12.

Heusser, L.E., Hendy, I.L., Barron, J.A., 2015. Vegetation response to southern California drought during the Medieval Climate Anomaly and early Little Ice Age (AD 800–1600). Quatern. Int. 387, 23-35.

Hoell, A., Hoerling, M., Eischeid, J., Wolter, K., Dole, R., Perlwitz, J., Xu, T., Cheng, L., 2016. Does El Niño intensity matter for California precipitation? GeoRL 43, 819-825.

Hopkins, S., Kennett, J., Nicholson, C., Pak, D., Sorlien, C., Behl, R., Normark, W., Sliter, R., Hill, T., Schimmelmann, A., Cannariato, K., 2006. Santa Barbara basin study extends global climate record. Eos, Transactions American Geophysical Union 87, 205.

Hopkins, S.E., 2006. Geometry and Quaternary evolution of a laterally propagating fold and fault system, Santa Barbara Channel, California. University of California, Santa Barbara, p. 50.

Hülsemann, J., Emery, K.O., 1961. Stratification in recent sediments of Santa Barbara Basin as controlled by organisms and water character. J. Geol. 69, 279-290.

Inman, D.L., Jenkins, S.A., 1999. Climate change and the episodicity of sediment flux of small California rivers. J. Geol. 107, 251-270.

Karamperidou, C., Di Nezio, P.N., Timmermann, A., Jin, F.-F., Cobb, K.M., 2015. The response of ENSO flavors to mid-Holocene climate: Implications for proxy interpretation. Paleoceanography 30, 527-547.

Kincaid, E., Thunell, R.C., Le, J., Lange, C.B., Weinheimer, A.L., Reid, F.M.H., 2000. Planktonic foraminiferal fluxes in the Santa Barbara Basin: response to seasonal and interannual hydrographic changes. DSR 47, 1157-1176.

Kodama, K.P., Hinnov, L.A., 2015. Rock magnetic cyclostratigraphy. Wiley Blackwell, Oxfordshire, England.

Koutavas, A., Joanides, S., 2012. El Niño–Southern Oscillation extrema in the Holocene and Last Glacial Maximum. Paleoceanography 27, n/a-n/a.

Koutsodendris, A., Brauer, A., Pälike, H., Müller, U.C., Dulski, P., Lotter, A.F., Pross, J., 2011. Sub-decadal- to decadal-scale climate cyclicity during the Holsteinian interglacial (MIS 11) evidenced in annually laminated sediments. Clim. Past 7, 987-999.

Koutsodendris, A., Pross, J., Müller, U.C., Brauer, A., Fletcher, W.J., Kühl, N., Kirilova, E., Verhagen, F.T.M., Lücke, A., Lotter, A.F., 2012. A short-term climate oscillation during the Holsteinian interglacial (MIS 11c): An analogy to the 8.2 ka climatic event? GPC 92–93, 224-235.

Kug, J., Jin, F., An, S., 2009. Two Types of El Niño Events: Cold Tongue El Niño and Warm Pool El Niño. J. Climate 22, 1499-1515.

Lambeck, K., Chappell, J., 2001. Sea Level Change Through the Last Glacial Cycle. Sci 292, 679-686.

Larkin, N.K., Harrison, D.E., 2005. On the definition of El Niño and associated seasonal average U.S. weather anomalies. GeoRL 32, n/a-n/a.

Lea, D.W., Pak, D.K., Spero, H.J., 2003. Sea Surface Temperatures in the Western Equatorial Pacific During Marine Isotope Stage 11, in: Droxler, A.W., Poore, R.Z., Burckle, L.H. (Eds.), Earth's Climate and Orbital Eccentricity: The Marine Isotope Stage 11 Question. American Geophysical Union, Washington, D.C., pp. 147-156.

Lindsey, R., 2013. In Watching for El Niño and La Niña, NOAA adapts to Global Warming, ClimateWatch Magazine. National Oceanic and Atmospheric Administration, Climate.gov.

Lisiecki, L.E., Raymo, M.E., 2005. A Pliocene-Pleistocene stack of 57 globally distributed benthic δ18O records. Paleoceanography 20, PA1003.

Liu, Z., Lu, Z., Wen, X., Otto-Bliesner, B.L., Timmermann, A., Cobb, K.M., 2014. Evolution and forcing mechanisms of El Nino over the past 21,000 years. Nature 515, 550-553.

Lora, J.M., Mitchell, J.L., Tripati, A.E., 2016. Abrupt reorganization of North Pacific and western North American climate during the last deglaciation. GeoRL 43, 11,796-711,804.

Loutre, M.F., Berger, A., 2003. Marine Isotope Stage 11 as an analogue for the present interglacial. GPC 36, 209-217.

Lu, R., Turco, R.P., Stolzenbach, K., Friedlander, S.K., Xiong, C., Schiff, K., Tiefenthaler, L., Wang, G., 2003. Dry deposition of airborne trace metals on the Los Angeles Basin and adjacent coastal waters. Journal of Geophysical Research: Atmospheres 108, n/a-n/a.

Lyle, M., Heusser, L., Ravelo, C., Yamamoto, M., Barron, J., Diffenbaugh, N.S., Herbert, T., Andreasen, D., 2012. Out of the Tropics: The Pacific, Great Basin Lakes, and Late Pleistocene Water Cycle in the Western United States. Sci 337, 1629-1633.

Mantua, N.J., Hare, S.R., 2002. The Pacific Decadal Oscillation. J. Oceanogr. 58, 35-44.

Mantua, N.J., Hare, S.R., Zhang, Y., 1997. A Pacific interdecadal climate oscillation with impacts on salmon production. Bull. Am. Meteorol. Soc. 78, 1069-1079.

Marchitto, T.M., Muscheler, R., Ortiz, J.D., Carriquiry, J.D., van Geen, A., 2010. Dynamical Response of the Tropical Pacific Ocean to Solar Forcing During the Early Holocene. Sci 330, 1378-1381.

Marshall, C.J., 2012. Sedimentation in an active fold and thrust belt, from 1 Ma to Present, Santa Barbara Channel, California, Department of Geological Sciences. California State University, Long Beach, p. 77.

Mo, K.C., Higgins, R.W., 1998. Tropical Influences on California Precipitation. J. Climate 11, 412-430.

Moffitt, S.E., Hill, T.M., Ohkushi, K., Kennett, J.P., Behl, R.J., 2014. Vertical oxygen minimum zone oscillations since 20 ka in Santa Barbara Basin: A benthic foraminiferal community perspective. Paleoceanography 29, 44-57.

Nezlin, N.P., DiGiacomo, P.M., Stein, E.D., Ackerman, D., 2005. Stormwater runoff plumes observed by SeaWiFS radiometer in the Southern California Bight. Remote Sens. Environ. 98, 494-510.

Normark, W.R., Piper, D.J.W., Sliter, R.A.Y., 2006. Sea-level and tectonic control of middle to late Pleistocene turbidite systems in Santa Monica Basin, offshore California. Sedimentology 53, 867.

Oppo, D.W., McManus, J.F., Cullen, J.L., 1998. Abrupt Climate Events 500,000 to 340,000 Years Ago: Evidence from Subpolar North Atlantic Sediments. Sci 279, 1335-1338.

Paillard, D., Labeyrie, L., Yiou, P., 1996. Macintosh Program performs time-series analysis. Eos, Transactions American Geophysical Union 77, 379-379.

Prokopenko, A.A., Karabanov, E.B., Williams, D.F., Kuzmin, M.I., Shackleton, N.J., Crowhurst, S.J., Peck, J.A., Gvozdkov, A.N., King, J.W., 2001. Biogenic Silica Record of the Lake Baikal Response to Climatic Forcing during the Brunhes. Quatern. Res. 55, 123-132.

Railsback, L.B., Gibbard, P.L., Head, M.J., Voarintsoa, N.R.G., Toucanne, S., 2015. An optimized scheme of lettered marine isotope substages for the last 1.0 million years, and the climatostratigraphic nature of isotope stages and substages. Quatern. Sci. Rev. 111, 94-106.

Rayner, N.A., Parker, D.E., Horton, E.B., Folland, C.K., Alexander, L.V., Rowell, D.P., Kent, E.C., Kaplan, A., 2003. Global analyses of sea surface temperature, sea ice, and night marine air temperature since the late nineteenth century. Journal of Geophysical Research: Atmospheres 108, n/a-n/a.

Regattieri, E., Giaccio, B., Galli, P., Nomade, S., Peronace, E., Messina, P., Sposato, A., Boschi, C., Gemelli, M., 2016. A multi-proxy record of MIS 11–12 deglaciation and glacial MIS 12 instability from the Sulmona basin (central Italy). Quatern. Sci. Rev. 132, 129-145.

Revesz, K.M., Landwehr, J.M., 2002. delta C-13 and delta O-18 isotopic composition of CaCO3 measured by continuous flow isotope ratio mass spectrometry: statistical evaluation and verification by application to Devils Hole core DH-11 calcite. Rapid Commun. Mass Spectrom. 16, 2102-2114.

Rodrigues, T., Voelker, A.H.L., Grimalt, J.O., Abrantes, F., Naughton, F., 2011. Iberian Margin sea surface temperature during MIS 15 to 9 (580–300 ka): Glacial suborbital variability versus interglacial stability. Paleoceanography 26, n/a-n/a.

Rohling, E.J., Braun, K., Grant, K., Kucera, M., Roberts, A.P., Siddall, M., Trommer, G., 2010. Comparison between Holocene and Marine Isotope Stage-11 sea-level histories. Earth Planet. Sci. Lett. 291, 97-105.

Romans, B.W., Normark, W.R., McGann, M.M., Covault, J.A., Graham, S.A., 2009. Coarse-grained sediment delivery and distribution in the Holocene Santa Monica Basin, California: Implications for evaluating source-to-sink flux at millennial time scales. Geol. Soc. Am. Bull. 121, 1394-1408.

Ropelewski, C.F., Halpert, M.S., 1987. Global and Regional Scale Precipitation Patterns Associated with the El Niño/Southern Oscillation. MWRv 115, 1606-1626.

Ryan, W.B.F., Carbotte, S.M., Coplan, J.O., O'Hara, S., Melkonian, A., Arko, R., Weissel, R.A., Ferrini, V., Goodwillie, A., Nitsche, F., Bonczkowski, J., Zemsky, R., 2009. Global Multi-Resolution Topography synthesis. Geochem. Geophys. Geosyst. 10, Q03014.

Schimmelmann, A., Hendy, I.L., Dunn, L., Pak, D.K., Lange, C.B., 2013. Revised ~2000-year chronostratigraphy of partially varved marine sediment in Santa Barbara Basin, California. GFF 135, 258-264.

Schimmelmann, A., Lange, C.B., Berger, W.H., 1990. Climatically controlled marker layers in Santa Barbara Basin sediments and fine-scale core-to-core correlation. Limnol. Oceanogr. 35, 165.

Schimmelmann, A., Lange, C.B., Berger, W.H., Simon, A., Burke, S.K., Dunbar, R.B., 1992. Extreme climatic conditions recorded in Santa Barbara Basin laminated sediments: the 1835–1840 Macoma event. Mar. Geol. 106, 279-299.

Schimmelmann, A., Lange, C.B., Roark, E.B., Ingram, B.L., 2006. Resources for paleoceanographic and paleoclimatic analysis: a 6,700-year stratigraphy and regional radiocarbon reservoir-age ({Delta}R) record based on varve counting and 14C-AMS dating for the Santa Barbara Basin, offshore California, U.S.A. J. Sed. Res. 76, 74.

Schimmelmann, A., Zhao, M., Harvey, C.C., Lange, C.B., 1998. A large California flood and correlative global climatic events 400 years ago. Quatern. Res. 49, 51-61.

Schonher, T., Nicholson, S.E., 1989. The relationship between California rainfall and ENSO events. J. Climate 2, 1258-1269.

Soutar, A., Crill, P.A., 1977. Sedimentation and climatic patterns in the Santa Barbara Basin during the 19th and 20th centuries. Geol. Soc. Am. Bull. 88, 1161-1172.

Spötl, C., 2011. Long-term performance of the Gasbench isotope ratio mass spectrometry system for the stable isotope analysis of carbonate microsamples. Rapid Commun. Mass Spectrom. 25, 1683-1685.

Spötl, C., Vennemann, T.W., 2003. Continuous‐flow isotope ratio mass spectrometric analysis of carbonate minerals. Rapid Commun. Mass Spectrom. 17, 1004-1006.

Sun, X., Renard, B., Thyer, M., Westra, S., Lang, M., 2015. A global analysis of the asymmetric effect of ENSO on extreme precipitation. JHyd 530, 51-65.

Swain, D.L., Horton, D.E., Singh, D., Diffenbaugh, N.S., 2016. Trends in atmospheric patterns conducive to seasonal precipitation and temperature extremes in California. Science Advances 2.

Thunell, R.C., Tappa, E., Anderson, D.M., 1995. Sediment fluxes and varve formation in Santa Barbara Basin, offshore California. Geology 23, 1083-1086.

Timmermann, A., Lorenz, S.J., An, S.-I., Clement, A., Xie, S.-P., 2007. The Effect of Orbital Forcing on the Mean Climate and Variability of the Tropical Pacific. J. Climate 20, 4147-4159.

Venrick, E.L., 2012. Phytoplankton in the California Current system off southern California: Changes in a changing environment. PrOce 104, 46-58.

Verdon, D.C., Franks, S.W., 2006. Long-term behaviour of ENSO: Interactions with the PDO over the past 400 years inferred from paleoclimate records. GeoRL 33, n/a-n/a.

Voelker, A.H.L., Rodrigues, T., Billups, K., Oppo, D., McManus, J., Stein, R., Hefter, J., Grimalt, J.O., 2010. Variations in mid-latitude North Atlantic surface water properties during the mid-Brunhes (MIS 9–14) and their implications for the thermohaline circulation. Clim. Past 6, 531-552.

Warrick, J.A., Farnsworth, K.L., 2009a. Dispersal of river sediment in the Southern California Bight. Geol. Soc. Am. Spec. Pap. 454, 53-67.

Warrick, J.A., Farnsworth, K.L., 2009b. Sources of sediment to the coastal waters of the Southern California Bight. Geol. Soc. Am. Spec. Pap. 454, 39-52.

Weng, H., Behera, S.K., Yamagata, T., 2009. Anomalous winter climate conditions in the Pacific rim during recent El Niño Modoki and El Niño events. ClDy 32, 663-674.

White, S.M., Hill, T.M., Kennett, J.P., Behl, R.J., Nicholson, C., 2013. Millennial-scale variability to 735 ka: High-resolution climate records from Santa Barbara Basin, CA. Paleoceanography 28, 213-226.

# CHAPTER 5

## Conclusions

This conclusion consists of a summary of the results of each research chapter and their impact on the use of Santa Barbara Basin lithogenic sediments as recorders of regional hydroclimate conditions, with insights to application in other marine systems. Finally, future research directions are proposed based on the results presented in this work.

### 5.1 Influences on Santa Barbara Basin lithogenic sediment

The composition of Santa Barbara Basin (SBB) lithogenic sediment reflects the terrigenous sediment sources in adjacent river catchment and anthropogenic modification of streams. In addition, the transportation of lithogenic sediment from the river catchments to SBB is influenced by hydroclimate, such that droughts result in diminished terrigenous lithogenic sediment flux to SBB, and extreme precipitation events generate flooding that enhances sediment flux (Hendy et al., 2015; Inman and Jenkins, 1999; Warrick and Farnsworth, 2009).

In **Chapter 2**, SBB Holocene flood deposits and sediments deposited during the Last Glacial Maximum (LGM) in SBB are compared to adjacent river catchment stream bed sediments using mineral and geochemical composition in order to identify their sources. Sample mineralogies and geochemical compositions are primarily controlled by adjacent and upstream lithologic units. Many units in the study area have undergone sedimentary recycling, and this is reflected in stream bed sediment sample composition through retention of immobile elements (e.g., Al and Ti) and increased quartz and clay mineral proportions. Sample compositions are also influenced by erosion rates; locations in the study area with high fault slip rates and high erosion contribute a larger proportion of sediment to the stream bed and SBB. Rare earth elemental patterns reflect a typical shale composition, and Sm/Nd and Rb/Sr sample values are generally similar to those measured in shales and sandstones. Enrichments in Eu are indicative of high feldspar abundance in the samples, consistent with the mineralogy. A positive Ce anomaly

in a sediment core sample associated with a 5 cm-thick flood deposit may indicate preserved Fe- and Mn oxyhydroxides, which could have escaped reduction in the SBB sediment column via the "coffin lid" effect of the impermeable flood deposit (Schimmelmann, 2012).

Six geochemically distinct composition groups/source areas were identified based on elemental principal component analysis and radiogenic Sr and Nd isotopic composition of the stream bed sediments: the Eastern Santa Clara sub-catchment, including the western San Gabriel Mountains; the Sierra Pelona sub-catchment; the Northern Santa Clara sub-catchment including Alamo, Frazier, and Liebre Mountains; the southern flanks of the Santa Ynez Mountains and the Western Santa Clara sub-catchment; the Eastern Santa Ynez sub-catchment; and Santa Rosa Island. The Eastern Santa Clara sub-catchment is characterized by $^{87}Sr/^{86}Sr$ values ranging from 0.704-0.708 and $\varepsilon_{Nd}$ values between -7 and -10, consistent with derivation from an ancient mafic crustal source (e.g., San Gabriel Mountains anorthosite complex). The Sierra Pelona sub-catchment sample bears a $^{87}Sr/^{86}Sr$ value of ~0.716 and an $\varepsilon_{Nd}$ value of -7.3. Samples from the Northern Santa Clara sub-catchment produced $^{87}Sr/^{86}Sr$ values around 0.716 and $\varepsilon_{Nd}$ values between -13 and -14. The southern slopes of the Santa Ynez Mountains and Western Santa Clara sub-catchment group bears $^{87}Sr/^{86}Sr$ values between ~0.710–0.715 and $\varepsilon_{Nd}$ values between ~-9 and -12. The Eastern Santa Ynez River catchment is characterized by $^{87}Sr/^{86}Sr$ values from ~0.709–0.711 and $\varepsilon_{Nd}$ values from -9 to -3. The Santa Rosa Island group has $^{87}Sr/^{86}Sr$ values ranging from ~0.705–0.708 and $\varepsilon_{Nd}$ values between ~0 to +2, reflective of sedimentary mixing with Miocene volcanics.

Santa Barbara Basin Holocene flood deposits and LGM sediments are derived from multiple onshore geologic sources. Consistent mineral composition and abundance among the flood deposits suggests relative contributions between different source areas do not vary through the Holocene. In major element principal component space, flood deposit samples compositions are most similar to the southern slopes of the Santa Ynez Mountains and Western Santa Clara sub-catchment (Topatopa Mountains). The Topatopa Mountains and the Santa Ynez Mountains are drained by the Santa Clara River, the Ventura River, and mountain streams, and are the primary sources of sediment in SBB flood deposits. The Western Santa Clara sub-catchment is a dominant contributor of flood deposit sediment based on chlorite abundances in the flood deposits, and the flood deposits also compare well to bed sediment samples collected from the Santa Ynez Mountains southern slopes. Estimation of provenance sources using radiogenic Sr-

Nd mixing lines suggests the southern slopes of the Santa Ynez Mountains provide ~80% of flood deposit sediment, the Eastern Santa Clara sub-catchment contributes <10%, and the Northern Santa Clara sub-catchment contributes ~10-20%.

The SBB glacial sediments differ from the Holocene flood deposits in the mineralogy, principal component results, and radiogenic isotopic composition, suggesting sediment sources were slightly different during the LGM. Chlorite is absent from the LGM samples, suggesting loss of Santa Clara River sediments during the glacial lowstand (Fleischer, 1972; Robert, 2004), consistent with hypothesized LGM drainage changes (Normark et al., 2006). Lower muscovite abundances in the LGM samples suggests decreased contribution from the Ventura River, while increased kaolinite abundance indicate enhanced sediment flux from Santa Rosa Island and perhaps the Channel Islands as a whole during the LGM. The LGM samples are more similar to the Santa Ynez Mountains southern slopes group in major element and isotopic compositions than the Holocene flood deposit samples. The lowstand in eustatic sea level during the LGM lowered the Santa Clara River base level, causing the river to discharge directly into Santa Monica Basin via the Hueneme Canyon and bypass SBB altogether (Normark et al., 2006). The loss of this sediment source was compensated, however, by increased sediment flux from the Santa Ynez Mountains southern slopes, and likely the Channel Islands, based on mineralogical and geochemical composition of the LGM samples. Radiogenic Sr-Nd mixing model estimates indicate the southern slopes of the Santa Ynez Mountains contributed ~90% of sediment to SBB during the LGM, and suggest that the Channel Islands' sediment contribution to SBB was ~10% greater during the LGM sea level low stand than during the Holocene high stand. The consistency in SBB sedimentation rates between the LGM and the Holocene (Hendy et al., 2002; Hill et al., 2006), despite the loss of input from the Santa Clara River, must be due to increased denudation of the Santa Ynez Mountains and Channel Islands during the wetter glacial climate (Robert, 2004), as occurred on Santa Rosa Island (Schumann et al., 2016).

The focus of **Chapter 3** (Napier and Hendy, in press) is to determine the veracity of SBB lithogenic sediment as a recorder of regional hydroclimate events over the past 250 years, and to discern the impact of anthropogenic modifications to the adjacent river catchments on the composition of SBB lithogenic sediments. The clay mineralogy and siliciclastic elemental composition of SBB lithogenic sediments generally records increased terrigenous sediment flux in response to individual precipitation events, strong El Niño events, and extreme flood deposits.

However there is no consistency in the magnitude of the response to floods or El Niño events in terms of sediment composition. While climate modes such as the Pacific Decadal Oscillation (PDO) and El Niño-Southern Oscillation (ENSO) do not appear to control the composition of recently deposited (past 250 years) lithogenic sediments in SBB, K, Ti, and kaolinite+chlorite are significantly correlated with precipitation, indicating that these components quickly respond to regional precipitation. Modeling results presented in Chapter 3 suggest that precipitation can be used to predict Ti concentrations and kaolinite+chlorite abundance in SBB sediments, and that in SBB sediments, Ti could be used as a paleoprecipitation proxy.

Weathering indices and clay mineral ratios, which reflect differential clay mineral formation in response to chemical alteration, were invariant downcore in the 250 year record. This suggests that processes that operate on geologic timescales (>11 kyr), such as chemical weathering, are not applicable to paleoclimate investigations on short timescales. Instead erosion and sediment transport in response to precipitation events control the composition of recent SBB sediments. Clay mineral abundances SBB sediments increase as regional precipitation increases. I posit that clay mineral erodibility increases during precipitation events because clays are able to sorb water to their crystal structure and become more mobile and erodible, while during droughts clays become progressively more immobile, resulting in diminished abundances in SBB.

Anthropogenic modification of the river catchments that discharge sediment into SBB, namely dam construction, also influences the composition of SBB lithogenic sediments. Dam impoundment, which began in 1912, has resulted in observed reductions in sediment discharge of regional rivers (Downs et al., 2013; Slagel and Griggs, 2008; Warrick and Farnsworth, 2009; Williams, 1979; Willis and Griggs, 2003). Significant negative correlations with percent of catchment area dammed indicate that damps trap sediments containing Al, K, Mg, Na, Ti, illite, and kaolinite+chlorite, preventing their deposition in SBB. Clay minerals are disproportionately impacted by dam impoundment. Kaolinite+chlorite is affected more by the dams than illite, and smectite is the least impacted. These differences reflect the sources of the clay minerals. Kaolinite is likely eroded from the upper reaches of each river catchment, but is trapped by dams during downstream transit. Illite is eroded from the mid-reaches, which are less impacted by damming, and smectite is eroded from the lower reaches where there are few dams to impede downstream sediment transport.

In **Chapter 4**, I investigate the natural hydroclimate variability of southern California during glacial Termination V ($T_V$; ~430-420 ka) using time series analysis, with a particular focus on ENSO, using the PC1 siliciclastic elemental paleoprecipitation proxy developed for the annually laminated sediments of SBB (Hendy et al., 2015). High scanning X-ray fluorescence (XRF) counts of elements associated with siliciclastic sediments in SBB core material (K, Ti, Si) are associated with increased precipitation and river runoff into SBB, while low counts are indicative of droughts (Hendy et al., 2015); as these siliciclastic sediments are derived from onshore river catchments.

Termination V is the transition from glacial Marine Isotope Stage (MIS 12) to interglacial MIS 11. Foraminiferal $\delta^{18}O$ values indicate that the sediment cores used in the analysis of $T_V$ hydroclimate were deposited during near-glacial conditions that were succeeded by rapid centennial warmings and gradual millennial coolings. Two abrupt warming events are recorded by decreases in planktonic (~1.6–2.1‰) and benthic (~0.6–1.0‰) foraminiferal $\delta^{18}O$ values over 200-400 years, and both are followed by gradual coolings. The rapid climate change events observed in the $T_V$ SBB record are likely coincident with events recorded in Atlantic Ocean sediments, suggesting climate coherence between the North Atlantic and North Pacific.

Comparison of time series power spectra from the PC1 paleoprecipitation proxy compiled from a 20$^{th}$ century SBB sediment core with the instrumental Southern Oscillation Index demonstrates that PC1 captures strong, low frequency ENSO variability (3-7 year periodicities), and indicates the fidelity of PC1 as a precipitation and hydroclimate proxy. The $T_V$ paleoprecipitation record reconstructed from PC1 indicates that the hydroclimate of southern California was variable, and influenced by ENSO-like interannual precipitation periodicities. Significant interdecadal and centennial precipitation periodicities also occur throughout $T_V$. In the Holocene, interannual and interdecadal precipitation periodicities in southern California are linked to ENSO and the PDO. The hydroclimate similarities between $T_V$ and the Holocene, as observed in analysis of the PC1 paleoprecipitation proxy, suggest precipitation patterns that impact southern California during warm climate states (e.g., interstadials, MIS 11, the Holocene) are persistent and have been since at least $T_V$ during the mid-Pleistocene.

The reconstructed $T_V$ precipitation record indicates both prolonged periods of drought and extreme flooding events occurred during this glacial-interglacial transition. Seven decadal-to-centennial droughts occurred in southern California during $T_V$, as indicated by low PC1.

During these droughts, ENSO-like precipitation variability was absent from southern California. I attribute the extended duration of these droughts to reorganized atmospheric circulation in response to orbitally-induced warming (Fawcett et al., 2011) that occurred during $T_V$. Expansion of the subtropical dry zone and poleward shifting of the mid-latitude Westerlies would have resulted in increased aridity in the American Southwest (Fawcett et al., 2011) because the North Pacific high pressure system would have blocked moisture transport from the northwest Pacific into southern California. Intervals of increased precipitation during $T_V$ coincide with the presence of ENSO-bandwidth (2-7 year) periodicities in PC1, therefore more frequent El Niño events may have lead in increased rainfall in southern California. The power of the ENSO-band variability decreased through time, which suggests that El Niño became less frequent or intense in southern California as deglaciation proceeded.

**5.2 Synthesis**

The marine record has been utilized for many years to reconstruct paleoclimate. Varved marine sediments provide up to annual resolution archives of paleoclimate, enabling investigation of interannual climate variability. However, prior to the construction of a paleoclimate record, the sediment from which the record is extracted must first be investigated such that the relationship between the climate processes that trigger an environmental response and the resulting characteristic sediment deposits in the marine basin is understood. In this dissertation, I have expanded on previous work which characterizes SBB sediments, and identifies hydroclimate signals in the siliciclastic, detrital fraction of SBB sediments (Hendy et al., 2015). The research presented in the preceding chapters indicates that the abundances of siliciclastic elements in varved SBB sediment can be used to reconstruct southern California precipitation and interannual ENSO variability throughout the Quaternary. Further, through the research presented here I have identified the sources of SBB detrital flood and glacial sediments, and also the impact of both natural and anthropogenic perturbations that alter the sediment pathways (e.g., sea level) and sediment flux (e.g., erosion, precipitation/drought, atmospheric circulation, damming) to SBB. Although this work was limited to southern California and SBB in particular, the results could also be applied to other near-shore marine basins and lakes to generate additional regional paleoclimate records.

While a qualitative relationship has been established between precipitation and the SBB sediment precipitation proxy, a quantitative relationship is needed in order to enable accurate infrastructure and response plans for southern California water resource managers. However, a quantitative relationship is difficult to attain due to attenuation of the precipitation signal during sediment transport, as a portion of the sediment settles out in-stream and on the shelf. How much precipitation is needed in the catchments in order to produce sufficient sediment flux to SBB such that the elemental composition of the deposit is measureable (i.e., thicker than 0.02 cm)? How much of the signal is deposited in-transit; how long does this sediment remain in the stream bed? Further, the highly extreme and variable nature of precipitation in a mediterranean climate, with decadal-to-centennial droughts and also numerous heavy precipitation events in a single year, adds an additional layer of convolution to the precipitation signal.

### 5.3 Future research directions

The work presented in this dissertation inspires several potential research directions. In the endeavor to develop a quantitative precipitation proxy using SBB siliciclastic detrital sediments, sediment tracer studies could be applied to the basin and adjacent river catchment sediment system. Applying tracer studies to the SBB sediment system would generate measurements of eroded and transported sediment masses in-stream and resulting sediment yield in SBB, as well as erosion rates and sediment flux rates. The sediment tracers should be applied in the catchment prior to a precipitation event or the rainy season, with subsequent sampling and sample analysis after the event/season; the results would then be compared with the precipitation totals. Several tracers are needed, such that one tracer could be added to hill slopes, and others to in-stream sediments. In addition the tracer study should take place every year for a number of years, with unique tracers each year. This would allow both heavy rainfall years and drought years to be sampled, and enable improved understanding of the erodibility of catchment sediments under multiple hydroclimate regimes, providing more accurate measurements of sediment yield in this dynamic system and climate. Rare earth elements (REEs) are potential tracers that could be applied to the SBB sediment system, as they bind well with the fine grain sizes that are the target for SBB sediments, have low natural background concentrations in soils and sediments, there are many REEs that could be used to tag sediments, they are easily measureable, and are not toxic to the environment (Guzmán et al., 2013; Kimoto et al., 2006).

However the tracer also needs to be immobile under the reducing conditions of SBB, therefore the potential REE tracers will first need to tested for solubility under both oxidizing and reducing conditions.

Scanning X-ray fluorescence (XRF) provides high-resolution, semi-quantitative elemental data of sediment cores and is non-destructive. If a quantitative SBB precipitation proxy is developed, the scanning XRF technique must also be quantitative in order to produce sub-annual paleoprecipitation records. This could be attained through calibration of the scanning XRF data to standard reference materials, a project currently underway at the Large Lakes Observatory at the University of Minnesota Duluth.

In regards to understanding the natural hydroclimate variability in southern California, including the El Niño-Southern Oscillation (ENSO) as discussed in **Chapter 4**, it is critical to target other glacial terminations, as well as investigating full interglacial sequences in order to determine if hydroclimate and ENSO responses to orbital forcing changes are consistent. Well-preserved and laminated sediment cores are needed for this pursuit, and numerous cores have been collected from SBB that correspond to several climate stages, including the Holocene, MIS 5e, and many interstadials in the Late Pleistocene (Marshall, 2012). It is critical to understand the current interglacial and the natural Holocene hydroclimate variability, and as such my colleague, Xiaojing Du of the University of Michigan, is currently investigating the hydroclimate of the mid and late Holocene in southern Cailfornia. Many of the already collected SBB sediment cores are not well laminated, and key climate intervals of rapid warming, such as glacial Terminations I and II, need to be targeted for sediment core extraction. These rapid warming events can be used as analogues for the projected climate state due to global warming, and can be compared with the results of **Chapter 4** to assess hydroclimate variability, particularly ENSO, in response to forcing changes that result in planetary warming.

### 5.4 References

Downs, P.W., Dusterhoff, S.R., Sears, W.A., 2013. Reach-scale channel sensitivity to multiple human activities and natural events: Lower Santa Clara River, California, USA. Geomorphology 189, 121-134.

Fawcett, P.J., Werne, J.P., Anderson, R.S., Heikoop, J.M., Brown, E.T., Berke, M.A., Smith, S.J., Goff, F., Donohoo-Hurley, L., Cisneros-Dozal, L.M., Schouten, S., Sinninghe Damste, J.S., Huang, Y., Toney, J., Fessenden, J., WoldeGabriel, G., Atudorei, V.,

Geissman, J.W., Allen, C.D., 2011. Extended megadroughts in the southwestern United States during Pleistocene interglacials. Nature 470, 518-521.

Fleischer, P., 1972. Mineralogy and sedimentation history, Santa Barbara Basin, California. J. Sed. Res. 42, 49-58.

Guzmán, G., Quinton, J.N., Nearing, M.A., Mabit, L., Gómez, J.A., 2013. Sediment tracers in water erosion studies: current approaches and challenges. J. Soils Sed. 13, 816-833.

Hendy, I.L., Kennett, J.P., Roark, E.B., Ingram, B.L., 2002. Apparent synchroneity of submillennial scale climate events between Greenland and Santa Barbara Basin, California from 30–10 ka. Quatern. Sci. Rev. 21, 1167-1184.

Hendy, I.L., Napier, T.J., Schimmelmann, A., 2015. From extreme rainfall to drought: 250 years of annually resolved sediment deposition in Santa Barbara Basin, California. Quatern. Int. 387, 3-12.

Hill, T.M., Kennett, J.P., Pak, D.K., Behl, R.J., Robert, C., Beaufort, L., 2006. Pre-Bølling warming in Santa Barbara Basin, California: surface and intermediate water records of early deglacial warmth. Quatern. Sci. Rev. 25, 2835-2845.

Inman, D.L., Jenkins, S.A., 1999. Climate change and the episodicity of sediment flux of small California rivers. J. Geol. 107, 251-270.

Kimoto, A., Nearing, M.A., Zhang, X.C., Powell, D.M., 2006. Applicability of rare earth element oxides as a sediment tracer for coarse-textured soils. CATENA 65, 214-221.

Marshall, C.J., 2012. Sedimentation in an active fold and thrust belt, from 1 Ma to Present, Santa Barbara Channel, California, Department of Geological Sciences. California State University, Long Beach, p. 77.

Napier, T.J., Hendy, I.L., in press. The impact of hydroclimate and dam construction on terrigenous detrital sediment composition in a 250-year Santa Barbara Basin record off southern California. Quatern. Int.

Normark, W.R., Piper, D.J.W., Sliter, R.A.Y., 2006. Sea-level and tectonic control of middle to late Pleistocene turbidite systems in Santa Monica Basin, offshore California. Sedimentology 53, 867.

Robert, C., 2004. Late Quaternary variability of precipitation in Southern California and climatic implications: clay mineral evidence from the Santa Barbara Basin, ODP Site 893. Quatern. Sci. Rev. 23, 1029-1040.

Schimmelmann, A., 2012. The "coffin lid" effect: flood layers and turbidites in Santa Barbara Basin affect diagenesis of organic matter in underlying varved sediment, in: Besonen, M.R. (Ed.), Second Workshop of the PAGES Varves Working Group, Program and Abstracts, 17-19 March, 2011, Corpus Christi, Texas, USA, pp. 83-86.

Schumann, R.R., Pigati, J.S., McGeehin, J.P., 2016. Fluvial system response to late Pleistocene-Holocene sea-level change on Santa Rosa Island, Channel Islands National Park, California. Geomorphology 268, 322-340.

Slagel, M.J., Griggs, G.B., 2008. Cumulative losses of sand to the California coast by dam impoundment. J. Coast. Res. 24, 571-584.

Warrick, J.A., Farnsworth, K.L., 2009. Sources of sediment to the coastal waters of the Southern California Bight. Geol. Soc. Am. Spec. Pap. 454, 39-52.

Williams, R.P., 1979. Sediment discharge in the Santa Clara River Basin, Ventura and Los Angeles Counties, California, Water-Resources Investigations Report, - ed, p. 51.

Willis, Cope M., Griggs, Gary B., 2003. Reductions in fluvial sediment discharge by coastal dams in California and implications for beach sustainability. J. Geol. 111, 167-182.

# APPENDICES

# APPENDIX A

## Supporting information for Chapter 2: Identification of onshore sources of Santa Barbara Basin flood deposits and glacial sediments

Analytical results of standards measured during analysis of sample elemental compositions (Appendix A Tables A.1 and A.2).

**Table A.1.** Major, minor, and trace element analytical results for laboratory standards GBM908-10 and MRGeo08.

| Standard | Al | Ca | Fe | Ga | In | K | Mg | Na | Nb | Rb | Sr | Ta | Ti | Y | Rb/Sr |
|---|---|---|---|---|---|---|---|---|---|---|---|---|---|---|---|
| **Sample Group** | % | % | % | ppm | ppm | % | % | % | ppm | ppm | ppm | ppm | % | ppm | |
| GBM908-10 Target Range | | | | | | | | | | | | | | | |
| Lower bound | 6.40 | 3.33 | 5.21 | 18.65 | 0.064 | 1.86 | 1.59 | 2.02 | 9.3 | 153.0 | 258 | 0.68 | 0.591 | 36.2 | |
| Upper bound | 7.84 | 4.10 | 6.39 | 22.90 | 0.092 | 2.29 | 1.97 | 2.50 | 11.6 | 187.0 | 316 | 0.97 | 0.733 | 44.5 | |
| **SPR0901-04BC** | | | | | | | | | | | | | | | |
| GBM908-10 | 7.08 | 4.01 | 5.71 | 20.40 | 0.081 | 2.14 | 1.91 | 2.18 | 10.9 | 174.0 | 297 | 0.82 | 0.673 | 39.1 | 0.59 |
| GBM908-10 | 7.23 | 3.84 | 5.62 | 21.00 | 0.069 | 2.26 | 1.88 | 2.26 | 11.1 | 186.0 | 303 | 0.82 | 0.684 | 41.8 | 0.61 |
| GBM908-10 | 7.19 | 3.89 | 5.65 | 21.40 | 0.086 | 2.10 | 1.87 | 2.19 | 10.7 | 176.5 | 301 | 0.75 | 0.666 | 39.9 | 0.59 |
| GBM908-10 | 7.16 | 3.73 | 5.45 | 20.30 | 0.080 | 2.02 | 1.80 | 2.12 | 10.3 | 177.5 | 290 | 0.75 | 0.650 | 37.9 | 0.61 |
| GBM908-10 | 7.39 | 4.01 | 5.84 | 21.40 | 0.067 | 2.22 | 1.89 | 2.30 | 10.3 | 181.5 | 304 | 0.78 | 0.697 | 41.0 | 0.60 |
| GBM908-10 | 7.01 | 3.78 | 5.56 | 19.60 | 0.073 | 2.13 | 1.79 | 2.20 | 9.9 | 160.0 | 291 | 0.72 | 0.648 | 37.9 | 0.55 |
| standard deviation | 0.13 | 0.12 | 0.13 | 0.71 | 0.007 | 0.09 | 0.05 | 0.06 | 0.4 | 8.9 | 6 | 0.04 | 0.019 | 1.6 | 0.02 |
| standard error | 0.05 | 0.05 | 0.05 | 0.29 | 0.003 | 0.04 | 0.02 | 0.03 | 0.2 | 3.6 | 2 | 0.02 | 0.008 | 0.7 | 0.01 |
| **MV0811-14JC** | | | | | | | | | | | | | | | |
| GBM908-10 | 6.98 | 3.64 | 5.40 | 20.7 | 0.074 | 2.07 | 1.78 | 2.11 | 10.1 | 166.0 | 294 | 0.75 | 0.638 | 37.7 | 0.56 |
| GBM908-10 | 6.97 | 3.75 | 5.53 | 20.6 | 0.077 | 2.10 | 1.84 | 2.14 | 10.4 | 173.0 | 293 | 0.73 | 0.659 | 39.1 | 0.59 |
| GBM908-10 | 6.97 | 3.73 | 5.51 | 20.8 | 0.074 | 2.08 | 1.85 | 2.15 | 10.0 | 163.0 | 297 | 0.71 | 0.667 | 35.4 | 0.55 |
| standard deviation | 0.01 | 0.06 | 0.07 | 0.1 | 0.002 | 0.02 | 0.04 | 0.02 | 0.2 | 5.1 | 2 | 0.02 | 0.015 | 1.9 | 0.02 |
| standard error | 0.00 | 0.03 | 0.04 | 0.1 | 0.001 | 0.01 | 0.02 | 0.01 | 0.1 | 3.0 | 1 | 0.01 | 0.009 | 1.1 | 0.01 |
| | | | | | | | | | | | | | | | |
| MRGeo08 Target Range | | | | | | | | | | | | | | | |
| Lower bound | 7.00 | 2.35 | 3.61 | 17.50 | 0.161 | 2.79 | 1.24 | 1.76 | 19.3 | 187.0 | 272 | 1.48 | 0.454 | 24.3 | |
| Upper bound | 8.57 | 2.90 | 4.43 | 21.50 | 0.207 | 3.43 | 1.54 | 2.18 | 23.8 | 229.0 | 332 | 1.92 | 0.566 | 29.9 | |
| **SPR0901-04BC** | | | | | | | | | | | | | | | |
| MRGeo08 | 7.57 | 2.71 | 3.88 | 18.75 | 0.178 | 3.13 | 1.34 | 1.96 | 20.9 | 211.0 | 308 | 1.49 | 0.497 | 27.8 | 0.69 |
| MRGeo08 | 7.35 | 2.72 | 4.00 | 18.25 | 0.168 | 3.10 | 1.34 | 1.97 | 20.5 | 199.5 | 308 | 1.49 | 0.493 | 27.0 | 0.65 |
| MRGeo08 | 7.63 | 2.80 | 4.24 | 19.40 | 0.171 | 3.31 | 1.37 | 2.11 | 22.8 | 189.0 | 318 | 1.52 | 0.526 | 27.0 | 0.59 |
| MRGeo08 | 7.33 | 2.71 | 4.00 | 18.90 | 0.172 | 3.20 | 1.32 | 2.08 | 22.1 | 191.5 | 326 | 1.55 | 0.512 | 27.8 | 0.59 |
| MRGeo08 | 6.67 | 2.42 | 3.60 | 18.35 | 0.171 | 2.84 | 1.19 | 1.85 | 20.5 | 172.0 | 285 | 1.60 | 0.457 | 23.9 | 0.60 |
| MRGeo08 | 7.63 | 2.81 | 4.15 | 18.95 | 0.159 | 3.31 | 1.40 | 2.10 | 21.1 | 186.0 | 325 | 1.64 | 0.53 | 27.2 | 0.57 |
| MRGeo08 | 7.68 | 2.67 | 3.98 | 18.70 | 0.173 | 3.19 | 1.36 | 2.03 | 22.6 | 208.0 | 315 | 1.52 | 0.502 | 29.0 | 0.66 |
| MRGeo08 | 7.48 | 2.67 | 4.01 | 18.25 | 0.174 | 3.18 | 1.32 | 2.03 | 22.0 | 192.5 | 311 | 1.52 | 0.489 | 27.0 | 0.62 |
| standard | 0.33 | 0.12 | 0.19 | 0.40 | 0.006 | 0.15 | 0.06 | 0.09 | 0.9 | 12.5 | 13 | 0.05 | 0.023 | 1.5 | 0.04 |

| | | | | | | | | | | | | | | | |
|---|---|---|---|---|---|---|---|---|---|---|---|---|---|---|---|
| deviation | | | | | | | | | | | | | | | |
| standard error | 0.12 | 0.04 | 0.07 | 0.14 | 0.002 | 0.05 | 0.02 | 0.03 | 0.3 | 4.4 | 5 | 0.02 | 0.008 | 0.5 | 0.01 |
| | | | | | | | | | | | | | | | |
| **MV0811-14JC** | | | | | | | | | | | | | | | |
| MRGeo08 | 7.00 | 2.57 | 3.87 | 19.05 | 0.175 | 3.04 | 1.29 | 2.00 | 20.7 | 175.5 | 310 | 1.44 | 0.499 | 26.0 | 0.57 |
| MRGeo08 | 7.25 | 2.55 | 3.80 | 18.30 | 0.180 | 3.03 | 1.29 | 1.93 | 21.6 | 199.5 | 304 | 1.53 | 0.492 | 27.9 | 0.66 |
| MRGeo08 | 7.51 | 2.52 | 3.89 | 18.70 | 0.174 | 3.11 | 1.32 | 1.91 | 19.7 | 197.0 | 307 | 1.48 | 0.472 | 26.3 | 0.64 |
| standard | | | | | | | | | | | | | | | |
| deviation | 0.26 | 0.03 | 0.05 | 0.38 | 0.003 | 0.04 | 0.02 | 0.05 | 1.0 | 13.2 | 3 | 0.05 | 0.014 | 1.0 | 0.05 |
| standard error | 0.15 | 0.01 | 0.03 | 0.22 | 0.002 | 0.03 | 0.01 | 0.03 | 0.5 | 7.6 | 2 | 0.03 | 0.008 | 0.6 | 0.03 |
| | | | | | | | | | | | | | | | |
| **Stream bed sediment samples, ODP 893A glacial samples** | | | | | | | | | | | | | | | |
| MRGeo08 | 7.52 | 2.70 | 4.03 | 20.30 | 0.189 | 3.28 | 1.34 | 2.04 | 22.0 | 200.0 | 311 | 1.68 | 0.515 | 26.7 | 0.64 |
| MRGeo08 | 7.15 | 2.62 | 3.92 | 19.65 | 0.180 | 3.21 | 1.28 | 2.00 | 21.3 | 184.0 | 303 | 1.59 | 0.497 | 25.5 | 0.61 |
| standard | | | | | | | | | | | | | | | |
| deviation | 0.26 | 0.06 | 0.08 | 0.46 | 0.006 | 0.05 | 0.04 | 0.03 | 0.5 | 11.3 | 6 | 0.06 | 0.013 | 0.8 | 0.03 |
| standard error | 0.19 | 0.04 | 0.06 | 0.33 | 0.005 | 0.03 | 0.03 | 0.02 | 0.4 | 8.0 | 4 | 0.04 | 0.009 | 0.6 | 0.02 |

**Table A.2.** Rare Earth Element analytical results for internal laboratory standards JA-1 and BCR-2.

| Sample Name | La (ppm) | 2σ | Ce (ppm) | 2σ | Pr (ppm) | 2σ | Nd (ppm) | 2σ | Sm (ppm) | 2σ |
|---|---|---|---|---|---|---|---|---|---|---|
| **JA-1** | 4.9 | 0.1 | 13.2 | 0.3 | 2.1 | 0.1 | 10.6 | 0.2 | 3.4 | 0.3 |
| **JA-1** | 4.8 | 0.1 | 13.0 | 0.4 | 2.0 | 0.1 | 10.4 | 0.3 | 3.3 | 0.2 |
| Error (%) | 0.9 | | 0.7 | | 1.4 | | 1.8 | | 0.8 | |
| GeoRem Preferred Values | 4.88 | 0.13 | 13.15 | 0.58 | 2.082 | 0.054 | 10.69 | 0.29 | 3.396 | 0.077 |
| **BCR-2** | 24.5 | 0.6 | 54.0 | 1.3 | 6.7 | 0.2 | 28.3 | 0.7 | 6.5 | 0.3 |
| Error (%) | 2.4 | | 1.7 | | 1.9 | | 0.0 | | 0.1 | |
| GeoRem Preferred Values | 25.1 | 0.2 | 53.1 | 0.3 | 6.8 | 0.0 | 28.3 | 0.4 | 6.5 | 0.0 |

| Sample Name | Eu (ppm) | 2σ | Gd (ppm) | 2σ | Dy (ppm) | 2σ | Er (ppm) | 2σ | Yb (ppm) | 2σ |
|---|---|---|---|---|---|---|---|---|---|---|
| **JA-1** | 1.1 | 0.1 | 4.1 | 0.2 | 4.7 | 0.2 | 3.0 | 0.1 | 3.0 | 0.1 |
| **JA-1** | 1.1 | 0.1 | 4.0 | 0.2 | 4.7 | 0.1 | 3.0 | 0.2 | 2.9 | 0.1 |
| Error (%) | 0.0 | | 2.1 | | 1.0 | | 0.1 | | 0.9 | |
| GeoRem Preferred Values | 1.112 | 0.027 | 4.15 | 0.12 | 4.75 | 0.11 | 2.959 | 0.065 | 2.949 | 0.085 |
| **BCR-2** | 2.0 | 0.1 | 6.5 | 0.3 | 6.4 | 0.3 | 3.7 | 0.1 | 3.4 | 0 |
| Error (%) | 1.5 | | 4.1 | | 0.0 | | 0.4 | | 0.5 | |
| GeoRem Preferred Values | 2.0 | 0.0 | 6.8 | 0.1 | 6.4 | 0.1 | 3.7 | 0.0 | 3.4 | 0.036 |

| Sample Name | Sm/Nd | La/Yb |
|---|---|---|
| **JA-1** | 0.3213 | 1.64 |
| **JA-1** | 0.3207 | 1.67 |
| Standard deviation | 0.0004 | 0.02 |

# APPENDIX B

## Supporting information for Chapter 3: The impact of historic precipitation events and dam construction on terrigenous detrital sediment composition in a 250-year Santa Barbara Basin record off southern California

### Derivation of Mean ENSO and PDO Indices

To enable linear regression between SPR0901-04BC sample geochemical and mineralogical data with the El Niño-Southern Oscillation (ENSO) Index, the Pacific Decadal Oscillation Index (PDO), the temporal resolution of the monthly ENSO and PDO Indices, respectively, had to be reduced so that they matched the temporal resolution of the sediment core age model, and thus the time span recorded by each individual sample. This combination was done by grouping the monthly values into bins that corresponded to the time span of each individual core sample to which the respective climate index overlapped in time. The mean value was then calculated for each time span bin (Table B.1).

### Derivation of Summed Precipitation and Ventura River Discharge Records

To enable linear regression between SPR0901-04BC sample geochemical and mineralogical data with the precipitation and river discharge records, the monthly Santa Barbara, California precipitation values, and the daily Ventura River discharge values (USGS gauge 11118500), respectively, had to be combined so that the temporal resolution of these records matched that of the sediment core age model, and thus the time span recorded by each individual sample. The combination was done by grouping the monthly and daily values, respectively, into bins that corresponded to the time span of each individual core sample to which the respective hydrologic variable overlapped in time. The values in each time span bin were then summed (Table B.1). The sediments in each core sample reflect a catchment response to each

precipitation and runoff event, not simply the average value over a period of time, thus a summation operation was chosen instead of a mean operation.

**Table B.1.** Modified climate and weather data.

| Sample Time/Age Span | | Climate Index | | Summed Monthly Santa Barbara, CA Precipitation (mm) | Summed Daily Ventura River Discharge (cfs) |
|---|---|---|---|---|---|
| Sample Age at Base (yr) | Sample Age at Top (yr) | ENSO Index Mean (SSTA [ºC]) | PDO Index Mean | | |
| 2005.00 | 2007.50 | 0.15 | 0.24 | 1544.83 | 140363.50 |
| 2002.50 | 2005.00 | 0.48 | 0.68 | 1033.27 | 14822.53 |
| 2000.00 | 2002.50 | -0.13 | -0.53 | 1422.15 | 47640.21 |
| 1996.33 | 2000.00 | 0.41 | 0.26 | 2034.54 | 149411.99 |
| 1992.67 | 1996.33 | 0.15 | 0.68 | 2528.32 | 249261.75 |
| 1989.00 | 1992.67 | 0.32 | -0.08 | 1354.58 | 36763.64 |
| 1985.73 | 1989.00 | 0.20 | 1.10 | 1240.54 | 26467.60 |
| 1982.00 | 1985.73 | 0.45 | 0.81 | 2027.17 | 125803.61 |
| 1978.33 | 1982.00 | 0.00 | 0.47 | 1681.48 | 94419.39 |
| 1974.67 | 1978.33 | -0.16 | -0.12 | 2128.52 | 118939.79 |
| 1971.00 | 1974.67 | -0.19 | -0.93 | 1524.25 | 34505.11 |
| 1968.67 | 1971.00 | 0.05 | -0.28 | 1192.02 | 134307.59 |
| 1966.33 | 1968.67 | -0.41 | -0.54 | 2130.04 | 17354.00 |
| 1964.00 | 1966.33 | 0.09 | -0.54 | 925.32 | 19064.30 |
| 1961.25 | 1964.00 | -0.10 | -1.02 | 1169.67 | 31155.20 |
| 1958.50 | 1961.25 | -0.08 | 0.15 | 733.04 | 5386.10 |
| 1952.67 | 1958.50 | -0.17 | -0.64 | 2830.32 | 95234.70 |
| 1946.83 | 1952.67 | -0.11 | -0.87 | 2216.15 | 70060.98 |
| 1941.00 | 1946.83 | -0.26 | 0.32 | 3003.30 | 270955.20 |
| 1936.50 | 1941.00 | -0.04 | 0.71 | 2088.90 | 168478.60 |
| 1932.00 | 1936.50 | 0.24 | 0.48 | 2020.06 | 78396.20 |
| 1927.00 | 1932.00 | 0.49 | 0.27 | 1901.70 | 6951.50 |
| 1922.00 | 1927.00 | -0.04 | 0.35 | 1997.71 | |
| 1917.00 | 1922.00 | 0.07 | -0.33 | 2104.90 | |
| 1913.00 | 1917.00 | -0.11 | 0.10 | 2424.68 | |
| 1909.00 | 1913.00 | -0.43 | -0.05 | 2577.34 | |
| 1905.50 | 1909.00 | -0.03 | 0.34 | 1850.14 | |
| 1902.00 | 1905.50 | 0.37 | 0.32 | 1829.31 | |
| 1899.20 | 1902.00 | 0.62 | | | |
| 1896.40 | 1899.20 | 0.24 | | | |
| 1893.60 | 1896.40 | -0.11 | | | |
| 1890.80 | 1893.60 | -0.50 | | | |
| 1888.00 | 1890.80 | 0.36 | | | |
| 1882.75 | 1888.00 | 0.04 | | | |
| 1877.50 | 1882.75 | 0.32 | | | |
| 1872.25 | 1877.50 | -0.53 | | | |
| 1867.00 | 1872.25 | -0.15 | | | |
| | Skewness | 0.00 | -0.28 | -0.01 | 1.02 |
| | Kurtosis | -0.53 | -0.70 | -0.46 | 0.54 |

Note:

Data sources located in manuscript figure captions.

The Ventura River discharge record is the longest, most continuous record in the study area, and thus was used for linear correlations. The Ventura, Santa Clara, and Santa Ynez river hydrographs are overlapped in the figures in the manuscript to account for portions were data is missing in some records. The hydrographs are plotted separately here (Figure B.1).

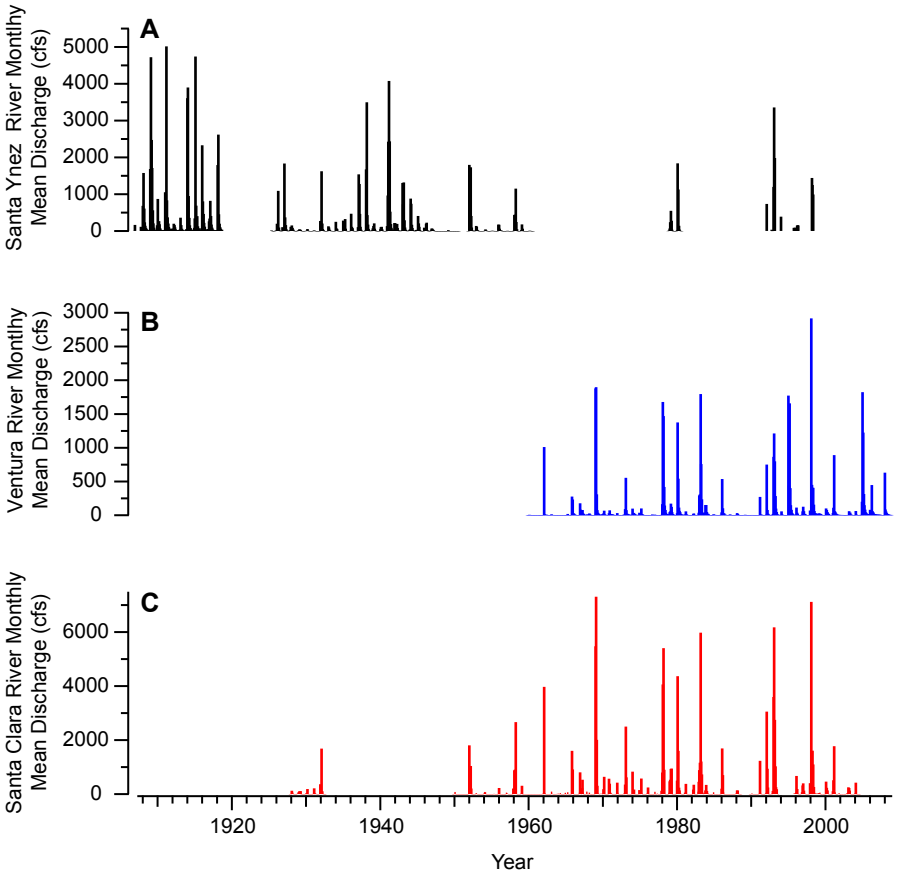


**Figure B.1.** Monthly mean discharge for major rivers in the study area.
A. Santa Ynez River (black; USGS site number 11133500), B. Ventura River (blue; USGS site number 11118500), and C. Santa Clara River (red; USGS site number 11114000).

## Data Tables

Most of the data analyzed in the accompanying manuscript is available in the tables below. Unmodified climate, weather, and river discharge data (i.e. ENSO Index, PDO Index, Santa Barbara, California precipitation record, and Ventura River Discharge) is not included in the tables, as the data sources have been provided in the manuscript. Raw X-ray diffraction (XRD) data, both bulk and clay size fraction (<2 μm) for each sample, is available upon request.

**Table B.2.** Santa Barbara Basin box core SPR0901-04BC sample detrital elemental concentrations and CIA Index data.

| Sample Depth Range in Core | | Sample Time/Age Span | | Core Sample Elemental Concentrations | | | | | | | | | Weathering Index |
|---|---|---|---|---|---|---|---|---|---|---|---|---|---|
| Sample Depth at Top (cm) | Sample Depth at Base (cm) | Sample Age at Base (yr) | Sample Age at Top (yr) | Al (%) | Ca* (%)[1] | Fe (%) | K (%) | Mg (%) | Mn (ppm) | Transformed Mn[2] | Na (%) | Ti (%) | CIA[3] |
| 0 | 1 | 2005.00 | 2007.50 | 5.65 | 4.34 | 3.77 | 1.78 | 1.73 | 245 | 2.39 | 3.72 | 0.323 | 33.06 |
| 1 | 2 | 2002.50 | 2005.00 | 5.63 | 3.23 | 3.83 | 1.75 | 1.70 | 254 | 2.40 | 3.91 | 0.324 | 35.68 |
| 2 | 3 | 2000.00 | 2002.50 | 5.99 | 2.75 | 3.58 | 1.82 | 1.72 | 263 | 2.42 | 3.57 | 0.346 | 39.57 |
| 3 | 4 | 1996.33 | 2000.00 | 6.42 | 2.52 | 3.79 | 1.94 | 1.77 | 280 | 2.45 | 3.30 | 0.362 | 42.71 |
| 4 | 5 | 1992.67 | 1996.33 | 6.30 | 2.84 | 3.69 | 1.89 | 1.69 | 275 | 2.44 | 3.17 | 0.358 | 41.59 |
| 5 | 6 | 1989.00 | 1992.67 | 6.09 | 3.06 | 3.59 | 1.86 | 1.65 | 272 | 2.43 | 3.29 | 0.352 | 39.67 |
| 6 | 7 | 1985.73 | 1989.00 | 6.01 | 3.63 | 3.58 | 1.83 | 1.69 | 267 | 2.43 | 3.42 | 0.349 | 37.16 |
| 7 | 8 | 1982.00 | 1985.73 | 6.27 | 3.06 | 3.64 | 1.91 | 1.74 | 277 | 2.44 | 3.43 | 0.363 | 39.85 |
| 8 | 9 | 1978.33 | 1982.00 | 6.60 | 1.88 | 3.86 | 1.98 | 1.77 | 287 | 2.46 | 3.20 | 0.366 | 46.32 |
| 9 | 10 | 1974.67 | 1978.33 | 6.02 | 3.60 | 3.71 | 1.84 | 1.66 | 262 | 2.42 | 3.50 | 0.347 | 37.07 |
| 10 | 11 | 1971.00 | 1974.67 | 6.19 | 3.37 | 3.70 | 1.92 | 1.69 | 271 | 2.43 | 3.51 | 0.358 | 38.27 |
| 11 | 12 | 1968.67 | 1971.00 | 6.57 | 3.23 | 3.77 | 2.01 | 1.76 | 282 | 2.45 | 3.33 | 0.366 | 40.53 |
| 12 | 13 | 1966.33 | 1968.67 | 6.04 | 3.53 | 3.82 | 1.84 | 1.61 | 252 | 2.40 | 3.69 | 0.332 | 36.83 |
| 13 | 14 | 1964.00 | 1966.33 | 6.00 | 3.53 | 3.67 | 1.80 | 1.55 | 252 | 2.40 | 3.51 | 0.326 | 37.22 |
| 14 | 15 | 1961.25 | 1964.00 | 6.21 | 3.91 | 3.66 | 1.91 | 1.70 | 275 | 2.44 | 3.64 | 0.364 | 36.40 |
| 15 | 16 | 1958.50 | 1961.25 | 6.38 | 3.56 | 3.67 | 2.01 | 1.77 | 283 | 2.45 | 3.58 | 0.374 | 38.06 |
| 16 | 17 | 1952.67 | 1958.50 | 6.58 | 2.97 | 3.89 | 2.04 | 1.85 | 285 | 2.45 | 3.72 | 0.388 | 40.24 |
| 17 | 18 | 1946.83 | 1952.67 | 6.19 | 3.80 | 3.72 | 1.91 | 1.74 | 268 | 2.43 | 3.70 | 0.367 | 36.47 |
| 18 | 19 | 1941.00 | 1946.83 | 6.44 | 3.21 | 3.66 | 2.03 | 1.75 | 280 | 2.45 | 3.59 | 0.371 | 39.34 |
| 19 | 20 | 1936.50 | 1941.00 | 6.03 | 3.18 | 3.45 | 1.91 | 1.67 | 262 | 2.42 | 3.70 | 0.351 | 37.74 |
| 20 | 21 | 1932.00 | 1936.50 | 6.42 | 2.83 | 3.61 | 1.98 | 1.78 | 274 | 2.44 | 3.88 | 0.369 | 39.75 |
| 21 | 22 | 1927.00 | 1932.00 | 6.75 | 3.05 | 3.73 | 2.11 | 1.87 | 287 | 2.46 | 3.81 | 0.384 | 40.22 |
| 22 | 23 | 1922.00 | 1927.00 | 6.52 | 3.44 | 3.71 | 2.02 | 1.86 | 274 | 2.44 | 3.94 | 0.376 | 37.96 |
| 23 | 24 | 1917.00 | 1922.00 | 6.31 | 3.08 | 3.57 | 1.98 | 1.79 | 269 | 2.43 | 3.73 | 0.365 | 38.94 |
| 24 | 25 | 1913.00 | 1917.00 | 6.31 | 3.70 | 3.61 | 2.02 | 1.80 | 281 | 2.45 | 3.77 | 0.377 | 36.87 |
| 25 | 26 | 1909.00 | 1913.00 | 6.24 | 3.37 | 3.65 | 1.99 | 1.82 | 267 | 2.43 | 3.87 | 0.364 | 37.38 |
| 26 | 27 | 1905.50 | 1909.00 | 6.56 | 3.31 | 3.77 | 2.06 | 1.89 | 279 | 2.45 | 3.83 | 0.381 | 38.73 |
| 27 | 28 | 1902.00 | 1905.50 | 6.33 | 4.02 | 4.13 | 1.93 | 1.85 | 343 | 2.54 | 3.94 | 0.365 | 35.77 |
| 28 | 29 | 1899.20 | 1902.00 | 6.53 | 3.39 | 3.72 | 2.02 | 1.87 | 275 | 2.44 | 3.72 | 0.374 | 38.75 |
| 29 | 30 | 1896.40 | 1899.20 | 6.07 | 3.57 | 3.74 | 1.91 | 1.86 | 266 | 2.42 | 4.28 | 0.364 | 35.25 |
| 30 | 31 | 1893.60 | 1896.40 | 6.23 | 3.95 | 3.59 | 1.96 | 1.81 | 275 | 2.44 | 3.78 | 0.368 | 35.93 |
| 31 | 32 | 1890.80 | 1893.60 | 6.21 | 3.82 | 3.58 | 1.98 | 1.82 | 270 | 2.43 | 3.96 | 0.359 | 35.75 |

| | | | | | | | | | | | | | |
|---|---|---|---|---|---|---|---|---|---|---|---|---|---|
| 32 | 33 | 1888.00 | 1890.80 | 6.20 | 3.86 | 3.70 | 1.98 | 1.90 | 271 | 2.43 | 4.19 | 0.363 | 35.07 |
| 33 | 34 | 1882.75 | 1888.00 | 6.39 | 3.30 | 3.66 | 2.03 | 1.89 | 277 | 2.44 | 3.77 | 0.371 | 38.36 |
| 34 | 35 | 1877.50 | 1882.75 | 5.85 | 4.44 | 3.49 | 1.87 | 1.75 | 264 | 2.42 | 4.02 | 0.339 | 32.81 |
| 35 | 36 | 1872.25 | 1877.50 | 6.16 | 4.05 | 3.63 | 1.98 | 1.79 | 278 | 2.44 | 3.83 | 0.356 | 35.27 |
| 36 | 37 | 1867.00 | 1872.25 | 6.23 | 3.74 | 3.68 | 1.97 | 1.79 | 281 | 2.45 | 3.84 | 0.357 | 36.38 |
| 37 | 38 | 1864.35 | 1867.00 | 6.34 | 4.13 | 3.77 | 2.03 | 1.81 | 287 | 2.46 | 3.70 | 0.365 | 35.93 |
| 38 | 39 | 1861.83 | 1864.35 | 7.19 | 2.13 | 4.09 | 2.39 | 1.87 | 344 | 2.54 | 3.34 | 0.422 | 46.03 |
| 39 | 40 | 1859.00 | 1861.83 | 7.01 | 2.56 | 4.08 | 2.26 | 1.82 | 332 | 2.52 | 3.39 | 0.410 | 43.82 |
| 40 | 41 | 1852.00 | 1859.00 | 6.19 | 3.28 | 3.68 | 2.03 | 1.75 | 277 | 2.44 | 3.29 | 0.359 | 39.01 |
| 41 | 42 | 1845.00 | 1852.00 | 6.31 | 4.18 | 3.64 | 2.01 | 1.76 | 278 | 2.44 | 3.54 | 0.360 | 36.09 |
| 42 | 43 | 1838.00 | 1845.00 | 6.45 | 1.92 | 3.73 | 2.10 | 1.73 | 287 | 2.46 | 3.36 | 0.368 | 44.70 |
| 43 | 44 | 1833.69 | 1838.00 | 6.57 | 3.06 | 3.81 | 2.12 | 1.72 | 294 | 2.47 | 3.25 | 0.378 | 41.16 |
| 44 | 45 | 1829.38 | 1833.69 | 6.63 | 2.96 | 3.87 | 2.16 | 1.75 | 295 | 2.47 | 3.33 | 0.381 | 41.42 |
| 45 | 46 | 1825.08 | 1829.38 | 6.66 | 2.82 | 3.88 | 2.17 | 1.76 | 295 | 2.47 | 3.33 | 0.382 | 42.00 |
| 46 | 47 | 1820.77 | 1825.08 | 6.73 | 3.13 | 3.89 | 2.16 | 1.76 | 295 | 2.47 | 3.25 | 0.383 | 41.43 |
| 47 | 48 | 1816.46 | 1820.77 | 6.58 | 2.38 | 3.77 | 2.13 | 1.71 | 292 | 2.47 | 3.25 | 0.378 | 43.67 |
| 48 | 49 | 1813.23 | 1816.46 | 6.62 | 2.56 | 3.75 | 2.16 | 1.66 | 279 | 2.45 | 3.15 | 0.380 | 43.41 |
| 49 | 50 | 1810.00 | 1813.23 | 6.27 | 1.95 | 3.11 | 2.07 | 1.36 | 275 | 2.44 | 2.89 | 0.351 | 45.71 |
| 50 | 51 | 1804.91 | 1810.00 | 5.97 | 2.65 | 3.09 | 1.94 | 1.42 | 267 | 2.43 | 3.01 | 0.343 | 41.42 |
| 51 | 52 | 1799.81 | 1804.91 | 5.82 | 3.28 | 3.14 | 1.85 | 1.56 | 261 | 2.42 | 3.21 | 0.334 | 38.10 |
| 52 | 53 | 1794.72 | 1799.81 | 5.68 | 3.57 | 3.16 | 1.80 | 1.59 | 254 | 2.40 | 3.29 | 0.323 | 36.42 |
| 53 | 54 | 1788.77 | 1794.72 | 5.93 | 3.54 | 3.30 | 1.91 | 1.62 | 270 | 2.43 | 3.27 | 0.343 | 37.40 |
| 54 | 55 | 1782.83 | 1788.77 | 5.93 | 3.23 | 3.27 | 1.93 | 1.62 | 271 | 2.43 | 3.23 | 0.344 | 38.52 |
| 55 | 56 | 1776.89 | 1782.83 | 5.77 | 2.82 | 3.31 | 1.88 | 1.61 | 260 | 2.41 | 3.33 | 0.334 | 39.05 |
| 56 | 57 | 1770.94 | 1776.89 | 6.04 | 3.78 | 3.44 | 1.92 | 1.66 | 268 | 2.43 | 3.40 | 0.344 | 36.74 |
| 57 | 58 | 1765.00 | 1770.94 | 6.05 | 3.52 | 3.47 | 1.96 | 1.65 | 272 | 2.43 | 3.31 | 0.347 | 37.76 |
| 58 | 59 | 1763.00 | 1765.00 | 6.56 | 2.31 | 3.83 | 2.08 | 1.73 | 284 | 2.45 | 3.25 | 0.367 | 43.96 |
| 59 | 60 | 1761.00 | 1763.00 | 7.12 | 1.24 | 4.04 | 2.30 | 1.85 | 294 | 2.47 | 2.66 | 0.419 | 52.72 |
| 60 | 61 | 1759.00 | 1761.00 | 7.37 | 1.97 | 4.13 | 2.36 | 1.81 | 316 | 2.50 | 2.54 | 0.433 | 50.36 |
| 61 | 62 | 1757.00 | 1759.00 | 5.89 | 1.19 | 3.76 | 1.89 | 1.59 | 267 | 2.43 | 3.26 | 0.334 | 46.66 |
| | | | Skewness | 0.63 | -0.78 | -0.59 | 0.89 | -1.05 | 1.71 | 1.41 | -0.28 | 0.739 | 1.16 |
| | | | Kurtosis | 0.78 | 0.63 | 0.94 | 1.05 | 1.85 | 4.31 | 3.35 | 0.46 | 1.442 | 1.65 |

Note:

[1]Silicate-derived calcium (Fedo et al., 1995; Nesbitt and Young, 1982).

[2]Common logarithm of Mn.

[3]Chemical Index of Alteration (Fedo et al., 1995; Nesbitt and Young, 1982).

**Table B.3.** Santa Barbara Basin box core SPR0901-04BC elemental enrichment factors.

| Sample Depth Range in Core | | Sample Time/Age Span | | Core Sample Elemental Enrichment Factors[1] | | | | | | |
|---|---|---|---|---|---|---|---|---|---|---|
| Sample Depth at Top (cm) | Sample Depth at Base (cm) | Sample Age at Base (yr) | Sample Age at Top (yr) | Al EF | Ca* EF | Fe EF | K EF | Mg EF | Mn EF | Na EF |
| 0 | 1 | 2005.00 | 2007.50 | 1.01 | 2.80 | 1.14 | 0.95 | 1.64 | 0.41 | 55.2 |
| 1 | 2 | 2002.50 | 2005.00 | 1.00 | 2.08 | 1.15 | 0.93 | 1.61 | 0.42 | 57.8 |
| 2 | 3 | 2000.00 | 2002.50 | 1.00 | 1.65 | 1.01 | 0.91 | 1.52 | 0.41 | 49.4 |
| 3 | 4 | 1996.33 | 2000.00 | 1.02 | 1.45 | 1.02 | 0.93 | 1.50 | 0.42 | 43.7 |
| 4 | 5 | 1992.67 | 1996.33 | 1.01 | 1.65 | 1.00 | 0.91 | 1.45 | 0.42 | 42.4 |
| 5 | 6 | 1989.00 | 1992.67 | 0.99 | 1.81 | 0.99 | 0.91 | 1.44 | 0.42 | 44.8 |
| 6 | 7 | 1985.73 | 1989.00 | 0.99 | 2.17 | 1.00 | 0.91 | 1.49 | 0.41 | 47.0 |
| 7 | 8 | 1982.00 | 1985.73 | 0.99 | 1.75 | 0.98 | 0.91 | 1.47 | 0.41 | 45.3 |
| 8 | 9 | 1978.33 | 1982.00 | 1.04 | 1.07 | 1.03 | 0.94 | 1.48 | 0.42 | 41.9 |
| 9 | 10 | 1974.67 | 1978.33 | 1.00 | 2.16 | 1.04 | 0.92 | 1.47 | 0.41 | 48.3 |
| 10 | 11 | 1971.00 | 1974.67 | 0.99 | 1.96 | 1.01 | 0.93 | 1.45 | 0.41 | 47.0 |
| 11 | 12 | 1968.67 | 1971.00 | 1.03 | 1.84 | 1.00 | 0.95 | 1.47 | 0.42 | 43.6 |
| 12 | 13 | 1966.33 | 1968.67 | 1.05 | 2.22 | 1.12 | 0.96 | 1.49 | 0.41 | 53.3 |
| 13 | 14 | 1964.00 | 1966.33 | 1.06 | 2.26 | 1.10 | 0.95 | 1.46 | 0.42 | 51.6 |
| 14 | 15 | 1961.25 | 1964.00 | 0.98 | 2.23 | 0.98 | 0.91 | 1.43 | 0.41 | 47.9 |
| 15 | 16 | 1958.50 | 1961.25 | 0.98 | 1.98 | 0.96 | 0.93 | 1.45 | 0.41 | 45.9 |
| 16 | 17 | 1952.67 | 1958.50 | 0.98 | 1.59 | 0.98 | 0.91 | 1.46 | 0.40 | 45.9 |
| 17 | 18 | 1946.83 | 1952.67 | 0.97 | 2.16 | 0.99 | 0.90 | 1.45 | 0.40 | 48.3 |
| 18 | 19 | 1941.00 | 1946.83 | 1.00 | 1.80 | 0.96 | 0.95 | 1.45 | 0.41 | 46.4 |
| 19 | 20 | 1936.50 | 1941.00 | 0.99 | 1.89 | 0.96 | 0.94 | 1.46 | 0.40 | 50.5 |
| 20 | 21 | 1932.00 | 1936.50 | 1.00 | 1.60 | 0.95 | 0.93 | 1.48 | 0.40 | 50.4 |
| 21 | 22 | 1927.00 | 1932.00 | 1.01 | 1.65 | 0.95 | 0.95 | 1.49 | 0.40 | 47.5 |
| 22 | 23 | 1922.00 | 1927.00 | 1.00 | 1.91 | 0.96 | 0.93 | 1.52 | 0.39 | 50.2 |
| 23 | 24 | 1917.00 | 1922.00 | 0.99 | 1.76 | 0.95 | 0.94 | 1.50 | 0.40 | 49.0 |
| 24 | 25 | 1913.00 | 1917.00 | 0.96 | 2.05 | 0.93 | 0.93 | 1.46 | 0.40 | 47.9 |
| 25 | 26 | 1909.00 | 1913.00 | 0.99 | 1.93 | 0.98 | 0.95 | 1.53 | 0.40 | 50.9 |
| 26 | 27 | 1905.50 | 1909.00 | 0.99 | 1.81 | 0.96 | 0.94 | 1.52 | 0.40 | 48.2 |
| 27 | 28 | 1902.00 | 1905.50 | 1.00 | 2.29 | 1.10 | 0.91 | 1.55 | 0.51 | 51.7 |
| 28 | 29 | 1899.20 | 1902.00 | 1.00 | 1.89 | 0.97 | 0.93 | 1.53 | 0.40 | 47.7 |

| | | | | | | | | | | |
|---|---|---|---|---|---|---|---|---|---|---|
| 29 | 30 | 1896.40 | 1899.20 | 0.96 | 2.04 | 1.00 | 0.91 | 1.57 | 0.40 | 56.3 |
| 30 | 31 | 1893.60 | 1896.40 | 0.97 | 2.23 | 0.95 | 0.92 | 1.51 | 0.40 | 49.2 |
| 31 | 32 | 1890.80 | 1893.60 | 0.99 | 2.22 | 0.97 | 0.95 | 1.55 | 0.41 | 52.9 |
| 32 | 33 | 1888.00 | 1890.80 | 0.98 | 2.21 | 0.99 | 0.94 | 1.61 | 0.40 | 55.3 |
| 33 | 34 | 1882.75 | 1888.00 | 0.99 | 1.85 | 0.96 | 0.95 | 1.56 | 0.40 | 48.7 |
| 34 | 35 | 1877.50 | 1882.75 | 0.99 | 2.72 | 1.00 | 0.95 | 1.58 | 0.42 | 56.8 |
| 35 | 36 | 1872.25 | 1877.50 | 0.99 | 2.37 | 0.99 | 0.96 | 1.54 | 0.42 | 51.6 |
| 36 | 37 | 1867.00 | 1872.25 | 1.00 | 2.18 | 1.00 | 0.95 | 1.54 | 0.43 | 51.5 |
| 37 | 38 | 1864.35 | 1867.00 | 1.00 | 2.36 | 1.01 | 0.96 | 1.52 | 0.43 | 48.6 |
| 38 | 39 | 1861.83 | 1864.35 | 0.98 | 1.05 | 0.94 | 0.98 | 1.36 | 0.44 | 37.9 |
| 39 | 40 | 1859.00 | 1861.83 | 0.98 | 1.30 | 0.97 | 0.95 | 1.36 | 0.44 | 39.6 |
| 40 | 41 | 1852.00 | 1859.00 | 0.99 | 1.90 | 1.00 | 0.98 | 1.49 | 0.42 | 43.9 |
| 41 | 42 | 1845.00 | 1852.00 | 1.01 | 2.42 | 0.99 | 0.97 | 1.50 | 0.42 | 47.1 |
| 42 | 43 | 1838.00 | 1845.00 | 1.01 | 1.09 | 0.99 | 0.99 | 1.44 | 0.42 | 43.8 |
| 43 | 44 | 1833.69 | 1838.00 | 1.00 | 1.68 | 0.98 | 0.97 | 1.40 | 0.42 | 41.2 |
| 44 | 45 | 1829.38 | 1833.69 | 1.00 | 1.61 | 0.99 | 0.98 | 1.41 | 0.42 | 41.9 |
| 45 | 46 | 1825.08 | 1829.38 | 1.00 | 1.54 | 0.99 | 0.98 | 1.41 | 0.42 | 41.8 |
| 46 | 47 | 1820.77 | 1825.08 | 1.01 | 1.70 | 0.99 | 0.98 | 1.41 | 0.42 | 40.7 |
| 47 | 48 | 1816.46 | 1820.77 | 1.00 | 1.31 | 0.97 | 0.97 | 1.39 | 0.42 | 41.2 |
| 48 | 49 | 1813.23 | 1816.46 | 1.00 | 1.40 | 0.96 | 0.98 | 1.34 | 0.40 | 39.7 |
| 49 | 50 | 1810.00 | 1813.23 | 1.03 | 1.16 | 0.86 | 1.02 | 1.19 | 0.42 | 39.5 |
| 50 | 51 | 1804.91 | 1810.00 | 1.00 | 1.61 | 0.88 | 0.98 | 1.27 | 0.42 | 42.0 |
| 51 | 52 | 1799.81 | 1804.91 | 1.00 | 2.04 | 0.92 | 0.96 | 1.43 | 0.42 | 46.1 |
| 52 | 53 | 1794.72 | 1799.81 | 1.01 | 2.30 | 0.95 | 0.96 | 1.51 | 0.43 | 48.8 |
| 53 | 54 | 1788.77 | 1794.72 | 0.99 | 2.15 | 0.94 | 0.96 | 1.45 | 0.43 | 45.7 |
| 54 | 55 | 1782.83 | 1788.77 | 0.99 | 1.95 | 0.93 | 0.97 | 1.44 | 0.43 | 45.0 |
| 55 | 56 | 1776.89 | 1782.83 | 0.99 | 1.76 | 0.97 | 0.97 | 1.48 | 0.42 | 47.8 |
| 56 | 57 | 1770.94 | 1776.89 | 1.01 | 2.29 | 0.97 | 0.97 | 1.48 | 0.42 | 47.4 |
| 57 | 58 | 1765.00 | 1770.94 | 1.00 | 2.11 | 0.97 | 0.98 | 1.46 | 0.42 | 45.7 |
| 58 | 59 | 1763.00 | 1765.00 | 1.03 | 1.31 | 1.02 | 0.98 | 1.45 | 0.42 | 42.4 |
| 59 | 60 | 1761.00 | 1763.00 | 0.98 | 0.62 | 0.94 | 0.95 | 1.35 | 0.38 | 30.4 |
| 60 | 61 | 1759.00 | 1761.00 | 0.98 | 0.95 | 0.93 | 0.94 | 1.28 | 0.39 | 28.1 |
| 61 | 62 | 1757.00 | 1759.00 | 1.01 | 0.74 | 1.10 | 0.98 | 1.46 | 0.43 | 46.8 |

Note:

[1]Enrichment factors (EFs) derived using the average shale elemental concentrations of Turekian and Wedepohl (1961).

**Table B.4.** Santa Barbara Basin box core SPR0901-04BC clay mineral abundances.

| Sample Depth Range in Core | | Sample Time/Age Span | | Clay Mineral Abundance | | | | | |
|---|---|---|---|---|---|---|---|---|---|
| Sample Depth at Top (cm) | Sample Depth at Base (cm) | Sample Age at Base (yr) | Sample Age at Top (yr) | Smectite (001) Peak Area (CPS-2Θ deg) | Transformed Smectite[1] | Illite (001) Peak Area (CPS-2Θ deg) | Transformed Illite[1] | Kaolinite (001) + Chlorite (002) Peak Area (CPS-2Θ deg) | Transformed Kaolinite + Chlorite[2] |
| 0 | 1 | 2005.00 | 2007.50 | 127.16 | 2.10 | 66.91 | 1.83 | 27.72 | 5.26 |
| 1 | 2 | 2002.50 | 2005.00 | 99.84 | 2.00 | 64.72 | 1.81 | 20.70 | 4.55 |
| 2 | 3 | 2000.00 | 2002.50 | 148.19 | 2.17 | 58.52 | 1.77 | 45.50 | 6.75 |
| 3 | 4 | 1996.33 | 2000.00 | 368.50 | 2.57 | 103.05 | 2.01 | 58.47 | 7.65 |
| 4 | 5 | 1992.67 | 1996.33 | 244.15 | 2.39 | 83.20 | 1.92 | 41.76 | 6.46 |
| 5 | 6 | 1989.00 | 1992.67 | 82.32 | 1.92 | 68.64 | 1.84 | 40.02 | 6.33 |
| 6 | 7 | 1985.73 | 1989.00 | 80.08 | 1.90 | 71.76 | 1.86 | 43.68 | 6.61 |
| 7 | 8 | 1982.00 | 1985.73 | 200.17 | 2.30 | 87.09 | 1.94 | 45.60 | 6.75 |
| 8 | 9 | 1978.33 | 1982.00 | 156.24 | 2.19 | 76.12 | 1.88 | 29.26 | 5.41 |
| 9 | 10 | 1974.67 | 1978.33 | 125.91 | 2.10 | 57.46 | 1.76 | 31.08 | 5.57 |
| 10 | 11 | 1971.00 | 1974.67 | 151.70 | 2.18 | 78.32 | 1.89 | 59.80 | 7.73 |
| 11 | 12 | 1968.67 | 1971.00 | 129.88 | 2.11 | 72.40 | 1.86 | 37.20 | 6.10 |
| 12 | 13 | 1966.33 | 1968.67 | 170.20 | 2.23 | 72.24 | 1.86 | 31.08 | 5.57 |
| 13 | 14 | 1964.00 | 1966.33 | 224.72 | 2.35 | 81.90 | 1.91 | 41.28 | 6.42 |
| 14 | 15 | 1961.25 | 1964.00 | 153.66 | 2.19 | 62.56 | 1.80 | 38.80 | 6.23 |
| 15 | 16 | 1958.50 | 1961.25 | 190.24 | 2.28 | 79.04 | 1.90 | 37.52 | 6.13 |
| 16 | 17 | 1952.67 | 1958.50 | 218.96 | 2.34 | 82.46 | 1.92 | 44.48 | 6.67 |
| 17 | 18 | 1946.83 | 1952.67 | 241.90 | 2.38 | 98.70 | 1.99 | 64.68 | 8.04 |
| 18 | 19 | 1941.00 | 1946.83 | 207.36 | 2.32 | 100.00 | 2.00 | 55.08 | 7.42 |
| 19 | 20 | 1936.50 | 1941.00 | 136.64 | 2.14 | 58.68 | 1.77 | 40.32 | 6.35 |
| 20 | 21 | 1932.00 | 1936.50 | 212.52 | 2.33 | 81.32 | 1.91 | 64.80 | 8.05 |
| 21 | 22 | 1927.00 | 1932.00 | 286.12 | 2.46 | 80.24 | 1.90 | 68.40 | 8.27 |
| 22 | 23 | 1922.00 | 1927.00 | 250.40 | 2.40 | 70.72 | 1.85 | 52.16 | 7.22 |
| 23 | 24 | 1917.00 | 1922.00 | 271.40 | 2.43 | 120.48 | 2.08 | 64.26 | 8.02 |
| 24 | 25 | 1913.00 | 1917.00 | 175.44 | 2.24 | 82.46 | 1.92 | 57.20 | 7.56 |
| 25 | 26 | 1909.00 | 1913.00 | 134.16 | 2.13 | 75.96 | 1.88 | 58.68 | 7.66 |
| 26 | 27 | 1905.50 | 1909.00 | 255.36 | 2.41 | 100.00 | 2.00 | 63.58 | 7.97 |
| 27 | 28 | 1902.00 | 1905.50 | 215.84 | 2.33 | 106.50 | 2.03 | 48.00 | 6.93 |
| 28 | 29 | 1899.20 | 1902.00 | 269.76 | 2.43 | 97.66 | 1.99 | 71.40 | 8.45 |

| | | | | | | | | | |
|---|---|---|---|---|---|---|---|---|---|
| 29 | 30 | 1896.40 | 1899.20 | 168.72 | 2.23 | 75.62 | 1.88 | 41.42 | 6.44 |
| 30 | 31 | 1893.60 | 1896.40 | 147.20 | 2.17 | 63.84 | 1.81 | 45.60 | 6.75 |
| 31 | 32 | 1890.80 | 1893.60 | 163.20 | 2.21 | 53.96 | 1.73 | 35.00 | 5.92 |
| 32 | 33 | 1888.00 | 1890.80 | 110.88 | 2.04 | 75.40 | 1.88 | 45.20 | 6.72 |
| 33 | 34 | 1882.75 | 1888.00 | 270.28 | 2.43 | 72.08 | 1.86 | 45.44 | 6.74 |
| 34 | 35 | 1877.50 | 1882.75 | 128.16 | 2.11 | 42.50 | 1.63 | 30.60 | 5.53 |
| 35 | 36 | 1872.25 | 1877.50 | 135.66 | 2.13 | 54.60 | 1.74 | 39.96 | 6.32 |
| 36 | 37 | 1867.00 | 1872.25 | 108.78 | 2.04 | 48.72 | 1.69 | 38.72 | 6.22 |
| 37 | 38 | 1864.35 | 1867.00 | 220.80 | 2.34 | 76.80 | 1.89 | 45.12 | 6.72 |
| 38 | 39 | 1861.83 | 1864.35 | 335.16 | 2.53 | 97.20 | 1.99 | 69.44 | 8.33 |
| 39 | 40 | 1859.00 | 1861.83 | 306.16 | 2.49 | 109.20 | 2.04 | 81.32 | 9.02 |
| 40 | 41 | 1852.00 | 1859.00 | 228.76 | 2.36 | 98.80 | 1.99 | 54.90 | 7.41 |
| 41 | 42 | 1845.00 | 1852.00 | 257.04 | 2.41 | 84.24 | 1.93 | 62.80 | 7.92 |
| 42 | 43 | 1838.00 | 1845.00 | 234.78 | 2.37 | 85.68 | 1.93 | 75.36 | 8.68 |
| 43 | 44 | 1833.69 | 1838.00 | 254.32 | 2.41 | 122.22 | 2.09 | 62.22 | 7.89 |
| 44 | 45 | 1829.38 | 1833.69 | 202.92 | 2.31 | 100.70 | 2.00 | 59.40 | 7.71 |
| 45 | 46 | 1825.08 | 1829.38 | 195.72 | 2.29 | 72.58 | 1.86 | 55.08 | 7.42 |
| 46 | 47 | 1820.77 | 1825.08 | 247.50 | 2.39 | 88.64 | 1.95 | 65.62 | 8.10 |
| 47 | 48 | 1816.46 | 1820.77 | 275.60 | 2.44 | 111.84 | 2.05 | 43.42 | 6.59 |
| 48 | 49 | 1813.23 | 1816.46 | 283.56 | 2.45 | 99.20 | 2.00 | 58.14 | 7.62 |
| 49 | 50 | 1810.00 | 1813.23 | 340.20 | 2.53 | 89.76 | 1.95 | 59.84 | 7.74 |
| 50 | 51 | 1804.91 | 1810.00 | 237.00 | 2.37 | 80.28 | 1.90 | 51.52 | 7.18 |
| 51 | 52 | 1799.81 | 1804.91 | 181.22 | 2.26 | 70.30 | 1.85 | 55.08 | 7.42 |
| 52 | 53 | 1794.72 | 1799.81 | 221.44 | 2.35 | 66.98 | 1.83 | 46.72 | 6.84 |
| 53 | 54 | 1788.77 | 1794.72 | 216.00 | 2.33 | 67.84 | 1.83 | 48.90 | 6.99 |
| 54 | 55 | 1782.83 | 1788.77 | 203.36 | 2.31 | 95.48 | 1.98 | 60.48 | 7.78 |
| 55 | 56 | 1776.89 | 1782.83 | 217.08 | 2.34 | 71.60 | 1.85 | 60.26 | 7.76 |
| 56 | 57 | 1770.94 | 1776.89 | 195.96 | 2.29 | 76.16 | 1.88 | 50.24 | 7.09 |
| 57 | 58 | 1765.00 | 1770.94 | 257.40 | 2.41 | 86.04 | 1.93 | 61.56 | 7.85 |
| 58 | 59 | 1763.00 | 1765.00 | 337.46 | 2.53 | 101.64 | 2.01 | 76.80 | 8.76 |
| 59 | 60 | 1761.00 | 1763.00 | 769.08 | 2.89 | 208.24 | 2.32 | 115.20 | 10.73 |
| 60 | 61 | 1759.00 | 1761.00 | 705.60 | 2.85 | 198.80 | 2.30 | 117.98 | 10.86 |
| 61 | 62 | 1757.00 | 1759.00 | 215.60 | 2.33 | 74.88 | 1.87 | 51.60 | 7.18 |
| | | | Skewness | 2.93 | 0.45 | 2.57 | 0.89 | 1.43 | 0.68 |
| | | | Kurtosis | 11.86 | 1.81 | 9.60 | 2.85 | 4.07 | 1.86 |

Note:
[1]Transformed by taking the common logarithm of the respective clay abundance value.
[2]Transformed by taking the square root of the respective clay abundance value.

**Table B.5.** Santa Barbara Basin catchment area dam information.

| Catchment/Dam Name | Year Built | Catchment Area ($km^2$) | Catchment Area Dammed ($km^2$) | Percentage of Catchment Dammed | Comment |
|---|---|---|---|---|---|
| *Santa Clara River* | | 4204.1[a] | | | |
| Dry Canyon | 1912 | 11.7[b] | 11.65 | 0.28 | Drained 1966 |
| Drinkwater | 1923 | 0.1[b] | 11.73 | 0.28 | |
| St. Francis Dam | 1925 | 96.6[a] | 108.34 | 2.58 | Failed 12 March 1928 |
| Bouquet Canyon | 1934 | 35.2[b] | 46.96 | 1.12 | |
| Santa Felicia | 1955 | 1093.0[b] | 1139.93 | 27.11 | Downstream of Pyramid |
| Pyramid | 1973 | 764.0[b] | 1139.93 | 27.11 | Upstream of Santa Felicia |
| Castaic | 1973 | 398.1[b] | 1526.36 | 36.31 | Downstream of Elderberry |
| Elderberry Forebay | 1974 | 211.3[b] | 1526.36 | 36.31 | Upstream of Castaic |
| Arundell Barranca | 1996 | 7.0[b] | 1533.38 | 36.47 | |
| Stevenson Ranch | 2004 | 13.2[b] | 1546.59 | 36.79 | |
| *Ventura River* | | 584.3[a] | | | |
| Anola | 1924 | 0.3[c] | 0.26 | 0.04 | Upstream of Casitas |
| Matilija | 1949 | 142.4[b] | 142.71 | 24.42 | |
| Casitas | 1959 | 99.2[d] | 241.65 | 41.36 | Downstream of Anola |
| Stewart Canyon Debris Basin | 1963 | 4.9[b] | 246.57 | 42.20 | |
| Senior Canyon | 1964 | 0.1[b] | 246.70 | 42.22 | |
| *Santa Ynez Mountains* | | 974.0[e] | | | |
| Los Carneros, Lake | 1932 | 0.9[b] | 0.88 | 0.09 | |
| Rancho Del Ciervo | 1938 | 2.0[b] | 2.85 | 0.29 | |
| Dos Pueblos | 1946 | 2.3[b] | 5.15 | 0.53 | |
| Lauro | 1952 | 1.8[a] | 6.97 | 0.72 | |
| Glen Anne | 1953 | 1.3[a] | 8.26 | 0.85 | |
| Santa Monica Debris Basin | 1978 | 9.8[b] | 18.10 | 1.86 | |
| Edwards Reservoir | 1985 | 1.2[b] | 19.27 | 1.98 | |
| *Santa Ynez River* | | 2322.2[a] | | | |
| Gibraltar | 1920 | 554.3[b] | 554.26 | 23.87 | Upstream of Bradbury, downstream of Juncal |
| Juncal | 1930 | 36.0[b] | 554.26 | 23.87 | Upstream of Gibraltar, Bradbury |

| | | | | | |
|---|---|---|---|---|---|
| Bradbury | 1953 | 1080.0[d] | 1080.03 | 46.51 | Downstream of Gibraltar, Juncal |
| Alisal Creek | 1971 | 20.2[b] | 1100.23 | 47.38 | |
| *Santa Barbara Basin Total Catchment Area* | | 8084.6 | 2912.78 | 36.03 | |

Note:

[a]Data derived from *StreamStats Program for California*, U.S. Geological Survey, http://water.usgs.gov/osw/streamstats/california.html.

[b]Data from *Dams within the Jurisdiction of the State of California (2014)*, State of California Department of Water Resources, http://www.water.ca.gov/damsafety/docs/Jurisdictional2014.pdf.

[c]Data from *Dams within Jurisdiction of the State of California (Fritzsche and Wong, 1968)*, State of California Department of Water Resources, http://www.water.ca.gov/waterdatalibrary/docs/historic/Bulletins/Bulletin_17/Bulletin_17__1968.pdf.

[d]Data from Projects & Facilities–*Dams*, U.S. Bureau of Reclamation, http://www.usbr.gov/projects/dams.jsp.

[e]Data From Willis and Griggs, 2003.

**Table B.6.** Mean percentage of dammed area in each catchment, and the total Santa Barbara Basin catchment area.

| Sample Time/Age Span | | Catchment | | | | |
|---|---|---|---|---|---|---|
| Sample Age at Base of Sample (yr) | Sample Age at Top of Sample (yr) | Mean Percentage of SBB Catchment Area Dammed | Mean Percentage of SCR Catchment Area Dammed | Mean Percentage of VR Catchment Area Dammed | Mean Percentage of SYM Catchment Area Dammed | Mean Percentage of SYR Catchment Area Dammed |
| 2005.00 | 2007.50 | 36.03 | 36.79 | 42.22 | 1.98 | 47.38 |
| 2002.50 | 2005.00 | 35.95 | 36.63 | 42.22 | 1.98 | 47.38 |
| 2000.00 | 2002.50 | 35.87 | 36.47 | 42.22 | 1.98 | 47.38 |
| 1996.33 | 2000.00 | 35.87 | 36.47 | 42.22 | 1.98 | 47.38 |
| 1992.67 | 1996.33 | 35.78 | 36.31 | 42.22 | 1.98 | 47.38 |
| 1989.00 | 1992.67 | 35.78 | 36.31 | 42.22 | 1.98 | 47.38 |
| 1985.73 | 1989.00 | 35.78 | 36.31 | 42.22 | 1.98 | 47.38 |
| 1982.00 | 1985.73 | 35.77 | 36.31 | 42.22 | 1.89 | 47.38 |
| 1978.33 | 1982.00 | 35.76 | 36.31 | 42.22 | 1.86 | 47.38 |
| 1974.67 | 1978.33 | 35.64 | 36.31 | 42.22 | 0.85 | 47.38 |
| 1971.00 | 1974.67 | 33.18 | 31.57 | 42.22 | 0.85 | 47.38 |
| 1968.67 | 1971.00 | 30.47 | 26.84 | 42.22 | 0.85 | 46.51 |
| 1966.33 | 1968.67 | 30.47 | 26.84 | 42.22 | 0.85 | 46.51 |
| 1964.00 | 1966.33 | 30.61 | 27.11 | 42.22 | 0.85 | 46.51 |
| 1961.25 | 1964.00 | 30.57 | 27.11 | 41.64 | 0.85 | 46.51 |
| 1958.50 | 1961.25 | 30.55 | 27.11 | 41.36 | 0.85 | 46.51 |
| 1952.67 | 1958.50 | 24.82 | 18.45 | 24.42 | 0.85 | 46.51 |
| 1946.83 | 1952.67 | 8.68 | 1.12 | 16.30 | 0.56 | 23.87 |
| 1941.00 | 1946.83 | 7.48 | 1.12 | 0.04 | 0.33 | 23.87 |
| 1936.50 | 1941.00 | 7.47 | 1.12 | 0.04 | 0.24 | 23.87 |
| 1932.00 | 1936.50 | 7.28 | 0.78 | 0.04 | 0.09 | 23.87 |
| 1927.00 | 1932.00 | 7.24 | 0.74 | 0.04 | 0.00 | 23.87 |
| 1922.00 | 1927.00 | 7.48 | 1.20 | 0.03 | 0.00 | 23.87 |
| 1917.00 | 1922.00 | 2.89 | 0.28 | 0.00 | 0.00 | 9.55 |
| 1913.00 | 1917.00 | 0.14 | 0.28 | 0.00 | 0.00 | 0.00 |
| 1909.00 | 1913.00 | 0.04 | 0.07 | 0.00 | 0.00 | 0.00 |
| 1905.50 | 1909.00 | 0.00 | 0.00 | 0.00 | 0.00 | 0.00 |

Note:

Abbreviations: SBB = Santa Barbara Basin, SCR = Santa Clara River, VR = Ventura River, SYM = Santa Ynez Mountains, SYR = Santa Ynez River.

**References**

Fedo, C.M., Nesbitt, H.W., Young, G.M., 1995. Unraveling the effects of potassium metasomatism in sedimentary rocks and paleosols, with implications for paleoweathering conditions and provenance. Geology 23, 921-924.

Moore, D.M., Reynolds, R.C., 1997. X-ray diffraction and the identification and analysis of clay minerals. Oxford University Press, Oxford.

Nesbitt, H.W., Young, G.M., 1982. Early Proterozoic climates and plate motions inferred from major element chemistry of lutites. Nature 299, 715-717.

Turekian, K.K., Wedepohl, K.H., 1961. Distribution of the elements in some major units of the Earth's crust. Geol. Soc. Am. Bull. 72, 175-192.

Willis, Cope M., Griggs, Gary B., 2003. Reductions in fluvial sediment discharge by coastal dams in California and implications for beach sustainability. J. Geol. 111, 167-182.

# APPENDIX C

## Supporting information for Chapter 4: Southern California hydroclimate during deglacial Termination V (~430-420 ka): The persistence of drought, flooding, and interannual precipitation variability

Data from this work will be available on the Pangaea Data Publisher: https://www.pangaea.de.

### 1. PC1 as a recorder of hydroclimate

Hendy et al. (2015) showed that the elemental composition of 20$^{th}$ century SBB sediment can be used as a proxy for river runoff and precipitation, which captures ENSO and PDO variability. In the 20$^{th}$ century, increased relative concentration of siliciclastic sediments are associated with wet years and river runoff into SBB, while decreased siliciclastic sediments are associated with drought (Figure C.1) (Hendy et al., 2015).

We compared the monthly Oceanic Niño Index (ONI), which measures the seasonal sea surface temperature anomalies in the Niño 3.4 region (5ºN–5ºS, 170ºW–120ºW) from multiple centered 30-year base periods that step in 5-year increments (Lindsey, 2013), to a monthly precipitation record from Santa Barbara, California to assess the relationship between the two climate series. We used a running cross-correlation (Matlab scripts *crosscorrelationconfident.m* and *corrcoef.m*, see Appendix C section 5) for this analysis, wherein the Pearson product-correlation coefficient is used to assess the strength of the correlation. Initially the ONI and precipitation records are aligned in time. As the running cross-correlation proceeds, the monthly precipitation record is shifted back in time at monthly time steps, and the correlation coefficient is calculated at each step. The highest correlation coefficient (R=0.109), and the only correlation coefficient to exceed the 95$^{th}$ percentile of the distribution of all values, occurred when the precipitation record was shifted back in time by two months (Figure 4.1). With this configuration, peaks in precipitation align with peaks in the ONI (ONI values >0.5 are El Niño

events) (Figure C.2). This suggests that southern California precipitation has a 2-month lagged response to El Niño events.

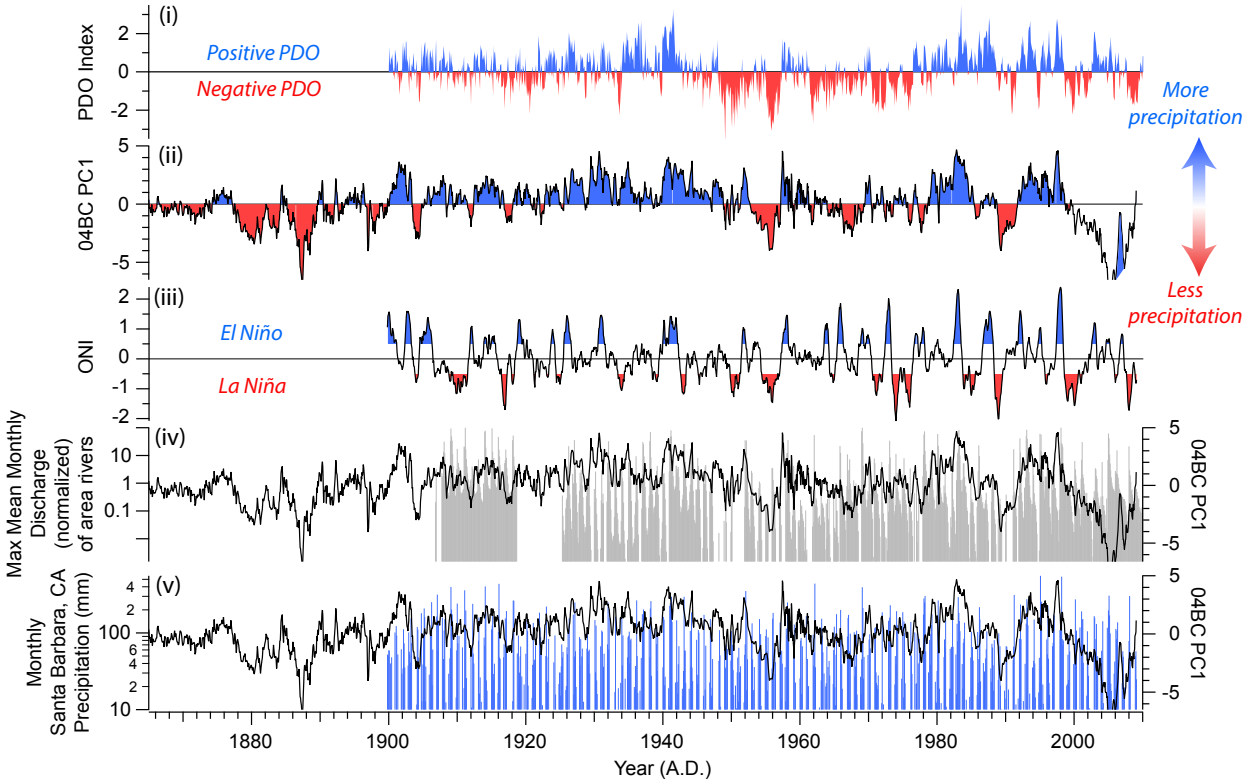


**Figure C.1.** Southern California instrumental hydroclimate records compared to the PC1 paleoprecipitation proxy. (i) The Pacific Decadal Oscillation (PDO) Index (Mantua, 2017; Mantua and Hare, 2002; Mantua et al., 1997). (ii) Sediment core SPR0901-04BC PC1, detrended. Above ~A.D. 2000 is the core top. (iii) The Oceanic Niño Index (ONI) (data from Rayner et al. (2003)). (iv) The maximum mean monthly river discharge (gray bars; log scale) among the Santa Clara River (station USGS 11114000), the Ventura River (station USGS 11118500), and the Santa Ynez River (station USGS 11133500). Each river discharge record was normalized to a 0-100 scale prior to computing the compiled maximum mean discharge. Gaps in the record denote absences in discharge data. Detrended 04BC PC1 (black line) for comparison. (v) Santa Barbara, California monthly precipitation (blue bars, log scale). Detrended 04BC PC1 (black line) for comparison. Precipitation data from County of Santa Barbara Public Works Water Resources Division, site: Santa Barbara Downtown, http://cosb.countyofsb.org/pwd/pwwater.aspx?id=3786; River discharge data from USGS Water Data, http://waterdata.usgs.gov/nwis/inventory.

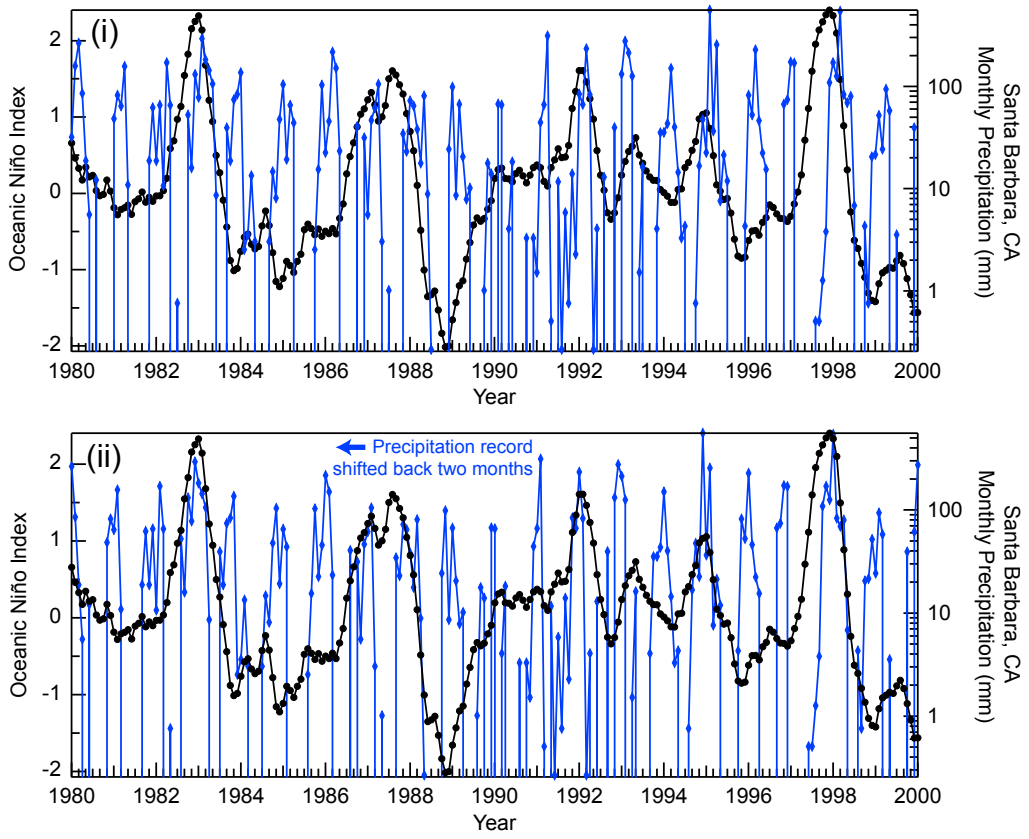


**Figure C.2. (i)** The Oceanic Niño Index (black line) and Santa Barbara, California monthly precipitation records (blue line).
(ii**)** The precipitation record has been shifted back in time by two months. ONI data from Rayner et al. (2003); precipitation data from County of Santa Barbara Public Works Water Resources Division, site: Santa Barbara Downtown, http://cosb.countyofsb.org/pwd/pwwater.aspx?id=3786.

## 2. Analysis of absolute elemental concentrations

Powdered bulk sediment samples were analyzed by ALS Laboratories in Vancouver, Canada for major, minor, and trace elemental concentrations using inductively coupled plasma-mass spectrometry and inductively coupled plasma-atomic emission spectroscopy. Analyses followed the procedure reported in Napier and Hendy (in press). Core SPR0901-04BC was sampled in contiguous 1 cm increments. Cores MV0508-33JPC, -21JPC, and -29JPC were sampled every 10 cm and collected samples were 1 cm in thickness. The standard error of measurements of standards GBM908-10 and MRGeo08 for core 04BC analysis are reported in Napier and Hendy (in press). The standard error of measurements of standards GBM908-10 and MRGeo08 for selected elements during analysis of cores 33JPC, 21JPC, and 29JPC (Table C.1) are as follows: sodium (Na): 1 st. err. = ±0.05 and ±0.02 % respectively; magnesium (Mg): 1 st. err. = ±0.04 and ±0.02 % respectively; aluminum (Al): 1 st. err. = ±0.14 %; potassium (K): 1 st.

err. = ±0.05 and ±0.04 % respectively; calcium (Ca): 1 st. err. = ±0.08 and ±0.04 %, respectively; titanium (Ti): = ± 0.01 %; manganese (Mn): 1 st. err. = ±12 and ±5 ppm; respectively, and iron (Fe): 1 st. err. = ±0.12 and ±0.05 %, respectively.

**Table C.1.** Element analytical results for laboratory standards GBM908-10 and MRGeo08.

| Standard | Al % | Ca % | Fe % | K % | Mg % | Mn ppm | Na % | Ti % |
|---|---|---|---|---|---|---|---|---|
| GBM908-10 Target Range | | | | | | | | |
| Lower bound | 6.40 | 3.33 | 5.21 | 1.86 | 1.59 | 704 | 2.02 | 0.591 |
| Upper bound | 7.84 | 4.10 | 6.39 | 2.29 | 1.97 | 871 | 2.50 | 0.733 |
| GBM908-10 | 7.11 | 3.75 | 5.56 | 2.07 | 1.85 | 833 | 2.15 | 0.654 |
| GBM908-10 | 6.88 | 3.61 | 5.43 | 2.07 | 1.79 | 808 | 2.08 | 0.659 |
| GBM908-10 | 7.36 | 3.87 | 5.83 | 2.23 | 1.93 | 849 | 2.25 | 0.706 |
| Standard Deviation | 0.24 | 0.13 | 0.20 | 0.09 | 0.07 | 21 | 0.09 | 0.029 |
| Standard Error | 0.14 | 0.08 | 0.12 | 0.05 | 0.04 | 12 | 0.05 | 0.017 |
| | | | | | | | | |
| MRGeo08 Target Range | | | | | | | | |
| Lower bound | 7.00 | 2.35 | 3.61 | 2.79 | 1.24 | 506 | 1.76 | 0.454 |
| Upper bound | 8.57 | 2.90 | 4.43 | 3.43 | 1.54 | 630 | 2.18 | 0.566 |
| MRGeo08 | 6.68 | 2.44 | 3.69 | 2.97 | 1.22 | 540 | 1.88 | 0.474 |
| MRGeo08 | 7.34 | 2.57 | 3.96 | 3.21 | 1.32 | 571 | 2.01 | 0.512 |
| MRGeo08 | 7.51 | 2.66 | 3.92 | 3.07 | 1.32 | 559 | 1.98 | 0.513 |
| MRGeo08 | 7.24 | 2.54 | 3.82 | 3.01 | 1.29 | 564 | 1.93 | 0.474 |
| MRGeo08 | 7.09 | 2.6 | 3.88 | 3.04 | 1.28 | 550 | 1.97 | 0.502 |
| Standard Deviation | 0.31 | 0.08 | 0.11 | 0.09 | 0.04 | 12 | 0.05 | 0.020 |
| Standard Error | 0.14 | 0.04 | 0.05 | 0.04 | 0.02 | 5 | 0.02 | 0.009 |

### 3. Core correlation

Offsets in elemental counts occur in the scanning XRF data of 29JPC and 33JPC that are not observed in elemental concentrations, and these were corrected prior to correlation. In 29JPC, the Si XRF count data is offset from the remaining Si XRF count data in core section 2 between 0 and 35.18 cm core section depth. In 33JPC offsets occur in the entirety of section 2 for Si, K, Ti, and Br. All elements used in this study were normalized to coherent scattering to remedy these offsets. This normalization corrected the offsets in 33JPC, but did not correct the Si offset in 29JPC. The Si XRF data in 29JPC section 1 and the offset Si XRF data in 29JPC section 2 were standardized independently to correct the Si offset in core 29JPC. The offsets could be the result of variability in the X-ray tube output and attenuation of fluorescence energy.

Core photos overlain with PC1 are presented in Figures C.3-C.6. Laminated intervals C1 and C2 in 21JPC (7.8 to 107.98 cm) were correlated to laminated interval C of 33JPC (158.54-256.44 cm) with the lineage tool in Analyseries using the respective laminated PC1 data series for each core. Tie points between these laminated intervals of 21JPC and 33JPC were created by matching high-resolution images of core fabric that were overlain with the respective core PC1 data series, and matching the trends in PC1 data series between the sediment cores (Table C.2; Figures C.4-C.6). Laminated interval D of 21JPC (146.42-252.54 cm) and the laminated interval of 29JPC (3.70-67.24 cm) were each correlated to laminated interval D of core 33JPC using the procedure detailed above (Tables C.2 and C.3; Figures C.4-C.6). The laminations in 21JPC and 29JPC continue beyond the base of 33JPC. Correlation proceeded between 21JPC (252.56-272.48 cm) and 29JPC (67.26-87.92 cm) using 29JPC as the reference sediment core, as the laminations in 29JPC are better preserved than in 21JPC.

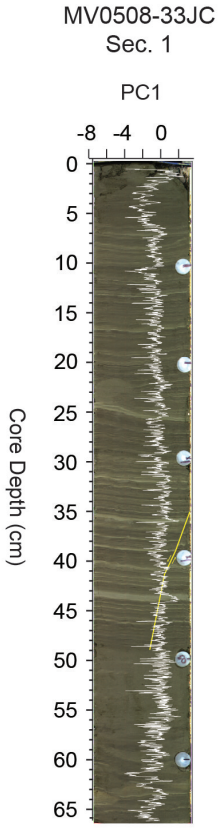


**Figure C.3.** High-resolution core photograph of MV0508-33JPC section 1, with PC1 (white lines). Yellow lines denote offsets in laminations that likely resulted from fault movement.

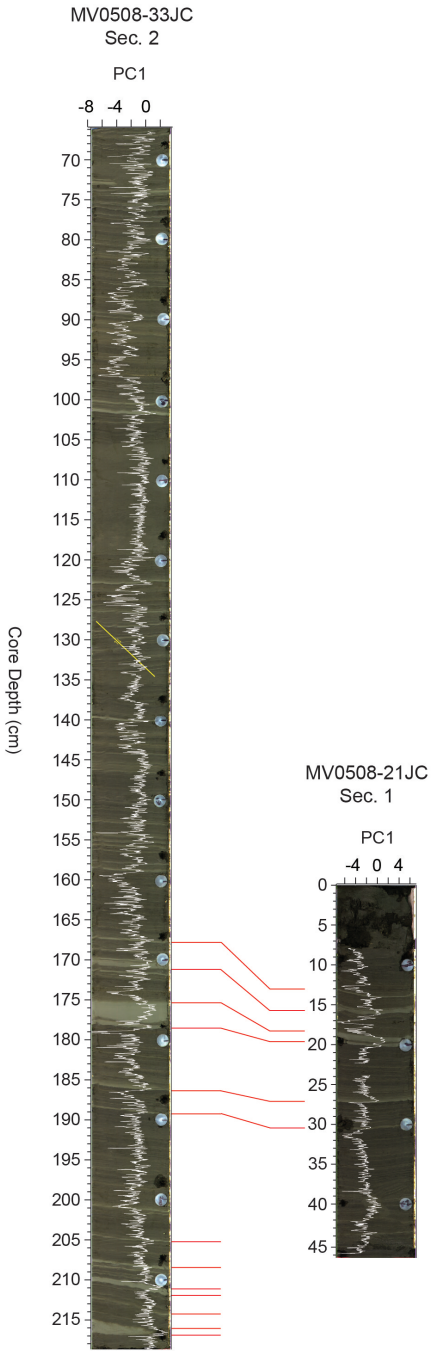


**Figure C.4.** Correlation of MV0508-33JPC section 2 to MV0508-21JPC section 1.
Red lines denote tie-points (Appendix C Table C.2). High-resolution core photographs are overlain with the computed PC1 of each core (white lines). Yellow lines denote offsets in laminations that likely resulted from fault movement.

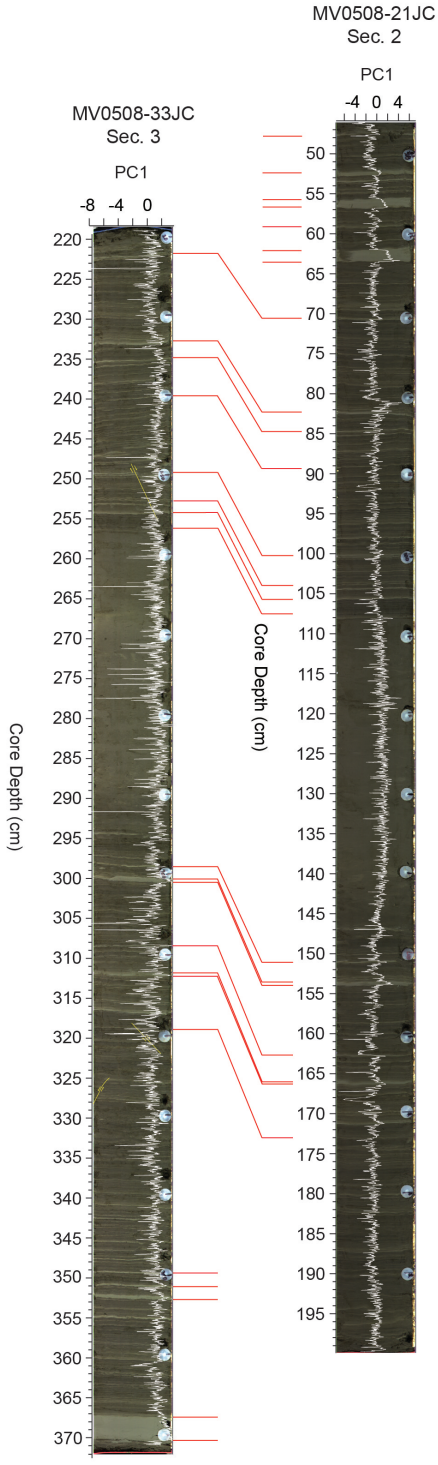


**Figure C.5.** Correlation of MV0508-33JPC section 3 to MV0508-21JPC section 2.
Red lines denote tie-points (Appendix C Table C.2). High-resolution core photographs are overlain with the computed PC1 of each core (white lines). Yellow lines denote offsets in laminations that likely resulted from fault movement.

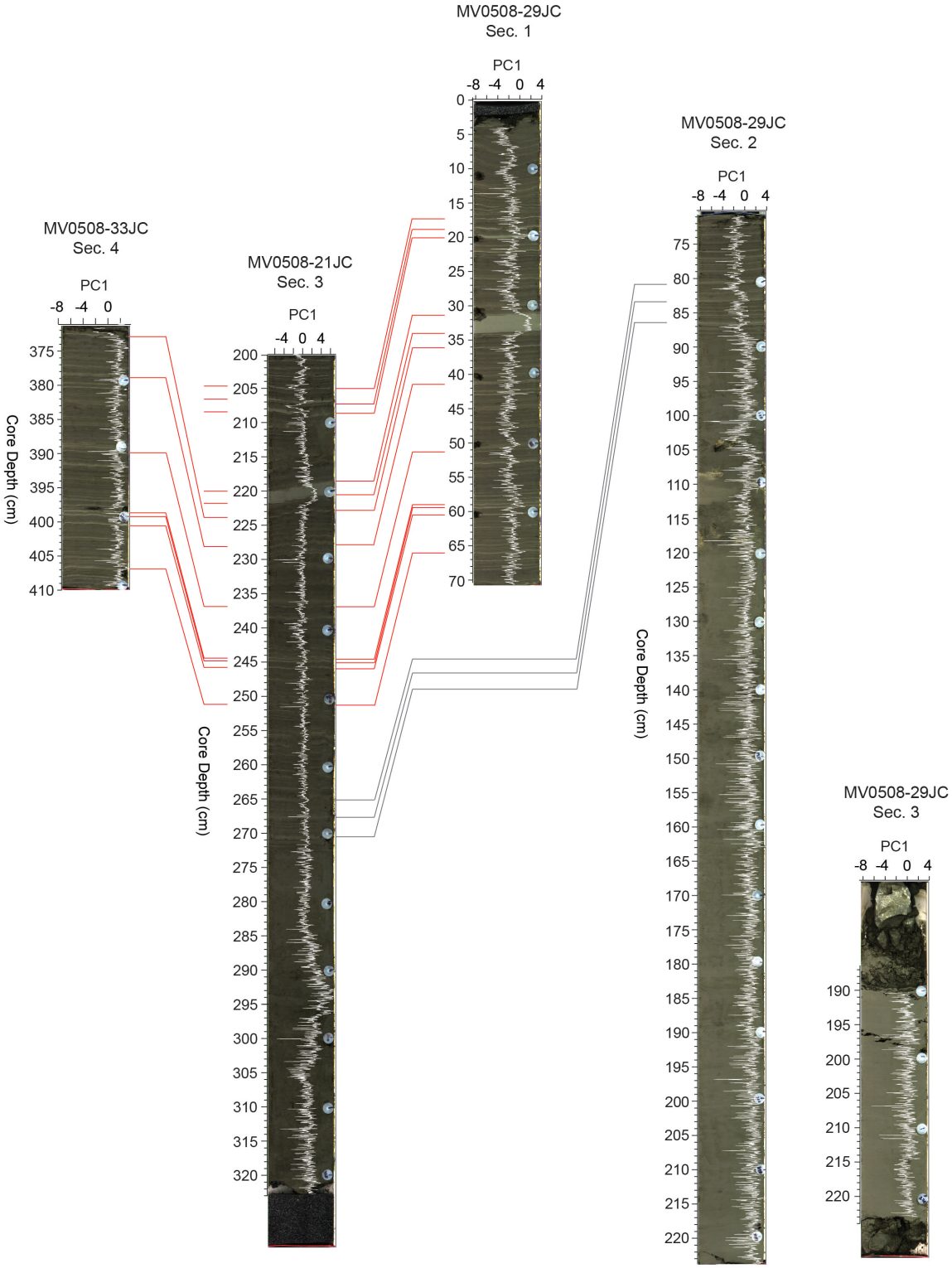


**Figure C.6.** Correlation of MV0508-33JPC section 4 to MV0508-21JPC section 3 and MV0508-29JPC section 1 (red lines), and correlation of 21JPC section 3 to 29JPC sections 1 and 2 (gray lines).
Red and gray lines denote tie-points (Appendix C Tables C.1 and C.2). Also shown is the high-resolution core photograph of 29JPC section 3. High-resolution core photographs are overlain with the computed PC1 of each core (white lines).

**Table C.2.** Correlation tie points between MV0508-33JPC and MV0508-21JPC.

| 33JPC Core Depth (cm) | 21JPC Core Depth (cm) |
|---|---|
| 167.12 | 13.52 |
| 171.05 | 15.95 |
| 175.29 | 18.59 |
| 178.67 | 19.84 |
| 186.14 | 26.71 |
| 189.10 | 30.09 |
| 204.99 | 46.80 |
| 208.00 | 52.36 |
| 210.19 | 55.22 |
| 211.16 | 56.52 |
| 212.74 | 57.96 |
| 215.53 | 61.73 |
| 216.80 | 63.21 |
| 220.99 | 70.47 |
| 232.88 | 82.27 |
| 235.41 | 84.86 |
| 239.66 | 90.01 |
| 248.81 | 99.87 |
| 252.76 | 103.97 |
| 254.05 | 105.43 |
| 256.11 | 107.57 |
| 298.16 | 150.92 |
| 299.69 | 153.43 |
| 300.20 | 153.86 |
| 308.21 | 162.87 |
| 311.40 | 166.08 |
| 311.92 | 166.40 |
| 318.50 | 173.07 |
| 349.43 | 204.92 |
| 350.82 | 207.06 |
| 352.53 | 209.08 |
| 367.15 | 219.31 |
| 370.14 | 221.39 |
| 372.85 | 222.81 |
| 378.83 | 227.68 |
| 389.87 | 236.87 |
| 398.70 | 244.56 |
| 399.23 | 244.88 |
| 400.44 | 245.83 |
| 406.85 | 251.25 |

**Table C.3.** Correlation tie points between MV0508-33JPC and MV0508-29JPC.

| 33JPC Core Depth (cm) | 29JPC Core Depth (cm) |
|---|---|
| 347.85 | 15.27 |
| 349.55 | 16.95 |
| 352.38 | 19.66 |
| 354.54 | 21.64 |
| 357.92 | 23.61 |
| 360.25 | 25.80 |
| 362.07 | 27.16 |
| 365.40 | 29.73 |
| 367.07 | 30.67 |
| 370.13 | 33.46 |
| 372.84 | 35.82 |
| 378.78 | 41.07 |
| 380.68 | 42.66 |
| 386.08 | 47.54 |
| 389.90 | 50.68 |
| 392.00 | 52.67 |
| 398.65 | 58.58 |
| 399.26 | 59.12 |
| 400.45 | 60.10 |
| 406.85 | 65.69 |
| 408.11 | 66.77 |

The composite PC1 record was created by splicing the standardized, detrended PC1 of the entire 33JPC core (laminated and bioturbated intervals, 0.14-409.78 cm) to the standardized, detrended PC1 of the entire 29JPC core. The 29JPC PC1 from depths 68.24 to 87.92 cm was spliced onto the base of 33JPC PC1 (Figure C.4, iii). The scanning XRF elemental counts are offset between 33JPC and 29JPC, but this offset is not observed in the quantitative elemental results. Therefore, we aligned the 29JPC PC1 with 33JPC PC1, as there is no observed quantitative elemental difference between the two cores (Figure C.7).

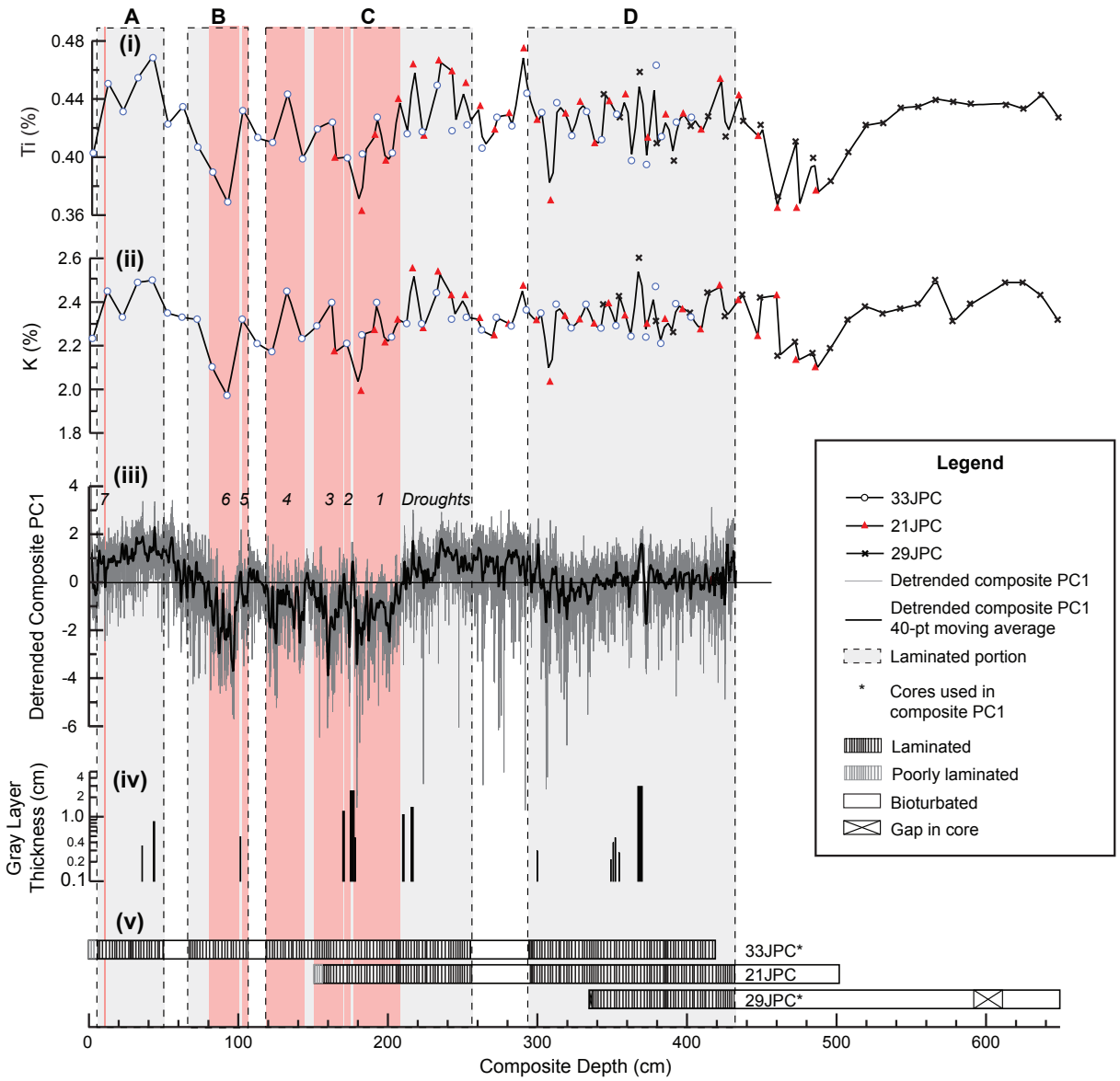


**Figure C.7.** Elemental composition and stratigraphy of cores MV0508-33JPC, -21JPC, and -29JPC. (i) Sample titanium (Ti) concentrations and linear re-sampling line (black). (ii) Sample potassium (K) concentrations and linear re-sampling line (black). (iii) Linearly detrended composite (33JPC and 29JPC) PC1 (gray line) with smoothing (black line, 40-point moving average) from scanning XRF elemental counts. (iv) Gray layer thickness and position in sediment core 33JPC. (v) Sediment core fabric descriptions with banding denoting laminations and massive intervals indicated by white shading. Gray shaded boxes represent laminated intervals A-D of the sediment cores. Red shaded boxes denote periods of drought.

## 4. Variability in floating annual timescales

Comparison of the floating annual timescales from 33JPC, 21JPC, and 29JPC for laminated interval D (328.6-409.78 cm, composite depth), and two 20 cm intervals, (330-350 cm and 375-395 cm composite depth intervals) demonstrates the variability of the annual tuning

method. For interval D in 33JPC, 929 years were resolved by the annual bandpass filter, with an average sedimentation rate of 87 cm/kyr. In 29JPC, 234 fewer years and in 21JPC, 117 fewer years were resolved than in 33JPC (Table C.4; Figure C.8, i). For the 330-350 cm composite depth interval, 252 years and an average sedimentation rate of 79 cm/kyr were resolved from 33JPC (Table C.4; Figure C.8, ii). The annual bandpass filter resolved eight additional years in 21JPC, while core 29JPC did not capture this entire depth interval and was excluded. The annual bandpass filter resolved 243 years for 33JPC in the 375-395 cm composite depth interval, with an average sedimentation rate of 82 cm/kyr, while 35 fewer years in 21JPC and 42 fewer years in 29JPC were resolved over the same depth interval (Table C.4, Figure C.8, iii). The differences in the number of years resolved by the annual tuning method range from a loss of 17% of years for 20 cm intervals to a 25% loss over an 80 cm interval.

**Table C.4.** Differences in the number of years resolved by the bandpass filter for correlated intervals of cores 33JPC, 21JPC, and 29JPC.

| | Number of Years Resolved | | | Average Sedimentation Rate (cm/kyr) | | |
|---|---|---|---|---|---|---|
| Interval \ Core | 33JPC | 21JPC | 29JPC | 33JPC | 21JPC | 29JPC |
| Laminated Portion D | 929 | 812 | 695 | 87 | 86 | 87 |
| 330-350 cm | 252 | 260 | | 79 | 77 | |
| 375-395 cm | 243 | 208 | 201 | 82 | 96 | 100 |

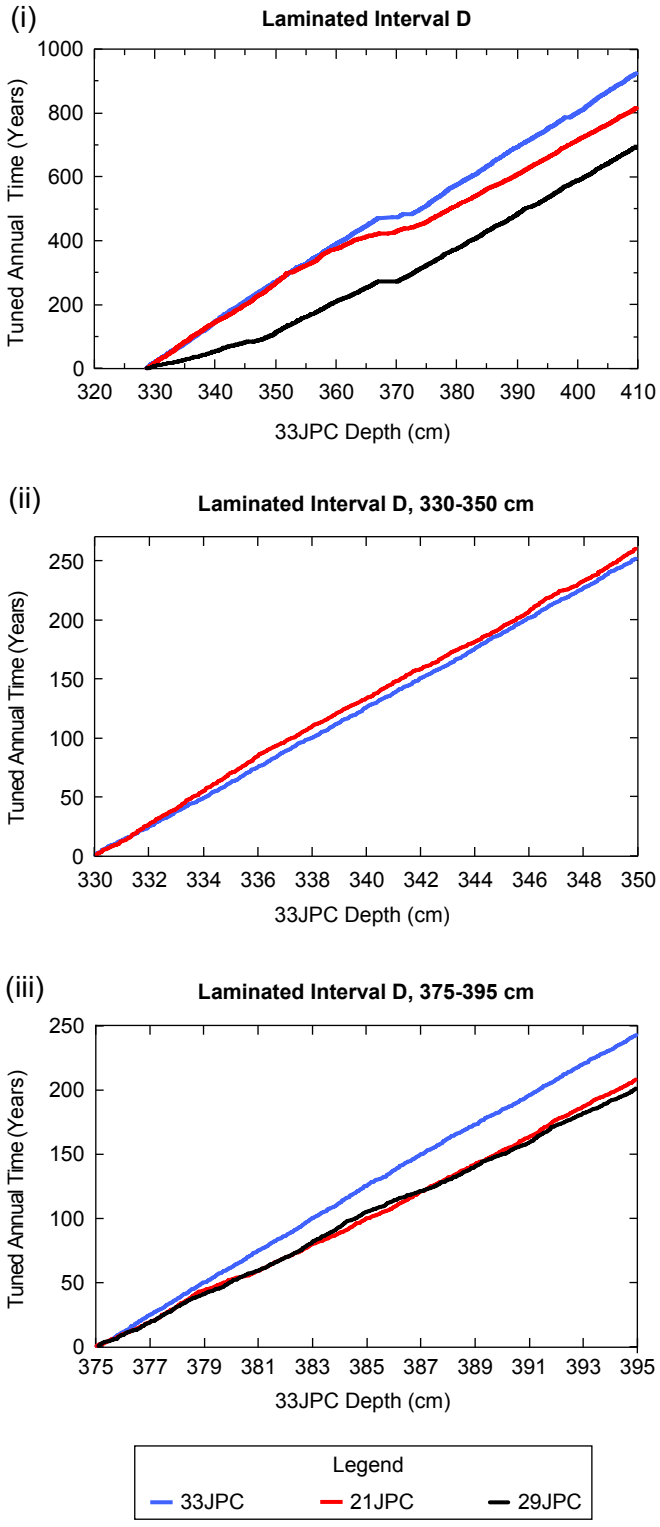


**Figure C.8.** Variability in computation of the annual timescales among correlated intervals of cores MV0508-33JPC (blue lines), 21JPC (red lines), and 29JPC (black lines).
(i) Comparison of the number of years determined during annual tuning in (i) laminated interval D (The flat portion around 370 cm marks the location of a thick gray layer.), (ii) 330-350 cm in laminated interval D, and (iii) 375-395 cm in laminated interval D.

## 5. Matlab Scripts

All Matlab scripts provided courtesy of Linda Hinnov, George Mason University, Fairfax, Virginia.

*maxima.m*

```
function [tmaxima]=maxima(signal);
tmaxima=[ ];
time=signal(:,1);
value=signal(:,2);
dtime=diff(time);
dvalue=diff(value);
nn=length(time);
nn1=length(dtime);
slope=dvalue./dtime;
m=0;
for n=2:nn1;
   if (slope(n-1) >= 0 & slope(n) < 0)
      m=m+1;
      tmaxima(m)=time(n);
   end
end
tmaxima=tmaxima';
```

*depthtotime.m*

```
%              depthtotime.m
%
% [time,sr]=depthtotime(depth,agemodel);
%
%  Converts depth scale to a time scale using a user-specified age model; written
%  for use by geologists developing chronologies for stratigraphic sections.
%
%  Inputs:
%
%   depth = array with all sampled depths of original series (increasing order)
%   agemodel = table with depth points assigned to specific times (increasing order)
%
%   Outputs:
%
%   time = array with times assigned to each depth of original series (increasing order)
%   sr = sedimentation rate for intervals between successive depth points
%
```

```
%   Linda Hinnov, May 24, 2006
%
function [time,sr]=depthtotime(depth,agemodel);
d=[ ];
t=[ ];
sr=[ ];
time=[ ];
d=agemodel(:,1);
t=agemodel(:,2);
m=length(d);
m1=m-1;
n=length(depth);
for i=2:m
   j=i-1;
   sr(j)=(d(i)-d(j))/(t(i)-t(j));
end
for j=1:m1
for i=1:n
  if depth(i) >= d(j) & depth(i) <= d(j+1)
  time(i)=t(j)+(depth(i)-d(j))/sr(j);
  end
end
end
for i=1:n
  if depth(i) <= d(1)
  time(i)=t(1)+(depth(i)-d(1))/sr(1);
  end
  if depth(i) >= d(m)
  time(i)=t(m1)+(depth(i)-d(m1))/sr(m1);
  end
end
time=time';
```

*deharm.m*

```
  function     [dataout]=deharm(data,period)
%    Program DEHARM - removes user-specified harmonic components
%     from a time series. (no uniform sampling needed)
%
%   Need inputs:
%      data=2-D array with (t,y)
%      period = period to estimate and remove
%   output:
%      y=1-D vector with detrended, deharmonized y variable
%      t=1-D vector with time variable
%      curve=1-D vector with fitted sinusoid
```

```
% This function is provided by Linda Hinnov to Mingsong Li for personal use
dataout=[ ];
s=[ ];
c=[ ];
curve=[ ];
t=data(:,1);                          % time or depth of data
y=data(:,2);                          % value
dataout(:,1)=t;                       % store t in dataout
y1=detrend(y);
ytrend=y-y1;
y=detrend(y);                         %
npts=length(y);                       % number of data points
freq=1.0/period;                      % calculate frequency
deharm_result=[];                     % Add by M.Li Nov16, 2014
fitcurve=[];                          % Add by M.Li Nov16, 2014
%%
for n=1:npts                          % circulation for calculate each
  tt=t(n);
  c(n)=cos(2.0*pi*tt*freq);           % normal cosine wave
  s(n)=sin(2.0 *pi*tt*freq);          % normal sine wave
end
X1=0.0;
X2=0.0;
X3=0.0;
X4=0.0;
X5=0.0;
X6=0.0;
for n=1:npts
 X1 = X1 + y(n)*c(n);
 X2 = X2 + c(n)*c(n);
 X3 = X3 + y(n)*s(n);
 X4 = X4 + c(n)*s(n);
 X5 = X5 + s(n)*c(n);
 X6 = X6 + s(n)*s(n);
end
B=(X1*X4-X2*X3)/(X4*X5-X2*X6);
A=(X1-B*X5)/X2;

for n=1:npts                          % calculate a fit curve using given period
  curve(n)=A*c(n)+B*s(n);
  dataout(n,2)=y(n) - curve(n);
end
dataout(:,2)=dataout(:,2)+ytrend;
%% plot and output
amp=sqrt(A*A+B*B);                    % Add by M.Li Nov16,2014
phase=atan2(A,B);                     % Add by M.Li Nov16,2014
```

```
%disp(' period freq amp phase A B');
deharm_result=[period,amp,phase];  % Add by M.Li Nov16,2014
% fitcurve=[t,curve'];
%figure;plot(t,curve);                    %
%figure;plot(t,y);                        %
end
```

*evofft.m*

```
%
% Function to compute a running periodogram of a uniformly sampled time series
% using FFTs of zero-padded (20x) segments. The output time-frequency
% running periodogram is plotted as a contour plot
%
% INPUT PARAMETERS
% data--2 columns with independent,dependent variables of time series
% (time,value); time must have increasing values
% dt--data sample rate (data must be uniformly sampled)
% window--window length for spectrogram (<< total data time) in time units
% step--step increment (<< window) in time units
% fmin--minimum output f (>= 0) in cycles/(time unit)
% fmax--maximum output f (<= Nyquist=1/(2dt)) in cycles/(time unit)
% unit--time unit of data, e.g. 'cm' or 'kyr'
% norm--1=normalize each spectrum; 2=no normalization (1 is recommended)
%
% CALCULATED PARAMETERS:
% kpts = 20 * mpts - padded FFT length of windows (frequency interpolation)
% df = 1/(kpts*dt) - output frequency bin size
% npts = length(xdata)
% nspec = (npts-mpts)/inc +1 - number of output spectra, must be a round number
% kfs = (fmax-fmin)/df+1 - number of points per output spectrum
%
% OUTPUT PARAMETERS:
%
% s -- 2 columns, each row contains one spectrum (fmin thru fmax by df)
% and contour plot in 'jet' colormap created by pcolor.m
%
% 2002: written by Linda Hinnov and Florian Maurer
% 2007: update Brian Zurek
% 2013: update by Nic Thibault
% 2014: title added by Tim Herbert
% 2015: adjustments by Linda Hinnov for Kodama and Hinnov, 2015 book
% 2017: plot axis corrections and normalization options added by Linda Hinnov
%
%TEST:
%
```

```
% Load "evoffttest.mat", note the settings in Workspace, and in the
% Command Window enter:
%
% s=evofft(data,window,step,dt,fmin,fmax,unit,norm);
%-------------------------------------------------------------------------------
function s=evofft(data,window,step,dt,fmin,fmax,unit,norm)
x=[ ];
sx=[ ];
s=[ ];
taxis=[ ];
faxis=[ ];
time=data(:,1);
xdata=data(:,2);
mpts=window/dt;
mpts=floor(mpts)
inc=step/dt;
inc=floor(inc);
kpts=20*mpts;
df=1./(kpts*dt);
kfs=(fmax-fmin)/df+1;
kfs=floor(kfs);
kmin=(fmin/df)+1;
kmin=floor(kmin);
kmax=kmin+kfs-1;
npts=length(xdata);
% number of spectra to be calculated
nspec=floor(npts-mpts)/inc+1;
%Start loop through all spectra
for n=1:nspec
m1=inc*(n-1)+1;
m2=m1+mpts-1;
taxis(n)=(m1+(mpts/2)-1)*dt;
                for m=m1:m2
                j=m-m1+1;
                x(j)=xdata(m);
                end
x=detrend(x);
sx=fft(x,kpts);
                for k=kmin:kmax
          k1=k-kmin+1;
          s(n,k1)=sqrt(sx(k)*conj(sx(k)));
                end
end
s=real(s); % prepares spectrogram for plotting
% normalize each spectrum unto itself if norm=1
if norm==1
```

```
maxval=max(s');
for i=1:nspec;
   for k=kmin:kmax;
      s(i,k)=s(i,k)/maxval(i);
   end
end
end
% 2-D plot (color contour)
figure;
[nrow,ncol]=size(s);
ddt=time(2)-time(1);
sign=round(ddt/dt);
% Set up x and y axes grids
x_grid=fmin:df:fmax;
% For y axis, start first label at half the window point
igrid=floor(0.5*mpts);
ttt1=time(igrid+1);
%ttt2= ttt1+(nrow-1)*sign*step
ttt2=time(npts-mpts/2-1);
stepit=(ttt2-ttt1)/nrow;
y_grid=ttt1:stepit:ttt2-stepit;
pcolor(x_grid,y_grid,s)
% adjust color and add basic annotations
colormap(jet)
shading interp
str=sprintf('Window = %d %s',window,unit);
title(str);
%title(['Time-frequency Landscape', window,' = ', unit])
xlabel(['frequency ( cycles per ',unit,' )'])
ylabel(['time ( in ',unit,' )'])
colorbar
% EOF
```

*crosscorrellationconfident.m*

```
%   CROSSITCONFIDENTnew(long,short)
%
%   Input:
%         long = 2-column array with col1=time, col2=value
%         short = 2-column arrary with col1=time, col2=value
%
%   Procedure slides "short" along "long" and calculates Pearson product-moment
%   correlation coefficient "rho" using the function "corrcoef" and estimates the
%   confidence limits (set presently to 95% limit).
%
%   The length of "short" (m) sets the degrees of freedom for the confidence limits, which
```

```
%   are estimated for normal, zero-mean z, then Fisher inverse-transformed to rho domain.
%   Correlation values are assigned to start position of "start" along the "long" series.
%   Correlation and confidence limits roll off at the end of the "long" series.
%   A future version will compute newer MATLAB options, i.e.:
%
%                   [R,P,RLO,RUP]=CORRCOEF(x,y) (e.g., Release 13)
%
%   Output:
%         time = 1-column array with time assignments for correlation (from "long")
%         rhosave = 1-column array with Pearson correlation coefficient
%         conhi = 1-column array with upper confidence limit (theoretical)
%         conlo = 1-column arry with lower confidence limit (theoretical)
%
%   L.A. Hinnov, Nov. 2007
function [time,rhosave,conhi,conlo]=crosscorrelationconfident(long,short)
rhosave=[ ];
conlo=[ ];
conhi=[ ];
long1=long(:,2);
short1=short(:,2);
time=long(:,1);
n=length(long1);
m=length(short1);
%nm=n-m;
nm=n-m+1;
%
% serror = estimated standard error in z
%
serror=1/(sqrt(m-3));
%
% 1.96 is 95%; 3.92 is 99%; convert to rho (Fisher inverse-trans.).
%
factor=3.92;
%factor=1.96;
zlimit=factor*serror;
rlimit=(exp(2*zlimit)-1)/(exp(2*zlimit)+1);
%
% Calculate running rho; store in rhosave
%
for i=1:nm;
   i;
   long2=long1(i:(i-1+m),1);
   rho=corrcoef(long2,short1);
   rhosave(i,1)=rho(1,2);
   conlo(i)=-1*rlimit;
   conhi(i)=+1*rlimit;
```

```
end
%
% roll off the confidence limits at end (progressively losing d.o.f.'s)
%
%nm=nm+1;
% WHY IS THIS 4????
nm4=n-4;
for i = nm:nm4;
   m=m-1;
   serror=1/(sqrt(m-3));
   zlimit=factor*serror;
   rlimit=(exp(2*zlimit)-1)/(exp(2*zlimit)+1);
   long2=long1(i:(i-1+m),1);
   short2=short1(1:m,1);
   rho=corrcoef(long2,short2);
   rhosave(i,1)=rho(1,2);
   conlo(i)=-1*rlimit;
   conhi(i)=+1*rlimit;
end
conhi=conhi';
conlo=conlo';
%save timescale time -ascii;
%save correlation rhosave -ascii;
%save confidencelow conlo -ascii;
%save confidencehigh conhi -ascii;
```

*corrcoef.m*

```
function [r,p,rlo,rup] = corrcoef(x,varargin)
%CORRCOEF Correlation coefficients.
%   R=CORRCOEF(X) calculates a matrix R of correlation coefficients for
%   an array X, in which each row is an observation and each column is a
%   variable.
%
%   R=CORRCOEF(X,Y), where X and Y are column vectors, is the same as
%   R=CORRCOEF([X Y]).  CORRCOEF converts X and Y to column vectors if they
%   are not, i.e., R=CORRCOEF(X,Y) is equivalent to R=CORRCOEF([X(:) Y(:)])
%   in that case.
%
%   If C is the covariance matrix, C = COV(X), then CORRCOEF(X) is
%   the matrix whose (i,j)'th element is
%
%        C(i,j)/SQRT(C(i,i)*C(j,j)).
%
%   [R,P]=CORRCOEF(...) also returns P, a matrix of p-values for testing
%   the hypothesis of no correlation.  Each p-value is the probability
```

```
%   of getting a correlation as large as the observed value by random
%   chance, when the true correlation is zero.  If P(i,j) is small, say
%   less than 0.05, then the correlation R(i,j) is significant.
%
%   [R,P,RLO,RUP]=CORRCOEF(...) also returns matrices RLO and RUP, of
%   the same size as R, containing lower and upper bounds for a 95%
%   confidence interval for each coefficient.
%
%   [...]=CORRCOEF(...,'PARAM1',VAL1,'PARAM2',VAL2,...) specifies additional
%   parameters and their values.  Valid parameters are the following:
%
%      Parameter  Value
%      'alpha'    A number between 0 and 1 to specify a confidence
%                 level of 100*(1-ALPHA)%.  Default is 0.05 for 95%
%                 confidence intervals.
%      'rows'     Either 'all' (default) to use all rows, 'complete' to
%                 use rows with no NaN values, or 'pairwise' to compute
%                 R(i,j) using rows with no NaN values in column i or j.
%                 The 'pairwise' option potentially uses different sets
%                 of rows to compute different elements of R, and can
%                 produce a matrix that is indefinite.
%
%   The p-value is computed by transforming the correlation to create a t
%   statistic having N-2 degrees of freedom, where N is the number of rows
%   of X.  The confidence bounds are based on an asymptotic normal
%   distribution of 0.5*log((1+R)/(1-R)), with an approximate variance equal
%   to 1/(N-3).  These bounds are accurate for large samples when X has a
%   multivariate normal distribution.
%
%   Example:  Generate random data having correlation between column 4
%             and the other columns.
%      x = randn(30,4);       % uncorrelated data
%      x(:,4) = sum(x,2);     % introduce correlation
%      [r,p] = corrcoef(x)    % compute sample correlation and p-values
%      [i,j] = find(p<0.05);  % find significant correlations
%      [i,j]                  % display their (row,col) indices
%
%   Class support for inputs X,Y:
%     float: double, single
%
%   See also COV, VAR, STD.

%   References:
%     [1] Fisher, R.A. (1958) Statistical Methods for Research Workers, 13th
%         ed., Hafner.
%     [2] Kendall, M.G., and Stuart, A. (1979), The Advanced Theory of
```

```
%         Statistics, 4th ed., Macmillan.
%      [3] Press, W.H., Teukolsky, S.A., Vetterling, W.T., and Flannery, B.P.
%         (1992) Numerical Recipes in C, 2nd ed., Cambridge University Press.

%   Copyright 1984-2011 The MathWorks, Inc.
%   $Revision: 5.11.4.16 $  $Date: 2011/05/17 02:22:15 $

if nargin<1
  error(message('MATLAB:corrcoef:NotEnoughInputs'));
end
if ~isempty(varargin) && isnumeric(varargin{1})
  y = varargin{1};
  varargin(1) = [];

  % Convert two inputs to equivalent single input.
  x = x(:);
  y = y(:);
  if length(x)~=length(y)
    error(message('MATLAB:corrcoef:XYmismatch'));
  end
  x = [x y];
elseif ~ismatrix(x)
  error(message('MATLAB:corrcoef:InputDim'));
end

% Quickly dispose of most common case.
if nargout<=1 && isempty(varargin)
  r = correl(x);
  return;
end

if ~isreal(x) && nargout>1
  error(message('MATLAB:corrcoef:ComplexInputs'));
end

% Deal with empty inputs
[n,m] = size(x);
if isempty(x)
   if n <= 1
      % Zero observations with m variables results in an m x m NaN,
      % unless m == 0 where we return a scalar NaN by convention.
      % Note, an empty row vector is treated as zero observations with
      % one variable, consistent with treatment of non-empty row vectors.
      r = NaN(max(m,1), class(x));
   else
      % n > 1 observations with no variables returns an empty matrix of
```

```
        % correlations.
        r = ones(0, class(x));
    end
    p = r; rlo = r; rup = r;
    return;
end

% Treat all vectors like column vectors.
if isvector(x)
    x = x(:);
    [~, m] = size(x);
end

% Process parameter name/value inputs.
[alpha,userows,emsg] = getparams(varargin{:});
if ~isempty(emsg)
    error(message(emsg));
end

% Compute correlations.
t = isnan(x);
removemissing = any(t(:));
if isequal(userows, 'all') || ~removemissing
    [r, n] = correl(x);
elseif isequal(userows, 'complete')
    % Remove observations with missing values.
    x = x(~any(t,2),:);
    [r, n] = correl(x);
else
    % Compute correlation for each pair.
    r = zeros(m,class(x));
    n = zeros(m,class(x));
    jk = 1:2;
    for j = 1:m
        jk(1) = j;
        for k=1:j-1
            jk(2) = k;
            tjk = ~any(t(:,jk),2);
            n(j,k) = sum(tjk);
            if n(j,k)<=1
                r(j,k) = NaN;
            else
                rjk = correl(x(tjk,jk));
                r(j,k) = rjk(1,2);
            end
        end
```

```
        tj = ~t(:,j);
        n(j,j) = sum(tj);
        if n(j,j)<=1
           r(j,j) = NaN;
        else
           r(j,j) = correl(x(tj,j));
        end
     end
     r = r + tril(r,-1)';
     n = n + tril(n,-1)';
end

% Compute p-value if requested.
if nargout>=2
   % Operate on half of symmetric matrix.
   lowerhalf = (tril(ones(m),-1)>0);
   rv = r(lowerhalf);
   if length(n)>1
      nv = n(lowerhalf);
   else
      nv = n;
   end

   % Tstat = +/-Inf and p = 0 if abs(r) == 1, NaN if r == NaN.
   Tstat = rv .* sqrt((nv-2) ./ (1 - rv.^2));
   p = zeros(m,class(x));
   p(lowerhalf) = 2*tpvalue(-abs(Tstat),nv-2);
   p = p + p' + diag(diag(r)); % Preserve NaNs on diag.

   % Compute confidence bound if requested.
   if nargout>=3
      % Confidence bounds are degenerate if abs(r) = 1, NaN if r = NaN.
      z = 0.5 * log((1+rv)./(1-rv));
      zalpha = NaN(size(nv),class(x));
      if any(nv>3)
         zalpha(nv>3) = (-erfinv(alpha - 1)) .* sqrt(2) ./ sqrt(nv(nv>3)-3);
      end
      rlo = zeros(m,class(x));
      rlo(lowerhalf) = tanh(z-zalpha);
      rlo = rlo + rlo' + diag(diag(r)); % Preserve NaNs on diag.
      rup = zeros(m,class(x));
      rup(lowerhalf) = tanh(z+zalpha);
      rup = rup + rup' + diag(diag(r)); % Preserve NaNs on diag.
   end
end
```

```
% ------------------------------------------------
function [r,n] = correl(x)
%CORREL Compute correlation matrix without error checking.

[n,m] = size(x);
r = cov(x);
d = sqrt(diag(r)); % sqrt first to avoid under/overflow
r = bsxfun(@rdivide,r,d); r = bsxfun(@rdivide,r,d'); % r = r ./ d*d';
% Fix up possible round-off problems, while preserving NaN: put exact 1 on the
% diagonal, and limit off-diag to [-1,1].
t = find(abs(r) > 1); r(t) = r(t)./abs(r(t));
r(1:m+1:end) = sign(diag(r));


% ------------------------------------------------
function p = tpvalue(x,v)
%TPVALUE Compute p-value for t statistic.

normcutoff = 1e7;
if length(x)~=1 && length(v)==1
   v = repmat(v,size(x));
end

% Initialize P.
p = NaN(size(x));
nans = (isnan(x) | ~(0<v)); % v == NaN ==> (0<v) == false

% First compute F(-|x|).
%
% Cauchy distribution.  See Devroye pages 29 and 450.
cauchy = (v == 1);
p(cauchy) = .5 + atan(x(cauchy))/pi;

% Normal Approximation.
normal = (v > normcutoff);
p(normal) = 0.5 * erfc(-x(normal) ./ sqrt(2));

% See Abramowitz and Stegun, formulas 26.5.27 and 26.7.1.
gen = ~(cauchy | normal | nans);
p(gen) = betainc(v(gen) ./ (v(gen) + x(gen).^2), v(gen)/2, 0.5)/2;

% Adjust for x>0.  Right now p<0.5, so this is numerically safe.
reflect = gen & (x > 0);
p(reflect) = 1 - p(reflect);
```

```
% Make the result exact for the median.
p(x == 0 & ~nans) = 0.5;


% ---------------------------------------------
function [alpha,userows,estruc] = getparams(varargin)
%GETPARAMS Process input parameters for CORRCOEF.
alpha = 0.05;
userows = 'all';
estruc = [];
while ~isempty(varargin)
  if length(varargin)==1
    estruc = ('MATLAB:corrcoef:unmatchedPVPair');
    return
  end
  pname = varargin{1};
  if ~ischar(pname)
    estruc = ('MATLAB:corrcoef:invalidArgName');
    return
  end
  pval = varargin{2};
  j = find(strcmp(pname,{'alpha' 'rows'}));
  if isempty(j)
    estruc = ('MATLAB:corrcoef:invalidArgName');
    return
  end
  if j==1
    alpha = pval;
  else
    userows = pval;
  end
  varargin(1:2) = [];
end

% Check for valid inputs.
if ~isnumeric(alpha) || ~isscalar(alpha) || alpha<=0 || alpha>=1
  estruc = ('MATLAB:corrcoef:invalidAlpha');
  return
end
oktypes = {'all' 'complete' 'pairwise'};
if isempty(userows) || ~ischar(userows)
  i = [];
else
  i = strcmpi(userows, oktypes);
end
if ~any(i)
```

```
    estruc = ('MATLAB:corrcoef:invalidRowChoice');
    return
  end
  userows = oktypes{i};
```

**References**


Hendy, I.L., Napier, T.J., Schimmelmann, A., 2015. From extreme rainfall to drought: 250 years of annually resolved sediment deposition in Santa Barbara Basin, California. Quatern. Int. 387, 3-12.

Lindsey, R., 2013. In Watching for El Niño and La Niña, NOAA adapts to Global Warming, ClimateWatch Magazine. National Oceanic and Atmospheric Administration, Climate.gov.

Mantua, N., 2017. PDO Index, in: Mantua, N. (Ed.).

Mantua, N.J., Hare, S.R., 2002. The Pacific Decadal Oscillation. J. Oceanogr. 58, 35-44.

Mantua, N.J., Hare, S.R., Zhang, Y., 1997. A Pacific interdecadal climate oscillation with impacts on salmon production. Bull. Am. Meteorol. Soc. 78, 1069-1079.

Napier, T.J., Hendy, I.L., in press. The impact of hydroclimate and dam construction on terrigenous detrital sediment composition in a 250-year Santa Barbara Basin record off southern California. Quatern. Int.

Rayner, N.A., Parker, D.E., Horton, E.B., Folland, C.K., Alexander, L.V., Rowell, D.P., Kent, E.C., Kaplan, A., 2003. Global analyses of sea surface temperature, sea ice, and night marine air temperature since the late nineteenth century. Journal of Geophysical Research: Atmospheres 108.